frontiers | Research Topics

Advanced EEG analysis techniques for neurological disorders

Edited by
Jisu Elsa Jacob, A. Amalin Prince, Omar Farooq and Saadullah Farooq Abbasi

Published in
Frontiers in Neuroinformatics

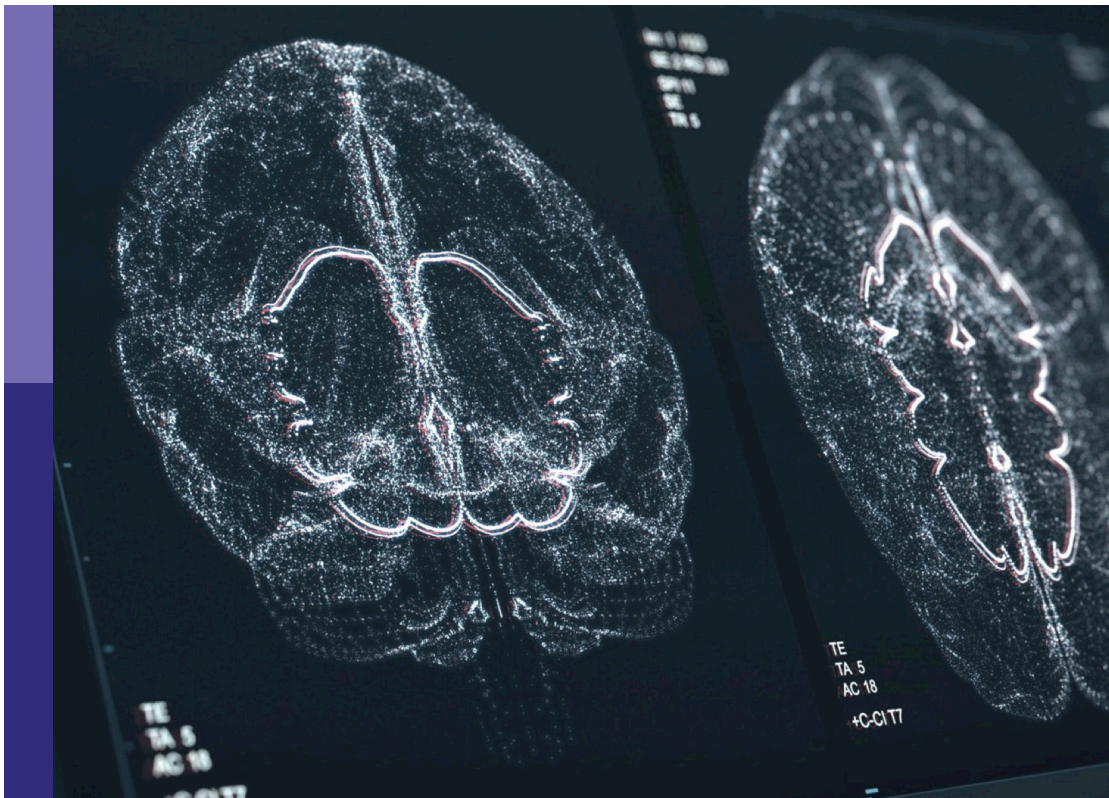

ISSN 1664-8714
ISBN 978-2-8325-6538-4
DOI 10.3389/978-2-8325-6538-4

Generative AI statement
Any alternative text (Alt text) provided alongside figures in the articles in this ebook has been generated by Frontiers with the support of artificial intelligence and reasonable efforts have been made to ensure accuracy, including review by the authors wherever possible. If you identify any issues, please contact us.

About Frontiers

Frontiers is more than just an open access publisher of scholarly articles: it is a pioneering approach to the world of academia, radically improving the way scholarly research is managed. The grand vision of Frontiers is a world where all people have an equal opportunity to seek, share and generate knowledge. Frontiers provides immediate and permanent online open access to all its publications, but this alone is not enough to realize our grand goals.

Frontiers journal series

The Frontiers journal series is a multi-tier and interdisciplinary set of open-access, online journals, promising a paradigm shift from the current review, selection and dissemination processes in academic publishing. All Frontiers journals are driven by researchers for researchers; therefore, they constitute a service to the scholarly community. At the same time, the *Frontiers journal series* operates on a revolutionary invention, the tiered publishing system, initially addressing specific communities of scholars, and gradually climbing up to broader public understanding, thus serving the interests of the lay society, too.

Dedication to quality

Each Frontiers article is a landmark of the highest quality, thanks to genuinely collaborative interactions between authors and review editors, who include some of the world's best academicians. Research must be certified by peers before entering a stream of knowledge that may eventually reach the public - and shape society; therefore, Frontiers only applies the most rigorous and unbiased reviews. Frontiers revolutionizes research publishing by freely delivering the most outstanding research, evaluated with no bias from both the academic and social point of view. By applying the most advanced information technologies, Frontiers is catapulting scholarly publishing into a new generation.

What are Frontiers Research Topics?

Frontiers Research Topics are very popular trademarks of the *Frontiers journals series*: they are collections of at least ten articles, all centered on a particular subject. With their unique mix of varied contributions from Original Research to Review Articles, Frontiers Research Topics unify the most influential researchers, the latest key findings and historical advances in a hot research area.

Find out more on how to host your own Frontiers Research Topic or contribute to one as an author by contacting the Frontiers editorial office: frontiersin.org/about/contact

Advanced EEG analysis techniques for neurological disorders

Topic editors

Jisu Elsa Jacob — Sree Chitra Thirunal College of Engineering, India

A. Amalin Prince — Birla Institute of Technology and Science, India

Omar Farooq — Aligarh Muslim University, India

Saadullah Farooq Abbasi — University of Birmingham, United Kingdom

Citation

Jacob, J. E., Prince, A. A., Farooq, O., Abbasi, S. F., eds. (2025). *Advanced EEG analysis techniques for neurological disorders*. Lausanne: Frontiers Media SA. doi: 10.3389/978-2-8325-6538-4

Table of contents

frontiers | Frontiers in Neuroinformatics

TYPE Editorial
PUBLISHED 18 June 2025
DOI 10.3389/fninf.2025.1637890

OPEN ACCESS

EDITED AND REVIEWED BY
Michael Denker,
Jülich Research Centre, Germany

*CORRESPONDENCE
Jisu Elsa Jacob
jisuelsa@sctce.ac.in

RECEIVED 29 May 2025
ACCEPTED 02 June 2025
PUBLISHED 18 June 2025

CITATION
Jacob JE and Chandrasekharan S (2025) Editorial: Advanced EEG analysis techniques for neurological disorders.
Front. Neuroinform. 19:1637890.
doi: 10.3389/fninf.2025.1637890

Editorial: Advanced EEG analysis techniques for neurological disorders

Jisu Elsa Jacob [1]* and Sreejith Chandrasekharan [2]

[1]Department of Electronics and Communication Engineering, Sree Chitra Thirunal College of Engineering, Trivandrum, Kerala, India, [2]Freelance Researcher, Trivandrum, Kerala, India

KEYWORDS

electroencephalogram (EEG), large language model (LLM), neurological disorders, visualization of EEG, Brain computer interface (BCI)

Editorial on the Research Topic
Advanced EEG analysis techniques for neurological disorders

1 Introduction

Electroencephalogram or EEG analysis has undergone a profound transformation with the addition of advanced artificial intelligence and computational methods to the domain. Contemporary EEG analysis expands beyond traditional methods that relied on visual inspection, employing refined algorithms that are capable of detecting subtle patterns that are not evident in time signals and to the human eye. Such state-of-the-art techniques include artificial intelligence, advanced statistical methods, and sophisticated signal processing approaches to unlock deeper insights into brain signals and dysfunctions. From using large language models (LLMs) for enhanced diagnostic interpretation to real-time Brain-Computer Interfaces (BCI), recent research has pushed the boundaries of EEG signal analysis.

2 Discussion of recent research in advanced EEG analysis

The technical summaries that follow are intended to provide an overview of recent and impactful peer-reviewed research that illustrates advanced approaches that address critical challenges in neurological care. Each of the topics represents a valuable leap forward in terms of the diagnosis and monitoring of complex neurological conditions with unparalleled precision and efficiency. The research papers included in this Research Topic address the following categories in this area of research.

2.1 Foundation AI models for neuroscience

Recent advances in large language models (LLMs) and the application of such models to EEG-based disease diagnostics, by tuning with a vast background knowledge base from neuroscience, disease diagnostics, and signal processing techniques, have helped in the transformation of such systems. Chandrasekharan et al. provide an overview of

the context, starting with a comparison of LLMs against traditional neural networks, such as sequence-to-sequence networks, which require large datasets, comprehensive training strategies, and learning parameter adjustments through hyperparameter tuning, demanding expert-level knowledge in Artificial Intelligence (AI). In contrast to such traditional systems, LLMs achieve expert-level performance through minimal training data, minor tuning through prompt engineering, and much less computational requirement, leading to shorter deployment times for highly effective diagnostic solutions. Such diagnostic methods not only aid in disease classification and analysis, but also generate human expert-like reasoning, justifying the decisions they make, which allows for review and further improvements under expert supervision. Optimization of such systems is achieved through Low-Rank Adaptation of Large Language Models (LoRA), addressing bottlenecks introduced by computational requirements. Furthermore, this survey highlights deployment challenges and ethical considerations, and stimulates research in EEG signal analysis through LLMs and related machine learning pipelines.

2.2 Brain-computer interface systems

The domain of the brain computer interface (BCI) generally requires a large amount of subject-specific labeled data for the training phase to achieve effective calibration of the models and ensure reliable classification on each new subject. With the motor imagery encephalographic signal analysis system (MI-EEG), the use of extended least squares regression-based inductive transfer learning helps achieve this knowledge transfer from the source domain to the target domain in the event of data insufficiency, as described in the study by Jiang et al.. By this approach, broader applications can be addressed with the inclusion of several classic base models such as neural networks, a custom fuzzy logic approach namely the Takagi-Sugeno-Kang fuzzy system and kernel methods, which can find patterns in complex data. In the context of the classification of physical actions studied by Gordienko et al., a fully connected deep neural network (FCN) in combination with layers of convolutional neural networks (CNN) classifies finger-palm-hand from the grasp-and-lift dataset. This study uses Natural Noise Augmentation (NDA) in contrast to a synthetic approach by increasing the sampling size and using different offset values for labeling introducing Gaussian noise and thus providing improved performance. The study performed with Detrended Fluctuation Analysis (DFA) investigated fluctuation properties and calculated Hurst components that revealed the ability of shorter EEG fragments to demonstrate higher complexity and enabled the system to run on low-resource-requirement systems.

2.3 Clinical data integration and visualization tools

EEG reports predominantly exist in unstructured textual formats, complicating data extraction and analysis for large-scale studies. A hierarchical algorithm transforms these reports using natural language processing (NLP) techniques through two phases: deep learning-based text classification followed by rule-based keyword extraction procedures in the study by Chung et al.. The algorithm categorizes reports into normal and abnormal groups, then systematically identifies key indicators of cerebral dysfunction or seizures, distinguishing between focal (localized) and generalized seizures while identifying epileptiform discharges and their anatomical locations. Analysis of 17,172 EEG reports from 3,423 pediatric patients achieved accuracy exceeding 98.5% for seizure type determination and over 88.5% for epileptiform discharge detection. In another study by Evans et al., stereoelectroencephalography (sEEG), combines preimplantation magnetic resonance imaging, post-implant computed tomography for electrode visualization, and temporally recorded electrophysiological data for surgical planning. SEEG4D creates automated containerized pipelines segmenting tissues and electrode contacts, aligning contacts with electrical activity, and animating based on relative power. This generates four-dimensional virtual reality components that allow simultaneous viewing of anatomy and seizure activity with automated contact segmentation within 1mm accuracy.

2.4 Disease specific diagnostic applications

The various EEG signal analyses have had a high impact in disease diagnosis and prediction, specifically in neurological diseases such as epilepsy, Alzheimer's disease, and even in the prediction of seizures and the diagnosis of early diseases such as dementia. In this Research Topic, Hernandez et al. analyzed the effects of Multiple sclerosis treatment using sample entropy that can measure signal regularity and Higuchi's fractal dimension that can quantify signal complexity in EEG signals from 175 subjects including Interferon-β (n=39), dimethyl fumarate (n=53), and healthy controls (n=83). Both treatment groups exhibited more complex EEG signals than controls, with sample entropy (SampEn) demonstrating significant sensitivity to treatment effects while Higuchi's fractal dimension (HFD) showed greater sensitivity to temporal changes. Absence seizure classification utilized power-to-power cross-frequency coupling (PPC) analysis in Medvedev et al., measuring interactions between oscillations across different time scales in brain rhythm organization. Stacked Sparse Autoencoder (SSAE) networks trained on coupling matrices between frequencies 2–120 Hz achieved 93.1% sensitivity, 99.5% specificity, and 96.8% overall accuracy. In another study in absence seizure, EEG phase synchronization analysis using wavelet phase Glaba et al., synchronization index with normalized amplitude features detected generalized spike-and-wave discharges with 99.2% identification rate. However, ictal-interictal overlap limited pure synchronization-based detection. In Hadeethi et al., alcoholism detection employed clustering technique-based bootstrap (CT-BS) to model sample selection, covariance matrix eigenvalue methods (Cov-Eig) for feature extraction, and the fruit fly optimization algorithm with radius-margin-based support vector machines (FOA-F-SVM). This approach achieved 99% accuracy in the classification of multichannel EEG signals.

3 Conclusion

The papers featured in this Research Topic demonstrate how advanced artificial intelligence and computational methods are revolutionizing EEG-based neurological diagnosis and brain-computer interface technologies. From leveraging foundation AI models like Large Language Models to developing sophisticated disease-specific diagnostic tools, these studies collectively address critical challenges in translating complex brain signals into actionable clinical insights. The integration of transfer learning approaches for brain-computer interfaces, advanced visualization tools for surgical planning, and precision diagnostic applications for conditions ranging from epilepsy to alcoholism illustrates the breadth and depth of current EEG research capabilities.

Author contributions

JJ: Conceptualization, Writing – original draft, Writing – review & editing, Investigation. SC: Writing – review & editing, Investigation, Conceptualization, Writing – original draft.

Conflict of interest

The authors declare that the research was conducted in the absence of any commercial or financial relationships that could be construed as a potential conflict of interest.

Publisher's note

frontiers in Neuroinformatics

ORIGINAL RESEARCH
published: 03 February 2022
doi: 10.3389/fninf.2021.808339

An Eigenvalues-Based Covariance Matrix Bootstrap Model Integrated With Support Vector Machines for Multichannel EEG Signals Analysis

Hanan Al-Hadeethi[1], Shahab Abdulla[2,3], Mohammed Diykh[4,5], Ravinesh C. Deo[4] and Jonathan H. Green[2,6]*

[1] School of Mathematics Physics and Computing, University of Southern Queensland, Toowoomba, QLD, Australia, [2] USQ College, University of Southern Queensland, Toowoomba, QLD, Australia, [3] Information and Communication Technology Research Group, Scientific Research Centre, Al-Ayen University, Nasiriyah, Iraq, [4] School of Sciences, University of Southern Queensland, Toowoomba, QLD, Australia, [5] College of Education for Pure Science, University of Thi-Qar, Nasiriyah, Iraq, [6] Faculty of the Humanities, University of the Free State, Bloemfontein, South Africa

Identification of alcoholism is clinically important because of the way it affects the operation of the brain. Alcoholics are more vulnerable to health issues, such as immune disorders, high blood pressure, brain anomalies, and heart problems. These health issues are also a significant cost to national health systems. To help health professionals to diagnose the disease with a high rate of accuracy, there is an urgent need to create accurate and automated diagnosis systems capable of classifying human bio-signals. In this study, an automatic system, denoted as (CT-BS- Cov-Eig based FOA-F-SVM), has been proposed to detect the prevalence and health effects of alcoholism from multichannel electroencephalogram (EEG) signals. The EEG signals are segmented into small intervals, with each segment passed to a clustering technique-based bootstrap (CT-BS) for the selection of modeling samples. A covariance matrix method with its eigenvalues (Cov-Eig) is integrated with the CT-BS system and applied for useful feature extraction related to alcoholism. To select the most relevant features, a nonparametric approach is adopted, and to classify the extracted features, a radius-margin-based support vector machine (F-SVM) with a fruit fly optimization algorithm (FOA), (i.e., FOA-F-SVM) is utilized. To assess the performance of the proposed CT-BS model, different types of evaluation methods are employed, and the proposed model is compared with the state-of-the-art models to benchmark the overall effectiveness of the newly designed system for EEG signals. The results in this study show that the proposed CT-BS model is more effective than the other commonly used methods and yields a high accuracy rate of 99%. In comparison with the state-of-the-art algorithms tested on identical databases describing the capability of the newly proposed FOA-F-SVM method, the study ascertains the proposed model as a promising medical diagnostic tool with potential implementation in automated alcoholism detection systems used by clinicians and other health practitioners. The proposed model, adopted as an expert

OPEN ACCESS

Edited by:
Rajesh Kumar Tripathy, Birla Institute of Technology and Science, India

Reviewed by:
Ram Bilas Pachori, Indian Institute of Technology Indore, India
Chang Li, Hefei University of Technology, China

***Correspondence:**
Mohammed Diykh
mohammed.diykh@usq.edu.au; mohammed.diykh@utq.edu.au

Received: *03 November 2021*
Accepted: *20 December 2021*
Published: *03 February 2022*

Citation:
Al-Hadeethi H, Abdulla S, Diykh M, Deo RC and Green JH (2022) An Eigenvalues-Based Covariance Matrix Bootstrap Model Integrated With Support Vector Machines for Multichannel EEG Signals Analysis. Front. Neuroinform. 15:808339. doi: 10.3389/fninf.2021.808339

system where EEG data could be classified through advanced pattern recognition techniques, can assist neurologists and other health professionals in the accurate and reliable diagnosis and treatment decisions related to alcoholism.

Keywords: alcoholism, electroencephalogram, covariance matrix, support vector machine (SVM), eigenvalues and fruit fly optimization

INTRODUCTION

The human brain, as an integral part of the central nervous system (CNS), operates normally by receiving signals from the body's organs and providing information to the muscles (Pelvig et al., 2008). The effects of alcohol on the CNS can lead to long- and short-term issues such as impaired vision, impaired hearing, dementia, and depression (Deiner and Silverstein, 2009). Alcoholism is a common neurological disorder caused by excessive and repetitive drinking of alcoholic beverages; the harmful effects of alcoholic beverages could be physical and mental as well as social, legal, and economic (Lieber, 1995; Volkow et al., 2017). The heavy consumption of alcohol disturbs the functioning of the entire nervous system, especially the brain. It not only weakens the brain neurons but also leads to cognitive and mobility weakness (Knight and Longmore, 1994; Oscar-Berman et al., 1997). Based on the latest reports issued by the WHO https://www.who.int/health-topics/alcohol#tab=tab_1, three million deaths every year are caused by the harmful use of alcohol. In addition, more than 200 disease- and injury-related conditions are caused by the excessive use of alcohol. An effective method of recognizing alcoholics from nonalcoholics could decrease unnecessary economic losses and social problems as well as expedite diagnosis in clinical settings.

Electroencephalogram (EEG) technology is becoming increasingly important in the identification, diagnosis, and treatment of mental and neurodegenerative diseases and abnormalities (Isaksson et al., 1981). The function of the EEG assists physicians in establishing an accurate diagnosis. Thus, it can be utilized as a diagnostic tool to discern alcoholics from nonalcoholic subjects based on the variation in the signals.

Much effort has been expended in deducing the preferred classification method in analyzing EEG signals for alcoholism. For instance, Faust et al. (2008) analyzed normal, epileptic, and alcoholic EEG signals utilizing fast Fourier transform (FFT) and autoregressive (AR) model and their techniques. Their results showed that the power spectral density (PSD) of these signals was varied. Patidar et al. (2017) applied tunable Q-wavelet transform (TQWT) to decompose EEG rhythms into different bands. The principal component analysis (PCA) was utilized for feature extraction and then fed to a least squares-support-vector machine (LS-SVM). Cao et al. (2017) utilized a synchronization likelihood to measure synchronization variations among 28 alcoholics and 28 control subjects. The study showed that the synchronization for the control group reflected the complexity levels of the cognitive tasks, while the alcoholics only displayed erratic changes. Lin et al. (2009) analyzed the clinical alcoholic and normal control FP1 EEG signals based on a Hilbert-Huang Transformation. The PCA and WT were also applied to analyze EEG data by Sun et al. (2006), and other studies have used the power spectrum of Haar mother wavelet, approximate entropy, sample entropy, and empirical mode decomposition. Kousarrizi et al. (2009) applied the power spectrum of the Haar mother wavelet to extract the features with PCA. The extracted features were fed to a support vector machine (SVM) and neural networks. The simulation results showed that their method achieved a higher rate of classification accuracy than other methods. Shooshtari and Setarehdan (2010) proposed a reduction method to select an optimum subset of EEG channels based on spectral analysis and correlation matrices: their technique was successful in selecting an optimal number of channels. Kumar et al. (2012) employed an approximate entropy and sample entropy to extract entropy features from EEG time series: they illustrated that the average value of ApEn and SampEn for an epileptic time series was less than that of a nonepileptic time series. The study of Priya et al. (2018) has used mode decomposition (EMD) for features extraction.

Time-frequency (T–F) image information, high-pass infinite impulse response (IIR) filter with zero phase distortion, Separability and Correlation analysis (SEPCOR), computer-aided diagnosis, and EEG rhythms-based features were utilized in many studies that follow. Bajaj et al. (2017) proposed a new hybrid method to classify automatically an alcoholic and a control EEG signal based on T–F image information and found it useful in conveying key characteristics in EEG signals. The results of this study were promising. Fattah et al. (2015) proposed a new method based on a high-pass IIR filter with zero phase distortion, which aimed to preserve the Gamma band and all higher frequencies with K-nearest neighbor (KNN) classifier and leave-one-out cross-validation technique. Their proposed scheme also classified alcoholic and nonalcoholic subjects with a higher rate of accuracy than did existing methods. To select an optimal feature subset automatically and to obtain a minimum correlation between selected channels and maximum class separation, a statistical feature selection technique based on SEPCOR was proposed by Shri and Sriraam (2016); a significant improvement in the classification accuracy based on the SEPCOR method was noted in that study compared with feature selection methods used in previous studies. The study of Acharya et al. (2014) presented a review of the known features of EEGs gained from people with alcoholism. EEG-rhythms-based features for automatic identification of alcohol EEG signals were also proposed by the study of Taran and Bajaj (2017); in that study, an extreme learning machine (ELM) and a least squares SVM classifiers were used to detect nonalcoholic and alcoholic EEG signals, with the investigators' techniques showing an accuracy of 97.92%.

Recently, there is a trend of using deep learning models for BP estimation; for example, Gao et al. (2021) designed an approach that combined recurrence plots and convolutional neural network to recognize fatigue driving. They showed that that complex network based on a deep learning model gave a high recognition rate. Tao et al. (2020) developed an attention-based convolutional recurrent neural network mode to classify emotion EEG signals. In that study, the convolutional recurrent neural network was used to extract spatial characteristics of EEG signals. Singhal et al. (2021) integrated FFT, a convolution neural network, and long short-term memory to classify EEG recordings into an alcoholic or control. Buriro et al. (2021) utilized wavelet scattering transform with a convolutional neural network and SVM to classify alcoholism from EEG signals. They found that wavelet scattering transform-based features with a conventional neural network had a high potential to detect alcoholic subjects.

As demonstrated in previous studies, finding new techniques for the detection of alcoholism can help in further clinical applications and research. The present study provides a new mechanism for the classification of alcoholism from multichannel EEG signals. This study has developed a new machine learning model for the reduction of data prior to the classification process by integrating the clustering and bootstrapping clustering technique-based bootstrap (CT-BS) technique in one phase of model design. To detect and further analyze the abnormalities in the EEG signal, the eigenvalues of the covariance matrix, determined from EEG signals, are investigated using a statistical method by extracting ten statistical features from the eigenvalues of the covariance matrix. These features are represented by the *mean, median, maximum, minimum, mode, range, SD, variation, skewness,* and *kurtosis* commonly used in EEG classification problems. To improve the automated detection system, a combination-based approach using the F-SVM and fruit fly optimization algorithm (FOA), i.e., FOA-F-SVM, has been proposed to correctly classify alcoholism from multichannel EEG signals. Based on an extensive literature search, the CT-BS-covariance matrix method with its eigenvalues (Cov-Eig)-based FOA-F-SVM model is proposed in this study for the first time to analyze and detect alcoholism from EEG signals. In respect to the results, compared with the other algorithms, the proposed model, CT-BS-Cov-Eig-based FOA-F-SVM, has promising performance, and can, therefore, be adopted as a classification technique for alcoholism-detection in EEG signals.

This research article is divided into several sections: Section 2 presents the methodology; Section 3 contains a description and explanation of the datasets, segmentation, sampling, feature extraction, and feature selection; Section 4 contains performance evaluation methods; Section 5 includes radius-margin-based SVM (F-SVM), fruit fly optimization algorithm (FOR), and the proposed classification model FOR-F-SVM; Section 6 includes experimental results, evaluation of the performance of the proposed FOA-F-SVM model, channels selection based on classification accuracy, comparison of classification accuracy of the proposed model FOA-F-SVM with KNN, k-means, and SVM, and comparison the proposed model, FOA-F-SVM, with previous studies and discussion; and Section 7 presents the conclusions.

MATERIALS AND METHODS

Experimental Effects of Alcoholism From Multichannel Electroencephalogram Dataset

In the work described in this study, we have utilized a public database known as the machine learning repository (UCI) Knowledge Discovery in Databases (KDD) Archive www.kdd.ics.usi.edu from Irvine, CA: the University of California, Department of Information and Computer Science (Hettich and Bay, 1999). Data were collected from 122 participants; for each participant, there were 120 trials with three kinds of stimuli (Zhang et al., 1997). The EEG signals were recorded from 64 channels, two electrooculography (EOG) channels, and one reference electrode. The duration of each trial was one second and the sampling rate of all channel data was 256 Hz. UCI KDD contains three types of datasets, which are SMNI CMI TEST, SMNI CMI TRAIN, and FULL, respectively. FULL datasets contain a few all-zero recordings (Zhu et al., 2011); therefore, the first two databases were utilized. There are 600 recorded files in SMNI CMI TEST and the same number in the SMNI CMI TRAIN, which equals 1,200 recorded files, and for each recording, there are signals from 64 electrode caps.

Methodology

This article describes the design of a new technique trained to classify alcoholism from multichannel EEG signals. A hybrid method called (CT-BS) by integrating clustering technique (CT) and bootstrapping (BS) has been developed to reduce the dimensions of the EEG data. Then, the covariance matrix with its eigenvalues, coupled with the FOA-F-SVM, is proposed to predict alcoholism in patients' recordings. KDD recorded at the University of California, Department of Information and Computer Science (Gao et al., 2021) is used for the evaluation of the proposed model. **Figure 1** demonstrates the proposed model. The EEG signals are divided into four segments; after that, each segment is sent into the CT-BS method for the sampling phase. To extract EEG features, the covariance matrix with its eigenvalues is applied. Following this, to detect and analyze abnormalities in the EEG signal, the eigenvalues of the covariance matrix are investigated and ten statistical features were extracted from eigenvalues of each covariance matrix. These features are *mean, median, maximum, minimum, mode, range, SD, variation, skewness,* and *kurtosis*. In this study, we used a nonparametric method, named the Kolmogorov–Smirnov test (KST), for selecting the most relevant features. The selected features are fed to the FOA-F-SVM to classify EEG signals. To estimate the performance of the proposed model, different types of assessment metrics, such as accuracy, sensitivity, and specificity, are used in the performance evaluation.

Segmentation

Based on our previous work (Diykh et al., 2018, 2019a,b, 2020, 2021), this project has applied the sliding window technique to split the EEG signals into their respective periods. It was found that the proposed method generated highly satisfactory

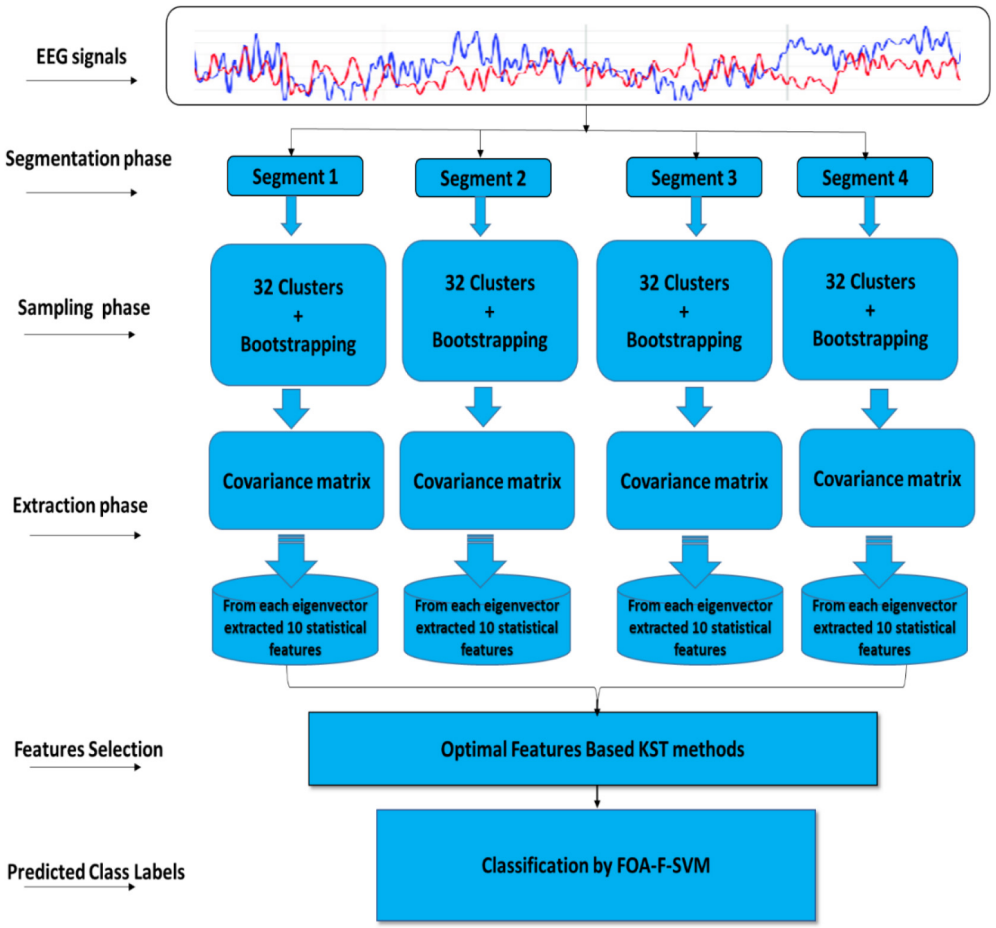

FIGURE 1 | A flow diagram representation of the algorithm developed for detection and classification of alcoholism-based EEG signals.

classification accuracy. Mathematically, let an EEG signal be denoted as: $X = x_1, x_2, \ldots\ldots, x_n$ with n being the data points. In this study, the EEG signal X was segmented into m segments, with each segment containing k datapoints (Diykh et al., 2020, 2021). **Figure 2** shows an example of an EEG signal being partitioned into segments.

Clustering Technique Coupled With-Based Bootstrap

To design a powerful sampling technique, a hybrid method that integrates the CT and BS, (CT-BS), is proposed in this study for reducing the dimensionality of EEG signals. This also prevents problems such as bias and variation that may occur when applying a CT. Not only is BS a method that depends on random sampling with replacement, but it also estimates the properties of an estimator. Adapting standard errors for clustering can be a very important part of any statistical analysis (Hennig, 2007); further, in terms of statistical modeling, validation is extremely important in cluster analysis because CTs resort to generate clustering even for completely homogeneous data groups. Most CTs suppose a certain paradigm for clusters, and this could be adequate for some portions of data, but not for others. The issue of stability in cluster analysis is complex, but it is considered an important part of cluster validity (Alonso et al., 2007). We propose to use the bootstrap method to reduce the error rate, which leads to reducing the bias and variation. The main concept behind utilizing the nonparametric bootstrap for the estimation of cluster constancy or stability is the following:

Suppose that there is a mixture distribution $K = \sum_{i=1}^{z} \varepsilon_i K_i$ where $i = 1, 2, 3, \ldots, z$, are the distributions generating z "true" clusters, and ε_i is the probability that a point from K_i is drawn (Hira and Gillies, 2015). For a given dataset with n points, the "true" clustering would then be composed of z clusters, each of which includes precisely the points generated by K_i, $i = 1, 2, 3,\ldots, z$. The dataset, when generated from K, is clustered; the generated clusters vary from the "true"' clusters because the clustering approach introduces an assured bias and variation.

The concept of bias and variation can be expressed *via* the maximum *Jaccard* coefficient. It is a measure of similarity for the two sets of data, with a range from 0 to 100%. A high percentage refers that two populations are similar among all the points created *via* K_i and the two sets belong to an identical cluster. The bootstrap is habitually utilized to grant an idea of bias and variation caused *via* a certain statistical approach because no true clustering is known and there is no true underlying distribution.

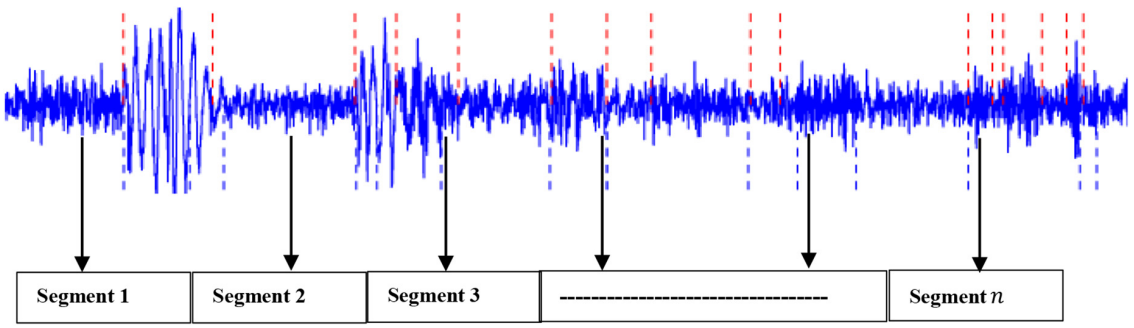

FIGURE 2 | An example of EEG being partitioned into segments.

To simulate *K*, the empirical distribution of the observed dataset is taken. The originally found clusters can be treated as the "true" ones, and the points can be drawn from the dataset. The mean maximal *Jaccard* coefficient can be explained as denoting the stability of the authentic clusters. Given a number *b* of bootstrap replications and a cluster *C* from the original clustering $E_n(y)$, the schema works as below:

Reiterate for $i = 1, 2, 3, \ldots, b$:

- For *n* points, draw a bootstrap sample y_n^i with replacement from the original dataset y_n.
- Calculate the clustering $E_n\left(y^i{}_n\right)$.
- Suppose $y_*^i = y_n \cap y_n^i$ be the points of the original dataset that are also in the bootstrap sample. Suppose $C^i{}_* = C \cap y_n^i$, $\triangle = E_n\left(y_n^i\right) \cap y_*^i$.
- If $C_*^i \neq \emptyset$, calculate the maximum *Jaccard* similarity between the induced cluster C_*^i and the induced new clustering $\triangle$ on y_*^i: $\tau_{C,i} = max_{D \in \triangle} \tau\left(C_*^i, D\right)$ (i.e., *D* is the maximizer of $\tau\left(C_*^i, D\right)$; else $\tau_{C,i} = 0$).
  where *Jaccard* coefficient (Jaccard, 1901): $\tau(C, D) = \frac{|C \cap D|}{|C \cup D|}$, $C, D \subseteq y_n$.

This generates a sequence $\tau_{(C,i)}$, $i = 1, 2, 3, \ldots, b$. Based on (Cameron et al., 2008; Diykh et al., 2019b) they suggested the mean: $\tau_C = \frac{1}{b^*} \sum_{i=1}^{b} \tau_{(C,i)}$ as stability measure (b^* being the number of bootstrap replications for which $C_*^i \neq \emptyset$ and is utilised here because in all other cases $\tau_{(C,i)} = 0$).

Features Extraction

In machine learning, with huge dimensions of data, the necessity to provide a reliable analysis grows exponentially (Alonso et al., 2007; Hira and Gillies, 2015). There are diverse types of mental and neurological conditions where the EEG data size is huge and requires observation by the clinician over an extended period. Alcoholism EEG signals may contain valuable and useful information about the different states of the brain. Since the biological signal is highly random in both the time and frequency domain, computerized analysis is indispensable. Due to the signals being nonstationary, appropriate analysis is fundamental for EEG to differentiate the alcoholic/control EEG signals. A covariance matrix method that was used in previous work (Al-Hadeethi et al., 2020) is proposed to reduce the EEG signal (and data) dimensionality while extracting the most important features for better classification accuracy.

The time series (EEG signals) can be defined as a vector of length $X = \{x_1, x_2, \ldots..,x_n\}$. Feature nominees can be integrated into a feature vector for a point in time series. Let P_i the number of features. The feature vector for the Nth point of the subsequence can be manifested as (Ergezer and Leblebicioğlu, 2016, 2018):

$$h_N = \left[P_{N1},\ P_{N2}, \ldots,\ P_{NQ}\right] \tag{4.1}$$

After combining the feature vectors for all points, this study gets a feature matrix *H*,

$$H = \begin{bmatrix} P_{11} & \cdots & P_{1Q} \\ & \vdots & \\ P_{W1} & \cdots & P_{WQ} \end{bmatrix} \tag{4.2}$$

It can be calculated as the covariance of the feature matrix as follows:

$$COV = \frac{1}{W-1} \sum_{i=1}^{W-1} (H_i - \mu)\ (H_i - \mu)^T \tag{4.3}$$

where μ is the mean vector of feature vectors $\{h_1, h_2, \ldots, h_W\}$.

Based on separating the time series into *L* overlapping subsequences with each having a length *W*, the general representation was adapted for the time series classification problem. In this study, to decrease the dimensionality of data which leads to enhance detection of possible abnormalities in the prescribed EEG signal, the eigenvalues of the covariance matrix are investigated by extracting 10 features from each eigenvector.

In this research, the data were derived from multichannel EEG signals, where each channel consists of a matrix (256 × 30), where 256 represents the number of rows and 30 represents the number of columns. For more clarification, we will explain using the following example: an experiment of 61channels that consists of a matrix (15,616 × 30) was used in this article. The time series was divided into four segments ($n = 4$), each segment containing (3,904 × 30) data points. Then, each segment of 3,904 datapoints was divided into 32 clusters with each cluster containing 120 data points. Based on our previous work (Zhu et al., 2011), it was found that dividing each EEG segment into 32 clusters gave

satisfactory results. As a result, each segment was represented by a matrix of 120 × 32. To reduce the dimensionality of each segment, the sampling technique was applied to reduce the number of clusters. The number of clusters was reduced from 32 to 30. Consequently, each segment was represented by 120 × 30 instead of 120 × 32. To remove any redundant information and extract features from each cluster, each cluster was divided into 4 sub-clusters, and a covariance matrix was applied to each subcluster, from each its eigenvector, 10 statistical features were selected to form a vector of 40 statistical features. As a result, each segment was represented by a matrix of 40 × 30, where 40 refers to the number of features and 30 indicates the number of clusters.

Feature Selection

In the work described in this study, one of the primary objectives of conducting many experiments was to find the optimal features that improved results. The features briefly summarize the most important information in the data, thus, this is used in cases where there is a large number of dimensions (Abdulla et al., 2019). Selecting the optimal features could lead to a high rate of classification accuracy. Therefore, six experiments were conducted on EEG channels to determine the features set using KST. More details are given in the results section.

CLASSIFICATION APPROACH BASED ON SVM

Radius-Margin-Based Support Vector Machine

Given the training set $q = (x_1,\ y_1)\ ,\ (x_n,\ y_n)$, the fundamental SVM paradigm is displayed below. The paradigm only deems the maximization of margin. However, an accurate description can explain that the generalization error bounds of SVM are the function of radius and margin (Hedges et al., 1999).

$$\begin{aligned} &\underset{d,b,\delta 2}{min}\ \tfrac{1}{2}||\ (n)\ ||_2^2 + Z\sum_i \delta_i \\ &s.t.\ y_i\left(n^T x_i b\right) \geq 1 - \delta_i \forall_i \\ &\delta_i = 0,\ i = 1,\ 2,\ 3,\ ..., \end{aligned} \tag{4.4}$$

Given the radius, a group of researchers, (Ergezer and Leblebicioğlu, 2016) have proposed a novel formula $\frac{1}{2}\overline{R} \leq R \leq \overline{R}$. Let the matrix $K = A^T A$ where A is denoted as transform matrix, the slack variables $\delta_i\ (i = 1,\ 2,\ 3,\ n)$. The paradigm of linear F-SVM is represented in (2):

$$\begin{aligned} &\underset{w,\ b,\delta,K}{\min}\ \tfrac{1}{2}\left(w^T K^{-1} w\right) Z\sum_{i=1}^{n}\delta_i + \rho tr\ (KS) \\ &s.t.\ y_i\left(w^T x_i b\right) \geq 1 - \delta_i\ \forall_i \\ &\delta_i = 0,\ i = 1,\ 2,\ 3,\ ..., \\ &K \succ 0 \end{aligned} \tag{4.5}$$

Wu et al. (2018) solved the nonlinear classification problems by incorporating kernel PCA into linear F-SVM. The proportion of cumulative eigenvalues to the sum of all eigenvalues is set as 0.9 in the dimension selection of kernel PCA. The paradigm can be formulated as follows:

$$\begin{aligned} &\min \tfrac{1}{2}\left(w^T K^{-1} w\right) Z\sum_{i=1}^{n}\delta_i + \rho tr\left(KNq\right) \\ &s.t.\ y_i\left(w^T f_i + b\right) = 1 - \delta_i\ \forall_i \\ &\delta_i = 0,\ i = 1,\ 2,\ 3,\ ..., \\ &K \succ 0 \end{aligned} \tag{4.6}$$

where $N_q = \sum_{i=1}^{n} w_i q_i q_i^T$, $q_i = Q^T \emptyset\ (x_i)$, $Q = [q_1, q_2, q_3, ..., q_{Go}]$ is indicated tothe eigenvectors corresponding to the first G eigenvalues. The mapping function of kernel F-SVM that is always utilized is radial-basis-function (RBF), i.e., $(x_i, x_j) = \exp\left(-\gamma||x_i - x_j||^2\right)$, where γ is the specified parameter to limit the width of the RBF (Chen et al., 2014). Between the minimization of training error and maximization of the classification margin in the paradigm, factor Z controls the trade-off (Tharwat and Hassanien, 2018). The classification accuracy differs between these two parameters. Therefore, defining the values of the parameters is essential to the performance of the SVM classifier.

Fruit Fly Optimization Algorithm

The fruit fly optimization algorithm is based on the foraging behavior of the insect after which it is named (Pan, 2012). The main concept of the algorithm is that the insect primarily flies toward food *via* utilizing its olfactory sensory neurons: one of the groups of neurons will emit a pheromone when it is near to food. Thereafter, the fruit fly will change its direction and fly to meet its peers. Through continually updating its status and flying direction, the fruit fly will finally get nearer to the food, the position of which is the optimum solution. The algorithm will be completed if the iteration reaches maximization or the outcome is to archive the permissible accuracy. The algorithm can be split into a number of steps:

1) The position of the fruit fly is random initialization (*InitX, InitY*).
2) For each fruit fly, given a random direction and distance to hunt for food *via* its olfactory sensory neurons:

$$X_i = X + Random\ value$$
$$Y_i = Y + Random\ value$$

3) Due to the unknown exact location of food, the distance will be computed from the location of the fly to the origin; thereafter, the mutual distance is computed. As a result, the value will be defined as a smell concentration judgment

value (d):

$$Dist_i = \left(X_i^2 + Y_i^2\right)^{1/2}$$

$$d1_i = \frac{1}{Dist_i}$$

4) to detect a better smell concentration, set the above smell concentricity judgment value into smell concentricity judgment function:

$$Smell_i = Function\ (n_i)$$

5) discover individuals with the raised concentricity in the population:

$$\left[bestSmell,\ bestIndex\right] = \max(Smell)$$

6) preserve the most appropriate concentricity and an assortment of the fruit fly, and other fruit flies to that coordinates utilizing vision:

$$X = X\left(bestindex\right)$$

$$Y = Y(bestindex)$$

7) In Steps 2-5, the iterative optimization was performed. Thereafter, judge whether the concentricity is higher than that of the former level. If so, perform Step 6.

Classification Based on FOA-F-SVM Model

This section introduces the main idea used in developing the newly proposed FOA-F-SVM system. In order to improve and further develop the performance accuracy of the traditional SVM model, the F-SVM for joint learning of the feature transformation and SVM classifier integrated with FOA were proposed for the analysis of alcoholism through multichannel EEG signals. As shown in **Figure 3**, the proposed model consists of different stages. The first five steps represent internal parameter optimization and the next five steps display the external evaluation of the classification performance. The path of the proposed model is this: tune parameters depend on the FOA, after that gain an optimum classifier. Eventually, by testing the dataset through external assessment, the performance of the classifier was measured.

The fruit fly optimization algorithm was utilized to set the parameters in the section of parameter optimization. Depending on the RBF kernel of the SVM classifier, the fruit fly's solution was used to represent the classifier parameters Z and γ. To direct the updating of the fruit fly location, the rate of classification accuracy of the structure SVM classifier was used. The optimum solution was gained *via* the iterative optimization procedure, depending on the location. The SVM classifier was built up with the optimum parameters gained above in the external assessment section; thereafter, the eventual classification outcomes were gained on the test set *via* this classifier.

Optimization Algorithm

In the FOA-F-SVM model, there are many unknown variables, such as in the formula (11). To solve obscure variables (matrix K and hyperplane (w,b)) of the FOA-F-SVM model, there are three main steps:

(i)* Initiating *K

Suppose the weighted covariance N_q performs eigenvalues decomposition, i.e., $N_q = D\bigwedge D^T$, where $\bigwedge = Diag\{\lambda_{1,2\ldots}, \lambda_n\}$ and λ is arranged in order from highest to lowest. After algebraic computation, matrix K_0 can be denoted as $K_0 = D\wedge^{-(1/2)}D^T$. Due to $K = A^TA$, the transformation matrix A can be written as $A_0 = \wedge^{-(1/4)}D^T$. Therefore, the samples are transformed into $z = dataset * A_0$.

(ii) Resolve hyperplane (w, b)

This step consists of an explanation of how the FOA model is adopted to gain an optimum SVM classifier. The particular operation is that: the range of each parameter is given; thereafter, various values are randomly allocated within this range for every fruit fly. In the meantime, the fruit fly is represented in every group solution. Subsequently, find the preferable of these solutions. The finding operation includes two portions: *via* a smell search procedure, every fruit fly adjusts its position; based on the preferable fruit fly through the vision-based search procedure, the worst fruit fly in the population will be encouraged. This will then lead to obtaining a solution of the parameters *via* the iteration. Eventually, the test samples from z and gained optimum parameters are fed to the F-SVM prediction model.

(iii) Resolve matrix K

Now, having gained the SVM classifier, formula (11) can be formulated again as follows:

$$\min_K f\ (K) = \tfrac{1}{2}\left(w^TK^{-1}w\right)Z\sum_{i=1}^{n}\delta_i + \rho tr\ (KN) \qquad (4.7)$$

$$s.t.\ K \succ 0$$

The function is cambered and is able to be differentiated for K, thus, to solve K, the gradient-projection method was chosen. The derived function for this term is given below. Thereafter, update K *via* $K_{h1} = PN(K_h - t_1\nabla f\ (K_h))$ until K converges.

$$\nabla f\ (K) = -\frac{1}{2}K^{-1}ww^TK^{-1} + \rho N \qquad (4.8)$$

(iv) From all the illustrations and explanations above, it is clear that the matrix K is a significant parameter in the FOA-F-SVM. Only *via* initializing K, it can transform the dataset into a new feature space. Thereafter, an SVM classifier is gained *via* optimizing parameters through FOA. Eventually, an optimal classifier is gained by constantly updating K.

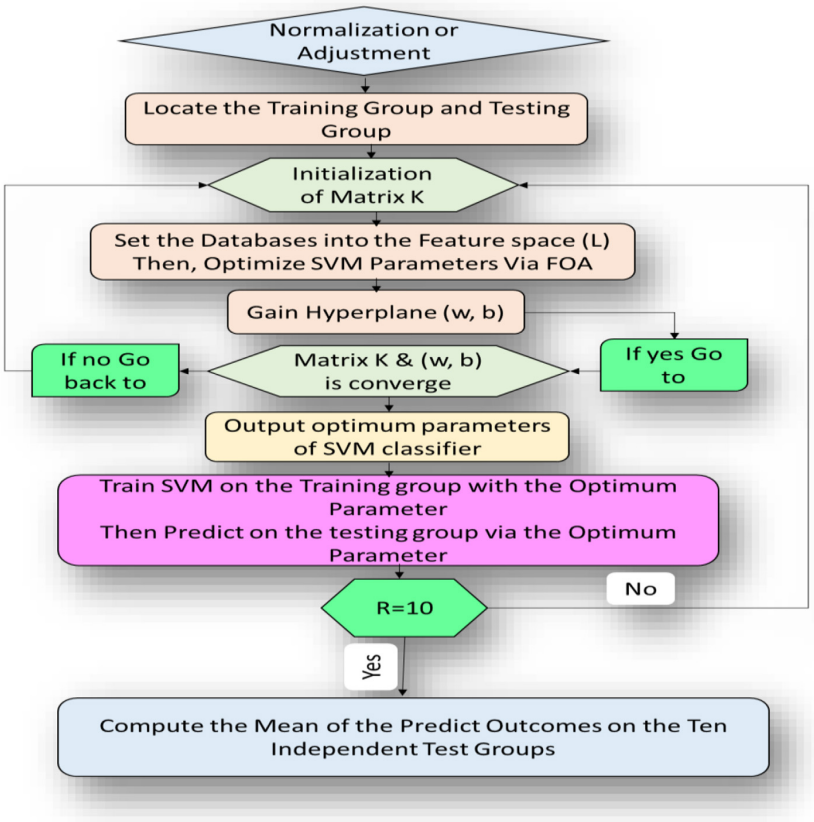

FIGURE 3 | Flow diagram representation algorithm of the proposed FOA-F-SVM model.

PERFORMANCE EVALUATION METHODS

It is important to evaluate the performance of any classification or detection system. A set of methods was used to assess the performance of the alcoholism classification and detection system based on the proposed FOA-F-SVM technique, as described below:

(a) Accuracy (Acc.) is a degree of proximity of a measured or calculated quantity to its actual (true) value. The term accuracy is utilized to assess the performance of the SVM method depending on the formula as given below:

$$Acc. = (TPTN)/(TPTNFPFN) \tag{4.9}$$

(b) Sensitivity (Sen.) is a statistical measure of the performance of a binary classification test used to measure the rate of the real positive prediction. This is defined as follows:

$$Sen. = TP/(TPFN) \tag{4.10}$$

(c) Specificity (Spe.) is utilized to measure the proportion of the real negative predication and is defined as follows:

$$Spe. = TN/(TNFP) \tag{4.11}$$

(d) Predictive positive value (PPV) is defined as the rate of positives that correspond to the presence of the condition described *via* the formula as below:

$$PPV = TP/(TPFP) \tag{4.12}$$

(e) Predictive negative value (PNV) is the ratio of negatives that correspond to the absence of the condition and is defined as follows:

$$PNV = TN/(TNFN) \tag{4.13}$$

EXPERIMENTAL RESULTS

To conduct the simulation effectively, the same number of iterations and the same population size were set for particle swarm optimization (PSO), genetic algorithm (GA), and FOA. According to our preliminary experiment, when the number of maximum iteration and population size are, respectively,

set as 100 and 20, the methods involved result in satisfactory classification performance. Furthermore, in the experiment, parameter Z is in range $Z \in \{2^{-10,1,20}\}$, parameter g is set *as* $g \in \{2^{20,1,10}\}$. The parameters of each model are as follows: for FOA-F-SVM, the x and y are denoted to initialize the location of fruit fly and the search direction *ax*, *bx*, *ay*, *and by* are set as 10, 20, 20, and 10, respectively, in the distance function. For PSO-SVM, the maximum velocity is 0.5 times the maximum parameter Z. The learning factors $Z1$, $Z2$ were set as 1.6, 1.5, and the intermediate variable w was set as 1 in the updating velocity function and updating location function. All experiments were carried out on a desktop computer with a CPU (2.30 GHz) and 8.00 GB RAM under the MATLAB 2020 programming environment.

The experimental EEG data used to assist the proposed model were obtained from the University of California, Irvine Knowledge Discovery in Databases Archive UCI KDD. The EEG signals were collected from 122 participants, and each subject performed 120 trials with three types of stimuli (Tao et al., 2020). The recordings were obtained from 61 channel EEG signals, two EOG channels, and one reference electrode. There are three datasets, named SMNI_CMI_- TRAIN, SMNI_CMI_TEST, and FULL, respectively. In this study, only the first two databases were utilized because the full datasets contain a few all-zero recordings. There were 600 recorded files in SMNI_CMI_TRAIN, with each recording containing the signals from 64 electrodes caps. The 64 electrodes are FC_4, FC_3, C_6, C_5, F_2, F_1, TP_8, TP_7, AFZ, CP_3, CP_4, P_5, P_6, C_1, C_2, PO_7, FP_1, FP_2, F_7, F_8, AF_1, AF_2, FZ, F_4, F_3, FC_6, FC_5, FC_2, FC_1, T_8, T_7, CZ, C_3, C_4, CP_5, CP_6, CP_1, CP_2, P_3, P_4, PZ, P_8, P_7, PO_2, PO_1, O_2, O_1, X, AF_7, AF_8, F_5, F_6, FT_7, FT_8, FPZ, PO_8, FCZ, POZ, OZ, P_2, P_1, CPZ, *nd*, and Y. The electrodes X and Y are EOG signals, and *nd* is reference electrode. The EOG and *nd* were removed in our analysis. However, the features were extracted from 61 channels.

Features Selection Using KST

In this section, six experiments were conducted to select the most powerful features to classify EEG signals.

In the first experiment, 11 channels were tested (AF_1, AF_2, AF_7, AF_8, AFZ, C_1, C_2, C_3, C_4, C_5, and C_6) to determine whether these channels were adequate to analyze the alcoholism signals. **Table 1** reports the results of feature selection using KST. Based on statistical analysis, the results showed that using these channels could explain 60% of the data.

In the second experiment, the channels AF_8, C_1, C_2, C_3, C_4, CP_1, CP_5, CP_6, FC_5, FT_7, P_8, PO_8, and P were utilized in the second experiment below. The outcomes indicate that the acceptance rate was high, reaching 90%, which means that the signal in these channels was suitable for detecting the EEG signals. **Table 2** reports the obtained results.

In the third experiment, the number of channels tested was 23. The success rate was 70%. The channels were CP_1, CP_2, CP_3, CP_4, CP_5, CP_6, CPZ, CZ, F_1, F_2, F_3, F_4, F_5, F_6, F_7, F_8, FC_1, FC_2, FC_3, FC_4, FC_5, FC_6, and FCZ. **Table 3** reports the results of experiment 3.

In the fourth experiment, the acceptance rate was 50%. A total of twenty-eight channels passed the test in this experiment. The channels used in this experiment were FP_1, FP_2, FPZ, FT_7, FT_8, FZ, O_1, O_2, OZ, P_1, P_2, P_3, P_4, P_5, P_6, P_7, P_8, PO_1, PO_2, PO_7, PO_8, POZ, PZ, S_1, T_7, T_8, TP_7, and TP_8 (**Table 4**).

In the fifth experiment, the channels AF_1, AF_2, AF_7, AF_8, AFZ, FP_1, FP_2, FPZ, FT_7, FT_8, P_1, P_2, P_3, P_4, P_5, P_6, P_6, P_7, P_8, PO_1, PO_2, PO_7, PO_8, POZ, F_1, F_2, F_3, F_4, F_5, F_6, F_7, F_8, T_7, T_8, TP_7,

TABLE 1 | Feature set outcome of Experiment No. 1.

Features	Testing	Training	Compared with the *p*-values
	Controlled vs. Alcohol	Controlled vs. Alcohol	
Mean	0.1088	0.2003	Rejected
Max	0.46	0.342	Rejected
Med	0.0017	2.9480×10^{-09}	Accepted
Min	0.011	0.02	Accepted
Mod	0.011	0.02	Accepted
Range	1.7552×10^{-05}	0.034	Accepted
Skew	0.1088	0.94	Rejected
Kur	0.1	0.93	Rejected
Std.	2.0212×10^{-04}	0.01088	Accepted
Var.	1.7552×10^{-05}	0.02003	Accepted

TABLE 2 | Feature set outcome of Experiment No. 2.

Features	Testing	Training	Compared with the *p*-values
	Controlled vs. Alcohol	Controlled vs. Alcohol	
Mean	5.5870×10^{-08}	0.02585	Accepted
Max	2.0480×10^{-09}	0.00455	Accepted
Med	1.7973×10^{-14}	3.5202×10^{-10}	Accepted
Min	1.4977×10^{-13}	0.00165	Accepted
Mod	1.4977×10^{-13}	0.00165	Accepted
Range	2.0480×10^{-09}	2.6199×10^{-07}	Accepted
Skew	0.10875	0.935	Rejected
Kur	0.045	6.1578×10^{-04}	Accepted
Std.	0.00465	0.045	Accepted
Var.	1.1088×10^{-08}	0.00165	Accepted

TABLE 3 | Feature set outcome of Experiment No. 3.

Features	Testing	Training	Compared with the *p*-values
	Controlled vs Alcohol	Controlled vs Alcohol	
Mean	0.055	0.3420	Rejected
Max	0.0259	0.0017	Accepted
Med	0.0113	1.7552×10^{-05}	Accepted
Min	1.1615×10^{-12}	5.6313×10^{-11}	Accepted
Mod	1.1615×10^{-12}	5.6313×10^{-11}	Accepted
Range	0.05	0.0113	Accepted
Skew	0.2003	0.76	Rejected
Kur	0.5372	0.9360	Rejected
Std.	6.1578×10^{-04}	0.011	Accepted
Var.	0.0113	0.002	Accepted

TABLE 4 | Feature set outcome of Experiment No. 4.

Features	Testing	Training	Compared with the *p*-values
	Controlled vs Alcohol	Controlled vs Alcohol	
Mean	0.34	0.2	Rejected
Max	0.53	0.20	Rejected
Med	0.002	0.005	Accepted
Min	0.06	0.2003	Rejected
Mod	0.06	0.2003	Rejected
Range	0.012	0.0017	Accepted
Skew	0.8	0.54	Rejected
Kur	0.026	0.0259	Accepted
Std.	0.005	0.0046	Accepted
Var.	6.1578×10^{-04}	0.005	Accepted

TABLE 5 | Feature set outcome of Experiment No. 5.

Features	Testing	Training	Compared with the *p*-values
	Controlled vs Alcohol	Controlled vs Alcohol	
Mean	6.1740×10^{-05}	0.012	Accepted
Max	2.0212×10^{-04}	0.109	Accepted
Med	1.7973×10^{-14}	0.03	Accepted
Min	0.34	0.9	Rejected
Mod	0.34	0.9	Rejected
Range	2.0212×10^{-04}	0.005	Accepted
Skew	0.55	0.54	Rejected
Kur	0.93	0.4	Rejected
Std.	0.76	0.46	Rejected
Var.	0.1088	0.01	Rejected

TABLE 6 | Feature set outcome of Experiment No. 6.

Features	Testing	Training	Compared with the *p*-values
	Controlled vs Alcohol	Controlled vs Alcohol	
Mean	0.045	0.0446	Accepted
Max	0.3420	0.1088	Rejected
Med	6.1740×10^{-05}	1.7973×10^{-14}	Accepted
Min	1.4977×10^{-13}	0.026	Accepted
Mod	1.4977×10^{-13}	0.026	Accepted
Range	0.011	0.03	Accepted
Skew	0.1	0.76	Rejected
Kur	0.046	0.034	Accepted
Std.	0.00238	0.01	Accepted
Var.	0.0476	0.02	Accepted

TABLE 7 | Classification accuracy of the comparison among FOA-F-SV, PSO-SVM, GA-SVM, F-SVM, and SVM.

Approach	Accuracy	Sensitivity	Specificity
FOA-F-SVM	99.2%	98.4%	98.5%
PSO-SVM	95.5%	94.3%	95.9%
GA-SVM	96.5%	95.2%	95.3%
F-SVM	92.5%	91.7%	92.4%
SVM	85.5%	86.2%	84.6%

and TP_8 were used in this experiment. The acceptance rate was very low, that is, 40%. This indicates that the channels used were not valid for classification (**Table 5**).

In the sixth experiment, the results obtained from Experiment No. 6 indicate that the use of 61 channels was efficient in the analysis. They could, thus, be used to classify EEG signals. The 61 channels were as follows: FC_4, FC_3, C_6, C_5, F_2, F_1, TP_8, TP_7, AFZ, CP_3, CP_4, P_5, P_6, C_1, C_2, PO_7, FP_1, FP_2, F_7, F_8, AF_1, AF_2, FZ, F_4, F_3, FC_6, FC_5, FC_2, FC_1, T_8, T_7, CZ, C_3, C_4, CP_5, CP_6, CP_1, CP_2, P_3, P_4, PZ, P_8, P_7, PO_2, PO_1, O_2, O_1, AF_7, AF_8, F_5, F_6, FT_7, FT_8, FPZ, PO_8, FCZ, POZ, OZ, P_2, P_1, CPZ (**Table 6**).

As a result, with the highest acceptance rates, the second and sixth experiments performed the best. The last group of features utilized to identify each pair of EEG groups (Controlled *vs.* Alcoholic) were *[Mean, Median, Minimum, Mode, Range, Kurtosis, SD, and Variance]*. Therefore, by conducting a number of experiments, we were able to thoroughly investigate the feature selection in order to select the most effective feature set to recognize EEG groups.

Evaluating the Performance of the Proposed FOA-F-SVM Model

To evaluate the performance of the FOA-F-SVM in alcoholic EEG signals, a comparison was made with SVM, PSO-SVM, GA-SVM, and F-SVM. **Table 7** shows the average results of the comparison among the FOA-F-SVM, PSO-SVM, GA-SVM, F-SVM, and SVM. Based on the results, the performance of the FOA-F-SVM attains higher classification accuracy than other approaches. However, the PSO-SVM and GA-SVM scored the second highest results, and they outperformed the basic SVM. These research findings indicate that tuning parameters were important in improving classification accuracy of EEG signals. In addition, the classification accuracy obtained by the F-SVM is higher than the basic SVM.

Figure 4 shows the detailed classification accuracy of 10 runs, as well the results of FOA-F-SVM, which are up to 98%, while the results of PSO-SVM and GA-SVM are distributed in the range from 90 to 94%. While the F-SVM and SVM gained a rate of accuracy from 86 to 93%. As a result, it can be observed that the FOA-F-SVM obtained the highest accuracy on each run and the best value is 100%. However, because of the robustness of the proposed method, the average result is the highest with 99.2%.

Channel Selection Based on Classification Accuracy

The accuracy of the proposed model based on 61-channel EEG signals is shown in **Figure 5**. In this experiment, the features were extracted from each channel and forwarded to the proposed model. The results show that not all channels yielded high classification accuracy. As a result, 13 optimal channels, including AF_8, C_1, C_2, C_3, C_4, CP_1, CP_5, CP_6, FC_5, FT_7, P_8, PO_8, PZ, were selected and used to classify EEG signals as shown in **Figure 5**.

The results in **Figure 5** are compatible with the results obtained by statistical metrics in the feature selection and enhanced the results (not all channels gave high classification accuracy). The present study thus demonstrates the ability of the proposed model to assess alcoholic EEG signals from multichannel EEG signals. The extracted features from electrodes C1, C3, and FC5 were found to be significantly effective in

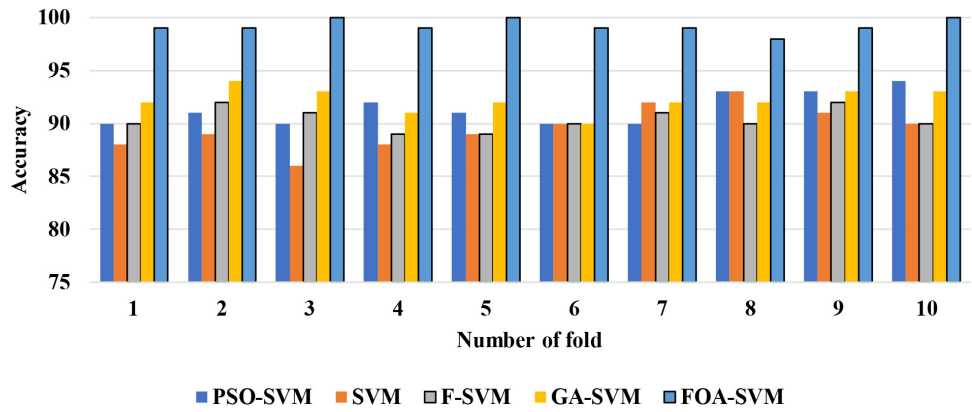

FIGURE 4 | The detailed classification accuracy of 10 folds.

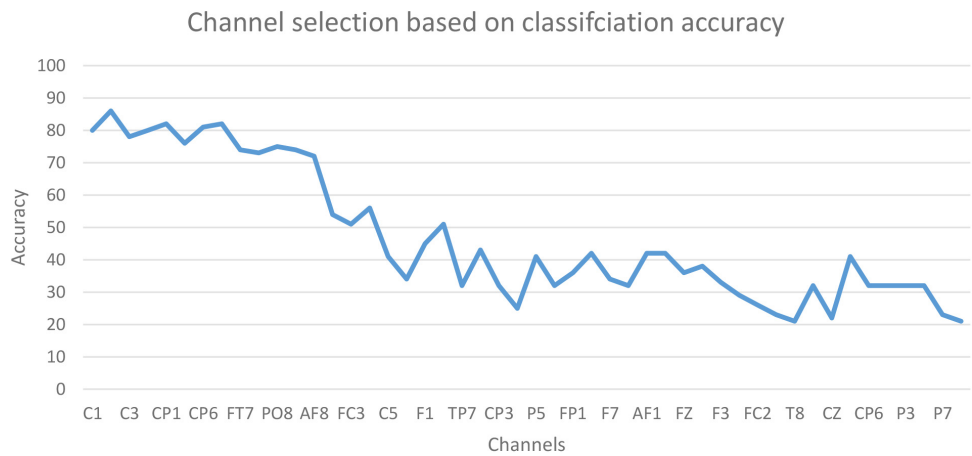

FIGURE 5 | The accuracy based on EEG channels.

classifying EEG signals: an accuracy of 87.6 % was achieved. In addition, it was found that when the 13 channels were used to extract the features, the classification accuracy was close to the whole 61-channel performance. **Table 8** presents the classification accuracy based on the number of channels.

DISCUSSION

This study carried out an analysis of EEG signals to detect the prevalence and health effects of alcoholism from multichannel EEG signals. We integrated the CT with BS, CT-BS, to reduce the dimensionality of EEG signals. Then, the covariance matrix with its eigenvalues was applied to investigate the EEG signals, and to extract the important features. Arithmetic operators based on the KST technique were utilized to remove the noisy features from the obtained features set. The FOA-F-SVM was proposed to classify the EEG signals. The proposed FOA-F-SVM classification mode was compared with different methods such as SVM, PSO-SVM, GA-SVM, and F-SVM. In this section, we summarized the following main findings:

(1) The novelty of this article lies in the utilization of CT and BS (CT-BS) coupled with the covariance matrix for feature extraction. It has been shown that the low dimensionality of EEG signals achieved by CT-BS can efficiently improve the classification rate. In comparison to other dimension-reduction techniques such as linear discriminate analysis (LDA) and PCA, the experimental results indicate that CT-BS performs better than PCA and LDA, and the classification rate of the FOA-F-SVM was increased with CT-BS by more than 9%. **Table 9** reports the classification rate based on dimension reduction techniques.

TABLE 8 | Classification accuracy based on the number channels.

Channel No.	Accuracy	Sensitivity	Specificity
C_1, C_3 and FC_5	85.6%	83.8%	82.4%
AF_8, C_1, C_2, C_3, C_4, CP_1, CP_5, CP_6, FC_5, FT_7, P_8, PO_8, P	99.4%	98.7%	99.1%
All 61 channels	99.5%	98.3%	99.2%

TABLE 9 | Classification rate based on different features reduction algorithms.

Technique \metrics	Accuracy	Sensitivity	Specificity
PCA with OA-F-SVM	89.1	90.2	88.2
LDA with OA-F-SVM	87.4	85.3	86.3
CT-BS with OA-F-SVM	99.2	98.1	99.3

(2) The proposed approach is a simple classification method for the identification of normal *versus* alcoholic EEG signals. The complexity of the proposed method was tested using a different number of samples. The results of the simulation showed that the proposed method achieved a better performance among traditional classification algorithms with acceptable time consumption. Therefore, this method could be a practical and feasible model for a real-time brain–computer interface (BCI) system. **Figure 6** reports the run time of the proposed classification model compared with LS-SVM, k-nearest, f-SVM, and GA-SVM. It can be noticed that the proposed model is faster than LS-SVM, k-nearest, f-SVM, and GA-SVM.

(3) The proposed model is still at the experimental stage. Larger datasets are required to make further validation of this model before it could be utilized as a tool in real-time applications.

(4) In this article, a small EEG dataset was used to evaluate the proposed model. The next work will focus on the use of a large EEG dataset such as EEG sleep stages, aesthetic EEG data, to analyze the performance of the proposed model under a huge dataset. This can guide us to improve the effectiveness of the proposed model.

(5) Although the CT-BS technique improved the performance of the classification model, it took more time than the PCA and LDA. In the future, we will work on how to reduce the complexity time of the CT-BS model.

(6) Comparison of classification accuracy of the proposed model FOA-F-SVM with KNN, k-means, and SVM: In this experiment, on the performance of the proposed model, FOA-F-SVM based on 13 EEG channels was reported. For further verification and to reach the highest level of reliability, the results were compared with KNN, k-means,

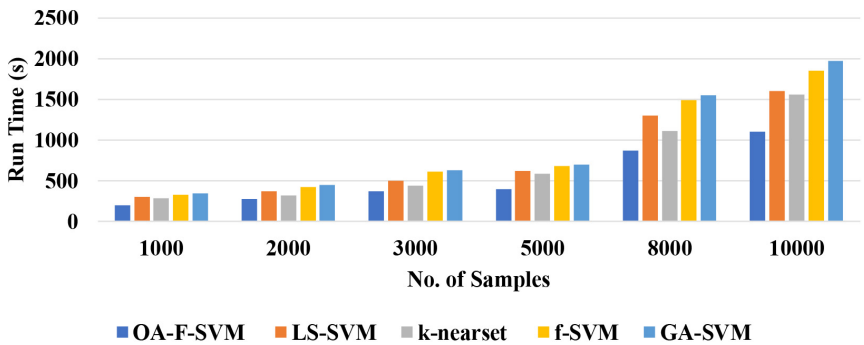

FIGURE 6 | A Comparison of run time among the proposed model with other.

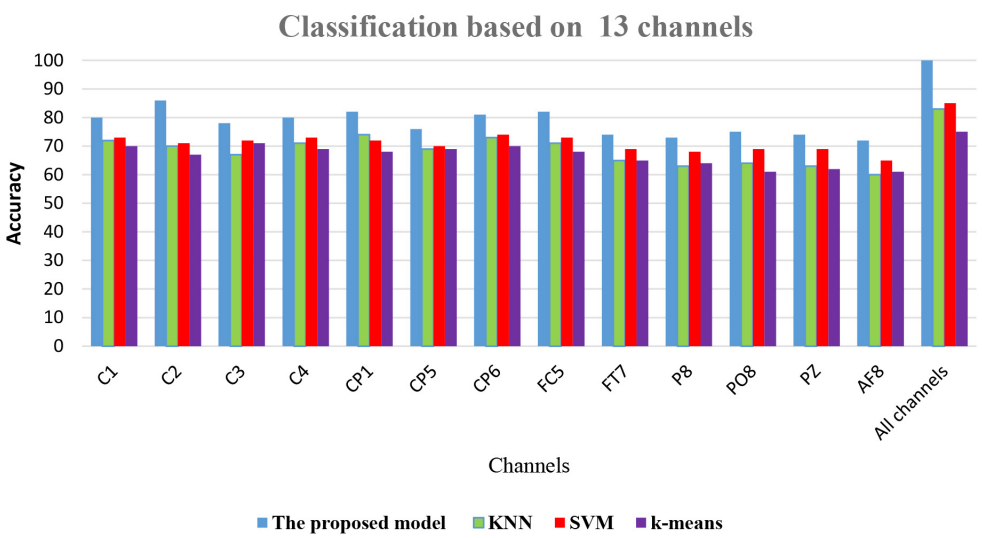

FIGURE 7 | A Comparison among the proposed model with SVM, *k*-means, and KNN.

TABLE 10 | Comparison with existing methods using the same database.

Authors	Features/ techniques	Analysis	Accuracy
Acharya et al. (2012)	APPENT, SAMENT, LLE	SVM	91.7%
Faust et al. (2013b)	WPT, energy measures	KNN	95.8%
Patidar et al. (2017)	TQWT, CE	LS-SVM	97.02%
Faust et al. (2013a)	HOS cumulants	FSC	92.4%
Kannathal et al. (2005)	CD, LLE, entropy, H	Unique ranges	90%
Anuragi and Sisodia (2020)	Empirical wavelet transform	LS-SVM, KNN	98.75%
Bavkar et al. (2021)	Empirical Mode Decomposition	KNN	93.87%
The proposed model	**CT-BS-Cov-Eig**	**FOA-F-SVM**	**99%**

and SVM. To the best of our knowledge after extensive research, this is the first time the FOA-F-SVM model has been proposed and applied to the analysis and detection of alcoholism EEG signals. The results showed that compared to other algorithms, the proposed model FOA-F-SVM has promising performance that can be adopted as a classification technique of alcoholism EEG signals. The database SMNI_CMI_TRAIN was used for the training, and the database SMNI_CMI_TEST was utilized for the testing set. To show clearly the classification results based on the 13 selected channels, **Figure 7** depicts the accuracy of the proposed model FOA-F-SVM with KNN, k-means, and SVM. The proposed model outperformed KNN, k-means, and SVM over all the 13 channels. In addition, the proposed model achieves 99% when all channels are used for the classification of EEG signals.

(7) Many studies were focused on finding a system that could be utilized for the automated detection of alcoholism EEG signals to estimate the effect of treatment and help significantly with clinical diagnosis. In this point, we shall review some of the previous studies that used the same data as this work did; for each, we shall provide a comparison of results. The identification of nonlinear features such as SAMENT, APPENT, largest Lyapunov exponent (LLE), and higher-order spectra (HOS) with LS-SVM classifier was used by Acharya et al. (2012), who obtained an average classification accuracy of 91.7%. However, the classification accuracy that is achieved by the proposed model is significantly higher than that of Acharya et al. (2012). Another group of researchers (Faust et al., 2013b) has improved an automated system utilizing wavelet packet-based energy measures with the KNN classifier; this method achieved a classification accuracy of 95.8%, which is less than the rate obtained by the proposed model.

A study by Patidar et al. (2017) suggested an automated system for the diagnosis of alcoholism. The study utilised TQWT to decompose EEG signals into various bands (SBS). Compared to the results obtained by the proposed method, the model of Patidar et al. (2017) obtained a classification accuracy of 97.02%, which is, again, less than our classification accuracy of 99%. For the detection of alcoholic-related changes in EEG signals, (Pan, 2012) have proposed the use of HOS cumulants-based features. Based on the fuzzy Sugeno classifier (FSC), the investigators achieved a classification accuracy of 92.4%, which is considerably less than the 99% obtained in the present work. Finally, the largest Lyapunov exponent (LLE), entropies, correlation dimension (CD), and Hurst exponent (H) were proposed by (Kannathal et al., 2005) to obtain the features for detecting alcoholism from EEG signals: the rate of accuracy was 90%, which is considerably less than the classification accuracy achieved by the model proposed in this study. Anuragi et al. (Anuragi and Sisodia, 2020) proposed an adaptive filtering model to extract time–frequency-domain characteristics from Hilbert–Huang transform. LS-SVM and KNN were used to classify the extracted features into alcoholic and normal signals. Bavkar et al., 2021) also applied empirical mode decomposition to classify alcoholic EEG signals. The extracted features using empirical mode decomposing were sent to the KNN classifier.

The results in **Table 10** show that the method proposed was superior to other studies and obtained a higher level of accuracy. After conducting many experiments and various types of comparisons, it has become clear that the proposed CT-BS-OFA-F-SVM model has a promising future in analyzing and classifying EEG signals with a high rate of accuracy. It was also noted that most of the previous studies were working on developing one part of the analysis, whereas, in this study, the focus was on most of the analysis steps.

CONCLUSION

Accurate detection algorithms can be used effectively to help clinical research as a fast, reliable, and easy-to-use tool in the diagnosis and monitoring of neurological disorders and in alcoholism. We developed an effective method that was designed for sampling by integrating CT and BS (CT-BS) in one phase. To detect and analyze abnormalities in the EEG signal, the eigenvalues of the covariance matrix were investigated utilizing a statistical method that extracted ten statistical features from the eigenvalues of the covariance matrix. To classify EEG signals, the FOA-F-SVM was proposed to detect and analyze multichannel EEG signals. The proposed model was compared to previous studies, and the results showed that the proposed model was superior, with a high accuracy rate of 99%.

The acquired results clearly illustrate the superior performance of the proposed CT-BS model coupled with FOA-F-SVM to the existing state-of-the-art methods. The proposed model can be used to assist neurologists and other medical specialists in the precise diagnosis of alcoholism EEG signals. Future studies may investigate the improvement of the performance of the proposed model by decreasing the number of features used in this initial study. Also, because there is a great similarity between the results of feature selection and the results of channel selection, the possibility of proposing and implementing feature selection methods will be studied to find the optimal channels. Furthermore, with regard to the few numbers of studies focused on designing feature extraction as well as a detection model for the reliable diagnosis of alcoholism EEG signals, there is a need for further research in this area.

DATA AVAILABILITY STATEMENT

The original contributions presented in the study are publicly available. This data can be found here: https://kdd.ics.uci.edu/databases/eeg/eeg.html.

AUTHOR CONTRIBUTIONS

SA: conceptualization, methodology, software, validation, data curation, formal analysis, and writing – review and editing. MD: methodology, resources, software, and validation. RD: investigation, methodology, resources, software, validation, visualization, and writing - review and editing. JG: writing - review and editing and investigation. All authors contributed to the article and approved the submitted version.

ACKNOWLEDGMENTS

The authors acknowledge the EEG data from the University of California, Department of Information and Computer Science. The authors also thank all reviewers and the journal Editor-in-Chief for considering this article and facilitating the review process.

REFERENCES

Abdulla, S., Diykh, M., Laft, R. L., Saleh, K., and Deo, R. C. (2019). Sleep EEG signal analysis based on correlation graph similarity coupled with an ensemble extreme machine learning algorithm. *Expert Syst. Appl.* 138:112790. doi: 10.1016/j.eswa.2019.07.007

Acharya, U. R., Bhat, S., Adeli, H., and Adeli, A. (2014). Computer-aided diagnosis of alcoholism-related EEG signals. *Epilepsy Behav.* 41, 257–263. doi: 10.1016/j.yebeh.2014.10.001

Acharya, U. R., Sree, S. V., Chattopadhyay, S., and Suri, J. S. (2012). Automated diagnosis of normal and alcoholic EEG signals. *Int. J. Neural Syst.* 22:1250011. doi: 10.1142/S0129065712500116

Al-Hadeethi, H., Abdulla, S., Diykh, M., Deo, R. C., and Green, J. H. (2020). Adaptive boost LS-SVM classification approach for time-series signal classification in epileptic seizure diagnosis applications. *Expert Syst. Appl.* 161:113676. doi: 10.1016/j.eswa.2020.113676

Alonso, I. P., Llorca, D. F., Sotelo, M. Á., Bergasa, L. M., de Toro, P. R., Nuevo, J., et al. (2007). Combination of feature extraction methods for SVM pedestrian detection. *IEEE Trans. Intell. Transp. Syst.* 8, 292–307. doi: 10.1109/TITS.2007.894194

Anuragi, A., and Sisodia, D. S. (2020). Empirical wavelet transform based automated alcoholism detecting using EEG signal features. *Biomed. Signal Process. Control* 57:101777. doi: 10.1016/j.bspc.2019.101777

Bajaj, V., Guo, Y., Sengur, A., Siuly, S., and Alcin, O. F. (2017). A hybrid method based on time–frequency images for classification of alcohol and control EEG signals. *Neural Comput. Appl.* 28, 3717–3723. doi: 10.1007/s00521-016-2276-x

Bavkar, S., Iyer, B., and Deosarkar, S. (2021). Optimal EEG channels selection for alcoholism screening using EMD domain statistical features and harmony search algorithm. *Biocybernetics* 41, 83–96. doi: 10.1016/j.bbe.2020.11.001

Buriro, A. B., Ahmed, B., Baloch, G., Ahmed, J., Shoorangiz, R., Weddell, S. J., et al. (2021). Classification of alcoholic EEG signals using wavelet scattering transform-based features. *Comput. Biol. Med.* 139:104969. doi: 10.1016/j.compbiomed.2021.104969

Cameron, A. C., Gelbach, J. B., and Miller, D. L. (2008). Bootstrap-based improvements for inference with clustered errors. *Rev. Econ. Stat.* 90, 414–427. doi: 10.1162/rest.90.3.414

Cao, R., Deng, H., Wu, Z., Liu, G., Guo, H., and Xiang, J. (2017). Decreased synchronization in alcoholics using EEG. *IRBM* 38, 63–70. doi: 10.1016/j.irbm.2017.02.002

Chen, H. l., Yang, B., Wang, S. j., Wang, G., Liu, D. y., Li, H. z., et al. (2014). Towards an optimal support vector machine classifier using a parallel particle swarm optimization strategy. *Appl. Mathemat. Comput.* 239, 180–197. doi: 10.1016/j.amc.2014.04.039

Deiner, S., and Silverstein, J. (2009). Postoperative delirium and cognitive dysfunction. *Br. J. Anaesth.* 103(Suppl._1), i41–i46. doi: 10.1093/bja/aep291

Diykh, M., Abdulla, S., Saleh, K., and Deo, R. C. (2019a). Fractal dimension undirected correlation graph-based support vector machine model for identification of focal and non-focal electroencephalography signals. *Biomed. Signal Process. Control* 54:101611. doi: 10.1016/j.bspc.2019.101611

Diykh, M., Abdulla, S., Siuly, S., Green, J. H., and Deo, R. C. (2021). A new framework for classification of multi-category hand grasps using EMG signals. *Artif. Intell. Med.* 112:102005. doi: 10.1016/j.artmed.2020.102005

Diykh, M., Li, Y., and Abdulla, S. (2020). EEG sleep stages identification based on weighted undirected complex networks. *Comput. Methods Programs Biomed.* 184:105116. doi: 10.1016/j.cmpb.2019.105116

Diykh, M., Li, Y., Wen, P., and Li, T. (2018). Complex networks approach for depth of anesthesia assessment. *Measurement* 119, 178–189. doi: 10.1016/j.measurement.2018.01.024

Diykh, M., Miften, F. S., Abdulla, S., Saleh, K., and Green, J. H. (2019b). Robust approach to depth of anaesthesia assessment based on hybrid transform and statistical features. *IET Sci. Meas. Technol.* 14, 128–136. doi: 10.1049/iet-smt.2018.5393

Ergezer, H., and Leblebicioğlu, K. (2016). Anomaly detection and activity perception using covariance descriptor for trajectories. *Paper Presented at the European Conference on Computer Vision*, Amsterdam. doi: 10.1007/978-3-319-48881-3_51

Ergezer, H., and Leblebicioğlu, K. (2018). Time series classification with feature covariance matrices. *Knowl. Inf. Syst.* 55, 695–718. doi: 10.1007/s10115-017-1098-1

Fattah, S., Fatima, K., and Shahnaz, C. (2015). An approach for classifying alcoholic and non-alcoholic persons based on time domain features extracted from EEG signals. *Paper Presented at the 2015 IEEE International WIE Conference on Electrical and Computer Engineering (WIECON-ECE)*, Dhaka. doi: 10.1109/WIECON-ECE.2015.7443972

Faust, O., Acharya, R., Allen, A. R., and Lin, C. (2008). Analysis of EEG signals during epileptic and alcoholic states using AR modeling techniques. *IRBM* 29, 44–52. doi: 10.1016/j.rbmret.2007.11.003

Faust, O., Yanti, R., and Yu, W. (2013a). Automated detection of alcohol related changes in electroencephalograph signals. *J. Med. Imaging Health Inform.* 3, 333–339. doi: 10.1166/jmihi.2013.1170

Faust, O., Yu, W., and Kadri, N. A. (2013b). Computer-based identification of normal and alcoholic EEG signals using wavelet packets and energy measures. *J. Mech. Med. Biol.* 13:1350033. doi: 10.1142/S0219519413500334

Gao, Z., Dang, W., Wang, X., Hong, X., Hou, L., Ma, K., et al. (2021). Complex networks and deep learning for EEG signal analysis. *Cogn. Neurodyn.* 15, 369–388. doi: 10.1007/s11571-020-09626-1

Hedges, L. V., Gurevitch, J., and Curtis, P. S. (1999). The meta-analysis of response ratios in experimental ecology. *Ecology* 80, 1150–1156. doi: 10.1890/0012-9658(1999)080[1150:TMAORR]2.0.CO;2

Hennig, C. (2007). Cluster-wise assessment of cluster stability. *Comput. Stat. Data Anal.* 52, 258–271. doi: 10.1016/j.csda.2006.11.025

Hettich, S., and Bay, S. (1999). *The UCI KDD Archive*. (Irvine, CA: University of California), 152.

Hira, Z. M., and Gillies, D. F. (2015). A review of feature selection and feature extraction methods applied on microarray data. *Adv. Bioinformatics* 2015:198363. doi: 10.1155/2015/198363

Isaksson, A., Wennberg, A., and Zetterberg, L. H. (1981). Computer analysis of EEG signals with parametric models. *Proc. IEEE* 69, 451–461. doi: 10.1109/PROC.1981.11988

Jaccard, P. (1901). Étude Comparative de la distribuition florale dans une portion des Alpes et des Jura. *Bull. Soc. Vaudoise Sci. Nat.* 7, 547–579.

Kannathal, N., Acharya, U. R., Lim, C. M., and Sadasivan, P. (2005). Characterization of EEG—a comparative study. *Comput. Methods Programs Biomed.* 80, 17–23. doi: 10.1016/j.cmpb.2005.06.005

Knight, R. G., and Longmore, B. E. (1994). *Clinical Neuropsychology of Alcoholism*. Mahwah, NJ: Lawrence Erlbaum Associates.

Kousarrizi, M. R. N., Ghanbari, A. A., Gharaviri, A., Teshnehlab, M., and Aliyari, M. (2009). "Classification of alcoholics and non-alcoholics via EEG using SVM and neural networks," in *Proceedings of the 2009 3rd International Conference on Bioinformatics and Biomedical Engineering*, Beijing.

Kumar, Y., Dewal, M., and Anand, R. (2012). "Features extraction of EEG signals using approximate and sample entropy," in *Proceedings of the 2012 IEEE Students' Conference on Electrical, Electronics and Computer Science*, Bhopal. doi: 10.1109/SCEECS.2012.6184830

Lieber, C. S. (1995). Medical disorders of alcoholism. *N. Engl. J. Med.* 333, 1058–1065. doi: 10.1056/NEJM199510193331607

Lin, C.-F., Yeh, S.-W., Chien, Y.-Y., Peng, T.-I., Wang, J.-H., and Chang, S.-H. (2009). A HHT-based time frequency analysis scheme for clinical alcoholic EEG signals. *WSEAS Trans. Biol. Biomed.* 5, 249–260.

Oscar-Berman, M., Shagrin, B., Evert, D. L., and Epstein, C. (1997). Impairments of brain and behavior: the neurological effects of alcohol. *Alcohol Health Res. World* 21, 65–75.

Pan, W.-T. (2012). A new fruit fly optimization algorithm: taking the financial distress model as an example. *Knowl. Based Syst.* 26, 69–74. doi: 10.1016/j.knosys.2011.07.001

Patidar, S., Pachori, R. B., Upadhyay, A., and Acharya, U. R. (2017). An integrated alcoholic index using tunable-Q wavelet transform based features extracted from EEG signals for diagnosis of alcoholism. *Appl. Soft Comput.* 50, 71–78. doi: 10.1016/j.asoc.2016.11.002

Pelvig, D. P., Pakkenberg, H., Stark, A. K., and Pakkenberg, B. (2008). Neocortical glial cell numbers in human brains. *Neurobiol. Aging* 29, 1754–1762. doi: 10.1016/j.neurobiolaging.2007.04.013

Priya, A., Yadav, P., Jain, S., and Bajaj, V. (2018). Efficient method for classification of alcoholic and normal EEG signals using EMD. *J. Eng.* 2018, 166–172. doi: 10.1049/joe.2017.0878

Shooshtari, M. A., and Setarehdan, S. K. (2010). "Selection of optimal EEG channels for classification of signals correlated with alcohol abusers," in *Proceedings of the 2010 IEEE 10th International Conference on Signal*, Beijing. doi: 10.1109/ICOSP.2010.5656482

Shri, T. P., and Sriraam, N. (2016). Spectral entropy feature subset selection using SEPCOR to detect alcoholic impact on gamma sub band visual event related potentials of multichannel electroencephalograms (EEG). *Appl. Soft Comput.* 46, 441–451. doi: 10.1016/j.asoc.2016.04.041

Singhal, V., Mathew, J., and Behera, R. K. (2021). Detection of alcoholism using EEG signals and a CNN-LSTM-ATTN network. *Comput. Biol. Med.* 138:104940. doi: 10.1016/j.compbiomed.2021.104940

Sun, Y., Ye, N., and Xu, X. (2006). "EEG analysis of alcoholics and controls based on feature extraction," in *Proceedings of the 2006 8th International Conference on Signal Processing*, Guilin. doi: 10.1109/ICOSP.2006.344501

Tao, W., Li, C., Song, R., Cheng, J., Liu, Y., Wan, F., et al. (2020). "EEG-based emotion recognition via channel-wise attention and self attention," in *Proceedings of the 2020 IEEE Transactions on Affective Computing*, Beijing. doi: 10.1109/TAFFC.2020.3025777

Taran, S., and Bajaj, V. (2017). Rhythm-based identification of alcohol EEG signals. *IET Sci. Meas. Technol.* 12, 343–349. doi: 10.1049/iet-smt.2017.0232

Tharwat, A., and Hassanien, A. E. (2018). Chaotic antlion algorithm for parameter optimization of support vector machine. *Appl. Intell.* 48, 670–686. doi: 10.1007/s10489-017-0994-0

Volkow, N. D., Wiers, C. E., Shokri-Kojori, E., Tomasi, D., Wang, G.-J., and Baler, R. (2017). Neurochemical and metabolic effects of acute and chronic alcohol in the human brain: studies with positron emission tomography. *Neuropharmacology* 122, 175–188. doi: 10.1016/j.neuropharm.2017.01.012

Wu, X., Zuo, W., Lin, L., Jia, W., and Zhang, D. (2018). F-SVM: combination of feature transformation and SVM learning via convex relaxation. *IEEE Trans. Neural Netw. Learn. Syst.* 29, 5185–5199. doi: 10.1109/TNNLS.2018.2791507

Zhang, X. L., Begleiter, H., Porjesz, B., and Litke, A. (1997). Electrophysiological evidence of memory impairment in alcoholic patients. *Biol. Psychiatry* 42, 1157–1171. doi: 10.1016/S0006-3223(96)00552-5

Zhu, G., Li, Y., and Wen, P. (2011). Evaluating functional connectivity in alcoholics based on maximal weight matching. *J. Adv. Comput. Intell. Intell. Inform.* 15, 1221–1227. doi: 10.20965/jaciii.2011.p1221

Conflict of Interest: The authors declare that the research was conducted in the absence of any commercial or financial relationships that could be construed as a potential conflict of interest.

Publisher's Note: All claims expressed in this article are solely those of the authors and do not necessarily represent those of their affiliated organizations, or those of the publisher, the editors and the reviewers. Any product that may be evaluated in this article, or claim that may be made by its manufacturer, is not guaranteed or endorsed by the publisher.

frontiers | Frontiers in Neuroinformatics

TYPE Original Research
PUBLISHED 19 June 2023
DOI 10.3389/fninf.2023.1169584

OPEN ACCESS

EDITED BY
Kais Gadhoumi,
Duke University, United States

REVIEWED BY
Edward M. Merricks,
Columbia University, United States
Aydin Akan,
Izmir University of Economics, Türkiye

*CORRESPONDENCE
Miroslaw Latka
✉ Miroslaw.Latka@pwr.edu.pl

RECEIVED 19 February 2023
ACCEPTED 25 May 2023
PUBLISHED 19 June 2023

CITATION
Glaba P, Latka M, Krause MJ, Kroczka S, Kuryło M, Kaczorowska-Frontczak M, Walas W, Jernajczyk W, Sebzda T and West BJ (2023) EEG phase synchronization during absence seizures. *Front. Neuroinform.* 17:1169584. doi: 10.3389/fninf.2023.1169584

EEG phase synchronization during absence seizures

Pawel Glaba[1], Miroslaw Latka[1]*, Małgorzata J. Krause[2], Sławomir Kroczka[3], Marta Kuryło[2], Magdalena Kaczorowska-Frontczak[4], Wojciech Walas[5], Wojciech Jernajczyk[6], Tadeusz Sebzda[7] and Bruce J. West[8]

[1]Department of Biomedical Engineering, Wroclaw University of Science and Technology, Wrocław, Poland, [2]Department of Pediatric Neurology, T. Marciniak Hospital, Wrocław, Poland, [3]Department of Child Neurology, Jagiellonian University Medical College, Kraków, Poland, [4]The Children's Memorial Health Institute, Warszawa, Poland, [5]Department of Anesthesiology, Intensive Care and Regional Extracorporeal Membrane Oxygenation (ECMO) Center, Institute of Medical Sciences, University of Opole, Opole, Poland, [6]Clinical Neurophysiology, Institute of Psychiatry and Neurology, Warszawa, Poland, [7]Department of Physiology and Pathophysiology, Medical University of Wroclaw, Wrocław, Poland, [8]Center for Nonlinear Science, University of North Texas, Denton, TX, United States

Absence seizures—generalized rhythmic spike-and-wave discharges (SWDs) are the defining property of childhood (CAE) and juvenile (JAE) absence epilepsies. Such seizures are the most compelling examples of pathological neuronal hypersynchrony. All the absence detection algorithms proposed so far have been derived from the properties of *individual* SWDs. In this work, we investigate EEG phase synchronization in patients with CAE/JAE and healthy subjects to explore the possibility of using the wavelet phase synchronization index to detect seizures and quantify their disorganization (fragmentation). The overlap of the ictal and interictal probability density functions was high enough to preclude effective seizure detection based solely on changes in EEG synchronization. We used a machine learning classifier with the phase synchronization index (calculated for 1 s data segments with 0.5 s overlap) and the normalized amplitude as features to detect generalized SWDs. Using 19 channels (10-20 setup), we identified 99.2% of absences. However, the overlap of the segments classified as ictal with seizures was only 83%. The analysis showed that seizures were disorganized in approximately half of the 65 subjects. On average, generalized SWDs lasted about 80% of the duration of abnormal EEG activity. The disruption of the ictal rhythm can manifest itself as the disappearance of epileptic spikes (with high-amplitude delta waves persisting), transient cessation of epileptic discharges, or loss of global synchronization. The detector can analyze a real-time data stream. Its performance is good for a six-channel setup (Fp1, Fp2, F7, F8, O1, O2), which can be implemented as an unobtrusive EEG headband. False detections are rare for controls and young adults (0.03% and 0.02%, respectively). In patients, they are more frequent (0.5%), but in approximately 82% cases, classification errors are caused by short epileptiform discharges. Most importantly, the proposed detector can be applied to parts of EEG with abnormal EEG activity to quantitatively determine seizure fragmentation. This property is important because a previous study reported that the probability of disorganized discharges is eight times higher in JAE than in CAE. Future research must establish whether seizure properties (frequency, length, fragmentation, etc.) and clinical characteristics can help distinguish CAE and JAE.

KEYWORDS

epilepsy, absence seizure, synchronization, wavelets, seizure detection, childhood absence epilepsy, juvenile absence epilepsy, seizure fragmentation

1. Introduction

Idiopathic generalized epilepsies (IGEs) are a subgroup of genetic generalized epilepsies (GGEs), composed of four syndromes: childhood absence epilepsy (CAE), juvenile absence epilepsy (JAE), juvenile myoclonic epilepsy (JME), and epilepsy with generalized tonic-clonic seizures alone (GTCA) (Hirsch et al., 2022). Absence seizures—generalized rhythmic (2.5–5.5 Hz) spike-and-wave discharges are the defining property of CAE and JAE. They can also be observed in about 33% of patients with JME.

CAE starts in otherwise normal children between 4 and 10 years of age and is more common in girls (60 to 75% of cases). It accounts for approximately 18% of epilepsy in school-aged children. Typical absence seizures begin suddenly and, in most children, lead to a deep loss of awareness and interruption of previously conducted activity. Seizures can be accompanied by staring, loss of facial expression, oral/manual automatism, blinking, or eye opening. Return to regular activity seems immediate, although children may initially be confused as they reorient themselves. The duration of seizures, which can occur multiple times a day, typically varies between 3 and 20 s, with a median of 10 s. CAE relapses in early adolescence in 60% of patients. In the rest, the disease can evolve into other IGE syndromes.

JAE is less common than CAE, accounting for 2.4–3.1% of new-onset epilepsy in children and adolescents, with a nearly equal distribution between men and women. However, it may be underdiagnosed as absences are less frequent (less than daily) and more subtle (less complete impairment of awareness). The age of onset is 12 ± 3 years (Asadi-Pooya et al., 2013). The ictal EEG is similar in CAE and JAE. However, disorganized (fragmented) discharges, defined as brief (<1 s) and transient interruptions in the ictal rhythm, are eight times more frequent in JAE (Sadleir et al., 2009). In most patients with JAE, lifelong seizure control pharmacotherapy is required.

The diagnosis of IGE requires the analysis of long video EEGs (on average about 30 min long) to detect seizures, their clinical manifestations (consciousness impairment, motor symptoms) and abnormal features in the interictal EEG. The 2010 Childhood Absence Epilepsy Study (Glauser et al., 2013) showed that after 1 year, the initial seizure-control pharmacotherapy was effective only in 37% of patients with CAE and JAE. Therefore, follow-up EEG recordings are necessary to ensure treatment efficacy and minimize potential side effects. It should be noted that parents notice only a small fraction (approximately 6%) of absences (Keilson et al., 1987), the estimate corroborated by a more recent study (Akman et al., 2009).

Low-cost portable EEG devices connected to the Internet (Krigolson et al., 2017) can be instrumental in personalizing pediatric epilepsy management. Children and adolescents may be more willing to tolerate regular EEG measurements if incorporated into daily routines, such as watching cartoons, playing mobile games, or listening to music. The potential benefits of remote long-term EEG monitoring include facilitation of diagnosis, personalized drug titration, and determining the duration of pharmacotherapy. Consequently, there is a strong demand for fast and accurate computer seizure detection that can be used on devices with as few EEG channels as possible. Global synchronization is the most conspicuous property of EEG dynamics during absence seizure. However, all the absence detection algorithms proposed so far (Adeli et al., 2003; Subasi, 2007; Sitnikova et al., 2009; Ovchinnikov et al., 2010; Xanthopoulos et al., 2010; Petersen et al., 2011; Duun-Henriksen et al., 2012; Bauquier et al., 2015; Zeng et al., 2016; Grubov et al., 2017; Kjaer et al., 2017; Tenneti and Vaidyanathan, 2018; Dan et al., 2020; Glaba et al., 2021; Japaridze et al., 2022) exploit only the properties of SWD complexes. In this work, we investigate EEG phase synchronization in patients with CAE/JAE and healthy subjects to explore the possibility of using the phase synchronization index to detect seizures and characterize their disorganization. The qualitative assessment of absence fragmentation could be used to discriminate between CAE and JAE, an important clinical problem.

2. Materials and methods

2.1. EEG recordings

The data set used in our previous study (Glaba et al., 2021) was slightly modified and expanded by routine EEG of healthy young adults (12 women and 7 men, mean age 22 years, range 20–24 years). For these adults, the EEG was recorded for 8 min, the first half in closed eyes and the second in open eyes condition. The recordings were made with Elmiko Digitrack (BRAINTRONICS B.V. ISO-1032CE amplifier, 250 Hz sampling frequency, impedance below 5kΩ). The ethics committee of the Warsaw Institute of Psychiatry and Neurology approved the reanalysis of the data. Subjects gave their informed consent.

The ethics committee of Wroclaw Medical University approved a retrospective analysis of routine anonymized video EEG recordings of patients (36 with CAE and 29 with JAE) as well as 30 EEGs of controls of the same age (Glaba et al., 2021). Epilepsy syndrome was established based on age of onset, the properties of the first video-EEG, and neuroimaging. Consequently, diagnosis should be considered as preliminary. EEGs were acquired with Elmiko Digitrack (BRAINTRONICS B.V. ISO-1032CE amplifier) or Grass Comet Plus EEG (AS40-PLUS amplifier) using a sampling frequency of 200 or 250 Hz. The international 10-20 standard was used to arrange 19 Ag/AgCl electrodes (impedance below 5kΩ). The total duration of the EEG was equal to 37 and 9 h for the patients and controls, respectively.

All EEGs were acquired with the reference electrode mounted on the subject's forehead.

We used two filters for EEG preprocessing: a second-order infinite impulse response (IIR) and a 6th-order high-pass Butterworth with a cutoff frequency of 0.5 Hz. These filters remove 50-Hz power line noise and EEG baseline drift, respectively.

2.2. Synchronization matrix

We quantify the EEG synchronization using a matrix made up of pairwise frequency-dependent synchronization coefficients $\gamma(k,l)$ calculated for EEG channels k and l ($k,l = 1..19$). $\gamma(k,l)$ can be defined with the help of the complex continuous wavelet

transform (CWT) (Lachaux et al., 1999):

$$T[s](a,t_0) = \frac{1}{\sqrt{a}} \int_{-\infty}^{+\infty} s(t)\psi^* \left(\frac{t-t_0}{a} \right) dt \quad (1)$$

which is the convolution of the signal $s(t)$ with wavelets $\psi(a,t_0)$. Such wavelets are generated from the mother function ψ by translation and scaling: $\psi(a,t_0) = \psi(t - t_0/a)$ (Mallat, 1999). Motivated by the results of the previous study (Glaba et al., 2021), we used the complex Morlet wavelet (Addison, 2017, 2018):

$$\psi(t) = \frac{1}{\pi^{1/4}} e^{2\pi i f_c t} e^{-t^2/2} \quad (2)$$

whose Fourier transform $\hat{\psi}(f)$ is given by

$$\hat{\psi}(f) = \sqrt{2}\sqrt[4]{\pi} e^{-2\pi^2 (f-fc)^2}. \quad (3)$$

The real parameter f_c is called the center frequency, since it equals the maximum point of the wavelet's Fourier power spectrum. The scale a corresponds to the following pseudo-frequency:

$$f_a = \frac{f_c}{a}. \quad (4)$$

The instantaneous phase of a signal s can be defined as

$$\phi(t_0, f_a) = -i \log \left[\frac{T[s](a,t_0)}{|T[s](a,t_0)|} \right], \quad (5)$$

where i is an imaginary number. The distribution $P[\Delta\phi(k,l)]$ of the phase difference $\Delta\phi(k,l) = \phi_k - \phi_l$ can be used to characterize the synchronization between two EEG channels. A uniform distribution corresponds to the absence of synchronization (two signals are statistically independent). In contrast, a well-pronounced peak in the distribution is a manifestation of phase locking, which means that one time series tracks the dynamics of the other. The stability of the phase difference $\Delta\phi$ is quantified with the index $\gamma(k,l)$ (Quiroga et al., 2002; Latka et al., 2005)

$$\gamma(k,l) = \langle \sin \Delta\phi(k,l) \rangle^2 + \langle \cos \Delta\phi(k,l) \rangle^2. \quad (6)$$

The angle brackets in the above equation denote the temporal average of the phase-difference fluctuations. The synchronization index can have values between 0 and 1, and in the case of human EEG, it is frequency dependent. When the distribution of phase differences is uniform, the time averages of both trigonometric functions in Equation (6) are zero which in turn makes the synchronization index equal to zero. From the trigonometric identity, it follows that $\gamma = 1$ corresponds to perfect synchronization (phase locking of two EEG channels).

The average synchronization index γ is the average value of the non-diagonal elements of the synchronization matrix:

$$\gamma = \sum_{k \in S_N} \sum_{l \in S_N, k>l} \gamma(k,l), \quad (7)$$

where S_N denotes subsets of 10-20 channels. We calculate γ for all 19 channels ($N = 19$) and for three subsets ($N < 19$):

- S_4 (Fp1, Fp2, T5, T6)
- S_6 (Fp1, Fp2, F7, F8, O1, O2)
- S_{12} (Fp1, Fp2, F7, F8, F3, F4, P3, P4, T5, T6, O1, O2).

The electrode arrangement in the above subsets is similar, but not always identical, to the low-cost EEG headsets currently available on the market (Pu et al., 2021). The applicability of such headsets to home monitoring of pediatric patients was the main reason for testing different S_N.

The channel synchronization index is defined as follows:

$$\gamma(k) = \sum_{k,l \in S_N, k>l} \gamma(k,l). \quad (8)$$

We calculate phase synchronization for 1-s intervals using a half-second overlap. We use the overlap to simulate live data stream analysis. For patients, there were 7,270 ictal and 266,653 interictal data segments. 1,540 windows partially overlapped absence seizures. The partitioning of the controls' EEG yielded 58,460 segments. For students, we obtained the 9,064 and 9,121 intervals for closed and open eyes, respectively.

The value of the synchronization index γ depends on the center frequency of the Morlet wavelet f_c and the pseudofrequency f_a. We use a grid search to determine optimal values for absence detection. In particular, we search for f_c and f_a that maximize the difference between ictal and interictal synchronization.

We would like to emphasize that the synchronization properties depend on the choice of reference electrode (Dominguez et al., 2005).

In this work, we used short EEG data segments. Consequently, when calculating the CWT with the help of a fast Fourier transform, boundary effects must be considered.

2.3. Absence seizure classifier

Prominent SWD and global EEG synchronization are hallmarks of absence seizures (Figure 1). Therefore, we decided to detect seizures using the normalized amplitude of the EEG $A_m^{(n)}$ and the synchronization index γ_m as machine learning features. The former is defined as

$$A_m^{(n)} = \frac{A_m}{A_{ref}}, \quad (9)$$

where A_m is the average absolute value of the EEG signal in segment m (we average across all channels). A_{ref} is the mean absolute value calculated for the 30 s segment taken from the interictal beginning of the EEG recording. Normalization by A_{ref} was necessary because the amplitude of EEG in children can decrease significantly with age and depends on the impedance of the electrodes.

We use the k-nearest neighbor (k-NN) classifier implemented in Matlab R2022a (MATLAB, 2022) Machine Learning Toolbox for absence detection. We accept the default values of the model parameters (10 neighbors, the Euclidean distance, data point scaling, and no weighting function). We employ leave-one-out cross-validation (LOOCV)—the number of folds equals the number of patients (65). For each patient, k-NN is built using the features extracted from the other 64 patients and applied to their

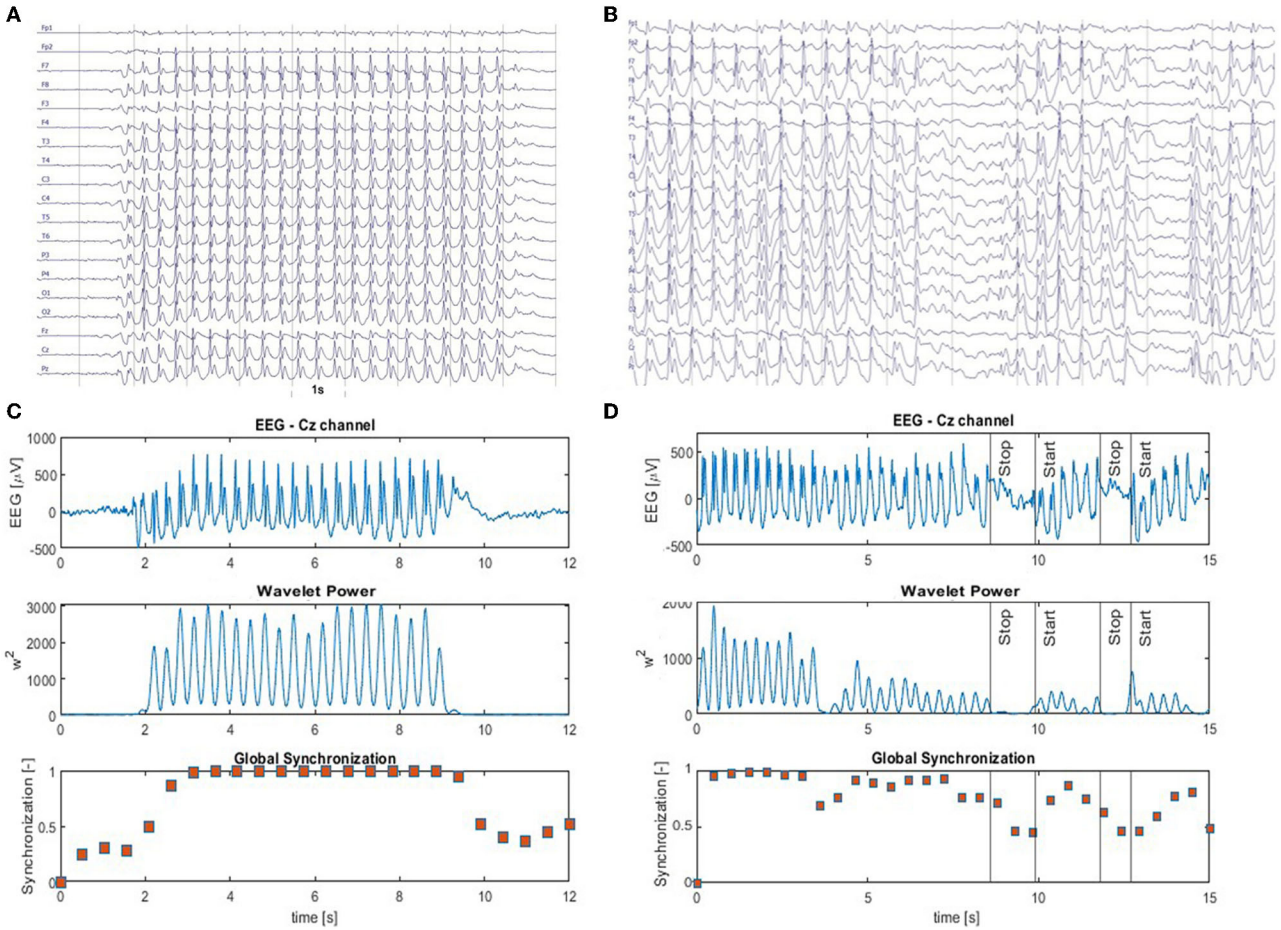

FIGURE 1
(A) Archetype of high-amplitude, continuous generalized spike and wave discharges with prominent epileptic spikes. The absence seizure in **(B)** is briefly interrupted two times. Panels **(C, D)** show the EEG from Cz channel (top panel) as well as the corresponding time series of the wavelet power (middle panel) and the global synchronization index (bottom panel). The wavelet power and synchronization index were calculated using $f_c = 1$ Hz and $f_a = 12$ Hz. These case studies demonstrate that global synchronization decreases when epileptic activity subsides.

segmented EEG (1 s windows with 0.5 s overlap). We prepare the training set as follows. We select only those ictal windows whose mean γ is greater than a threshold determined from the interictal synchronization distribution. In particular, for this threshold, 95% of interictal segments have a smaller mean γ. We disregard all data windows that partially overlap absence seizures. The sets of ictal and interictal segments are highly unbalanced (7,270 vs. 266,653). Therefore, we randomly select only a small fraction of the interictal segments for the training set. We use the 1:3 ratio of the ictal and interictal windows.

We evaluated the performance of the detector in the same way as in our previous article (Glaba et al., 2021) using the relative overlap (OVR) of segments classified as ictal with absence seizures and relative duration of false positives (PERR). During the PERR computation, we apply the logical OR function to determine the status of the common part of two consecutive EEG data segments. In other words, the common part is ictal if any segment is ictal. We also report the number of false positives (FP) and the number of different trains of misclassified segments (MT).

Supplementary Figure 1 elucidates the relationship between the number of erroneously classified EEG segments and PERR. For overlapping segments, this relationship can sometimes be counterintuitive.

Short (<2 s) epileptiform discharges, quite common in patients with CAE/JAE, usually do not produce clinical manifestations (Szaflarski et al., 2010). Therefore, we also tested the possibility of reducing the number of false positives by post-processing the k-NN classification results. In particular, we labeled any isolated ictal segment as non-ictal. In other words, the shortest possible ictal interval can have a length of 1.5 s (two consecutive segments).

2.4. Seizure fragmentation

We apply the absence detector described in Section 2.3 (with the post-processing turned off) to the parts of the EEG marked by neurologists as abnormal activity. Then, we calculate the percentage overlap of the segments classified as ictal with the analyzed fragment. As before, the common part of the adjacent segments is considered ictal if at least one of the segments is ictal. Seizure fragmentation

is defined as

$$SFRAG = 100\% - OVR. \quad (10)$$

3. Results

3.1. Synchronization

When calculating γ, we used $f_c = 1$ Hz and $f_a = 12$ Hz. For these values, the percentage difference between ictal and interictal synchronization was highest (168%). In the same vein, we determined these parameters for each patient. The median values were similar: $f_c = 0.8$ Hz and $f_a = 13$ Hz. Supplementary Figures 2, 3 elucidate the determination of the wavelet parameters.

Figure 1A shows an archetypal absence seizure with continuous high-amplitude generalized SWDs. In contrast, the seizure in Figure 1B was briefly interrupted twice. For both absences, for the chosen f_c and f_a, the power $|T|^2$ peaks at the location of epileptic spikes (Figures 1C, D). It is apparent that wavelet power and global synchronization are low when epileptic activity subsides. In Figure 2, we compare the ictal synchronization matrices calculated for the EEG segments presented in Figures 1A, B.

Figures 3A, B show that γ increases at the beginning and on average gradually subsides towards the end of the seizure. For the eight types of data segments (labeled from 0 to 7) presented in these figures, the average γ was equal to 0.28 ± 0.09, 0.46 ± 0.17, 0.62 ± 0.19, 0.79 ± 0.18, 0.75 ± 0.19, 0.58 ± 0.19, 0.44 ± 0.16, 0.36 ± 0.12. γ in ictal segments (1 to 7) was significantly higher than the interictal baseline 0.28 ± 0.09 ($p < 0.0001$ for the Mann–Whitney test).

The probability density function (PDF) of γ for the interictal and ictal segments strongly overlaps. In Figure 3C, PDF was calculated using global synchronization for the 19 channels (S_{19}) while Figure 3D shows PDF for the four-channel subset S_4 (Fp1, Fp2, T5, T6). The cut-off value for which 95% of the interictal segments had smaller synchronization was equal to 0.49, 0.65, 0.45, and 0.48 for S_{19}, S_{12}, S_6, and S_4, respectively.

3.2. Seizure detection

We detected absences with the k-NN classifier using synchronization and normalized amplitude as features. Supplementary Table 1 shows that the accuracy of other classifiers, such as neural networks or decision trees, is comparable. In actual implementations, these classifiers would be preferable because they do not require the attachment of training samples (feature vectors with the corresponding labels). We chose k-NN because of its short training time, which speeds up cross-validation.

Figure 4 elucidates the building of a seizure detector for patient P1, who had six absences with a mean duration of 10.5 s. One of the absences of P1 is presented in Figure 1A. The training set was created using data from the other 64 patients using the 19 channels (S_{19}) or the four-channel subset S_4. The scatter plots in Figures 4A, C show the spread of the synchronization and the normalized amplitude for S_{19} and S_4, respectively. Patient P1's EEG was partitioned into 3,598 windows. 108 were fully embedded in the seizures, while 24 partially overlapped them. Please note that for testing purposes, we consider any data segment that even partially overlaps a seizure as ictal. Of the 132 ictal windows, 14 (FN = 10.6%) and 17 (FN = 12.9%) were misclassified for S_{19} and S_4, respectively. For both subsets, all 3,464 interictal segments were correctly labeled.

Supplementary Figure 4 shows the construction of a seizure detector for patient P18. One of his absences is presented in Figure 1B.

The overlap OVR was the largest for S_{19} ($82.90 \pm 20.83\%$) and the smallest for S_4 ($69.31 \pm 25.09\%$) (Table 1). For S_{19}, PERR was equal to $0.87 \pm 1.23\%$, $0.12 \pm 0.26\%$, $0.07 \pm 0.14\%$ for patients, controls, and young adults, respectively. The corresponding values for S_4 were $0.68 \pm 1.32\%$, $0.03 \pm 0.07\%$, and $0.02 \pm 0.06\%$.

The false detection rate of the patients was five times higher than that of controls (0.5 vs. 0.1%) for S_{19} setup (Table 1). For smaller subsets, the detector performance was markedly better. For S_6, the false detection rate was equal to 0.5, 0.03, and 0.04% for patients, controls, and young adults, respectively. Comparison of the number of distinct trains of misclassified segments with the number of false positives reveals that parts of the EEG marked incorrectly as ictal are, on average, shorter than 2 s. We found by visual inspection that about 82% of the false positives were caused by short epileptiform discharges, which are quite common in epilepsy patients and rare in controls and young adults. The EEG artifacts comprise the rest: 7% were caused by spike-like high-amplitude artifacts and 7% by artifacts of more complicated morphology. The seizure detection performance for each patient is presented in Supplementary Table 2. The post-processing cuts approximately in half the number of FP (Table 1).

For two patients, P1 and P18, we built the detector for different combinations of wavelet parameters f_c and f_a. OVR, PERR, and FP for these calculations are presented in Supplementary Tables 3, 4. The results show that the detector performance is weakly affected by small changes in the wavelet parameters. For example, for P1, the grid search yielded $f_c = 0.8$ Hz and $f_a = 10$ Hz. For these values $OVR = 99.17\%$, $PERR = 0.30\%$, and $FP = 1$. For the standard parameters $f_c = 1.0$ Hz and $f_a = 12$ Hz (used for all subjects), we obtained $OVR = 99.15\%$, $PERR = 0.22\%$, and $FP = 0$. For P1, for 10 runs, we obtained the following average values: $OVR = 99.16 \pm 0.00\%$, $PERR = 0.22 \pm 0.01$, and $FP = 1 \pm 0$. For P18, the corresponding values were equal to $98.38 \pm 0.15\%$, 1.25 ± 0.02, and $FP = 33 \pm 1$.

Supplementary Table 5 shows the group average characteristics of seizure detection for different combinations of wavelet parameters. There are a number of combinations (e.g., $f_a = 11$ Hz and $f_c = 1$ Hz or $f_a = 14$ Hz and $f_c = 1.4$ Hz) for which the detection performance is comparable (the trade-off between the overlap and the number of false positives) with $f_a = 12$ Hz and $f_c = 1$ Hz used in this study. We chose the latter parameters because they have a clear physical interpretation (the difference between interictal and ictal synchronization is highest) and the number of false positives for the controls is acceptable (Supplementary Table 6).

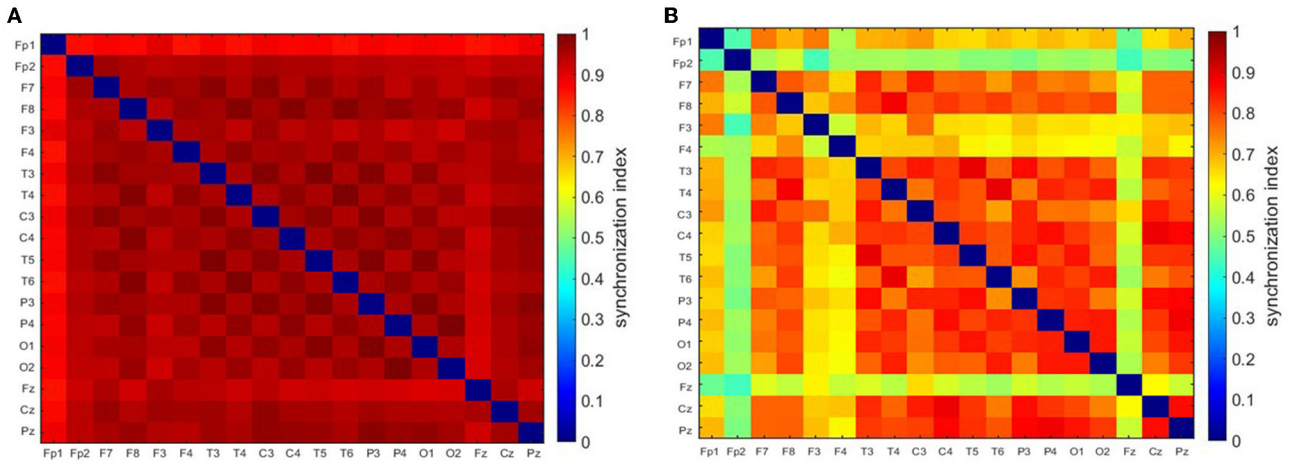

FIGURE 2
Synchronization matrices for the regular **(A)** and disorganized **(B)** seizure. These seizures are shown in Figure 1.

3.3. Seizure fragmentation

In Figure 5, we compare the EEG dynamics with the classifier output (detection function). SWDs do not emerge simultaneously from the background EEG in all channels. At the end of the seizure, ictal activity gradually subsides: epileptic spikes disappear, the amplitude of the EEG decreases, and global synchronization is lost. However, the initial and final transients were very short (< 0.5 s), and consequently, the first and last segments were classified as ictal. Two segments during which the ictal rhythm was interrupted were correctly identified. For the absence seizure presented, *SFRAG* was equal to 6.4%. Two EEG intervals in Figure 5 were marked blue to draw attention to the limitations of fragmentation analysis. First, seizure disorganizations shorter than 0.5 s are, in most cases, undetected. Second, the duration of the disorganization can be underestimated because of the size of the data window used to calculate the synchronization.

We analyzed all EEG segments classified as noictal that were fully embedded in seizures to find that in approximately 98% of these segments, seizure activity was disorganized or SWDs were simply absent. The other 2% contained artifacts.

For S_{19} set-up, the group-averaged *SFRAG* was equal to 20 ± 24%. For 46 patients (71%), the average fragmentation of seizures was less than 25% (Figure 6A). Of the 385 absences, 280 (73%) had *SFRAG* smaller than 25% (Figure 6B). Disorganization did not occur in 120 cases. For such seizures, *SFRAG* < 5%.

SFRAG was equal to 18 ± 24%, 24 ± 26%, and 30 ± 29% for S_{12}, S_6, and S_4, respectively.

4. Discussion

An epileptic seizure is "a transient occurrence of signs and/or symptoms due to abnormal excessive or synchronous neuronal activity in the brain" (Fisher et al., 2005). Childhood and juvenile absences are the most compelling examples of pathological neuronal synchrony. Interestingly enough, all the absence detection algorithms proposed so far (Adeli et al., 2003; Subasi, 2007; Sitnikova et al., 2009; Ovchinnikov et al., 2010; Xanthopoulos et al., 2010; Petersen et al., 2011; Duun-Henriksen et al., 2012; Bauquier et al., 2015; Zeng et al., 2016; Grubov et al., 2017; Kjaer et al., 2017; Tenneti and Vaidyanathan, 2018; Dan et al., 2020; Glaba et al., 2021; Japaridze et al., 2022) have been derived from the properties of *individual* SWD complexes. Figures 3C, D provide an explanation, the overlap of the ictal and interictal probability density functions is so large that it precludes seizure detection based solely on changes in EEG synchronization. This conclusion agrees with previous studies on epileptic synchronization (Altenburg et al., 2003; Slooter et al., 2006).

This paper used the phase-synchronization index and the normalized amplitude as classification features. False detections are rare in controls and young adults. Although the PERR for the patients (0.55% for S_6) was even lower than that of the detector we had presented earlier (Glaba et al., 2021), the false detection rate per hour (8/h) was an order of magnitude higher. However, visual inspection of the EEG showed that 82% of the false positives corresponded to epileptiform discharges.

Of 385 absences, all but three were identified (accuracy (99.2%). Misclassified seizures were highly disorganized. The group-average overlap of EEG segments classified as ictal with seizures never exceeded 83%. There are two reasons for such a low value. The first is trivial, since we calculate γ for 1-s sliding windows. For windows that only partially cover the absences, γ is inevitably lower, which can lead to errors. The second reason is more fundamental and can be traced back to the disorganization of absences. Non-ictal classification within abnormal EEG activity was always associated with such disorganization. Apart from the segments that partially overlap seizures, we did not find a convincing example of a false negative.

The detection algorithm employs short data segments, making it suitable for real-time EEG analysis as several algorithms described previously (Xanthopoulos et al., 2010; Petersen et al., 2011; Duun-Henriksen et al., 2012; Kjaer et al., 2017; Dan et al., 2020; Japaridze et al., 2022). It is computationally more expensive

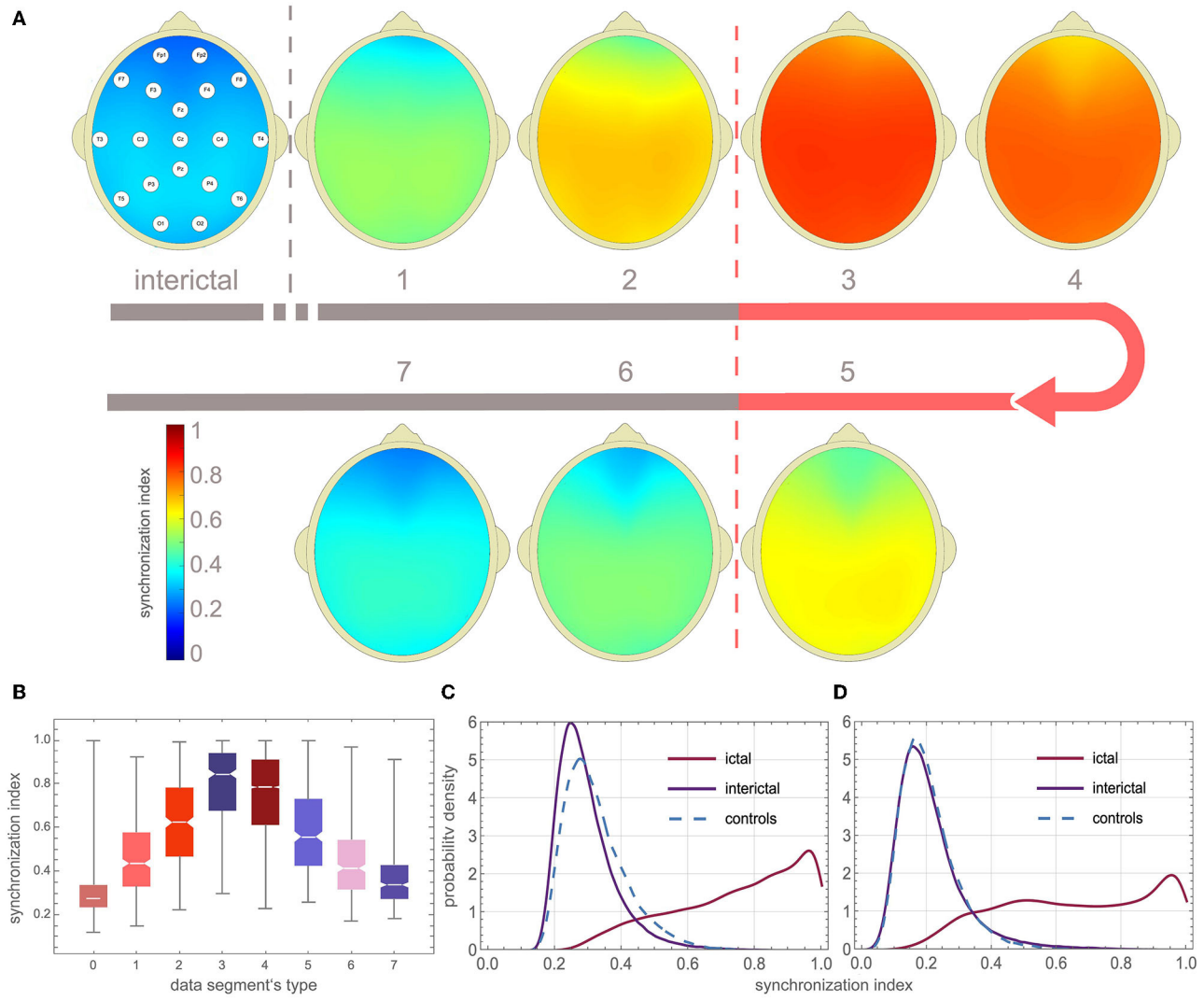

FIGURE 3
EEG synchronization during absence seizures. **(A)** Topographic map of channel synchronization (cohort average) for all interictal segments (0), the first window that partially overlaps seizures (1), the second partially overlapping (2), the first fully embedded in the seizure (3), all embedded without the first and last (4), the last embedded (5), the last but one overlapping (6) and last overlapping (7). **(B)** Global synchronization boxplots for data segments 0–7 (segments from all patients were used). **(C, D)** Probability density function (PDF) of the average synchronization index for the 19 channels (S_{19}) and the four-channel subset S_4 (Fp1, Fp2, T5, T6), respectively. One can see that global synchronization is high during seizures and that there is a strong overlap of the interictal and ictal distributions of the synchronization index.

than those derived from the properties of SWDs. This drawback is largely irrelevant today, except for portable EEGs with severely limited computing power. It should be noted that while the spectral and amplitude properties of EEG change significantly during maturation (Schomer and da Silva, 2018), the detector works equally well in children, juveniles, and young adults. The classification accuracy is good for a six-channel setup (Fp1, Fp2, F7, F8, O1, O2), which can be implemented as an unobtrusive EEG headband—a crucial requirement from the point of view of pediatric applications.

In the previous paper (Glaba et al., 2021), we used a delta frequency envelope to identify abnormal EEG activity. However, to detect absence seizures, we had to use two arbitrarily chosen heuristic criteria. First, we checked whether there were epileptic spikes in the envelope by calculating the percentage of EEG samples for which the beta wavelet power was greater than the threshold value. Second, if the envelope was shorter than 5 s, we also calculated the variance of the beta wavelet power. Although this algorithm was very fast and worked well, the approach presented here is not only more elegant, but it also allows quantifying seizure fragmentation.

The proposed detector cannot determine the fragmentation of the seizure in the live data stream. This can only be accomplished retrospectively when the detector (with post-processing turned off) is applied to EEG segments with abnormal EEG activity. Such segments can be marked by a neurologist or by building a delta wave envelope as demonstrated in Glaba et al. (2021). To our knowledge, we present the first qualitative characterization of absence seizure fragmentation. The analysis showed that seizures were disorganized in approximately half

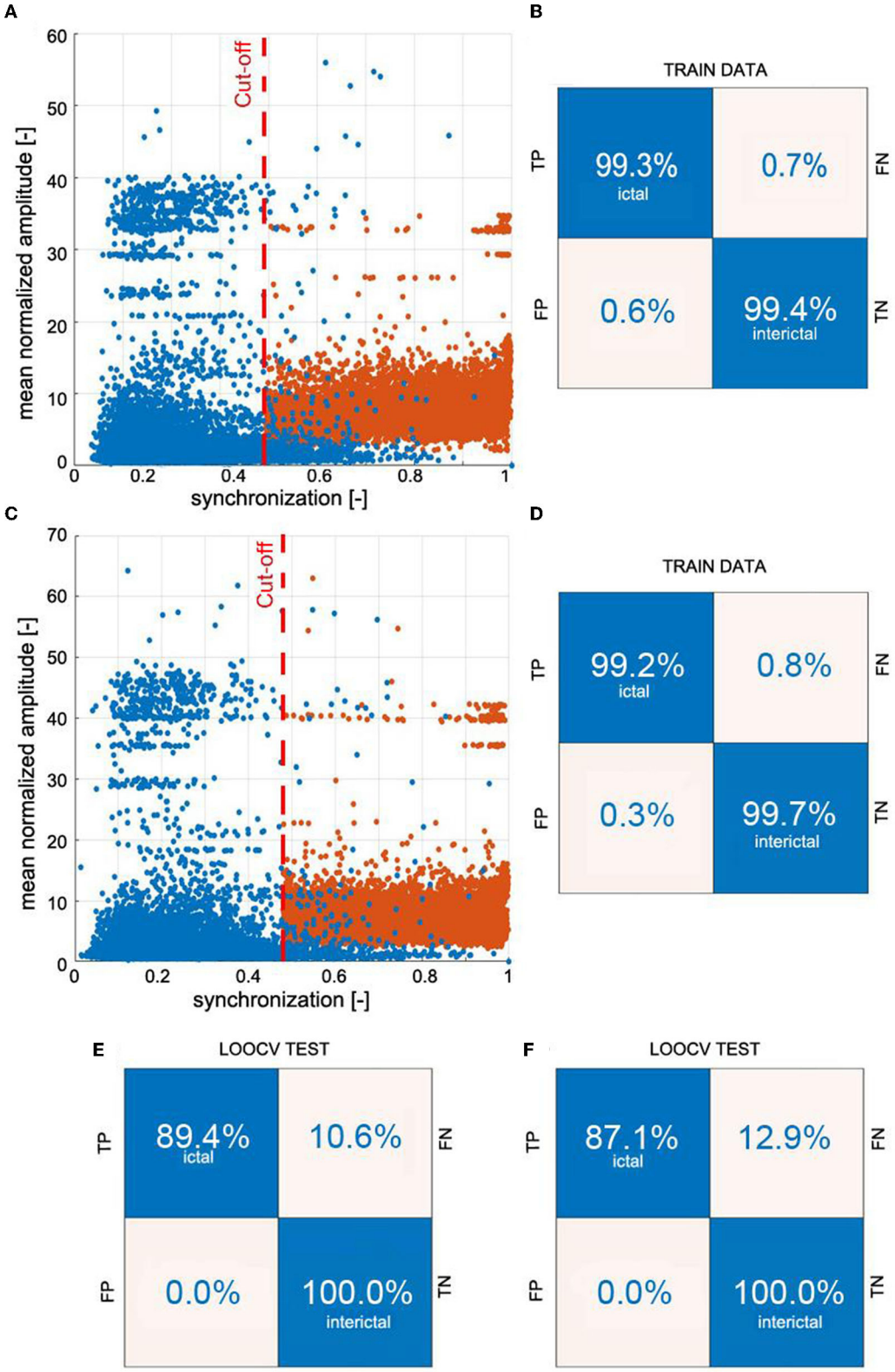

FIGURE 4
Example of building a k-NN seizure detector with the leave-one-out cross-validation (LOOCV) for patient P1. We used the global synchronization index and mean normalized EEG amplitude as the features. The learning set comprised randomly chosen interictal and segments fully embedded in absences with average synchronization greater than the cut-off value. We used 3:1 ratio of interictal to ictal windows. Panels **(A, C)** show the spread of the data generated for all 19 channels of 10-20 EEG setup (S_{19}) and the subset S_4 (channels Fp1, Fp2, T5, and T6), respectively. The confusion matrices in **(B, D)** show the results of 10-fold cross-validation. The classifiers were applied to the segmented EEG of patient P1 (1 s windows with 0.5 s overlap). Panels **(E, F)** show P1's confusion matrices for S_{19} and S_4, respectively.

10.3389/fninf.2023.1169584

TABLE 1 Seizure detection characteristics for the 19 channels (S_{19}) and three subsets with a smaller number of electrodes.

EEG SETUP	OVR [%]	PERR (FP, MT) [%, -, -]			
		P	C	Y	T
Synchronization and normalized amplitude					
S_{19}	82.9	0.87 (1437, 832)	0.12 (44, 32)	0.07 (7, 6)	0.36 (1488, 870)
S_{12}	78.01	0.71 (1147, 735)	0.23 (77, 58)	0.13 (13, 11)	0.36 (1237, 804)
S_6	79.36	0.86 (1282, 775)	0.05 (18, 14)	0.04 (4, 4)	0.32 (1304, 793)
S_4	69.31	0.68 (1196, 743)	0.03 (11, 9)	0.02 (2, 2)	0.25 (1209, 754)
Synchronization and normalized amplitude with post-processing					
S_{19}	80.93	0.57 (985, 381)	0.13 (21, 9)	0.03 (4, 2)	0.24 (1010, 392)
S_{12}	75.56	0.40 (652, 267)	0.22 (35, 15)	0.03 (4, 2)	0.22 (691, 284)
S_6	76.85	0.55 (868, 311)	0.06 (5, 2)	0.00 (0, 0)	0.21 (873, 313)
S_4	65.10	0.38 (746, 278)	0.03 (4, 2)	0.00 (0, 0)	0.13 (750, 280)

We used a k-nearest neighbor classifier with the synchronization index and normalized amplitude as the features. The overlap (OVR) of segments classified as ictal with absence seizures and relative duration of false positives (PERR) are presented for patients (P), controls (C), young adults (Y), and for segments from all cohorts (T). In parentheses, we give the number of distinct trains of misclassified windows (MT) and false positives (FP). In patients, false detections are predominantly caused by short (< 2 s) epileptiform discharges. Therefore, we also tested the possibility of reducing the number of false positives by post-processing the k-nearest neighbors classification. In particular, any isolated ictal segment was labeled non-ictal.

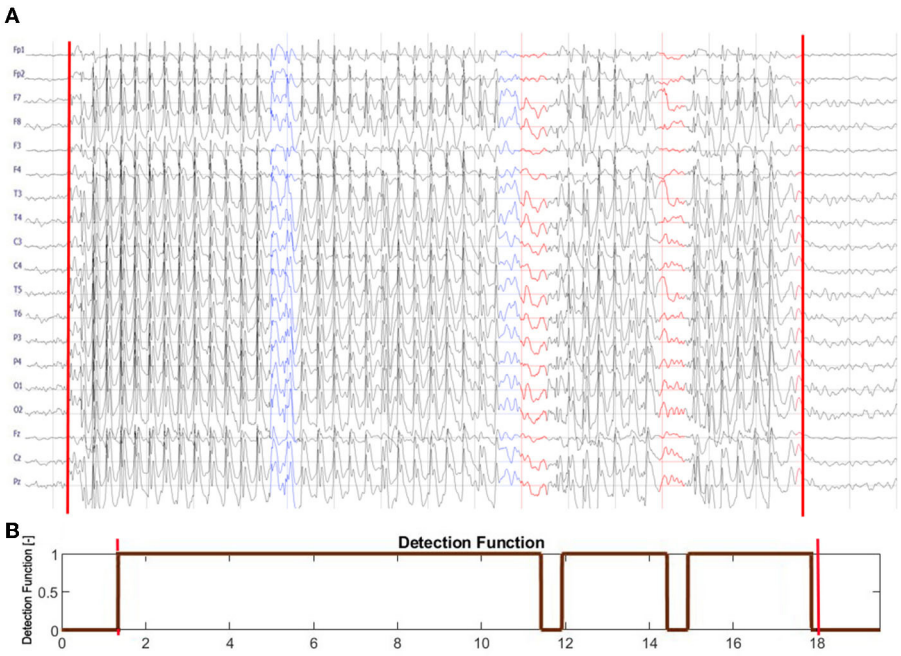

FIGURE 5
(A) Seizure from Figure 1B is shown with the leading and trailing interictal segments. **(B)** The output of the seizure detector. The detection function equals 1 for the segments classified as ictal and 0 otherwise. The red vertical lines in both subplots delineate the abnormal EEG activity marked by a neurologist. Note that SWDs do not simultaneously emerge from the background EEG in all channels. At the end of the seizure, ictal activity gradually subsides: epileptic spikes disappear, the amplitude of the EEG decreases, and global synchronization is lost. The initial and final transients are shorter than 0.5 s. The detector correctly identified the two interruptions in the ictal rhythm, marked in **(A)** in red. Two EEG intervals were marked blue to draw attention to the limitations of fragmentation analysis. Seizure disorganization shorter than about 0.5 s are, in most cases, undetected. Due to the finite size of the data window used to calculate phase synchronization, the fragmentation can be underestimated.

of the 65 subjects. On average, generalized SWDs lasted about 80% of the duration of abnormal EEG activity. The disruption of the ictal rhythm can manifest itself as the disappearance of epileptic spikes (with high-amplitude delta waves persisting), transient (about 1 s) cessation of epileptic discharges, or loss of global synchronization.

Although CAE and JAE are distinct epilepsy syndromes, there is considerable age overlap between them. Consequently, the diagnosis is not always obvious. This is an important clinical problem, as JAE is a lifelong disease. Sadleir et al. reported that disorganized discharges are eight times more frequent in JAE (Sadleir et al., 2009). For most patients, we

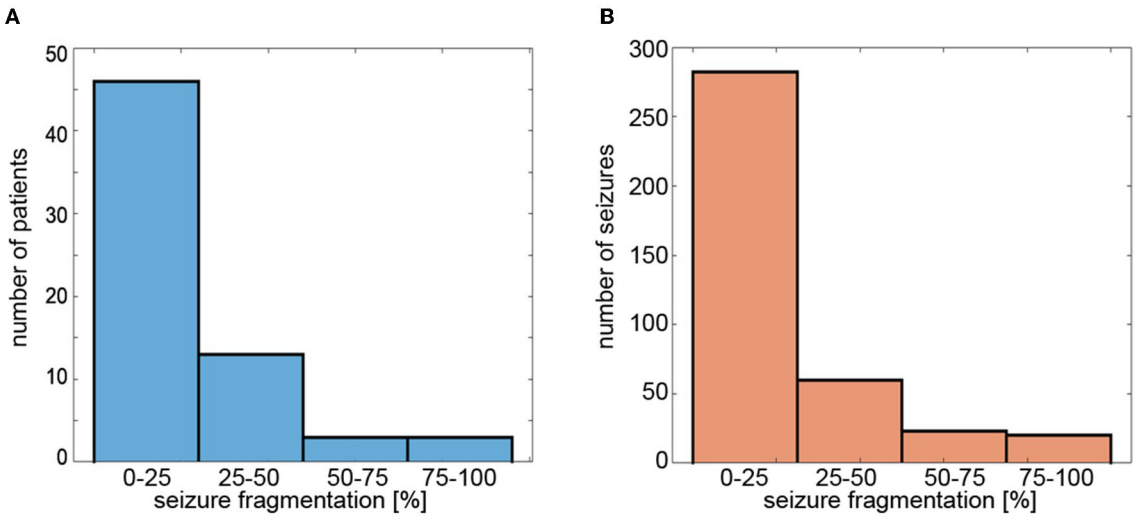

FIGURE 6
Histograms of **(A)** average fragmentation of the patient's seizures and **(B)** fragmentation of individual seizures. Seizure fragmentation is defined as the duration of segments classified as non-ictal embedded in the abnormal EEG activity interval divided by the length of such an interval.

only had the electroencephalogram recorded before the onset of pharmacotherapy. Therefore, future research must establish whether seizure properties (frequency, length, fragmentation, etc.) and clinical characteristics can distinguish CAE and JAE.

It should be noted that some EEG synchronization properties are unique to absence seizures. Figure 3B shows that γ peaks at the beginning of the seizure and is approximately twice the mean interictal value, in agreement with the recent study of (Zhong et al., 2022). However, Majmundar et al. argue that for most focal-onset seizures, synchronization occurs toward the end of the seizure rather than at the time of onset (Majumdar et al., 2014). Absence seizures exhibit longer-range synchrony than generalized tonic motor seizures of secondary (symptomatic) generalized epilepsy or frontal lobe epilepsy (Dominguez et al., 2005).

Epilepsy has historically been perceived as a functional brain disorder associated with hypersynchronization. Interestingly, desynchronization can precede seizures (Aarabi et al., 2008; Jiruska et al., 2013; Zeng et al., 2016). Figure 3C shows that the peak of the interictal distribution of γ is shifted to low values relative to the controls. Therefore, the question arises of whether this shift is a manifestation of desynchronization in patients with CAE / JAE. We will present a detailed analysis of interictal EEG synchronization properties elsewhere.

Data availability statement

The raw data supporting the conclusions of this article will be made available by the authors, without undue reservation.

Ethics statement

The studies involving human participants were reviewed and approved by Wroclaw Medical University's and Warsaw Institute of Psychiatry and Neurology Ethics Committees. Written informed consent from the participants' legal guardian/next of kin was not required to participate in this study in accordance with the national legislation and the institutional requirements.

Author contributions

ML, PG, and MK: conceptualization and methodology. PG, ML, and MJK: investigation original draft preparation. BW, WW, SK, TS, and WJ: review and editing. All authors contributed to formal analysis. All authors contributed to the article and approved the submitted version.

Funding

This research was supported by the grand of Wroclaw Medical University (SUBZ.A422.22.014).

Acknowledgments

We thank Łukasz Bratos for the help with the numerical calculations.

Conflict of interest

The authors declare that the research was conducted in the absence of any commercial or financial relationships that could be construed as a potential conflict of interest.

Publisher's note

All claims expressed in this article are solely those of the authors and do not necessarily represent those of their affiliated organizations, or those of the publisher, the editors and the reviewers. Any product that may be evaluated in this article, or claim that may be made by its manufacturer, is not guaranteed or endorsed by the publisher.

Supplementary material

The Supplementary Material for this article can be found online at: https://www.frontiersin.org/articles/10.3389/fninf.2023.1169584/full#supplementary-material

References

Aarabi, A., Wallois, F., and Grebe, R. (2008). Does spatiotemporal synchronization of EEG change prior to absence seizures? *Brain Res.* 1188, 207–221. doi: 10.1016/j.brainres.2007.10.048

Addison, P. S. (2017). *The Illustrated Wavelet Transform Handbook: Introductory Theory and Applications in Science, Engineering, Medicine and Finance*. Boca Raton, FL: CRC Press.

Addison, P. S. (2018). Introduction to redundancy rules: the continuous wavelet transform comes of age. *Philos. Trans. R. Soc. A Math. Phys. Eng. Sci.* 376, 20170258. doi: 10.1098/rsta.2017.0258

Adeli, H., Zhou, Z., and Dadmehr, N. (2003). Analysis of EEG records in an epileptic patient using wavelet transform. *J. Neurosci. Methods* 123, 69–87. doi: 10.1016/S0165-0270(02)00340-0

Akman, C. I., Montenegro, M. A., Jacob, S., Eck, K., Chiriboga, C., and Gilliam, F. (2009). Seizure frequency in children with epilepsy: factors influencing accuracy and parental awareness. *Seizure* 18, 524–529. doi: 10.1016/j.seizure.2009.05.009

Altenburg, J., Vermeulen, R. J., Strijers, R. L., Fetter, W. P., and Stam, C. J. (2003). Seizure detection in the neonatal EEG with synchronization likelihood. *Clin. Neurophysiol.* 114, 50–55. doi: 10.1016/S1388-2457(02)00322-X

Asadi-Pooya, A. A., Emami, M., and Sperling, M. R. (2013). A clinical study of syndromes of idiopathic (genetic) generalized epilepsy. *J. Neurol. Sci.* 324, 113–117. doi: 10.1016/j.jns.2012.10.014

Bauquier, S. H., Lai, A., Jiang, J. L., Sui, Y., and Cook, M. J. (2015). Evaluation of an automated spike-and-wave complex detection algorithm in the EEG from a rat model of absence epilepsy. *Neurosci. Bull.* 31, 601–610. doi: 10.1007/s12264-015-1553-5

Dan, J., Vandendriessche, B., Paesschen, W. V., Weckhuysen, D., and Bertrand, A. (2020). Computationally-efficient algorithm for real-time absence seizure detection in wearable electroencephalography. *Int. J. Neural Syst.* 30, 2050035. doi: 10.1142/S0129065720500355

Dominguez, L. G., Wennberg, R. A., Gaetz, W., Cheyne, D., Snead, O. C., and Velazquez, J. L. P. (2005). Enhanced synchrony in epileptiform activity? Local versus distant phase synchronization in generalized seizures. *J. Neurosci.* 25, 8077–8084. doi: 10.1523/JNEUROSCI.1046-05.2005

Duun-Henriksen, J., Madsen, R. E., Remvig, L. S., Thomsen, C. E., Sorensen, H. B., and Kjaer, T. W. (2012). Automatic detection of childhood absence epilepsy seizures: toward a monitoring device. *Pediatr. Neurol.* 46, 287–292. doi: 10.1016/j.pediatrneurol.2012.02.018

Fisher, R. S., Boas, W. V. E., Blume, W., Elger, C., Genton, P., Lee, P., et al. (2005). Epileptic seizures and epilepsy: definitions proposed by the international league against epilepsy (ILAE) and the international bureau for epilepsy (IBE). *Epilepsia* 46, 470–472. doi: 10.1111/j.0013-9580.2005.66104.x

Glaba, P., Latka, M., Krause, M. J., Kroczka, S., Kuryło, M., Kaczorowska-Frontczak, M., et al. (2021). Absence seizure detection algorithm for portable EEG devices. *Front. Neurol.* 12, 685814. doi: 10.3389/fneur.2021.685814

Glauser, T. A., Cnaan, A., Shinnar, S., Hirtz, D. G., Dlugos, D., Masur, D., et al. (2013). Ethosuximide, valproic acid, and lamotrigine in childhood absence epilepsy: initial monotherapy outcomes at 12 months. *Epilepsia.* 54, 141–155.

Grubov, V., Sitnikova, E., Pavlov, A., Koronovskii, A., and Hramov, A. (2017). Recognizing of stereotypic patterns in epileptic EEG using empirical modes and wavelets. *Phys. A Stat. Mech. Appl.* 486, 206–217. doi: 10.1016/j.physa.2017.05.091

Hirsch, E., French, J., Scheffer, I. E., Bogacz, A., Alsaadi, T., Sperling, M. R., et al. (2022). Ilae definition of the idiopathic generalized epilepsy syndromes: position statement by the ILAE task force on nosology and definitions. *Epilepsia* 63, 1475–1499. doi: 10.1111/epi.17236

Japaridze, G., Loeckx, D., Buckinx, T., Armand Larsen, S., Proost, R., Jansen, K., et al. (2022). Automated detection of absence seizures using a wearable electroencephalographic device: a phase 3 validation study and feasibility of automated behavioral testing. *Epilepsia*. doi: 10.1111/epi.17200

Jiruska, P., De Curtis, M., Jefferys, J. G., Schevon, C. A., Schiff, S. J., and Schindler, K. (2013). Synchronization and desynchronization in epilepsy: controversies and hypotheses. *J. Physiol.* 591, 787–797. doi: 10.1113/jphysiol.2012.239590

Keilson, M. J., Hauser, W. A., Magrill, J. P., and Tepperberg, J. (1987). Ambulatory cassette EEG in absence epilepsy. *Pediatr. Neurol.* 3, 273–276.

Kjaer, T. W., Sorensen, H. B., Groenborg, S., Pedersen, C. R., and Duun-Henriksen, J. (2017). Detection of paroxysms in long-term, single-channel EEG-monitoring of patients with typical absence seizures. *IEEE J. Transl. Eng. Health Med.* 5, 1–8. doi: 10.1109/JTEHM.2017.2649491

Krigolson, O. E., Williams, C. C., Norton, A., Hassall, C. D., and Colino, F. L. (2017). Choosing muse: validation of a low-cost, portable EEG system for erp research. *Front. Neurosci.* 11, 109. doi: 10.3389/fnins.2017.00109

Lachaux, J.-P., Rodriguez, E., Martinerie, J., and Varela, F. J. (1999). Measuring phase synchrony in brain signals. *Hum. Brain Mapp.* 8, 194–208.

Latka, M., Turalska, M., Glaubic-Latka, M., Kolodziej, W., Latka, D., and West, B. J. (2005). Phase dynamics in cerebral autoregulation. *Am. J. Physiol. Heart Circ. Physiol.* 289, H2272–H2279. doi: 10.1152/ajpheart.01307.2004

Majumdar, K., Prasad, P. D., and Verma, S. (2014). Synchronization implies seizure or seizure implies synchronization? *Brain Topogr.* 27, 112–122. doi: 10.1007/s10548-013-0284-z

Mallat, S. (1999). *A Wavelet Tour of Signal Processing*. San Diego, CA: Elsevier.

MATLAB (2022). *version 9.13.0.2049777 (R2022a)*. The MathWorks Inc., Natick, MA.

Ovchinnikov, A., Lüttjohann, A., Hramov, A., and Van Luijtelaar, G. (2010). An algorithm for real-time detection of spike-wave discharges in rodents. *J. Neurosci. Methods* 194, 172–178. doi: 10.1016/j.jneumeth.2010.09.017

Petersen, E. B., Duun-Henriksen, J., Mazzaretto, A., Kjær, T. W., Thomsen, C. E., and Sorensen, H. B. (2011). "Generic single-channel detection of absence seizures," in *2011 Annual International Conference of the IEEE Engineering in Medicine and Biology Society* (Boston, MA: IEEE), 4820–4823.

Pu, L., Lion, K. M., Todorovic, M., and Moyle, W. (2021). Portable EEG monitoring for older adults with dementia and chronic pain-a feasibility study. *Geriatr. Nurs.* 42, 124–128. doi: 10.1016/j.gerinurse.2020.12.008

Quiroga, R. Q., Kraskov, A., Kreuz, T., and Grassberger, P. (2002). Performance of different synchronization measures in real data: a case study on electroencephalographic signals. *Phys. Rev. E* 65, 041903. doi: 10.1103/PhysRevE.65.041903

Sadleir, L. G., Scheffer, I. E., Smith, S., Carstensen, B., Farrell, K., and Connolly, M. B. (2009). EEG features of absence seizures in idiopathic generalized epilepsy: impact of syndrome, age, and state. *Epilepsia* 50, 1572–1578. doi: 10.1111/j.1528-1167.2008.02001.x

Schomer, D. L. and da Silva, F. L. (2018). *Niedermeyer's Electroencephalography: Basic Principles, Clinical Applications, and Related Fields*. Oxford: Oxford University Press.

Sitnikova, E., Hramov, A. E., Koronovsky, A. A., and van Luijtelaar, G. (2009). Sleep spindles and spike–wave discharges in EEG: their generic features, similarities

and distinctions disclosed with fourier transform and continuous wavelet analysis. *J. Neurosci. Methods* 180, 304–316. doi: 10.1016/j.jneumeth.2009.04.006

Slooter, A., Vriens, E., Leijten, F., Spijkstra, J., Girbes, A., van Huffelen, A., et al. (2006). Seizure detection in adult ICU patients based on changes in EEG synchronization likelihood. *Neurocrit. Care* 5, 186–192. doi: 10.1385/NCC:5:3:186

Subasi, A. (2007). Application of adaptive neuro-fuzzy inference system for epileptic seizure detection using wavelet feature extraction. *Comput. Biol. Med.* 37, 227–244. doi: 10.1016/j.compbiomed.2005.12.003

Szaflarski, J. P., DiFrancesco, M., Hirschauer, T., Banks, C., Privitera, M. D., Gotman, J., et al. (2010). Cortical and subcortical contributions to absence seizure onset examined with EEG/fMRI. *Epilepsy Behav.* 18, 404–413. doi: 10.1016/j.yebeh.2010.05.009

Tenneti, S. V., and Vaidyanathan, P. (2018). "Absence seizure detection using ramanujan filter banks," in *2018 52nd Asilomar Conference on Signals, Systems, and Computers* (Pacific Grove, CA: IEEE), 1913–1917.

Xanthopoulos, P., Rebennack, S., Liu, C.-C., Zhang, J., Holmes, G. L., Uthman, B. M., et al. (2010). "A novel wavelet based algorithm for spike and wave detection in absence epilepsy," in *2010 IEEE International Conference on BioInformatics and BioEngineering* (Philadelphia, PA: IEEE), 14–19.

Zeng, K., Yan, J., Wang, Y., Sik, A., Ouyang, G., and Li, X. (2016). Automatic detection of absence seizures with compressive sensing EEG. *Neurocomputing* 171, 497–502. doi: 10.1016/j.neucom.2015.06.076

Zhong, L., Wan, J., Wu, J., He, S., Zhong, X., Huang, Z., and Li, Z. (2022). Temporal and spatial dynamic propagation of electroencephalogram by combining power spectral and synchronization in childhood absence epilepsy. *Front. Neuroinform.* 16, 962466. doi: 10.3389/fninf.2022.962466

frontiers | Frontiers in Neuroinformatics

TYPE Technology and Code
PUBLISHED 03 September 2024
DOI 10.3389/fninf.2024.1465231

OPEN ACCESS

EDITED BY
Saadullah Farooq Abbasi,
University of Birmingham, United Kingdom

REVIEWED BY
Muhammad Irfan,
University of Turku, Finland
Roman Rodionov,
University College London, United Kingdom

*CORRESPONDENCE
James L. Evans
✉ jamese4@illinois.edu

RECEIVED 15 July 2024
ACCEPTED 21 August 2024
PUBLISHED 03 September 2024

CITATION
Evans JL, Bramlet MT, Davey C, Bethke E, Anderson AT, Huesmann G, Varatharajah Y, Maldonado A, Amos JR and Sutton BP (2024) SEEG4D: a tool for 4D visualization of stereoelectroencephalography data. *Front. Neuroinform.* 18:1465231. doi: 10.3389/fninf.2024.1465231

SEEG4D: a tool for 4D visualization of stereoelectroencephalography data

James L. Evans[1,2]*, Matthew T. Bramlet[3,4], Connor Davey[4], Eliot Bethke[1], Aaron T. Anderson[2,5], Graham Huesmann[2,5,6,7], Yogatheesan Varatharajah[8], Andres Maldonado[9], Jennifer R. Amos[1,7] and Bradley P. Sutton[1,2,7]

[1]Department of Bioengineering, University of Illinois Urbana-Champaign, Urbana, IL, United States, [2]Beckman Institute for Advanced Science and Technology, University of Illinois Urbana-Champaign, Urbana, IL, United States, [3]University of Illinois College of Medicine, Peoria, IL, United States, [4]Jump Trading Simulation and Education Center, Peoria, IL, United States, [5]Department of Neurology, Carle Foundation Hospital, Urbana, IL, United States, [6]Department of Molecular and Integrative Physiology, University of Illinois Urbana-Champaign, Urbana, IL, United States, [7]Carle Illinois College of Medicine, University of Illinois Urbana-Champaign, Urbana, IL, United States, [8]Department of Computer Science and Engineering, University of Minnesota, Minneapolis, MN, United States, [9]Department of Neurosurgery, OSF Healthcare, Peoria, IL, United States

Epilepsy is a prevalent and serious neurological condition which impacts millions of people worldwide. Stereoelectroencephalography (sEEG) is used in cases of drug resistant epilepsy to aid in surgical resection planning due to its high spatial resolution and ability to visualize seizure onset zones. For accurate localization of the seizure focus, sEEG studies combine pre-implantation magnetic resonance imaging, post-implant computed tomography to visualize electrodes, and temporally recorded sEEG electrophysiological data. Many tools exist to assist in merging multimodal spatial information; however, few allow for an integrated spatiotemporal view of the electrical activity. In the current work, we present SEEG4D, an automated tool to merge spatial and temporal data into a complete, four-dimensional virtual reality (VR) object with temporal electrophysiology that enables the simultaneous viewing of anatomy and seizure activity for seizure localization and presurgical planning. We developed an automated, containerized pipeline to segment tissues and electrode contacts. Contacts are aligned with electrical activity and then animated based on relative power. SEEG4D generates models which can be loaded into VR platforms for viewing and planning with the surgical team. Automated contact segmentation locations are within 1 mm of trained raters and models generated show signal propagation along electrodes. Critically, spatial–temporal information communicated through our models in a VR space have potential to enhance sEEG pre-surgical planning.

KEYWORDS

stereoelectroencephalography, SEEG, virtual reality, presurgical planning, epilepsy, visualization tools

1 Introduction

Epilepsy is a chronic neurological condition affecting more than 50 million people worldwide. Epilepsy is characterized by recurrent, spontaneous seizures and is defined as two unprovoked seizures occurring more than 24 h apart, an unprovoked seizure if the risk of recurrence is high, or a diagnosis of an epilepsy syndrome (Fisher et al., 2014; Thijs et al., 2019). EEG recordings and physical behaviors clearly show how seizures produce strong electrical activity and spread throughout other areas of the brain. The exact pathophysiology producing the seizures (e.g., neurotransmitters, structural abnormalities, environmental factors), occurring at the seizure onset zone (SOZ), and how the electrical signals spread throughout the brain is not well understood. Identification of the SOZ is critical for treatment, particularly for surgical interventions. Imperfect identification of the SOZ renders imperfect treatments, which leads to continued seizures, additional surgical treatments, and overall reduction in quality of life (Andrews et al., 2020; Paulo et al., 2022).

Approximately 30–40% of patients who are diagnosed with epilepsy have symptoms which are not fully controlled by currently available antiepileptic medications, a condition known as drug-resistant epilepsy (DRE) (Kalilani et al., 2018). Such patients are at an increased risk of serious adverse effects resulting in significant degradation of their quality of life or premature death (Mula and Cock, 2015). For these patients, an effective treatment is a surgical resection of the area in the brain triggering the seizures, the SOZ (Ryvlin et al., 2014; Andrews et al., 2020). The goal of resective surgery planning is to outline the epileptogenic zone for an accurate surgery so that the patient can achieve seizure freedom (Ryvlin et al., 2014; Andrews et al., 2020). While the procedure is not risk free, cognition, behavior and quality of life can improve after resective surgery and it has proven to be an effective procedure (Ryvlin et al., 2014).

Determining the SOZ is often a difficult task because of the lack of morphological identifying characteristics distinguishable from healthy tissue in standard medical imaging evaluations (Ryvlin et al., 2014; Minkin et al., 2019). Localizing the SOZ typically involves a multi-modal approach combining various imaging modalities, such as magnetic resonance imaging (MRI), functional MRI (fMRI), computed tomography (CT), positron emission tomography (PET), magnetoencephalography (MEG), and electrophysiology using electroencephalography (EEG), along with neuropsychological testing and Wada testing (van Mierlo et al., 2020; Kakinuma et al., 2022; Bearden et al., 2023). A more invasive process, stereoelectroencephalography (sEEG), is used to obtain precise recordings from depth electrodes to identify SOZs that are deep in the brain or difficult to localize (Gonzalez-Martinez et al., 2014). In sEEG, neurosurgeons place electrodes into the brain, penetrating deep into the tissue, targeting regions that are suspected of being the SOZ to provide highly localized recordings in a 3D space to identify and confirm the seizure initiation site (Bartolomei et al., 2017). Electrode trajectories are often manually computed, but tools are being developed to assist with planning (De Momi et al., 2014).

Currently, epileptologists and neurosurgeons manually review the 1D sEEG recordings with the 2D multiplanar views of the 3D imaging data to localize the SOZ and epileptogenic activity (Hassan et al., 2020). Their goal is to construct a mental model of the patient's specific anatomy when preparing for resective surgery (Minkin et al., 2019). This multimodal information is challenging for experts to mentally combine and extract actionable data (Lyuksemburg et al., 2023). Better mental representations of anatomy can be created from directly interacting with the 3D models as opposed to 1D and 2D views of the multimodal data (Guillot et al., 2007; Wu et al., 2010; Mattus et al., 2022). 3D models have proven useful for navigating through patient-specific anatomy in planning epilepsy surgery for both the surgeons and for patient education due to the integrated visualization of the complex multimodal data (Minkin et al., 2019; Phan et al., 2022). VR technologies can enable an interactive view of complex 3D models and have been used in other complex resection cases where they have demonstrated improvements in the operative experience for the surgeon (Quero et al., 2019; Louis et al., 2021). The seizure activity from the sEEG recordings creates even more complex data that are 4D, with 3 spatial dimensions and changes over time. In the current work, we further merge the clinical dataset from a sEEG study into a unified model for viewing anatomy and dynamic electrophysiological data in a 4D VR presurgical planning platform. This tool will enable surgeons to focus their attention and expertise on patient-specific details directly relevant to the surgery.

Several toolboxes have been developed to lessen the challenges involved with merging multimodal spatial information from sEEG studies (Armin Vosoughi et al., 2022). Some of these tools automate critical image information steps, such as isolating electrode contacts or making predictions about the SOZ or the epileptogenic zones on patient specific anatomy. A few examples include sEEG Assistant (Narizzano et al., 2017), which is a set of tools built as a 3D Slicer[1] extension (Fedorov et al., 2012), and Epitools (Medina Villalon et al., 2018), which also uses Freesurfer (Dale et al., 1999) pial surfaces, or LeGUI (Davis et al., 2021). Many 2D sEEG visualization tools, such as Brainquake (Cai et al., 2021), opt to highlight or enlarge electrode contacts to indicate some degree of epileptogenicity while other software packages, like MNE-Python, project the data onto brain tissue and predict a SOZ in the brain based on the sEEG recordings (Gramfort et al., 2013; Cai et al., 2021). Several of the tools note if the contact predominately resides in gray matter or white matter, as tissue type can impact some of the computations made to analyze activity (Arnulfo et al., 2015). Some of the packages listed here require a brain atlas or a set of standard naming conventions which is not the case for all clinically acquired sEEG data sets. However, most of these tools are not maintained and are reliant on outdated dependencies that do not work with modern workstations as noted by Armin Vosoughi et al. (2022). Software such as EpiNav (CMIC, UCL, London, United Kingdom) (Vakharia et al., 2019) or CNSprojects[2] are available in a limited manner and merge anatomical data with sEEG biomarkers. The virtual epileptic patient (Makhalova et al., 2022) based on Virtual Brain (Sanz-Leon et al., 2015) can take sEEG data and generate simulations of patients seizures, compute the SOZ and display a glass brain model and waveforms of the epileptic data. All these visualizations *present their models confined to a 2D display* requiring the surgeon to mentally extrapolate the data to 3D space and merge this activity data with the patient's 3D anatomy for diagnosis and surgical planning. These tools do not resolve challenges with taking data presented in a 2D format and extrapolating it to generate 3D

1 https://www.slicer.org

2 https://cnsprojects.nl/products/

mental representations of the surgical case. SyncAR is an augmented reality and virtual reality platform which works with the data from surgical devices and uses VR for surgical planning and augmented reality to navigate during the resection procedure (Louis et al., 2021). SyncAR's usage highlights a need for temporally dynamic visualization tools for sEEG evaluation and resection planning (Louis et al., 2021).

In this work, we propose SEEG4D, an open-source tool which presents the pre-implant MRI, post-implant CT, and dynamic sEEG data as a *4D dynamic model for use in a virtual reality (VR) presurgical planning environment* as opposed to the traditional 2D environment. By animating the time series data onto the electrode contacts in VR, we enable neurosurgeons to view the common components of the clinical data but in a platform that integrates spatial information with dynamic seizure activity to supplement the traditional resective surgery workflow. Users can virtually explore the 3D brain tissue, see electrode activation over time, and make surgical plans accordingly. 3D model use in pre-surgical planning capitalizes on this impact by creating improved mental representations of patient-specific anatomy through a personalized medicine approach (Wu et al., 2010). Previous research has shown that developing 3D VR models of patient anatomy has the potential to assist surgeons in presurgical planning and may reduce complications (Herfarth et al., 2002; Oldhafer et al., 2009; Chen et al., 2010; Quero et al., 2019). Further, situational awareness research analyzing expert performance over novice performance indicates improved mental models of pre-surgical anatomy are characteristic of the expert performer by shifting the mental burden from working memory to long term memory (Maan et al., 2012; Sadideen et al., 2013; Robertson et al., 2024). Additionally, VR has been shown to provide information which may alter the surgical approach (Quero et al., 2019; Mahajan et al., 2021; Robertson et al., 2024). SEEG4D seeks to automatically generate dynamic 4D models to supplement the presurgical workflow and enable VR-based presurgical planning. To our knowledge, SEEG4D is the first time that animated 3D VR models of electrical activity have been automatically generated and used for epilepsy pre-surgical planning.

2 Materials and methods

2.1 Software overview

Our software package is split into two components. The first component is a Python-based GUI to handle user preferences, inputs, and provide status updates. The second component is a Docker container to perform the neuroimaging processing steps and generate VR-ready models. These components automatically interconnect and interact; users of the software need only install Docker and the bare minimum requirements to run the Python graphical user interface (GUI). Containerization of critical software components enables easier use and reproducibility of medical imaging software technologies (Matelsky et al., 2018). Key software included in our container is: Python 3.8 for FSL 6.0.5.1, Python 3.9 for MNE-Python 1.6.1 using nibabel 5.2.1 with scikit-image 0.22.0, Python 3.10 for Blender 4.0.0 (Python Software Foundation, https://www.python.org/) (Blender Foundation, https://www.blender.org/) (Woolrich et al., 2009; Gramfort et al., 2013; van der Walt et al., 2014; Brett, 2024). An overview of the multimodal image processing pipeline is shown in Figure 1.

There are many steps to processing sEEG data and merging the electrophysiology information into the patient's 3D anatomical data. These steps are outlined in the flow chart in Figure 1 and briefly described here. More details are given in the following sections. The pre-implantation MRI is registered to the post-implantation CT which serves as the working space for anatomical images. The image processing steps, briefly, include: Segmentation of the pre-implantation MRI data into gray matter, white matter, cerebrospinal fluid (CSF), and any other regions of interest. Next, the electrode locations must be extracted, and the different electrode contacts must be merged into multi-contact electrodes. The naming of the electrodes is performed in the main GUI where the user associates the electrode names from the sEEG data and selects the corresponding segmented electrode in consultation with the sEEG implantation planning map. This is the only processing step which requires manual input as there is not a universal naming convention for implanted electrodes. sEEG data must be processed to identify the seizure timing and filtered according to a powerline noise notch filter combined with a user-selected bandpass filter design. By default, SEEG4D uses a frequency band of 80–250 HZ as this band is commonly used for the detection of high frequency oscillations which are correlated with epileptogenic activity (Remakanthakurup Sindhu et al., 2020). Electrode activity is then converted to an average windowed power. All 3D imaging processes and the SEEG processing are handled in the container, along with the Blender processes to generate the VR-ready 4D model as output. All code and containers are available on https://github.com/mrfil/SEEG4D.

2.2 3D image processing

Image processing is done automatically using pre-existing neuroimaging software packages and customized python scripts installed inside the Docker container. A brain mask is generated using the FSL Brain Extraction Tool (bet) on the pre-implantation T1-weighted MRI (Smith, 2002). FSL FAST is used to segment the brain into gray, white, cerebrospinal fluid (Zhang et al., 2001). Registration between the CT and brain extracted MRI is performed by estimating a rigid body (6 DOF) transformation between the CT and MRI image using a mutual information cost function and FSL FLIRT (Jenkinson and Smith, 2001; Jenkinson et al., 2002). We apply the estimated registration to the brain mask and tissue type maps from MRI to put all MRI information into the CT space, with a nearest neighbor interpolation as shown in Figure 2. We erode the registered MRI mask three times so that there is little to no remaining overlap with the skull on the resulting registered mask. All images in the CT space are further resampled into 1 mm isotropic space and flipped, if necessary to align imaging space left/right to the future VR space left/right, to assist in the creation of 3D objects. SEEG contacts on the CT images are isolated from the skull by first applying the registered brain mask, followed by a threshold at the 99.5th percentile to leave only voxels containing metal and metal artifacts. Through iterating, we found this chosen threshold removes the most noise, skull and scanner artifacts, and reduced contact blur (streaking artifact) without deleting contacts. A median filter with a sphere kernel of 0.5 mm is applied to the thresholded image to reduce contact streaking. Then, the filtered image is converted to isotropic space and a 40th percentile

10.3389/fninf.2024.1465231

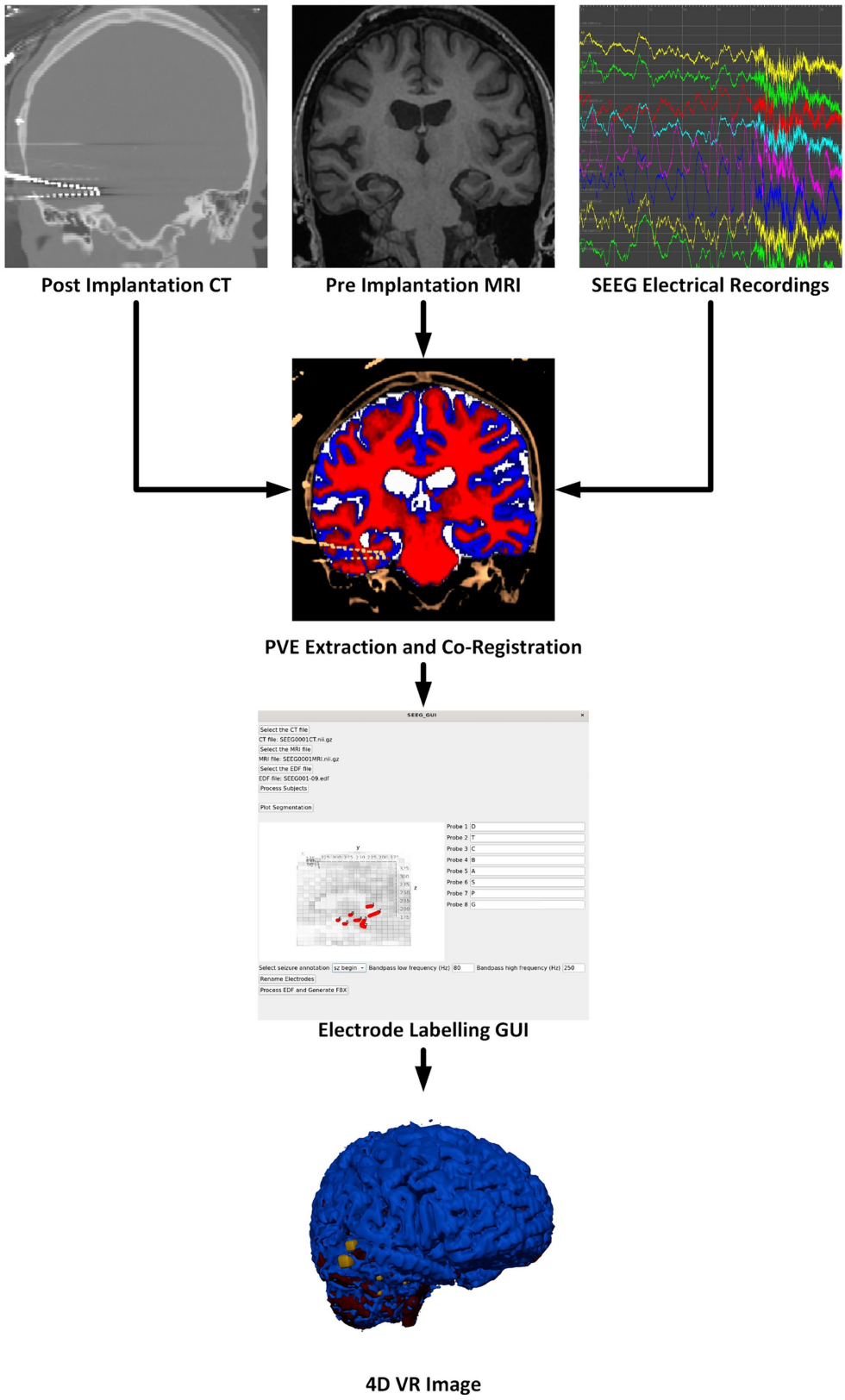

FIGURE 1
Overview of the software pipeline outlining input of CT, MRI, and sEEG data (as EDF files) through the GUI to create a VR image of the sEEG activity with the chosen bandwidth and window width. Labeling electrodes in the GUI with the sEEG planning map is the only manual step.

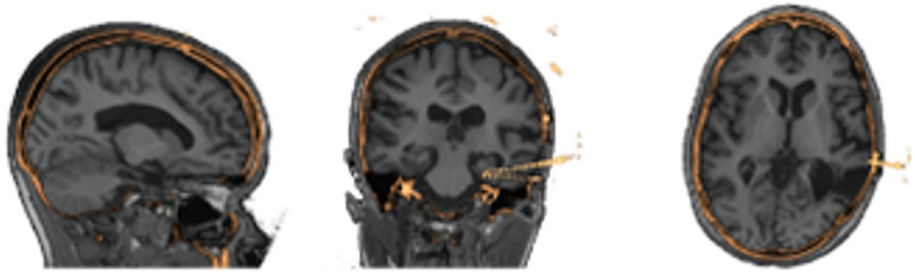

FIGURE 2
Results of image processing and registration as seen in three different views from the same patients' MRI (grayscale) to their processed CT (gold) showing alignment of the two image spaces.

threshold is applied to remove interpolation artifacts. We note that our CT data did not have metal artifact reduction enabled in the acquisition leading to significant metal artifacts associated with the electrodes.

2.3 Electrode contact segmentation and aggregation

With the contacts isolated, SEEG4D locates the position of the contacts in space using a custom automated algorithm written in Python. A representative contact, which is a 3 mm x 3 mm x 3 mm isotropic voxel cube, was manually created to act as a template for future processing steps. Isolated voxels are treated as outliers and removed.

Voxels are classified into contacts by grouping neighboring, non-diagonal voxels together recursively until every non-zero voxel has been grouped into a contact. We note that, due to streaking artifacts, this may group voxels from separate contacts together. Preventing the contacts from acquiring diagonal voxels helps prevent contacts which almost touch from clumping together. To further isolate contacts, we iteratively apply 1D erosions to electrode contacts until they are smaller than or the same size as the representative electrode via the following procedure, which is motivated by thinning connecting regions between contacts: If the contact is wider along the z direction than the representative, an x-directional erosion is applied; if the contact is wider along the x direction than the representative, a y-directional erosion is applied; if the contact is wider along the y direction than the representative, an x-directional erosion is applied. Once an electrode has been eroded to be smaller than half the size of the representative, it is replaced by the representative contact by aligning the midpoint of the representative to the replaced contact. Grouping and erosion algorithms run repeatedly on the entire image until all contacts have been replaced by the representative. This electrode segmentation process is demonstrated in Figure 3.

Electrode contacts can blur together due to scanner artifacts and orientation of electrodes in the scanner, so a contact-by-contact erosion method is preferred to separate the contacts and preserve spatial location of the contacts. Further, this individualized erosion approach works even with the difficult arrangements of electrodes that are not aligned with a main axis of the image, i.e., diagonal electrodes such as in Figure 3. Contact midpoints are saved and used to label them and orient them in space.

Collections of contacts to form electrodes are built from the midpoints of contacts by computing the outermost electrode contact and finding the closest contact and treating the pair as an electrode. The next contact within a search distance of 15 mm, and that does not deviate more than 20° from the second most recently added contact, is added to the electrode. Through iterative testing, we found 20° accounts for some bending along the electrode without merging parallel electrodes. This process repeats until all contacts have been classified into electrodes such as in Figure 3.

Electrodes are manually labeled using the main GUI, see Figure 4, but contact numbering is done automatically. Axial and sagittal MRI slices are plotted along with the electrodes in a rotatable, zoomable interface. The center of the brain is computed and contacts along an electrode are labeled inner-most to out-most (e.g., A1 is electrode A contact 1 and is the contact at the end of the electrode) following our clinical site's naming conventions.

2.4 sEEG data processing

Electrical data from the sEEG electrodes is provided to the software as EDF files. These files are loaded, through the Docker container, into MNE Python for signal processing (Gramfort et al., 2013). In the main GUI, a dropdown box is populated with the event flags in the EDF file where the user can select the flag belonging to the electrical activity of interest, such as a particular seizure. In this paper, we use events that were clinically marked as seizure start flags. By default, the signal is cropped around the chosen event with a two-second window on either side, creating a four-second clip in total for our 4D visualization. Data is notch filtered to remove power line noise and then any bandpass filters chosen are applied. By default, an 80 Hz-250 Hz windowed finite impulse response filter is used as this filter band is commonly used to identify high-frequency oscillations for SOZ localization (Remakanthakurup Sindhu et al., 2020).

2.5 VR model generation

Now that the SEEG contacts have been automatically segmented, named, and labeled with corresponding electrical data, SEEG4D generates VR models using Blender's Python scripting capabilities. SEEG contacts, gray matter, white matter, and cerebral spinal fluid are each converted to object files using Scikit-Image's implementation of

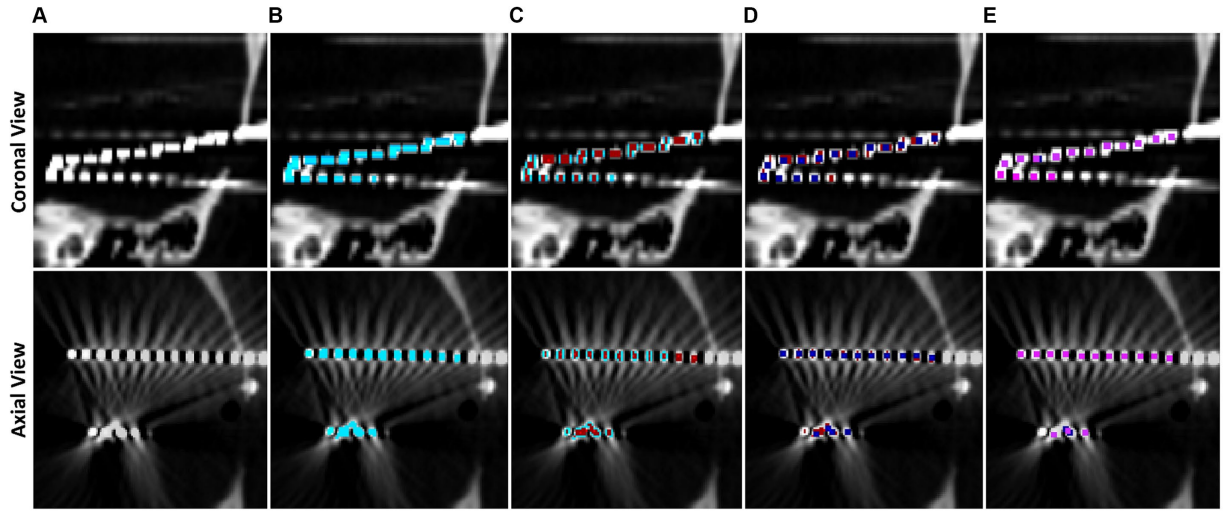

FIGURE 3
Step by step example of electrode contact segmentation and representative replacement. The top row is a cropped coronal slice while the bottom row is a cropped axial slice. **(A)** Base CT image, note that the ends of two electrodes have blended on the imaging and there is streaking artifact connecting two contacts. **(B)** Post masking, filtered, and thresholded electrode contact mask overlaid in blue. **(C)** Electrode contact mask after first pass of erosion in red, note that the ends of the electrodes have separated. **(D)** Second pass of erosion in dark blue. Contacts connected by streaking artifact have separated. **(E)** Final pass of the algorithm in pink. All contacts have been replaced by the representative contact by now.

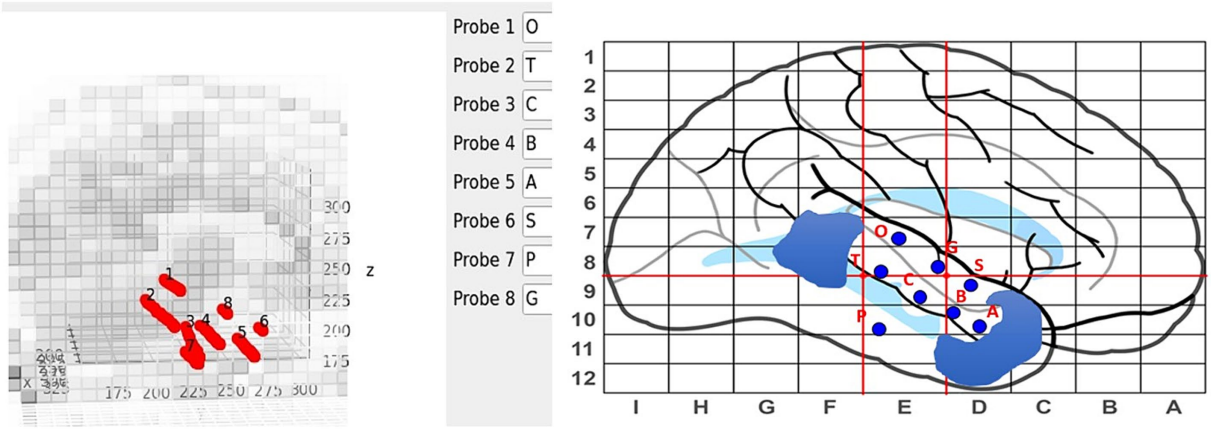

FIGURE 4
Labeling interface on the main GUI (left) with the sEEG planning map and naming scheme (right). Blue regions on the sEEG planning map indicate cavities.

the Lewiner Marching Cubes algorithm (Lewiner et al., 2003; van der Walt et al., 2014). Our sampling rate in the EDF files is approximately 1KHz, and we chose to make 24 ms wide long frames. Meaning that each second of the animation contains 24 ms of data. This turns a 4-s-long EDF clip into a 167-s-long animation. We compute the power over our sliding window by:

$$P_x = \left\| \frac{1}{N} \sum_{n=1}^{N} = 10 \left(x[n] \right)^2 \right\|_2$$

Where N is our sliding window length ($N = 24$). Min-max scaling is applied to the power data, across all electrodes by subtracting the minimum power and dividing by the range of power across all windows and contacts.

Electrode contacts are animated by evenly scaling their size at the frame being animated, where the maximum size is 6 cm, to make the difference in power between electrodes more apparent. Visually larger contacts have proportionally more power at that frame than smaller contacts. A timeline was manually created using blender to indicate time along the animation. This timeline includes markers for every second of the electrical data and a red marker indicating the marked seizure start. Once all contacts have been animated, and the brain segmentations and timeline have been loaded into the Blender model, the model is saved as both an FBX file and a GLTF 2.0 file which can be loaded into VR.

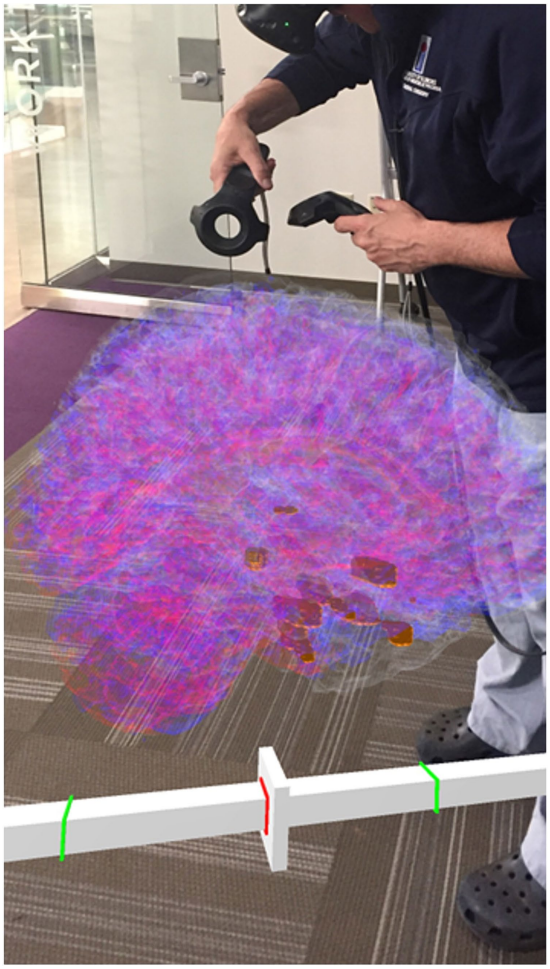

FIGURE 5
A clinician interacting with the 4D SEEG4D generated model in virtual reality. Electrodes are shown in gold and their size indicates relative power, whereas electrodes with a higher power are larger. A timeline appears underneath the brain to indicate the currently viewed timing relative to the marked seizure event (red line).

Our SEEG4D creates the 4D FBX model and converts other supplementary documents into pdf versions for loading into the VR software, including the electrode surgical map and the electrode recording data graphs. Visualizing the data and model requires a VR platform for viewing and interacting with the generated assets. Many options exist for this. In this study, we imported the data into Enduvo,[3] as shown in Figure 5, and Blender, as shown in Figure 6.

2.6 Test patient data

To test the capabilities of SEEG4D and the automated electrode location labeling, data from 3 temporal lobe epilepsy patients undergoing clinical epilepsy monitoring at the OSF Saint Francis Medical Center, Peoria, Illinois, were run through our software in a fully automated processing, except for the manual selection of the electrode names in the GUI based on the sEEG planning map. DIXI sEEG electrodes (DIXI Medical) 0.8 mm in diameter and 2 mm apart were sampled at 1 KHz during monitoring. Deindentifiedatient data was acquired through OSF HealthCare under an IRB approved by University of Illinois College of Medicine at Peoria IRB.

To test the accuracy of our automated electrode-contact labeling process, we had two trained anatomists with a combined 5 years of segmentation experience label the electrode contacts manually. Our trained manual raters used 3D Slicer to mark the location of the electrode contacts from all electrodes from the 1 mm isotropic CT image to identify the recording locations (Fedorov et al., 2012). In the event a rater marked a position in between voxels, their marker was rounded to the nearest voxel. This manually labeled electrode contact center was compared to the corresponding automated electrode contact's center and to the positions from the other rater.

3 Results

SEEG4D processed 3 cases on a machine running Ubuntu 22.04.4 LTS with 96 GB of memory, an Intel® Xeon® Gold 6,254 CPU @ 3.10GHz x 72, and three NVIDIA Quadro RTX 8000. Brain extraction and electrode segmentation took approximately 50 min per patient. Processing the sEEG data took approximately 5 s per patient while animating the data with Blender took approximately 30 s leading to a total runtime of under an hour per patient.

3.1 Electrode segmentation validation

After processing our 3 cases, SEEG4D identified 271 contacts in total. From visual inspection, we found that the contacts had good concurrence with the ground truth CT data. The average distance between these automatically identified coordinates and the manually labeled coordinates was variable per case, but as shown in Table 1 the electrode localization algorithm was generally closer to the raters than the raters were to each other indicating good concurrence with the ground truth position. As an example, for case SEEG1, our algorithm was an average of 0.85 mm away with a standard deviation of 0.68 mm from rater 1's midpoints and an average of 0.71 ± 0.74 mm from rater 2's midpoints while the raters were an average of 0.94 ± 0.52 mm from one another. We note that 94.8 and 85.2% of the contacts automatically identified were within 1 voxel of rater 1 and rater 2, respectively. Additionally, 89.7% of the raters' contacts were within 1 voxel of each other. We define a contact that the algorithm 'missed' as a contact residing in brain tissue that was not labeled by the software. Notably, contacts in the skull or outside the head are not counted as 'missed'. Shown in Table 2, for SEEG1, there were 2 missed contacts of 116 (1.7%); for SEEG2, there were 3 missed contacts of 91 (3.3%), and for SEEG3 there were 0 missed contacts of 71 (0%). Of these 5 missed contacts, all were within 5 voxels of the edge of the cortex and were either masked out or eroded during imaging preprocessing. Table 2 also shows that 82, 93, and 80% of segmented contacts were within 1 voxel for cases SEEG1, SEEG2, and SEEG3. Segmented contacts that were more than 2 voxels away were due to blurring and streaking on the contacts from the CT causing the contacts to appear larger, and when erosions were applied it offset the midpoint of the contact.

3 https://enduvo.com/

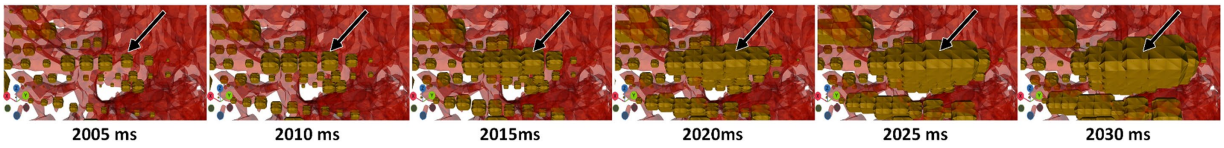

FIGURE 6
4D signal propagation along an electrode at time points varying by 5 ms during a seizure. Contacts along this electrode become larger in sequence. Timepoints were extracted from Blender.

TABLE 1 Quantitative analysis of electrode localization algorithm showing the average distance and the standard deviation between the raters and algorithm per patient case as well as the distance between each rater.

Average distance per contact (mm)					
SEEG1		SEEG2		SEEG3	
Rater 1	Rater 2	Rater 1	Rater 2	Rater 1	Rater 2
0.85 ± 0.68	0.71 ± 0.74	0.76 ± 0.60	1.0 ± 0.57	0.61 ± 0.62	1.0 ± 0.71

Raters distance from each other (mm)		
SEEG1	SEEG2	SEEG3
0.94 ± 0.52	0.93 ± 0.40	0.98 ± 0.49

The top table is the difference between the automated algorithm and each of the 2 manual raters. The bottom table is the differences between the 2 manual raters.

TABLE 2 Voxel distance of algorithmically determined contact midpoints to averaged rater-labeled midpoints.

Voxel distance of algorithm to rater average			
Distance	SEEG1	SEEG2	SEEG3
N < = 1 Voxel	92	82	57
1 < N < = 2 Voxels	17	6	14
2 < N < = 3 Voxels	3	0	0
Missed	2	3	0
Number of contacts (*N*)	112	88	71

82, 93, and 80% of segmented contacts were within 1 voxel for cases SEEG1, SEEG2, and SEEG3, respectively. five contacts were missed by the algorithm in total, all of which were within 5 voxels of the edge of the brain.

4 Discussion

We have developed a tool, SEEG4D, which merges pre-implant MRI, post-implant CT, and SEEG data to create a 3D model of an sEEG case with time series data mapped onto the contacts. This enables the automated creation of digital assets for use in a 4D VR surgical planning process to enable the clinical care team to localize the SOZ and plan surgical interventions.

4.1 Visualization analysis

Presurgical planning for resection of SOZ is a highly complex process involving multi-modal 2D and 1D (SEEG) medical data. When one considers that interpretation of this complex patient-specific data by one medical expert is then communicated to a different surgical expert to resect a specific SOZ in the brain, there is tremendous opportunity to improve the precision of shared mental models of the pathology.

This project was initiated to improve knowledge transfer of patient-specific, complex, multimodal information on the location and pathology of the SOZ from epileptologist to neurosurgeon. To achieve translational impact, automated tools were developed along with stereoscopic time-sequential 3D digital models. These were necessary to allow integration into a clinical workflow where time constraints prevent manual efforts of 4D model creation. We have successfully deployed our software package, enabled by the containerization of the algorithms, in the clinical environment for research purposes and ran cases for this study on the clinic computational hardware.

Preliminary qualitative feedback revealed that the clinical sEEG expert sees tremendous potential of SEEG4D to expedite review of the standard of care data by helping to merge multimodal information about a seizure to provide an improved understanding of the patient's electrophysiological data. Our surgical expert indicated significant potential of SEEG4D to improve communication of the 3D location of the SOZ from epileptologist to surgeon. Our experts, combined, see this tool as a new framework for forming mental models to allow for more efficient yet robust discussion for each patient.

SEEG4D allows users to automatically animate the electrical data at electrode contacts over time. Since the timescale is slowed down, we see clear visual onset and propagation of signals between electrode

contacts during a seizure, as shown in Figure 6 and Supplementary Video S1. This can facilitate understanding of propagation of the seizure and localization of SOZ. Incorporation of additional data into the visualization is straightforward, such as including white matter fiber pathways identified through diffusion tensor imaging to examine the relationship between the electrical signal propagation and tractography. Further work is required to understand the impact of increasing visual complexity of the visualized model on improving understanding of the patient case.

One of the limitations with SEEG4D is that it requires T1-weighted non-contrast MRI data. Additionally, our CT scanner was configured in a way which caused a substantial amount of metal artifacts at acquisition, leading to the automatic processing steps requiring higher thresholds and more aggressive erosion schemes. All cases processed for this study used DIXI electrodes and our tool is optimized based on these electrodes. It will be necessary to test SEEG4D against data from other clinical sites to ensure that these optimizations do not degrade cases that have little streaking or use other electrode manufacturers. Additionally, our clinical data did not use a standard naming convention for electrodes, so the software does not support loading of an atlas-based automatic naming scheme for electrodes.

While our clinicians have expressed qualitative feedback indicating that this tool would lead to a significant reduction in the time it takes to determine and understand a SOZ, quantitative analysis of this impact will be provided in a future study. To demonstrate quantitative impact on the clinical workflow, we will evaluate the efficacy of this model and quantify the reduction in mental load during the pre-surgical planning period for new cases. Additionally, the inclusion of source localization using automated SOZ localization algorithms to show the SOZ in the VR space could provide useful information to the clinical team.

5 Conclusion

We developed SEEG4D, a tool for automatically visualizing SEEG data with 4D virtual reality models for presurgical planning for epilepsy resection surgery. SEEG4D improves presurgical planning in epilepsy resection cases by automatically merging multimodal imaging data from MRI, CT, and sEEG recordings to produce dynamic 4D VR visualizations of seizure onset and propagation to facilitate the formation of an accurate mental model of the case. Our automated sEEG electrode contact detector was demonstrated to be accurate to within 1 mm of our ground truth raters. Models generated from SEEG4D provide an advantage over traditional sEEG models due to their interactive, 4D spatiotemporal nature. Our interactive models show signal propagation along electrodes and through local networks to additional recording sites. With this automated tool, epilepsy care teams may realize the potential of integrating dynamic sEEG data with VR for enhanced presurgical planning and the formation of shared mental models.

Data availability statement

The datasets presented in this article are not readily available because the software directly integrates with clinical data which may not be fully de-identified. Requests to access the datasets should be directed to Bradley Sutton, bsutton@illinois.edu.

Ethics statement

The studies involving humans were approved by University of Illinois College of Medicine Peoria. The studies were conducted in accordance with the local legislation and institutional requirements. The participants provided their written informed consent to participate in this study.

Author contributions

JE: Data curation, Formal analysis, Investigation, Software, Writing – original draft. MB: Conceptualization, Data curation, Funding acquisition, Project administration, Writing – review & editing. CD: Data curation, Formal analysis, Investigation, Writing – review & editing. EB: Writing – review & editing. AA: Writing – review & editing. GH: Writing – review & editing. YV: Conceptualization, Funding acquisition, Project administration, Writing – review & editing. AM: Data curation, Writing – review & editing. JA: Conceptualization, Funding acquisition, Project administration, Writing – review & editing. BS: Conceptualization, Funding acquisition, Project administration, Writing – review & editing.

Funding

The author(s) declare that financial support was received for the research, authorship, and/or publication of this article. This project has been funded by Jump ARCHES endowment grant P366 through the Health Care Engineering Systems Center at the University of Illinois Urbana-Champaign.

Acknowledgments

The authors would like to thank Reid D. Jockisch for assistance with rating the electrode segmentations and Alexa Waltz for assisting with coordination between clinical and research sites.

Conflict of interest

MB declares conflict of interest with Enduvo Inc. as co-founder and board officer.

The remaining authors declare that the research was conducted in the absence of any commercial or financial relationships that could be construed as a potential conflict of interest.

Publisher's note

Supplementary material

The Supplementary material for this article can be found online at: https://www.frontiersin.org/articles/10.3389/fninf.2024.1465231/full#supplementary-material

Supplementary Videos are provided to help demonstrate the rich information that is present in the 4D models and VR environment for an epilepsy case. It is challenging to convey the breadth of information present in a 4D model using a 2D print format. Without being able to interact with the models and play the animations, sense of time, depth, and texture are impeded. To help alleviate this, we have included Supplementary Videos of the models and user interactions with them. In addition, our code and sample data are available on our GitHub at https://github.com/mrfil/SEEG4D, DOI: 10.5281/zenodo.12741316.

References

Andrews, J. P., Ammanuel, S., Kleen, J., Khambhati, A. N., Knowlton, R., and Chang, E. F. (2020). Early seizure spread and epilepsy surgery: a systematic review. *Epilepsia* 61, 2163–2172. doi: 10.1111/epi.16668

Armin Vosoughi, D. B., Kheder, A., Bonilha, L., Dickey, A., Drane, D., Gutman, D., et al. (2022). Toolboxes for SEEG electrode localization and visualization. Nashville: American Epilepsy Society.

Arnulfo, G., Hirvonen, J., Nobili, L., Palva, S., and Palva, J. M. (2015). Phase and amplitude correlations in resting-state activity in human stereotactical EEG recordings. *NeuroImage* 112, 114–127. doi: 10.1016/j.neuroimage.2015.02.031

Bartolomei, F., Lagarde, S., Wendling, F., McGonigal, A., Jirsa, V., Guye, M., et al. (2017). Defining epileptogenic networks: contribution of SEEG and signal analysis. *Epilepsia* 58, 1131–1147. doi: 10.1111/epi.13791

Bearden, D. J., Ehrenberg, A., Selawski, R., Ono, K. E., Drane, D. L., Pedersen, N. P., et al. (2023). Four-way Wada: SEEG-based mapping with electrical stimulation, high frequency activity, and phase amplitude coupling to complement traditional Wada and functional MRI prior to epilepsy surgery. *Epilepsy Res.* 192:107129. doi: 10.1016/j.eplepsyres.2023.107129

Brett, M. (2024). nipy/nibabel: 5.2.1. Genève: Zenodo.

Cai, F., Wang, K., Zhao, T., Wang, H., Zhou, W., and Hong, B. (2021). BrainQuake: an open-source Python toolbox for the Stereoelectroencephalography spatiotemporal analysis. *Front. Neuroinform.* 15:773890. doi: 10.3389/fninf.2021.773890

Chen, G., Li, X. C., Wu, G. Q., Wang, Y., Fang, B., Xiong, X. F., et al. (2010). The use of virtual reality for the functional simulation of hepatic tumors (case control study). *Int. J. Surg.* 8, 72–78. doi: 10.1016/j.ijsu.2009.11.005

Dale, A. M., Fischl, B., and Sereno, M. I. (1999). Cortical surface-based analysis. I. Segmentation and surface reconstruction. *NeuroImage* 9, 179–194. doi: 10.1006/nimg.1998.0395

Davis, T. S., Caston, R. M., Philip, B., Charlebois, C. M., Anderson, D. N., Weaver, K. E., et al. (2021). LeGUI: a Fast and accurate graphical user Interface for automated detection and anatomical localization of intracranial electrodes. *Front. Neurosci.* 15:769872. doi: 10.3389/fnins.2021.769872

De Momi, E., Caborni, C., Cardinale, F., Casaceli, G., Castana, L., Cossu, M., et al. (2014). Multi-trajectories automatic planner for StereoElectroEncephaloGraphy (SEEG). *Int. J. Comput. Assist. Radiol. Surg.* 9, 1087–1097. doi: 10.1007/s11548-014-1004-1

Fedorov, A., Beichel, R., Kalpathy-Cramer, J., Finet, J., Fillion-Robin, J. C., Pujol, S., et al. (2012). 3D slicer as an image computing platform for the quantitative imaging network. *Magn. Reson. Imaging* 30, 1323–1341. doi: 10.1016/j.mri.2012.05.001

Fisher, R. S., Acevedo, C., Arzimanoglou, A., Bogacz, A., Cross, J. H., Elger, C. E., et al. (2014). ILAE official report: a practical clinical definition of epilepsy. *Epilepsia* 55, 475–482. doi: 10.1111/epi.12550

Gonzalez-Martinez, J., Mullin, J., Vadera, S., Bulacio, J., Hughes, G., Jones, S., et al. (2014). Stereotactic placement of depth electrodes in medically intractable epilepsy. *J. Neurosurg.* 120, 639–644. doi: 10.3171/2013.11.JNS13635

Gramfort, A., Luessi, M., Larson, E., Engemann, D. A., Strohmeier, D., Brodbeck, C., et al. (2013). MEG and EEG data analysis with MNE-Python. *Front. Neurosci.* 7:267. doi: 10.3389/fnins.2013.00267

Guillot, A., Champely, S., Batier, C., Thiriet, P., and Collet, C. (2007). Relationship between spatial abilities, mental rotation and functional anatomy learning. *Adv. Health Sci. Educ. Theory Pract.* 12, 491–507. doi: 10.1007/s10459-006-9021-7

Hassan, A. R., Subasi, A., and Zhang, Y. (2020). Epilepsy seizure detection using complete ensemble empirical mode decomposition with adaptive noise. *Knowl.-Based Syst.* 191:105333. doi: 10.1016/j.knosys.2019.105333

Herfarth, C., Lamadé, W., Fischer, L., Chiu, P., Cardenas, C., Thorn, M., et al. (2002). The effect of virtual reality and training on liver operation planning. *Swiss Surg.* 8, 67–73. doi: 10.1024/1023-9332.8.2.67

Jenkinson, M., Bannister, P., Brady, M., and Smith, S. (2002). Improved optimization for the robust and accurate linear registration and motion correction of brain images. *NeuroImage* 17, 825–841. doi: 10.1006/nimg.2002.1132

Jenkinson, M., and Smith, S. (2001). A global optimisation method for robust affine registration of brain images. *Med. Image Anal.* 5, 143–156. doi: 10.1016/s1361-8415(01)00036-6

Kakinuma, K., Osawa, S. I., Hosokawa, H., Oyafuso, M., Ota, S., Kobayashi, E., et al. (2022). Determination of language areas in patients with epilepsy using the super-selective Wada test. *IBRO Neurosci. Rep.* 13, 156–163. doi: 10.1016/j.ibneur.2022.08.002

Kalilani, L., Sun, X., Pelgrims, B., Noack-Rink, M., and Villanueva, V. (2018). The epidemiology of drug-resistant epilepsy: a systematic review and meta-analysis. *Epilepsia* 59, 2179–2193. doi: 10.1111/epi.14596

Lewiner, T., Lopes, H., Vieira, A. W., and Tavares, G. (2003). Efficient implementation of marching Cubes' cases with topological guarantees. *J. Graph. Tool.* 8, 1–15. doi: 10.1080/10867651.2003.10487582

Louis, R. G., Steinberg, G. K., Duma, C., Britz, G., Mehta, V., Pace, J., et al. (2021). Early experience with virtual and synchronized augmented reality platform for preoperative planning and intraoperative navigation: a case series. *Oper. Neurosurg. (Hagerstown)* 21, 189–196. doi: 10.1093/ons/opab188

Lyuksemburg, V., Abou-Hanna, J., Marshall, J. S., Bramlet, M. T., Waltz, A. L., Pieta Keller, S. M., et al. (2023). Virtual reality for preoperative planning in complex surgical oncology: a single-center experience. *J. Surg. Res.* 291, 546–556. doi: 10.1016/j.jss.2023.07.001

Maan, Z. N., Maan, I. N., Darzi, A. W., and Aggarwal, R. (2012). Systematic review of predictors of surgical performance. *Br. J. Surg.* 99, 1610–1621. doi: 10.1002/bjs.8893

Mahajan, U. V., Sunshine, K. S., Herring, E. Z., Labak, C. M., Wright, J. M., and Smith, G. (2021). Virtual reality in presurgical patient education: a scoping review and recommended trial design guidelines. *Am. J. Surg.* 222, 704–705. doi: 10.1016/j.amjsurg.2021.03.022

Makhalova, J., Medina Villalon, S., Wang, H., Giusiano, B., Woodman, M., Bénar, C., et al. (2022). Virtual epileptic patient brain modeling: relationships with seizure onset and surgical outcome. *Epilepsia* 63, 1942–1955. doi: 10.1111/epi.17310

Matelsky, J., Kiar, G., Johnson, E., Rivera, C., Toma, M., and Gray-Roncal, W. (2018). Container-based clinical solutions for portable and reproducible image analysis. *J. Digit. Imaging* 31, 315–320. doi: 10.1007/s10278-018-0089-4

Mattus, M. S., Ralph, T. B., Keller, S. M. P., Waltz, A. L., and Bramlet, M. T. (2022). Creation of patient-specific silicone cardiac models with applications in pre-surgical plans and hands-on training. *J. Vis. Exp.* 10:180. doi: 10.3791/62805

Medina Villalon, S., Paz, R., Roehri, N., Lagarde, S., Pizzo, F., Colombet, B., et al. (2018). EpiTools, a software suite for presurgical brain mapping in epilepsy: intracerebral EEG. *J. Neurosci. Methods* 303, 7–15. doi: 10.1016/j.jneumeth.2018.03.018

Minkin, K., Gabrovski, K., Sirakov, S., Penkov, M., Todorov, Y., Karakostov, V., et al. (2019). Three-dimensional neuronavigation in SEEG-guided epilepsy surgery. *Acta Neurochir.* 161, 917–923. doi: 10.1007/s00701-019-03874-9

Mula, M., and Cock, H. R. (2015). More than seizures: improving the lives of people with refractory epilepsy. *Eur. J. Neurol.* 22, 24–30. doi: 10.1111/ene.12603

Narizzano, M., Arnulfo, G., Ricci, S., Toselli, B., Tisdall, M., Canessa, A., et al. (2017). SEEG assistant: a 3DSlicer extension to support epilepsy surgery. *BMC Bioinform.* 18:124. doi: 10.1186/s12859-017-1545-8

Oldhafer, K. J., Stavrou, G. A., Prause, G., Peitgen, H. O., Lueth, T. C., and Weber, S. (2009). How to operate a liver tumor you cannot see. *Langenbeck's Arch. Surg.* 394, 489–494. doi: 10.1007/s00423-009-0469-9

Paulo, D. L., Wills, K. E., Johnson, G. W., Gonzalez, H. F. J., Rolston, J. D., Naftel, R. P., et al. (2022). SEEG functional connectivity measures to identify epileptogenic zones: stability, medication influence, and recording condition. *Neurology* 98, e2060–e2072. doi: 10.1212/WNL.0000000000200386

Phan, T. N., Prakash, K. J., Elliott, R. J. S., Pasupuleti, A., Gaillard, W. D., Keating, R. F., et al. (2022). Virtual reality-based 3-dimensional localization of stereotactic EEG (SEEG) depth electrodes and related brain anatomy in pediatric epilepsy surgery. *Childs Nerv. Syst.* 38, 537–546. doi: 10.1007/s00381-021-05403-5

Quero, G., Lapergola, A., Soler, L., Shahbaz, M., Hostettler, A., Collins, T., et al. (2019). Virtual and augmented reality in oncologic liver surgery. *Surg. Oncol. Clin. N. Am.* 28, 31–44. doi: 10.1016/j.soc.2018.08.002

Remakanthakurup Sindhu, K., Staba, R., and Lopour, B. A. (2020). Trends in the use of automated algorithms for the detection of high-frequency oscillations associated with human epilepsy. *Epilepsia* 61, 1553–1569. doi: 10.1111/epi.16622

Robertson, D. J., Abramson, Z. R., Davidoff, A. M., and Bramlet, M. T. (2024). Virtual reality applications in pediatric surgery. *Semin. Pediatr. Surg.* 33:151387. doi: 10.1016/j.sempedsurg.2024.151387

Ryvlin, P., Cross, J. H., and Rheims, S. (2014). Epilepsy surgery in children and adults. *Lancet Neurol.* 13, 1114–1126. doi: 10.1016/S1474-4422(14)70156-5

Sadideen, H., Alvand, A., Saadeddin, M., and Kneebone, R. (2013). Surgical experts: born or made? *Int. J. Surg.* 11, 773–778. doi: 10.1016/j.ijsu.2013.07.001

Sanz-Leon, P., Knock, S. A., Spiegler, A., and Jirsa, V. K. (2015). Mathematical framework for large-scale brain network modeling in the virtual brain. *NeuroImage* 111, 385–430. doi: 10.1016/j.neuroimage.2015.01.002

Smith, S. M. (2002). Fast robust automated brain extraction. *Hum. Brain Mapp.* 17, 143–155. doi: 10.1002/hbm.10062

Thijs, R. D., Surges, R., O'Brien, T. J., and Sander, J. W. (2019). Epilepsy in adults. *Lancet* 393, 689–701. doi: 10.1016/S0140-6736(18)32596-0

Vakharia, V. N., Sparks, R., Miserocchi, A., Vos, S. B., O'Keeffe, A., Rodionov, R., et al. (2019). Computer-assisted planning for Stereoelectroencephalography (SEEG). *Neurotherapeutics* 16, 1183–1197. doi: 10.1007/s13311-019-00774-9

van der Walt, S., Schönberger, J. L., Nunez-Iglesias, J., Boulogne, F., Warner, J. D., Yager, N., et al. (2014). Scikit-image: image processing in Python. *PeerJ* 2:e453. doi: 10.7717/peerj.453

van Mierlo, P., Vorderwulbecke, B. J., Staljanssens, W., Seeck, M., and Vulliemoz, S. (2020). Ictal EEG source localization in focal epilepsy: review and future perspectives. *Clin. Neurophysiol.* 131, 2600–2616. doi: 10.1016/j.clinph.2020.08.001

Woolrich, M. W., Jbabdi, S., Patenaude, B., Chappell, M., Makni, S., Behrens, T., et al. (2009). Bayesian analysis of neuroimaging data in FSL. *NeuroImage* 45, S173–S186. doi: 10.1016/j.neuroimage.2008.10.055

Wu, B., Klatzky, R. L., and Stetten, G. (2010). Visualizing 3D objects from 2D cross sectional images displayed in-situ versus ex-situ. *J. Exp. Psychol. Appl.* 16, 45–59. doi: 10.1037/a0018373

Zhang, Y., Brady, M., and Smith, S. (2001). Segmentation of brain MR images through a hidden Markov random field model and the expectation-maximization algorithm. *IEEE Trans. Med. Imaging* 20, 45–57. doi: 10.1109/42.906424

frontiers | Frontiers in Neuroinformatics

TYPE Brief Research Report
PUBLISHED 10 February 2025
DOI 10.3389/fninf.2025.1513661

OPEN ACCESS

EDITED BY
Omar Farooq,
Aligarh Muslim University, India

REVIEWED BY
Sabato Santaniello,
University of Connecticut, United States
Garima Chandel,
Chandigarh University, India

*CORRESPONDENCE
A.V. Medvedev
✉ am236@georgetown.edu

RECEIVED 18 October 2024
ACCEPTED 21 January 2025
PUBLISHED 10 February 2025

CITATION
Medvedev AV and Lehmann B (2025) The classification of absence seizures using power-to-power cross-frequency coupling analysis with a deep learning network. *Front. Neuroinform.* 19:1513661. doi: 10.3389/fninf.2025.1513661

The classification of absence seizures using power-to-power cross-frequency coupling analysis with a deep learning network

A.V. Medvedev* and B. Lehmann

EEG and Optical Imaging Laboratory, Center for Functional and Molecular Imaging, Georgetown University Medical Center, Washington, DC, United States

High frequency oscillations are important novel biomarkers of epileptic tissue. The interaction of oscillations across different time scales is revealed as cross-frequency coupling (CFC) representing a high-order structure in the functional organization of brain rhythms. Power-to-power coupling (PPC) is one form of coupling with significant research attesting to its neurobiological significance as well as its computational efficiency, yet has been hitherto unexplored within seizure classification literature. New artificial intelligence methods such as deep learning neural networks can provide powerful tools for automated analysis of EEG. Here we present a Stacked Sparse Autoencoder (SSAE) trained to classify absence seizure activity based on this important form of cross-frequency patterns within scalp EEG. The analysis is done on the EEG records from the Temple University Hospital database. Absence seizures (n = 94) from 12 patients were taken into analysis along with segments of background activity. Power-to-power coupling was calculated between all frequencies 2–120 Hz pairwise using the EEGLAB toolbox. The resulting CFC matrices were used as training or testing inputs to the autoencoder. The trained network was able to recognize background and seizure segments (not used in training) with a sensitivity of 93.1%, specificity of 99.5% and overall accuracy of 96.8%. The results provide evidence both for (1) the relevance of PPC for seizure classification, as well as (2) the efficacy of an approach combining PPC with SSAE neural networks for automated classification of absence seizures within scalp EEG.

KEYWORDS

absence seizure, epilepsy, seizure classification, EEG, spectral analysis, cross-frequency coupling (CFC), power-to-power coupling

1 Introduction

Brain oscillations span frequencies across a range of several orders of magnitude from the Berger bands below 30 Hz (delta, theta, alpha, beta) up to the high frequency bands of gamma, ripple, and fast ripple (30–600 Hz). This study was inspired by emerging evidence that brain oscillations do not work independently from each other but interact in a very complex and well-coordinated way known as cross-frequency coupling (CFC) (Buzsaki and Draguhn, 2004; Klimesch, 2013). Cross-frequency coupling plays an important role in the functional organization of neural networks at different spatial and temporal scales. This coupling represents a high-order structure in the functional organization of brain rhythms and is likely to reflect different functional states of the brain (Buzsaki and Draguhn, 2004). It is reasonable to suppose that optimal biomarkers of complex neurological processes would have sensitivity to this structure, going beyond isolated features (e.g., frequency or spectral characteristics).

In recent years, there has been a burgeoning interest in high-frequency oscillations (HFOs) driven by emerging evidence suggesting their involvement in cognitive functions (Gross and Gotman, 1999; Hosseinzadeh et al., 2005; Axmacher et al., 2008; Medvedev and Kanwal, 2008; Buzsaki and Silva, 2012; Kucewicz et al., 2014; Pail et al., 2020; Dickey et al., 2022). Also, heightened activity in these frequency ranges has been observed in pathological conditions and, in particular, numerous studies have demonstrated a significant increase in HFOs in the context of epilepsy. Those studies have revealed that HFOs are one of the most common early manifestations recorded within minutes before seizure onset and appear to be a reliable EEG correlate of ictal onset zone (Lee et al., 2000; Medvedev, 2002; Worrell et al., 2004; Gardner et al., 2007; Jacobs et al., 2008; Blanco et al., 2010; Medvedev et al., 2011). Several research groups have suggested that detection of HFOs is necessary for a more accurate localization of epileptogenic tissue. Improvements in accuracy may improve surgical outcome in patients with localization-related intractable epilepsy because the removal of HFO-generating areas correlates with good surgical outcomes (Bragin et al., 1999; Worrell et al., 2004; Gardner et al., 2007; Besio et al., 2010; Zijlmans et al., 2012; Staba et al., 2014; Frauscher et al., 2017; Medvedev et al., 2019; Thomschewski et al., 2019). Thus, in addition to epileptic discharges, HFOs are now considered as an important biomarker of epileptogenic tissue.

High-frequency bursts are frequently accompanied by low-frequency waveforms, such as sharp waves and spikes. These patterns may signify specific forms of cross-frequency coupling. The most typical examples pertinent to epilepsy include the Ripple-on-Spike, where a high-frequency burst is riding on a spike, as well as the Ripple-on-Oscillation, where a high-frequency burst is riding on a slow wave. Given that epileptic seizures are often accompanied by specific patterns of cross-frequency coupling between slow and fast activity, it is important to explore the possibility that cross-frequency coupling may be used as a tool for automated detection of seizures.

Absence seizures are traditionally characterized by spike-and-wave activity with the dominant frequency of 3–4.5 Hz. This specific narrow frequency range and the regular morphological features of absence seizures offer a good starting point from which to evaluate epilepsy using a new CFC approach. More specifically, these reliable characteristics of absence epilepsy in combination with research connecting HFO's with epileptogenic tissue (Chaitanya et al., 2015) suggest the possibility of interaction between low and high frequency bands. Furthermore, approaches that can unveil these dynamic relationships may identify more comprehensive signatures of absence epilepsy (e.g., beyond describing which waveband amplitudes are merely involved). Therefore, such approaches hold promise both for optimal classification power and for advancing the understanding of the neurobiology of seizures.

Methods utilizing cross-frequency coupling have shown predictive power in various areas of EEG research including epilepsy state classification (Jacobs et al., 2018). There are various types of coupling (i.e., power-to-power, power-to-phase, phase-to-phase, etc.). These different types are thought to have independent neural mechanisms as well as different or complimentary functional significance (Jirsa and Muller, 2013). While many forms of CFC have not been well-researched, one of the better-studied forms of CFC is phase-to-amplitude coupling (PAC), which is well known to have an association with various cognitive processes related to memory and perception (Gross and Gotman, 1999; Axmacher et al., 2008; Medvedev and Kanwal, 2008; Buzsaki and Silva, 2012; Kucewicz et al., 2014; Dickey et al., 2022). In many cases, PAC refers to the phase of a slower wave modulating the amplitude of the faster wave. In regards to seizure classification, prior studies (including both EEG and intracranial EEG) have linked delta-HFO coupling with epileptogenic tissue, and have employed this feature in discriminating between ictal and interictal states (Ibrahim et al., 2014; von Ellenrieder et al., 2016; Edakawa et al., 2016). For example, Jacobs et al. (2018) used a random forest algorithm on PAC and obtained a sensitivity (*Sens*) of 87.9% and specificity (*Spec*) of 82.4% for classification of pre-clinical seizure states. More specifically, they found increases in coupling between delta (2–4 Hz) and gamma (20–50 Hz) bands to be a key feature for classifying the seizure EEG patterns (Jacobs et al., 2018). Fujita et al. (2022) using a deep learning (DL) classifier found training the network on PAC significantly improved seizure classification over training on the raw data, achieving 90% accuracy (*Acc*) using the former method (Fujita et al., 2022). It is notable that the delta-theta activity coupled with the gamma band is not strictly pathological, and is thought to be involved in working memory, sensory and other cognitive processes (Lisman and Jensen, 2013). While highly informative, PAC remains just one of many presumably complimentary forms of cross-frequency coupling that may hold keys to functional and pathological states of the brain.

Power-to-power coupling (PPC) is another type of cross-frequency coupling having a solid research base (Llinas et al., 1999; Shirvalkar et al., 2010; Popov et al., 2018; Wang et al., 2018; Sheremet et al., 2019) attesting to its significance, yet in contrast with PAC, it has a surprising lack of research in the area of seizure classification. PPC has been used for well over two decades in both murine and human studies, and across data types including local field potential (LFP), EEG and MEG. Some examples include tracking coupling between theta and gamma or other sets of frequencies within the rat hippocampus (Sheremet et al., 2019). PPC is found to be involved with successful memory retrieval (Shirvalkar et al., 2010) and other PPC patterns have been associated with specific states including sleep and anesthesia (Ferraris et al., 2018). While there is a sound foundation of research attesting to the value of PPC for identifying biomarkers, it has not been researched in the area of seizure classification.

Power-to-power coupling should be particularly amenable to long-term monitoring of patients due to its methodological simplicity (standard time course correlations). For these reasons of computational efficiency and speed, PPC would seem to lend itself well to real-time implementation when compared to other CFC methods. Additionally, this mode of coupling may be more robust to noise due to its reliance on power (or amplitude) rather than phase, the latter of which may be more susceptible to signal noise (Giehl et al., 2021). For these reasons, the PPC metric was chosen as the mode of analysis.

In this study we focus on absence seizures because they are the most common type of childhood epilepsy and represent several challenges to clinicians. These challenges stem from the unique characteristics of absence seizures and their impact on the individuals who experience them. Absence seizures are often subtle and brief, lasting only a few seconds. The lack of convulsions or dramatic physical movements can make them less noticeable to observers, including clinicians. This subtlety may lead to under-recognition and misinterpretation of the seizures. Furthermore, the presentation of absence seizures can vary among individuals. Some may experience

typical absences with staring spells, while others may exhibit more atypical features, such as subtle facial movements or eye fluttering. This variability makes diagnosis and recognition challenging for clinicians. The symptoms of absence seizures can also overlap with other neurological or psychiatric conditions. Clinicians must differentiate absence seizures from conditions like daydreaming, attention-deficit/hyperactivity disorder (ADHD), or other types of seizures. This requires a comprehensive clinical evaluation, including EEG monitoring.

Thus, while absence seizures are generally considered less severe than some other types of seizures, they present a range of challenges for clinicians, from the subtlety of their presentation to their potential impact on cognitive function and daily life. Accurate counting of absence seizures is crucial for optimizing therapy. Current diagnostics rely on clinical history, in-hospital video-EEG monitoring, and patient-maintained seizure diaries. However, research indicates that patients report only 6% of all experienced absences (Keilson et al., 1987), while caregivers report 14% (Akman et al., 2009). Therefore, a multipronged approach, including careful clinical evaluation and long-term EEG monitoring, is essential to address those challenges and to provide optimal care for individuals with absence seizures.

Scalp EEG is being used for long-term continuous monitoring with patients both in the intensive care units (ICU) and outside of the hospital. Patients may have spontaneous absence seizures that are easy to miss by the ICU staff or others, and long-term scalp EEG monitoring reduces the possibility of such oversight. Detecting seizures is critical for proper diagnostics and the increasing development of more portable and wearable EEG devices is making long-term monitoring of patients more practical and accurate.

Automated analysis is obviously important for real-time monitoring, and cutting-edge artificial intelligence techniques, particularly deep learning neural networks, offer robust tools for the automated analysis of EEG, including the exploration of cross-frequency coupling between distinct EEG rhythms. Deep learning stands out from other types of machine learning (ML) in that it is specialized for big datasets (including image matrices), complex features, and has superior ability to detect multifaceted latent patterns. For these reasons, it is not surprising that many successful classification studies have relied on various DL networks (Schirrmeister et al., 2017; Liu et al., 2022). This method is thus optimally suited for validating intricate cross-frequency coupling patterns for seizure classification. In this context, we introduce a Stacked Sparse Autoencoder (SSAE) specifically trained to identify absence seizure activity based on unique cross-frequency coupling patterns within scalp EEG.

2 Methods

EEG records (sampling frequency = 250 Hz) from the open source Temple University Hospital database [the TUSZ corpus, (Shah et al., 2018)] were used in the study. This dataset contains de-identified relatively short records of EEG from epilepsy patients of different ages with seizures annotated by neurologists (including both the seizure type as well as the start and stop times of the seizure). The dataset contained recordings that include 19 scalp EEG channels in accordance with the 10–20 configuration. The recordings' sampling rate of 250 Hz allows for a range of high frequencies to be evaluated in the data (up to 120 Hz). The studies were conducted in accordance with the local legislation and institutional requirements and the relevant ethical guidelines and regulations, and was approved by the Georgetown-MedStar Institutional Review Board. All records with absence seizures available in the TUSZ corpus were taken into analysis. The total number of patients was 12. The annotations for each EEG record contained the seizure type (as determined both by EEG as well as clinical/behavioral characteristics) alongside the respective onset and offset times of that seizure. The duration of EEG records in the dataset varied from 5 to 35 min and the number of seizures in each record varied from one to 18. Although the TUSZ EEG records are not very long, they do represent continuous recordings which may include interictal, preictal and postictal activity. For the classification purposes, all segments containing only seizures (i.e., from the annotated onsets to the corresponding offsets) were cut from the initial records and used as the first data class comprising 94 seizure segments. Non-seizure segments (the second data class) were cut from the initial records such that they matched the number and the durations of seizure segments for each patient. The second class is referred to as 'background' activity. Thus, the overall dataset was balanced across two classes (the same number and the same duration of both seizure and background segments for each patient) with the average segment duration = 8.6 ± 5.3 s (mean ± standard deviation).

All EEG segments were taken into analysis as raw signals (i.e., without any preprocessing) in order to test the suitability of the current method to be applied to the raw EEG either online or offline. The analysis was performed using a modified script based on the PowPowCAT toolbox for EEGLAB (Thammasan and Miyakoshi, 2020). First, the spectrogram based on short-time Fourier transform was calculated for each EEG segment using the Matlab *spectrogram* function with half-overlapping one-second epochs and a Hamming window, for frequencies from 1 to 120 Hz (logarithmic scale: [1 1.28 1.56 1.85 … 19.1 19.8 20.6 … 110.6 113.7 116.8 120] Hz). The spectrogram provided the modulations of spectral power across time (within a given EEG segment) for each frequency, channel and segment. For each pair of frequencies and each EEG channel, power-to-power coupling was calculated as a Pearson correlation between the corresponding spectral-power time courses across a given EEG segment resulting in the channel-specific PPC matrices. Those matrices were averaged across all 19 EEG channels resulting in the CFC matrix for a given EEG segment.

The segment-specific PPC matrices (of size 100×100) were converted into the 4,950-point vectors by taking only the elements below the main diagonal (because PPC matrices are symmetrical around the main diagonal). These vectors were then used as training and testing sets for the Stacked Sparse Autoencoder (SSAE). The SSAE method begins by using unsupervised training to find the most characteristic features of the input classes and thus reduces the dimensionality of the inputs. This feature may be important to make the data analysis more robust against the intrinsic noise and individual variations of the EEG signal (see Results and Discussion below). The SSAE network was created with Matlab (v. R2023b) and consisted of two hidden encoder-decoder layers and the softmax layer with two outputs for binary classification 'seizure vs. background'. The default (i.e., recommended by Matlab) values of the SSAE network internal hyper-parameters and structure were used which included L2 and sparsity regularizers. Regularizers are usually used to prevent overfitting of the network and increase its ability to generalize. L2

TABLE 1 Demographic information and clinical features of patients' absence seizures.

Subject #	Gender	Age	Clinical features of absence seizures
675	F	4, 6	Atypical absence seizure (blinking).
1113	F	20	Absence seizures.
1413	F	10, 14	3 to 6 Hz generalized spike and slow wave activity; seizures lasting 10–16 s.
1795	F	9	Atypical absence seizures. 3 to 5 Hz spike and slow wave activity preceded by symmetric focal (frontal) activity.
1984	M	6	Atypical absence associated with involuntary twitching and motion arrest.
2448	M	4	Typical of absence seizures but with a possibility of a secondarily generalized mechanism including the left frontal activity seen at the onset.
2657	M	5	Multiple absence seizures.
3053	F	5	EEG suggests more than one mechanism for seizures in this patient.
3281	M	13	The seizures were frontally predominant and relatively characteristic of absence epilepsy.
3306	F	13	Typical absence seizures.
3635	M	6	Generalized SW discharge with a clear underlying frontal focality.
8608	F	22	Atypical absence seizure with focal features (subtle focal slowing and sharp waves at T3, T5, and C3).

regularization adds the squared magnitude of coefficients to the loss function thus penalizing large weights while the sparsity constraint penalizes the loss function such that only a few neurons are active in a hidden layer. This helps the automatic detection of the most relevant features in the training sets. As a result of a preliminary exploration of the autoencoder with the given dataset, the optimal parameters of the hidden layers were found as achieving the stop condition during training (see Methods) in a shortest time (~6 min). The first encoder-decoder layer had 500 elements/neurons and the second layer had 50 elements/neurons. Thus, the reduction in input dimensionality by a factor of ~100 was achieved with two hidden layers.

A well-established approach 'leave-one-subject-out' was used for cross-validation purposes. For each subject, the SSAE training was performed using data from all other subjects and the selected subject's segments (not used in training) were then tested and classified by the trained network. This approach eliminates bias in the results if the data from a single subject is included in both the train and test set and thus tests the model generalizability for data not used in training. The results from all subject-specific tests were then averaged across all subjects for the final values (mean ± standard deviation) of sensitivity, specificity and accuracy. To further evaluate the performance of the SSAE classifier, the receiver operating characteristic (ROC) curve as well as the precision-recall (PR) curve were calculated using Matlab function *rocmetrics*. As a result, the following parameters: AUC (area under the ROC curve), AUPRC (area under the PR curve) and the F1 score were derived.

3 Results

Among the 12 patients whose data were used in this study, there were 5 males and 7 females. The max/min age of the patients was 22/4 years and the average age was 10 ± 6.1 years. Demographic data of patients and clinical characteristics of their absence seizures are presented in Table 1. Half of patients had 'atypical' absence seizures due to their 'focal' features at the onset (for example, seizure activity predominantly at the frontal or temporal electrodes with rapid secondary generalization) or the presence of minor muscular phenomena (eye blinking or involuntary twitching).

Two typical examples of cross-frequency matrices for EEG activity during absence seizures taken from two different patients are shown in Figure 1. The overall pattern of the power-to-power frequency coupling was characterized by multiple discrete local maxima forming a 'grid' always symmetrical along the main diagonal. An approximately equal spacing between those maxima suggested that they reflected cross-frequency coupling between *harmonics*. Harmonics are integer multiples of the fundamental frequency arising in the spectral domain as a consequence of the main waveform not being strictly sinusoidal. Therefore, a relatively high coupling between the main frequency and its spectral harmonics is expected because harmonics occur at predictable intervals within the main waveform. For example, in Figure 1A some maxima (off the main diagonal) are present at the xy-coordinates of (15, 30) and (30, 15) Hz and (15, 45) and (45, 15) Hz (black solid circles). These maxima are likely to represent harmonics of the main frequency 15 Hz. Also, there are maxima at (28, 56) and (56, 28) Hz (brown dashed circles) which represent the first harmonic of frequency 28 Hz. Similarly, in Figure 1B there are maxima at the xy-coordinates of (20, 40) and (40, 20) Hz (black solid circles) which represent the first harmonic of the main frequency 20 Hz.

The cross-frequency patterns in the data, however, were not limited to the harmonics of the frequencies within the beta range. For example, Figure 1B also shows maxima at the coordinates of (20, 54) and (54, 20) Hz (the brown dashed ovals), and clearly the frequencies 20 Hz and 54 Hz are *not* harmonically related. Moreover, there are multiple maxima within the gamma band 40–80 Hz (the pink dashed circle) which demonstrate the coupling of gamma frequencies not harmonically related to each other (e.g., 58 and 66 Hz, arrows in Figure 1B).

Cross-frequency coupling matrices group-averaged over all background as well as absence seizure EEG segments are shown in Figures 2A,B. Statistical testing for the difference between the two conditions (seizure versus background) showed that power-to-power coupling during seizures was significantly stronger for a wide range of frequencies from 6 to ~60–90 Hz (Figure 2C) (Mann–Whitney U-test, $p < 0.05$, FDR-corrected for multiple comparisons).

During training, the network with L2 and sparsity regularizers achieved a squared error smaller than 10^{-2} (the stop condition) with

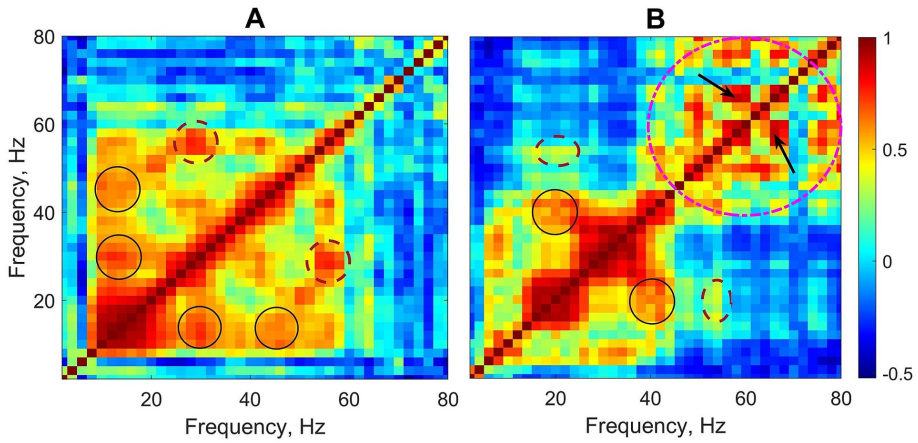

FIGURE 1
Two examples of cross-frequency matrices of EEG activity during absence seizures from two patients (linear frequency scale is used to demonstrate the arithmetic progression-like frequency relationships between harmonics). Circles, ovals and arrows show examples of a relatively stronger coupling between different frequencies including both harmonic and non-harmonic relations. See text for details.

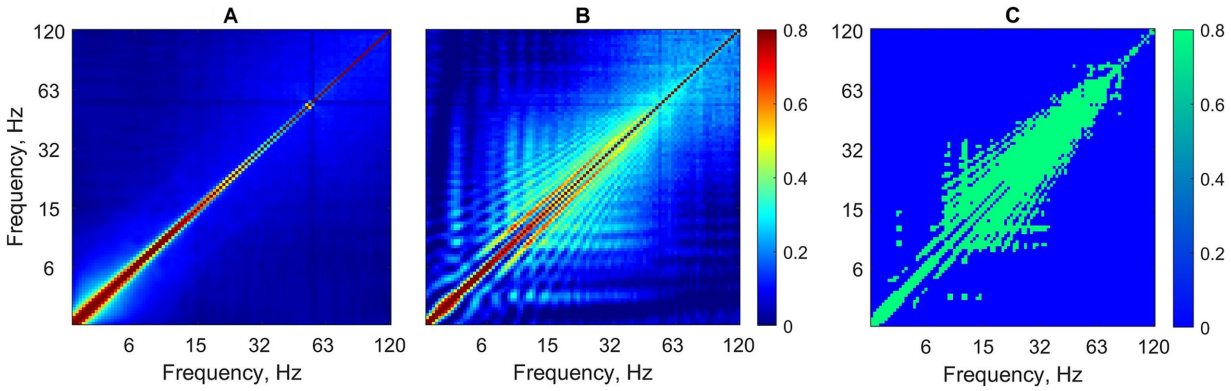

FIGURE 2
Cross-frequency coupling analysis without EEG preprocessing. Power-to-power matrices are group-averaged over all background segments **(A)** as well as absence seizures **(B)** (logarithmic frequency scale). **(C)** Statistically significant differences between two conditions for each frequency–frequency pair are shown in green (Mann–Whitney test, $p < 0.05$, FDR-corrected for multiple comparisons).

about 400 iterations. After that, fine tuning was performed. Figure 3A shows the confusion matrix with the results of classifying seizures versus background segments by the SSAE network. On average, the trained network was able to correctly classify EEG segments (not used in training) at a sensitivity of 93.13%, a specificity of 99.48%, and an overall accuracy of 96.83%. Given the total duration of all EEG segments analyzed, the false positive rate of 0.52% = 100% - specificity; (Figure 3A) translates to 3.2 false alarms per hour.

The ROC and the PR curves are shown in Figures 3B,C with the corresponding values of the areas under the curve: AUC = 0.94 ± 0.057 (for the two-class average ROC), AUPRC = 0.92 ± 0.062 (for seizures), and the F1 score = 0.96 ± 0.046 (mean ± standard deviation).

Although the primary analysis of EEG records described above was purposefully done without conventional EEG preprocessing, in order to see whether preprocessing might improve the classification results, we repeated the same analysis after the following preprocessing steps: high-pass filtering at 0.1 Hz cutoff (a zero-phase FIR filter with the *filtfilt* function), notch filtering (filtering out the line frequency and its harmonics using the CleanLine EEGLAB toolbox), re-referencing to common average, Independent Component (IC) decomposition using the AMICA algorithm, and the automated removal of artifactual ('bad') ICs using the ICLabel algorithm (Pion-Tonachini et al., 2019). An IC was removed based on the following two criteria. First, if any of its probabilities (assigned by the ICLabel algorithm as a percentage) of being 'muscle', 'eye', 'heart', 'line noise' or 'channel noise' was greater than the probability of being 'brain' or 'other'. Second, if the sum of the percentages of all the above artifactual assignments for this IC was greater than 50%.

The average CFC matrices after preprocessing are shown in Supplementary Figure S1, and, in comparison to the CFC matrices without preprocessing, they look very similar (compare Figure 2 and Supplementary Figure S1). EEG preprocessing slightly improved the classification of EEG segments ('seizure versus background') with the following results: *Sens* = 96.31%, *Spec* = 99.87%, and *Acc* = 98.51% (Supplementary Figure S2). However, all these classification metrics as well as the areas under the corresponding curves (the ROC curve and the precision-recall curve) were not significantly higher in

TABLE 2 Performance comparison of the PPC-SSAE classifier with other classifiers.

	Sensitivity		Specificity		Accuracy	
	Mean, %	St. Dev., %	Mean, %	St. Dev., %	Mean, %	St. Dev., %
PPC-SSAE	93.1	5.0	99.5	1.8	96.8	6.4
Spectra-SSAE	90.1	21.0***	98.4	5.0**	95.5	10.0*
PPC-SVM	81.1	32.0**	97.1	14.0***	90.0*	16.0**
PPC-Random Forest	78.0*	24.6***	91.5**	13.2***	85.6***	11.6**

PPC, power-to-power coupling; SSAE, stacked sparse autoencoder; SVM, support vector machine. PPC-SSAE, algorithm based on PPC as a classifying feature and the stacked sparse autoencoder as a classifier; Spectra-SSAE, algorithm based on the EEG spectrum as a classifying feature and the SSAE classifier; PPC-SVM, algorithm based on PPC as a classifying feature and the SVM classifier; PPC-Random Forest, algorithm based on PPC as a classifying feature and the Random Forest classifier. The PPC-SSAE algorithm is compared to all three other algorithms with statistically significant differences indicated by asterisks: $p < 0.05$ (*), $p < 0.01$ (**) and $p < 0.001$ (***) (t-test for the comparison of the mean values, Bonferroni-corrected; Bartlett's test for the comparison of variances, Matlab function vartestn).

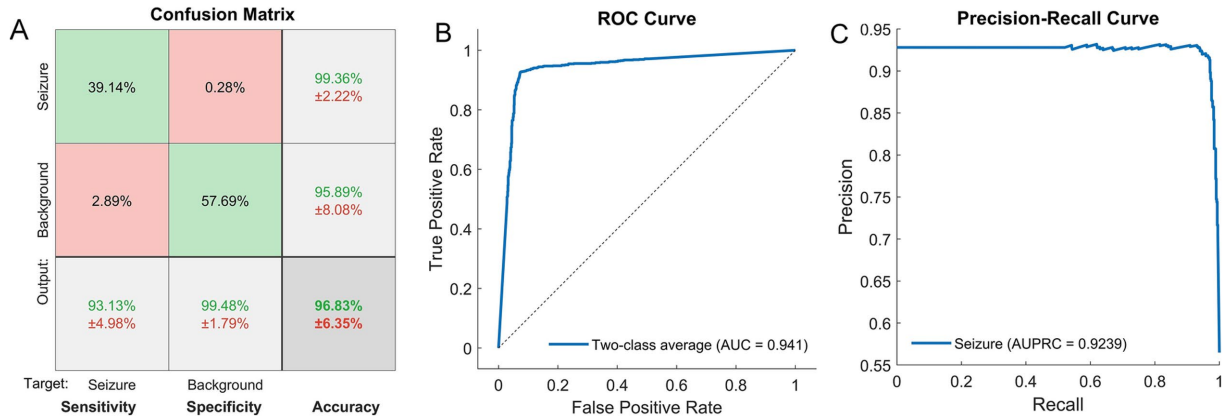

FIGURE 3
(A) Confusion matrix showing the results of recognition of seizures and background segments by the SSAE network. The mean values (%) ± standard deviations (%) are shown for sensitivity, specificity and overall accuracy (the bottom row) as well as for positive predictive values for each class (two upper cells in the right-hand column). (B, C) The results of two-class classification (seizure versus background) for the trained SSAE neural network. The ROC curve representing the classification results over both classes **(B)**. The precision-recall curve for the seizure class **(C)**. The corresponding metrics, i.e., the areas under the curves, AUC **(B)** and AUPRC **(C)**, are also shown.

comparison with the metrics obtained without preprocessing (Mann–Whitney test, $p > 0.1$ for all individual comparisons).

There is a question whether cross-frequency coupling, as an EEG feature, presents any advantage compared to the spectral power used in many published classification approaches. To address this question, we ran an additional analysis using spectral power for classification purposes. For each EEG segment, the output of the PowPowCAT function also provided power spectra (i.e., the spectrogram averaged across time). Similar to the PPC matrices, the channel-specific spectra were averaged across channels and the resulting segment-specific spectra were used as an input to the SSAE (Supplementary Figure S3, *left*). Classification based on the power spectrum produced slightly worse but non-significantly different results compared to the classification based on PPC: 90.1 ± 21 vs. 93.1 ± 4.98; 98.4 ± 5 vs. 99.5 ± 1.8; 95.5 ± 10 vs. 96.8 ± 6.4 (%, mean ± st. dev.; for *Sens*, *Spec*, and *Acc*, respectively) (Supplementary Figure S3, *right*). Importantly, however, the standard deviations for the spectrum-based classification metrics were significantly larger compared to the PPC-based classification (Bartlett's test; Table 2). The larger variance of the spectrum-based classification results was likely due to the individual differences in spectral characteristics of the EEG. Also, this result indicates that cross-frequency coupling may provide an EEG feature which is more robust against the individual variations.

To compare the performance of the SSAE-based classifier with the ML algorithms, we used the Support Vector Machine (SVM) and the Random Forest (RF) classifiers using the same PPC matrices as input and the same 'leave-one-subject-out' cross-validation approach. Matlab functions *fitclinear* and *fitensemble* were used for the SVM and RF classifiers, respectively. For each subject 'left-out', the SVM training was performed using 5-fold cross-validation on the remaining subjects with the subsequent testing of the excluded subject. For the RF classifier, the number of trees varied from 1 to 250 with the control of the out-of-bag error. It appeared that the error leveled out in the range of 20–140 trees and remained at the lowest value thereafter, insignificantly affecting the classification accuracy. After the preliminary testing, the RF-based classification was performed with number of trees = 140 with the same 'leave-one-subject-out' procedure. Both SVM and RF classifiers performed worse than the SSAE classifier with lower values of *Sens*, *Spec* and *Acc* as well as a significantly greater variance of those metrics (Table 2).

4 Discussion

Ongoing research in machine learning and deep learning is actively exploring absence seizures to identify their critical features,

aiming to gain deeper insights into the electrophysiological roles that these features play, with the goal of improving seizure detection and prediction. In both murine and human studies, successful training of the networks usually involves using relevant time and frequency domain metrics especially frequency and amplitude, and sometimes phase (Fanselow et al., 2000; Xanthopoulos et al., 2009; Richard et al., 2015; Kumar et al., 2021). Most studies use wavelet analysis techniques to account for non-stationarity of the EEG signal and improve time and frequency localization of various EEG patterns. Entropy-related metrics, especially permutation entropy (PE), was also very useful in training networks, and decreases in PE were found in both preictal and ictal segments in comparison to background (Li et al., 2007). Furthermore, specific spatial features were found to characterize absence seizures such as increased cortico-thalamo-cortical synchrony in murine models, or reductions in overall functional connectivity patterns during generalized spike-and-wave discharges in humans (van Luijtelaar et al., 2016; Kumar et al., 2021).

Many studies found that the harmonics of the fundamental frequencies of seizures are highly specific and critical to the classification success (Sitnikova et al., 2009; Buteneers et al., 2013). Harmonic spectral analysis involves broad wavebands (i.e., 1–120 Hz) that include HFOs which are increasingly recognized as crucially important in the pathophysiology of epilepsy. The energy in these higher frequency harmonics are found to be important signatures differentiating between regular sleep spindles, artifacts and true spike-and-wave discharges that all share the same fundamental frequency (Sitnikova et al., 2009). The interdependent and harmonic architecture of the EEG frequency spectrum has been well described by authors such as Buzsáki Buzsaki and Draguhn (2004) and Klimesch (2013) and indicates that a comprehensive analysis of EEG activity should involve a view of the cross-frequency dynamics.

4.1 Comparison with other machine learning and deep learning methods

The use of ML algorithms and DL neural networks in studies attempting to recognize and predict absence seizure EEG activity has been rapidly advancing in the past decades, generating promise in improving both clinical treatment as well as the neurobiological understanding of this disorder. Studies since the early 1990's describe the ability of ML and DL methods to recognize absence seizures with high level of sensitivity (~95%) albeit often with higher rates of false positives (Jando et al., 1993; Vadasz et al., 1995). Many of these earlier studies used genetic murine models of absence epilepsy and implanted EEG electrodes. More recent ones apply these techniques to humans using only scalp EEG and with the ability to run the computation not only offline, but also in real time (Alam et al., 2024).

This ability to differentiate the pre-seizure from the seizure state is now being successfully applied to humans using scalp EEG with as few as 19 scalp electrodes (Kumar et al., 2021). Schirrmeister et al. (2017) used spectral power between alpha-high gamma bands with a convolutional neural network (CNN) and achieved accuracies as high as 84% (Schirrmeister et al., 2017). In a more recent exploration with a shallow CNN applied to scalp EEG data from human subjects, Zhang et al. achieved a sensitivity of 92.2% with a low false positives rate (FPR) of 0.12 per hour (Zhang et al., 2020). Other studies too have used various ML and DL models for seizure detection and/or prediction in human scalp EEG using different features with accuracy ranging from ~70% to higher than 90–95% (Li et al., 2016; Sridevi et al., 2019; Ansari et al., 2021; Liu et al., 2022; Thara et al., 2023; Alam et al., 2024).

The current SSAE-based classification results are on par with or better than several studies based on other DL neural network classifiers such as: CNN and BiLSTM (Liu et al., 2022; Schirrmeister

TABLE 3 Seizure classification/detection studies using deep learning neural networks.

Author and year	Feature	Classifier	*Sens*	*Spec*	*Acc*	Dataset	Fs, Hz	No. of subjects	Subject-specific algorithm
Lin et al. (2016)	Raw data	SSAE	93–100%	90–100%	96%	Bonn	173	5	No
Schirrmeister et al. (2017)	Raw data	CNN	-	-	84%	TUH	250	14	Yes
Akut (2019)	Raw data	CNN	100%	100%	100%	Bonn	173	5	No
Zhang et al. (2020)	Raw data	Shallow CNN	92%	-	-	CHB-MIT	256	-	No
Liu et al. (2022)	Raw data	CNN, BiLSTM	86%, 89%	-	97.5% 93.7%	CHB-MIT, SH-SDU	256	33	No
Fujita et al. (2022)	PAC	DCNN	90%	90%	90%	Innov. AI Hosp.	1000–2000	180	No
Khan et al. (2022)	Scalogram	Various CNNs	95%	95%	95%	TUH	250	9	No
Yang et al. (2023)	Temporal spectral	Multiple NNs	98%	100%	85%	TUH	250	14	No
Thara et al. (2023)	Raw data	CNN, VGGNet, ResNet	-	-	97%	TUH	250	-	No
This work	PPC	SSAE	93%	99%	97%	TUH	250	12	No

Sens, sensitivity; *Spec*, specificity; *Acc*, accuracy; Fs, sampling frequency, hyphen (−), no data.

et al., 2017; Zhang et al., 2020; Thara et al., 2023; Khan et al., 2022), DCNN (Fujita et al., 2022), multiple neural networks (not specified) (Yang et al., 2023) (see Table 3). We are aware of only one study based on a convolutional neural network which reported 100% for sensitivity, specificity and accuracy (Akut, 2019). However, this study was done on a dataset of only 5 patients which raises a question about the generalizability of this result. A comprehensive comparison of various CNN networks, including pretrained GoogLeNet and AlexNet as well as the authors' original hybrid model (AG86), was done in Khan et al. (2022). Their hybrid model AG86 combined the best features of GoogLeNet (inception layer) and AlexNet (starting and ending layers) and demonstrated a better performance than several other pretrained networks (Khan et al., 2022). Although the proposed SSAE classifier showed a slightly lower sensitivity (93%) compared to the AG86 model (95%), it achieved better specificity (99%) and accuracy (97%) (Table 3). Also, the SSAE classifiers usually have just two hidden layers and thus have a simpler architecture compared to the CNN networks which require multiple hidden layers to achieve a comparable reduction in dimensionality (Akut, 2019), and this requires more computational resources. For example, in Akut's study the training was done on Tesla K80 GPU to achieve faster computation time. The GPU used 12 GB Memory, 61 GB RAM and 100 GB SSD (Akut, 2019). In comparison, the proposed SSAE classifier was realized on a laptop (with the Windows 10 Enterprise OS) with Intel(R) Core(TM) i5-5300U CPU at 2.30GHz, 16 GB RAM and ~ 1 GB hard drive space. This speaks to an excellent computational efficiency of the SSAE classifier. EEG classification using SSAE is a novel approach and we are aware of only one study where a SSAE classifier for seizure detection also demonstrated very good performance (*Sens* = 93%÷100%; *Spec* = 90%÷100% and *Acc* = 96%) (Lin et al., 2016).

It is also important to compare the DL-based models with more traditional ML algorithms. Since 2012, emerging research in epilepsy classification utilizing ML has shown dramatic improvements in sensitivity, specificity, and/or accuracy (up to 100% sensitivity). For example, one of these studies used increasingly larger datasets than previous studies such as with the number of patients up to 23 (Chandel et al., 2016), and still obtaining a sensitivity of 100%. It is worth noting that the ML methods typically outperformed DL neural networks in seizure classification on certain datasets achieving sensitivity at 100% as well as specificity and accuracy at 99% (Saeed et al., 2016; Chandel et al., 2016; Khan et al., 2012; Ansari et al., 2021) (see Tables 3, 4). Moreover, the ML algorithms are more compact and allow an effective implementation in hardware (Alam et al., 2024). However, more recent research on DL has shown similar capabilities (Khan et al., 2022; Thara et al., 2023; Akut, 2019), and more research with DL is warranted. The DL-based classification algorithms can continue to improve by broadening their approach to patient-independent training, including larger datasets with more patients, and optimizing sensitivity, specificity and accuracy. In the current study, the performance of the SVM and Random Forest classifiers were significantly lower compared with the SSAE classifier and lower than the reported results for the ML classifiers in many other studies (see Tables 2, 4). It is likely that the more modest results with the SVM and RF classifiers were due to a more stringent 'leave-one-subject-out' cross-validation used in the current study. Also, the larger variance of the classification metrics (*Sens*, *Spec*, and *Acc*) with the SVM and

TABLE 4 Seizure classification/detection studies using machine learning algorithms.

Author and year	Feature	Classifier	*Sens*	*Spec*	*Acc*	Dataset	Fs, Hz	No. of subjects	Subject-specific algorithm
Khan et al. (2012)	Skewness kurtosis	Simple linear classifier	100%	-	-	CHB-MIT	256	10	Yes
Li et al. (2016)	Entropy	LDA	-	-	89.0%	Peking Univ. Hosp.	256	10	No
Saeed et al. (2016)	Entropy, CSD	SVM	100%	-	-	CHB-MIT	256	10	Yes
Chandel et al. (2016)	Spectral, entropy	Linear classifier	100%	-	-	CHB-MIT	256	23	Yes
Jacobs et al. (2018)	PAC	Random Forest	87.9–97.5%	82.4–95%	80–95%	Toronto Western Hosp.	500–1,024	12	Both
Liu et al. (2018)	PAC	SVM	-	-	97.5–100%	CHB-MIT, Bonn	256, 173	28	-
Sridevi et al. (2019)	Spectral, entropy	LDA, NB, DT, SVM, KNN	80%	86%	83%	SCTIMST, Fortis Malar Hosp.	256–400	18	No
Ansari et al. (2021)	Spectral	Linear classifier	100%	99%	99%	AIIMS, CHB-MIT	128–256	30	No
Alam et al. (2024)	Various	QDA classifier	100%	-	99.4%	Bonn	173	5	No

Sens, sensitivity; *Spec*, specificity; *Acc*, accuracy; Fs, sampling frequency, hyphen (–), no data.

Random Forest algorithms point to the lower generalizability of the ML classifiers compared to the SSAE classifier in the current study.

Growing interest in using DL for seizure classification is partly related to how its unique characteristics may allow for increased generalizability including across individuals, seizure types, sleep vs. wake conditions, and eventually moving from dual classification (e.g., seizure vs. background) to ternary classification (e.g., seizure vs. preictal vs. background). The ability of the DL networks to eliminate or at least reduce the need for feature extraction may be part of this generalization. Getting rid of the human bias on what features define a seizure may improve seizure classification. In place of the 'extracted-by-a-human' features, DL has an ability to find more abstract and higher-level representations (Akut, 2019). DL's greater number of hidden layers alongside nonlinear activation functions expand its abilities for finding intricate and nonlinear patterns in the data. Given that the brain is non-linear and its EEG signals are non-stationary and complex, it seems appropriate to continue to evaluate whether and how DL may match or improve traditional ML accuracy in seizure classification.

Our method has built on the efficacious components of the existing research in regard to the deep learning techniques, significant CFC biomarkers, and the emerging relationships of HFOs to epilepsy. The novelty and significance of this approach includes validation of a hitherto unexplored phenomenon of cross-frequency interactions (specifically, power-to-power coupling) in the context of identifying new biomarkers of absence seizures. Building on prior research which suggests the key importance of HFOs in epilepsy, this approach also holds promise for clinical application in long-term monitoring of patients with absence seizures.

It is becoming clear that there is a complex interplay between spectral, harmonic and spatial features that can reliably characterize absence epilepsy. PPC analysis has a level of sensitivity to these features already known to have utility in seizure classification (i.e., spectral power), and in addition, it provides important information on cross-frequency interaction. In this way, PPC represents a novel powerful, hitherto underutilized, tool to probe the unique cross-frequency signatures of epileptiform activity. It holds promise for further enhancing the optimization between sensitivity and specificity. This becomes particularly crucial in scenarios where data is less pristine or encompassing multiple states such as sleep and wakefulness. The results not only confirm the utility of a new approach to classify absence seizures with high accuracy, but also strongly suggest that continuing research on cross-frequency coupling will deepen our knowledge of the underpinnings of epileptic seizures by further clarifying the involvement of HFOs (which are already known to be deeply related to epilepsy), harmonic patterns, as well as interdependent relationships between different frequency bands more generally.

5 Limitations of the study

A limitation of the current study is the use of a single public dataset (TUSZ) which has EEG records of absence seizures from just 12 patients. Also, the available EEG records are not very long (5 to 35 min in duration). While the number of patients (12) is comparable to other classification studies (Table 3; with the exception of Chandel et al., 2016; Ansari et al., 2021; Fujita et al., 2022), this may still limit the generalizability of our results. However, the absence seizure dataset from the TUSZ corpus is relatively balanced by the gender of patients (7 females and 5 males) and it also contains a wide range of patient ages, from pediatric to young adult (4–22 years). The 'one-subject-out' cross-validation did demonstrate good generalizability across this range of patients' ages.

Another limitation is that it is unclear whether the classification performance in the present study is achieved due to a specific feature set (i.e., power-to-power coupling matrices) or a specific classifier type (i.e., the autoencoder). However, the use of another feature namely, power spectrum, which has been used in many other studies, (e.g., Ansari et al., 2021; Yang et al., 2023), did not improve classification. Importantly, the PPC-based classification had significantly smaller variance compared to the spectrum-based one.

6 Conclusion

The results provide evidence both for the parameters of power-to-power coupling having utility for seizure classification and also for an approach using PPC alongside SSAE neural networks being efficacious for automated classification of seizures within scalp EEG. Importantly, the trained SSAE network showed generalizability in detecting seizures with high sensitivity (93%), very high specificity (99.5%) and accuracy higher than 96% with all patients tested. Automated analysis based on deep learning networks can significantly accelerate the analysis of EEG data and increase their diagnostic value.

Data availability statement

Publicly available datasets were analyzed in this study. This data can be found at: Temple University Hospital database (the TUSZ corpus) https://isip.piconepress.com/projects/tuh_eeg.

Ethics statement

The studies involving public records of human EEG were approved by Institutional Review Board, Georgetown University-Medstar. The studies were conducted in accordance with the local legislation and institutional requirements. Written informed consent for participation was not required from the participants or the participants' legal guardians/next of kin in accordance with the national legislation and institutional requirements.

Author contributions

AM: Conceptualization, Data curation, Formal analysis, Funding acquisition, Investigation, Methodology, Project administration, Resources, Software, Supervision, Validation, Visualization, Writing – original draft, Writing – review & editing. BL: Data curation, Formal analysis, Investigation, Software, Writing – original draft, Writing – review & editing.

Funding

The author(s) declare that financial support was received for the research, authorship, and/or publication of this article. Research reported in this publication was supported by the National Institute of Mental Health of the National Institutes of Health under Award Number RF1MH123192 to AM. The content is solely the responsibility of the authors and does not necessarily represent the official views of the National Institutes of Health.

Acknowledgments

The authors wish to thank the team of the Temple University Hospital EEG data portal for giving us access to the EEG data.

Conflict of interest

The authors declare that the research was conducted in the absence of any commercial or financial relationships that could be construed as a potential conflict of interest.

Generative AI statement

The authors declare that no Gen AI was used in the creation of this manuscript.

Publisher's note

All claims expressed in this article are solely those of the authors and do not necessarily represent those of their affiliated organizations, or those of the publisher, the editors and the reviewers. Any product that may be evaluated in this article, or claim that may be made by its manufacturer, is not guaranteed or endorsed by the publisher.

Supplementary material

The Supplementary material for this article can be found online at: https://www.frontiersin.org/articles/10.3389/fninf.2025.1513661/full#supplementary-material

References

Akman, C. I., Montenegro, M. A., Jacob, S., Eck, K., Chiriboga, C., and Gilliam, F. (2009). Seizure frequency in children with epilepsy: factors influencing accuracy and parental awareness. *Seizure* 18, 524–529. doi: 10.1016/j.seizure.2009.05.009

Akut, R. (2019). Wavelet based deep learning approach for epilepsy detection. *Health Inf. Sci. Syst.* 7:8. doi: 10.1007/s13755-019-0069-1

Alam, M. S., Khan, U., Hasan, M., and Farooq, O. (2024). Energy efficient FPGA implementation of an epileptic seizure detection system using a QDA classifier. *Expert Syst. Appl.* 249:123755. doi: 10.1016/j.eswa.2024.123755

Ansari, A. Q., Sharma, P., and Tripathi, M. (2021). A patient-independent classification system for onset detection of seizures. *Biomed. Tech.* 66, 267–274. doi: 10.1515/bmt-2020-0250

Axmacher, N., Elger, C. E., and Fell, J. (2008). Ripples in the medial temporal lobe are relevant for human memory consolidation. *Brain* 131, 1806–1817. doi: 10.1093/brain/awn103

Besio, W., Gale, K., and Medvedev, A. (2010). Possible therapeutic effects of transcutaneous electrical stimulation via concentric ring electrodes. 10th workshop on neurobiology of epilepsy (WONOEP 2009). *Epilepsia* 51, 85–87. doi: 10.1111/j.1528-1167.2010.02617.x

Blanco, J. A., Stead, M., Krieger, A., Viventi, J., Marsh, W. R., Lee, K. H., et al. (2010). Unsupervised classification of high-frequency oscillations in human neocortical epilepsy and control patients. *J. Neurophysiol.* 104, 2900–2912. doi: 10.1152/jn.01082.2009

Bragin, A., Engel, J. Jr., Wilson, C. L., Fried, I., and Mathern, G. W. (1999). Hippocampal and entorhinal cortex high-frequency oscillations (100–500 Hz) in human epileptic brain and in Kainic acid-treated rats with chronic seizures. *Epilepsia* 40, 127–137. doi: 10.1111/j.1528-1157.1999.tb02065.x

Buteneers, P., Verstraeten, D., Nieuwenhuyse, B. V., Stroobandt, D., Raedt, R., Vonck, K., et al. (2013). Real-time detection of epileptic seizures in animal models using reservoir computing. *Epilepsy Res.* 103, 124–134. doi: 10.1016/j.eplepsyres.2012.07.013

Buzsaki, G., and Draguhn, A. (2004). Neuronal oscillations in cortical networks. *Science* 304, 1926–1929. doi: 10.1126/science.1099745

Buzsaki, G., and Silva, F. L. (2012). High frequency oscillations in the intact brain. *Prog. Neurobiol.* 98, 241–249. doi: 10.1016/j.pneurobio.2012.02.004

Chaitanya, G., Sinha, S., Narayanan, M., and Satishchandra, P. (2015). Scalp high frequency oscillations (HFOs) in absence epilepsy: an independent component analysis (ICA) based approach. *Epilepsy Res.* 115, 133–140. doi: 10.1016/j.eplepsyres.2015.06.008

Chandel, G., Farooq, O., Khan, Y. U., and Chawla, M. (2016). Seizure onset detection by analyzing long-duration EEG signals. *Proc. Sec. Int. Conf. Comput. Commun.* 2, 215–224. doi: 10.1007/978-81-322-2523-2_20

Dickey, C. W., Verzhbinsky, I. A., Jiang, X., Rosen, B. Q., Kajfez, S., Stedelin, B., et al. (2022). Widespread ripples synchronize human cortical activity during sleep, waking, and memory recall. *Proc. Natl. Acad. Sci. USA* 119:e2107797119. doi: 10.1073/pnas.2107797119

Edakawa, K., Yanagisawa, T., Kishima, H., Fukuma, R., Oshino, S., Khoo, H. M., et al. (2016). Detection of epileptic seizures using phase-amplitude coupling in intracranial electroencephalography. *Sci. Rep.* 6:25422. doi: 10.1038/srep25422

Fanselow, E. E., Reid, A. P., and Nicolelis, M. A. (2000). Reduction of pentylenetetrazole-induced seizure activity in awake rats by seizure-triggered trigeminal nerve stimulation. *J. Neurosci.* 20, 8160–8168. doi: 10.1523/JNEUROSCI.20-21-08160.2000

Ferraris, M., Ghestem, A., Vicente, A. F., Nallet-Khosrofian, L., Bernard, C., and Quilichini, P. P. (2018). The nucleus Reuniens controls long-range Hippocampo-prefrontal gamma synchronization during slow oscillations. *J. Neurosci.* 38, 3026–3038. doi: 10.1523/JNEUROSCI.3058-17.2018

Frauscher, B., Bartolomei, F., Kobayashi, K., Cimbalnik, J., Rampp, S., Otsubo, H., et al. (2017). High-frequency oscillations: the state of clinical research. *Epilepsia* 58, 1316–1329. doi: 10.1111/epi.13829

Fujita, Y., Yanagisawa, T., Fukuma, R., Ura, N., Oshino, S., and Kishima, H. (2022). Abnormal phase-amplitude coupling characterizes the interictal state in epilepsy. *J. Neural Eng.* 19:026056. doi: 10.1088/1741-2552/ac64c4

Gardner, A. B., Worrell, G. A., Marsh, E., Dlugos, D., and Litt, B. (2007). Human and automated detection of high-frequency oscillations in clinical intracranial EEG recordings. *Clin. Neurophysiol.* 118, 1134–1143. doi: 10.1016/j.clinph.2006.12.019

Giehl, J., Noury, N., and Siegel, M. (2021). Dissociating harmonic and non-harmonic phase-amplitude coupling in the human brain. *NeuroImage* 227:117648. doi: 10.1016/j.neuroimage.2020.117648

Gross, D. W., and Gotman, J. (1999). Correlation of high-frequency oscillations with the sleep-wake cycle and cognitive activity in humans. *Neuroscience* 94, 1005–1018. doi: 10.1016/S0306-4522(99)00343-7

Hosseinzadeh, H., Asl, M. N., Parvardeh, S., and Tagi Mansouri, S. M. (2005). The effects of carbenoxolone on spatial learning in the Morris water maze task in rats. *Med. Sci. Monit.* 11:BR88

Ibrahim, G. M., Wong, S. M., Anderson, R. A., Singh-Cadieux, G., Akiyama, T., Ochi, A., et al. (2014). Dynamic modulation of epileptic high frequency oscillations by the phase of slower cortical rhythms. *Exp. Neurol.* 251, 30–38. doi: 10.1016/j.expneurol.2013.10.019

Jacobs, D., Hilton, T., Del Campo, M., Carlen, P. L., and Bardakjian, B. L. (2018). Classification of pre-clinical seizure states using scalp EEG cross-frequency coupling features. *IEEE Trans. Biomed. Eng.* 65, 2440–2449. doi: 10.1109/TBME.2018.2797919

Jacobs, J., Levan, P., Chander, R., Hall, J., Dubeau, F., and Gotman, J. (2008). Interictal high-frequency oscillations (80-500 Hz) are an indicator of seizure onset areas independent of spikes in the human epileptic brain. *Epilepsia* 49, 1893–1907. doi: 10.1111/j.1528-1167.2008.01656.x

Jando, G., Siegel, R. M., Horvath, Z., and Buzsaki, G. (1993). Pattern recognition of the electroencephalogram by artificial neural networks. *Electroencephalogr. Clin. Neurophysiol.* 86, 100–109. doi: 10.1016/0013-4694(93)90082-7

Jirsa, V., and Muller, V. (2013). Cross-frequency coupling in real and virtual brain networks. *Front. Comput. Neurosci.* 7:78. doi: 10.3389/fncom.2013.00078

Keilson, M. J., Hauser, W. A., Magrill, J. P., and Tepperberg, J. (1987). Ambulatory cassette EEG in absence epilepsy. *Pediatr. Neurol.* 3, 273–276. doi: 10.1016/0887-8994(87)90067-1

Khan, I. D., Farooq, O., and Khan, Y. U. (2022). Automatic seizure detection using modified CNN architecture and activation layer. *J. Phys. Conf. Ser.* 012013. doi: 10.1088/1742-6596/2318/1/012013

Khan, Y. U., Farooq, O., and Sharma, P. (2012). Automatic detection of seizure onset in pediatric EEG. *Int. J. Embedded Syst. Appl.* 2, 81–89. doi: 10.5121/ijesa.2012.2309

Klimesch, W. (2013). An algorithm for the EEG frequency architecture of consciousness and brain body coupling. *Front. Hum. Neurosci.* 7:766. doi: 10.3389/fnhum.2013.00766

Kucewicz, M. T., Cimbalnik, J., Matsumoto, J. Y., Brinkmann, B. H., Bower, M. R., Vasoli, V., et al. (2014). High frequency oscillations are associated with cognitive processing in human recognition memory. *Brain* 137, 2231–2244. doi: 10.1093/brain/awu149

Kumar, A., Lyzhko, E., Hamid, L., Srivastav, A., Stephani, U., and Japaridze, N. (2021). Differentiating ictal/subclinical spikes and waves in childhood absence epilepsy by spectral and network analyses: a pilot study. *Clin. Neurophysiol.* 132, 2222–2231. doi: 10.1016/j.clinph.2021.06.011

Lee, S. A., Spencer, D. D., and Spencer, S. S. (2000). Intracranial EEG seizure-onset patterns in neocortical epilepsy. *Epilepsia* 41, 297–307. doi: 10.1111/j.1528-1157.2000.tb00159.x

Li, J., Liu, X., and Ouyang, G. (2016). Using relevance feedback to distinguish the changes in EEG during different absence seizure phases. *Clin. EEG Neurosci.* 47, 211–219. doi: 10.1177/1550059414548721

Li, X., Ouyang, G., and Richards, D. A. (2007). Predictability analysis of absence seizures with permutation entropy. *Epilepsy Res.* 77, 70–74. doi: 10.1016/j.eplepsyres.2007.08.002

Lin, Q., Ye, S. Q., Huang, X. M., Li, S.-Y., Zhang, M.-Z., Xue, Y., et al. (2016). Intelligent computing methodologies. Lecture Notes in Computer Science. 9773, 802–810. doi: 10.1007/978-3-319-42297-8_74

Lisman, J. E., and Jensen, O. (2013). The theta-gamma neural code. *Neuron* 77, 1002–1016. doi: 10.1016/j.neuron.2013.03.007

Liu, G., Tian, L., and Zhou, W. (2022). Patient-independent seizure detection based on channel-perturbation convolutional neural network and bidirectional long short-term memory. *Int. J. Neural Syst.* 32:2150051. doi: 10.1142/S0129065721500519

Liu, Y., Wang, J., Cai, L., Chen, Y., and Qin, Y. (2018). Epileptic seizure detection from EEG signals with phase–amplitude cross-frequency coupling and support vector machine. *Int. J. Mod. Phys. B.* 32:1850086. doi: 10.1142/s0217979218500868

Llinas, R. R., Ribary, U., Jeanmonod, D., Kronberg, E., and Mitra, P. P. (1999). Thalamocortical dysrhythmia: a neurological and neuropsychiatric syndrome characterized by magnetoencephalography. *Proc. Natl. Acad. Sci. USA* 96, 15222–15227. doi: 10.1073/pnas.96.26.15222

Medvedev, A. V. (2002). Epileptiform spikes desynchronize and diminish fast (gamma) activity of the brain. An "anti-binding" mechanism? *Brain Res. Bull.* 58, 115–128. doi: 10.1016/S0361-9230(02)00768-2

Medvedev, A. V., Agoureeva, G. I., and Murro, A. M. (2019). A long short-term memory neural network for the detection of epileptiform spikes and high frequency oscillations. *Sci. Rep.* 9:19374. doi: 10.1038/s41598-019-55861-w

Medvedev, A. V., and Kanwal, J. S. (2008). Communication call-evoked gamma-band activity in the auditory cortex of awake bats is modified by complex acoustic features. *Brain Res.* 1188, 76–86. doi: 10.1016/j.brainres.2007.10.081

Medvedev, A. V., Murro, A. M., and Meador, K. J. (2011). Abnormal interictal gamma activity may manifest a seizure onset zone in temporal lobe epilepsy. *Int. J. Neural Syst.* 21, 103–114. doi: 10.1142/S0129065711002699

Pail, M., Cimbalnik, J., Roman, R., Daniel, P., Shaw, D. J., Chrastina, J., et al. (2020). High frequency oscillations in epileptic and non-epileptic human hippocampus during a cognitive task. *Sci. Rep.* 10:18147. doi: 10.1038/s41598-020-74306-3

Pion-Tonachini, L., Kreutz-Delgado, K., and Makeig, S. (2019). ICLabel: an automated electroencephalographic independent component classifier, dataset, and website. *NeuroImage* 198, 181–197. doi: 10.1016/j.neuroimage.2019.05.026

Popov, T., Jensen, O., and Schoffelen, J. M. (2018). Dorsal and ventral cortices are coupled by cross-frequency interactions during working memory. *NeuroImage* 178, 277–286. doi: 10.1016/j.neuroimage.2018.05.054

Richard, C. D., Tanenbaum, A., Audit, B., Arneodo, A., Khalil, A., and Frankel, W. N. (2015). SWDreader: a wavelet-based algorithm using spectral phase to characterize spike-wave morphological variation in genetic models of absence epilepsy. *J. Neurosci. Methods* 242, 127–140. doi: 10.1016/j.jneumeth.2014.12.016

Saeed, M. T., Zuhaib, M., Khan, Y. U., and Azeem, M. F. (2016). Automatic seizure onset detection in long term pediatric EEG signals. *J. Comput. Sci. Syst. Biol* 9, 125–131. doi: 10.4172/jcsb.1000230

Schirrmeister, R. T., Springenberg, J. T., Fiederer, L. D. J., Glasstetter, M., Eggensperger, K., Tangermann, M., et al. (2017). Deep learning with convolutional neural networks for EEG decoding and visualization. *Hum. Brain Mapp.* 38, 5391–5420. doi: 10.1002/hbm.23730

Shah, V., Von Weltin, E., Lopez, S., Mchugh, J. R., Veloso, L., Golmohammadi, M., et al. (2018). The Temple University Hospital seizure detection Corpus. *Front. Neuroinform.* 12:83. doi: 10.3389/fninf.2018.00083

Sheremet, A., Kennedy, J. P., Qin, Y., Zhou, Y., Lovett, S. D., Burke, S. N., et al. (2019). Theta-gamma cascades and running speed. *J. Neurophysiol.* 121, 444–458. doi: 10.1152/jn.00636.2018

Shirvalkar, P. R., Rapp, P. R., and Shapiro, M. L. (2010). Bidirectional changes to hippocampal theta-gamma comodulation predict memory for recent spatial episodes. *Proc. Natl. Acad. Sci. USA* 107, 7054–7059. doi: 10.1073/pnas.0911184107

Sitnikova, E., Hramov, A. E., Koronovsky, A. A., and Van Luijtelaar, G. (2009). Sleep spindles and spike-wave discharges in EEG: their generic features, similarities and distinctions disclosed with Fourier transform and continuous wavelet analysis. *J. Neurosci. Methods* 180, 304–316. doi: 10.1016/j.jneumeth.2009.04.006

Sridevi, V., Ramasubba Reddy, M., Srinivasan, K., Radhakrishnan, K., Rathore, C., and Nayak, D. S. (2019). Improved patient-independent system for detection of electrical onset of seizures. *J. Clin. Neurophysiol.* 36, 14–24. doi: 10.1097/WNP.0000000000000533

Staba, R. J., Stead, M., and Worrell, G. A. (2014). Electrophysiological biomarkers of epilepsy. *Neurotherapeutics* 11, 334–346. doi: 10.1007/s13311-014-0259-0

Thammasan, N., and Miyakoshi, M. (2020). Cross-frequency power-power coupling analysis: a useful cross-frequency measure to classify ICA-decomposed EEG. *Sensors* 20:20. doi: 10.3390/s20247040

Thara, D. K., Premasudha, B. G., and Krivic, S. (2023). Detection of epileptic seizure events using pre-trained convolutional neural network, VGGNet and res net. *Expert. Syst.* 2023:e13447. doi: 10.1111/exsy.13447

Thomschewski, A., Hincapie, A. S., and Frauscher, B. (2019). Localization of the epileptogenic zone using high frequency oscillations. *Front. Neurol.* 10:94. doi: 10.3389/fneur.2019.00094

Vadasz, C., Carpi, D., Jando, G., Kandel, A., Urioste, R., Horvath, Z., et al. (1995). Genetic threshold hypothesis of neocortical spike-and-wave discharges in the rat: an animal model of petit mal epilepsy. *Am. J. Med. Genet.* 60, 55–63. doi: 10.1002/ajmg.1320600111

Van Luijtelaar, G., Luttjohann, A., Makarov, V. V., Maksimenko, V. A., Koronovskii, A. A., and Hramov, A. E. (2016). Methods of automated absence seizure detection, interference by stimulation, and possibilities for prediction in genetic absence models. *J. Neurosci. Methods* 260, 144–158. doi: 10.1016/j.jneumeth.2015.07.010

Von Ellenrieder, N., Frauscher, B., Dubeau, F., and Gotman, J. (2016). Interaction with slow waves during sleep improves discrimination of physiologic and pathologic high-frequency oscillations (80-500 Hz). *Epilepsia* 57, 869–878. doi: 10.1111/epi.13380

Wang, L., Hagoort, P., and Jensen, O. (2018). Language prediction is reflected by coupling between frontal gamma and posterior alpha oscillations. *J. Cogn. Neurosci.* 30, 432–447. doi: 10.1162/jocn_a_01190

Worrell, G. A., Parish, L., Cranstoun, S. D., Jonas, R., Baltuch, G., and Litt, B. (2004). High-frequency oscillations and seizure generation in neocortical epilepsy. *Brain* 127, 1496–1506. doi: 10.1093/brain/awh149

Xanthopoulos, P., Liu, C. C., Zhang, J., Miller, E. R., Nair, S. P., Uthman, B. M., et al. (2009). A robust spike and wave algorithm for detecting seizures in a genetic absence seizure model. *Annu. Int. Conf. IEEE Eng. Med. Biol. Soc.* 2009, 2184–2187. doi: 10.1109/IEMBS.2009.5334941

Yang, Y., Li, F., Qin, X., Wen, H., Lin, X., and Huang, D. (2023). Feature separation and adversarial training for the patient-independent detection of epileptic seizures. *Front. Comput. Neurosci.* 17:1195334. doi: 10.3389/fncom.2023.1195334

Zhang, Y., Guo, Y., Yang, P., Chen, W., and Lo, B. (2020). Epilepsy seizure prediction on EEG using common spatial pattern and convolutional neural network. *IEEE J. Biomed. Health Inform.* 24, 465–474. doi: 10.1109/JBHI.2019.2933046

Zijlmans, M., Jiruska, P., Zelmann, R., Leijten, F. S., Jefferys, J. G., and Gotman, J. (2012). High-frequency oscillations as a new biomarker in epilepsy. *Ann. Neurol.* 71, 169–178. doi: 10.1002/ana.22548

frontiers | Frontiers in Neuroinformatics

TYPE Original Research
PUBLISHED 27 February 2025
DOI 10.3389/fninf.2025.1521805

OPEN ACCESS

EDITED BY
A. Amalin Prince,
Birla Institute of Technology and Science, India

REVIEWED BY
Anurag Nishad,
Birla Institute of Technology and Science, India
Saif Nalband,
Thapar Institute of Engineering & Technology, India

*CORRESPONDENCE
Yuri Gordienko
✉ gord@comsys.kpi.ua

RECEIVED 02 November 2024
ACCEPTED 13 February 2025
PUBLISHED 27 February 2025

CITATION
Gordienko Y, Gordienko N, Taran V, Rojbi A, Telenyk S and Stirenko S (2025) Effect of natural and synthetic noise data augmentation on physical action classification by brain–computer interface and deep learning. *Front. Neuroinform.* 19:1521805. doi: 10.3389/fninf.2025.1521805

Effect of natural and synthetic noise data augmentation on physical action classification by brain–computer interface and deep learning

Yuri Gordienko[1]*, Nikita Gordienko[1], Vladyslav Taran[1], Anis Rojbi[2], Sergii Telenyk[1,3] and Sergii Stirenko[1]

[1]Computer Engineering Department, National Technical University of Ukraine "Igor Sikorsky Kyiv Polytechnic Institute," Kyiv, Ukraine, [2]Laboratoire Cognitions Humaine et Artificielle, Université Paris 8, Paris, France, [3]Department of Automation and Computer Science, Faculty of Electrical and Computer Engineering, Cracow University of Technology, Cracow, Poland

Analysis of electroencephalography (EEG) signals gathered by brain–computer interface (BCI) recently demonstrated that deep neural networks (DNNs) can be effectively used for investigation of time sequences for physical actions (PA) classification. In this study, the relatively simple DNN with fully connected network (FCN) components and convolutional neural network (CNN) components was considered to classify finger-palm-hand manipulations each from the grasp-and-lift (GAL) dataset. The main aim of this study was to imitate and investigate environmental influence by the proposed noise data augmentation (NDA) of two kinds: (i) natural NDA by inclusion of noise EEG data from neighboring regions by increasing the sampling size *N* and the different offset values for sample labeling and (ii) synthetic NDA by adding the generated Gaussian noise. The natural NDA by increasing *N* leads to the higher micro and macro area under the curve (AUC) for receiver operating curve values for the bigger *N* values than usage of synthetic NDA. The detrended fluctuation analysis (DFA) was applied to investigate the fluctuation properties and calculate the correspondent Hurst exponents *H* for the quantitative characterization of the fluctuation variability. *H* values for the low time window scales (< 2 s) are higher in comparison with ones for the bigger time window scales. For example, *H* more than 2–3 times higher for some PAs, i.e., it means that the shorter EEG fragments (< 2 s) demonstrate the scaling behavior of the higher complexity than the longer fragments. As far as these results were obtained by the relatively small DNN with the low resource requirements, this approach can be promising for porting such models to Edge Computing infrastructures on devices with the very limited computational resources.

KEYWORDS

deep neural network, brain-computer interface, grasp-and-lift, physical action, data augmentation, noise, noise data augmentation, detrended fluctuation analysis

1 Introduction

Recently, deep learning (DL) methods based on deep neural networks (DNNs) were effectively used for processing different data (LeCun et al., 2015). In healthcare and elderly care, they become very popular for processing the very complex multimodal medical data (Chen and Jain, 2020; Esteva et al., 2019). Usage of DL is especially important in the view

of availability of various brain–computer interfaces (BCI) used for collection and analysis of electroencephalography (EEG) signals generated by brain activities (Roy et al., 2019; Kotowski et al., 2020; Lawhern et al., 2018). In the context of critically important tasks, for example, for air-space applications, BCIs are intensively used for the mental workload assessment on professional air traffic controllers during realistic air traffic control tasks (Aricò et al., 2016b,a; Di Flumeri et al., 2019).

DNNs were actively used for analysis of EEG data in a different fields (Li et al., 2020; Aggarwal and Chugh, 2022; Zabcikova et al., 2022) such as air-space (Aricò et al., 2016b,a; Di Flumeri et al., 2019), medicine (Chen et al., 2022; Wan et al., 2019; Gu et al., 2021), education (Xu and Zhong, 2018; Gang et al., 2018; Belo et al., 2021), entertainment (Kerous et al., 2018; Gang et al., 2018; Vasiljevic and de Miranda, 2020; Cattan, 2021), and other applications (Zabcikova et al., 2022). Usually, components of convolutional neural network (CNN) (Lawhern et al., 2018; Lin et al., 2020; Gu et al., 2021; Gatti et al., 2019; Gordienko et al., 2021c), recurrent neural networks (RNN) (An and Cho, 2016; Wang et al., 2018b; Pancholi et al., 2021; Kostiukevych et al., 2021), and other including components of fully connected networks (FCN) (Gordienko et al., 2021c; Kostiukevych et al., 2021) are used in them. These models combine some methods of EEG feature extraction with the use of various filters and show significant improvement of performance in comparison with other models. For instance, 3D CNN model based on multi-dimensional feature combination improves the classification accuracy of sensorimotor area activated tasks in the brain (Wei and Lin, 2020). Some of the DNN models demonstrated their quite high efficiency on some tasks such as sleep stage classification, stress recognition, fatigue detection, motor imagery classification, emotion recognition, and emotion classification (Gu et al., 2021). As to the domain operator-specific scenarios, some interesting results were obtained for EEG hand movement force and speed forecasting with the accuracy $>$ 80% (Gatti et al., 2019) and the conflict prediction accuracy $\approx$ 60% (Vahid et al., 2020).

Some hybridization approaches become popular recently. For example, CNN components combined with RNN components (including long short-term memory (LSTM) blocks) were investigated recently to resolve action classification problem. For instance, various RNN architectures were compared in performance for identifying hand motions for GAL dataset from EEG recordings (An and Cho, 2016; Kostiukevych et al., 2021) and for AJILE dataset (Wang et al., 2018b).

As it is well-known in computer vision, for example, for image classification tasks, data augmentation (DA), in general, and noise data augmentation (NDA), in part, can improve the performance of DNNs. Various strategies for applying DA methods to EEG data were considered recently that allow to improve classification accuracy when the limited volume of the data is available (George et al., 2022). NDA methods can be performed by adding Gaussian noise (Cecotti et al., 2015; Freer and Yang, 2020; Gordienko et al., 2021c) or by creating synthetic EEG data (Zhang and Liu, 2018; Aznan et al., 2019; Fahimi et al., 2020). The similar numerous NDA-related approaches were proposed (Freer and Yang, 2020; Gordienko et al., 2021c; George et al., 2022), and many others were reviewed recently in several surveys (Rommel et al., 2022; Lashgari et al., 2020; Talavera et al., 2022).

Although the results are promising and intriguing, their statistical reliability remains uncertain due to potential external influences under real-world conditions. That is why the main of this study was to imitate and investigate environmental influence by the proposed NDA of two kinds: (i) natural NDA by inclusion of noise EEG data from neighboring regions by increasing the sampling size N and the different offset values for sample labeling (see details below) and (ii) synthetic NDA by adding the generated Gaussian noise.

It should be noted that DA is a widely used technique that enhances a model's ability to generalize by making it more robust to variations in input data. Common DA methods include geometric transformations, noise-based modifications (such as roughening, adding, or mixing), and generative approaches. However, in EEG analysis, geometric transformations such as scaling, rotation, and reflection are not directly applicable. Unlike structured tables, text, or images, EEG signals are continuous and vary over time. Even after feature extraction, they remain time series data. Applying geometric transformations, such as rotation, to EEG signals would disrupt their temporal structure, compromising their meaningful features.

Among various ways for adding noise to the EEG signals in purpose of DA Li et al. (2019); Parvan et al. (2019); Ko et al. (2021); Sun and Mou (2023), the following are of great interest due to their intuitive understanding:

- inject various types of noise (such as uniform, Gaussian, Poisson, salt, and pepper noise, and various color noise types) with different parameters (for instance: mean and standard deviation).
- manipulate the time segment of interest by shifting/adding/cropping/combining operations with including/subtracting the information about background and signal.
- synthesize the signal by encoding/decoding and generative approaches.

Like geometric transformation methods, noise addition-based DA has been widely applied in successful DL studies for CV (Simonyan and Zisserman, 2014; He et al., 2016). This approach enhances DA by introducing randomly sampled noise values into the original data. Injecting structured noise patterns (e.g., white Gaussian or pink noise) with a specific signal-to-noise ratio (SNR) can alter the spectral characteristics of a time series by introducing additional frequency components to the signal spectrum (Borra et al., 2024).

In the context of DA for EEG, numerous studies were performed to investigate the impact the noise-induced DA for EEG. Some of the recent results are shortly summarized in Table 1.

DA by Gaussian noise involves adding Gaussian white noise to recorded EEG signals (Wang et al., 2018a). In practice, a perturbation $E(t) \sim N(0, \sigma^2)$ is independently sampled for each channel and acquisition time and added to the original signal X, resulting in the augmented data: $[X](t) = X(t) + E(t)$ Here, σ represents the standard deviation of the noise distribution. This parameter determines the magnitude of the transformation as larger values lead to greater distortion of the original signal. The

TABLE 1 Examples of EEG classification studies ("Reference" column) with noise-based DA with various noise parameters ("Noise Type") on some standard or custom datasets ("Dataset Reference") with the different numbers of classes ("N_c"), neural network architectures ("NNA"), and the reported improved accuracy ("Accuracy, (%)") by absolute values or changes (denoted with + sign).

References	Noise	Dataset	N_c	NNA	Accuracy (%)
Gaussian White Noise					
Zhang et al., 2017	NA	custom (Zhang et al., 2017)	4	CNN	97.5
Behncke et al., 2018	NA	KPO (Behncke et al., 2018)	2	ConvNet	75±9
Behncke et al., 2018	NA	RGO (Behncke et al., 2018)	2	ConvNet	62±7
Lashgari et al., 2021	$N(0, set)$	BCI C 2008 2a (Brunner et al., 2008)	4	CNNwA	93.6 ≥ 91.57
Lashgari et al., 2021	$N(0, set)$	BCI C 2008 2b (Leeb et al., 2008)	2	CNNwA	87.83 ≥ 87.60
George et al., 2022	$N(0, c_{mean})$	custom (Cho et al., 2017b)	4	CNN	78.30-86.51 ≥ 77.73
George et al., 2022	$N(0, c_{mean})$	EEG-BCI (Kaya et al., 2018)	2	CNN	81.74-83.01 ≥ 80.73
Tunnell et al., 2022	$N(0, 1)$	DEAP (Koelstra et al., 2011)	2	EEGNet	77.16 ≥ 66.30
Wu et al., 2022	$N(0, set)$	SleepEDF (Kemp et al., 2000)	5	neuro2vec	86.53 ≥ 85.49
Wu et al., 2022	$N(0, set)$	Epilepsy (Andrzejak et al., 2001)	2	neuro2vec	44.30 ≥ 40.24
Wu et al., 2022	$N(0, set)$	Ninapro (Pizzolato et al., 2017)	18/40	neuro2vec	86.69 ≥ 84.32
Gou et al., 2022	NA	BCI-CRC-WRC (Pizzolato et al., 2017)	3	EEGNet	54.72 ≥ 48.34
Collazos-Huertas et al., 2023	NA	GigaScience (Cho et al., 2017a)	10	EEGNet+ScoreCam	78.2 ≥ 69.7
Lopez et al., 2023	$N(0, MW)$	MAHNOB-HCI (Soleymani et al., 2011)	3(a)	HyperFuseNet	41.56 ≥ 40.90
Lopez et al., 2023	$N(0, MW)$	MAHNOB-HCI (Soleymani et al., 2011)	3(v)	HyperFuseNet	44.30 ≥ 40.24
Ashfaq et al., 2024	$N(0, 0.01)$	CogAge (Nisar et al., 2020)	7	MHyCoL	+5, +30
Ashfaq et al., 2024	$N(0, 0.01)$	UniMiB-SHAR Micucci et al., 2017	17	MHyCoL	+5, +30
Lee et al., 2024	NA	BCI C 2020 (Jeong et al., 2022)	6	DeiT	+0.49 . . . 10.57
Cai et al., 2024	$N(set, set)$	custom (Cai et al., 2024)	6	CNN	85.2 ≥ 58.6
Wang et al., 2024	NA	OpenBMI (Lee et al., 2019)	2	MRCNN	82.47 ≥ 79.45
Wang et al., 2024	NA	SingleArmMI (Wang et al., 2024)	4	MRCNN	43.19 ≥ 37.36
Falaschetti et al., 2024	$N(0, 0.03)$	custom (Falaschetti et al., 2024)	6	LSTM	95.2
Borra et al., 2024	NA	9 MOABB sets (Jayaram and Barachant, 2018)	2/4	SpeechBrain-MOABB	+14. . . 25.2
Cho et al., 2017b	NA	custom (Cho et al., 2017b)	3	CNN	93–95
Ouyang et al., 2024	NA	custom Brainlink (Ouyang et al., 2024)	4	BRIEDGE	98.78 ≥ 98.07
Ouyang et al., 2024	NA	custom EyeState (Ouyang et al., 2024)	2	BRIEDGE	92.51 ≥ 84.75
Ouyang et al., 2024	NA	custom BCI-2000 (Ouyang et al., 2024)	4	BRIEDGE	66.02 ≥ 56.05
Ouyang et al., 2024	NA	custom Hybrid (Ouyang et al., 2024)	10	BRIEDGE	86.50 ≥ 63.72
Uniform noise					
Freer and Yang, 2020	[−0.5,5] scaled	BCI C IV (Tangermann et al., 2012)	4	CNN	+5.3
Various noise types (uniform, white, pink, impulse)					
Sun et al., 2024	NA	Multi-dataset (Sun et al., 2024)	3	CNN+GCN+Transf	96.7,93.3,93.3

[1] NA, the noise parameters were not detailed (not available) in the studies.
[2] *set*, the set of various values was investigated.
[3] c_{mean}, the Gaussian noise is generated with zero mean and standard deviation equal to the class mean.
[4] MW, the Gaussian noise signal with zero mean is added to each sample, with its standard deviation being computed modality-wise (MW).
[5] (a), (v), two classification schemes: (a) - the arousal scheme (3 classes: calm, medium aroused, and excited), (v) - the valence scheme (3 classes: unpleasant, neutral valence, and pleasant).

primary motivation for this DA is to enhance model robustness against noise in EEG recordings, which are known to have a limited SNR. Gaussian noise augmentation is controlled by the parameter σ, which dictates the standard deviation of the sampled noise. Selecting an appropriate σ value is as crucial as choosing the DA method itself. For example, when σ exceeds 0.2, EEG signals become excessively noisy, making the DA systematically detrimental to learning (Rommel et al., 2022).

For instance, spectrogram images of motor imagery EEG have been augmented by introducing Gaussian noise (Zhang et al.,

2020). White noise manifests as random fluctuations uniformly distributed across all frequencies in the EEG signal. It can originate from various sources, including thermal noise in EEG equipment, sensor artifacts, or external electrical interference. This noise reduces the SNR, making it challenging to discern neural patterns and potentially masking true neural activity. The effect is especially problematic for low-amplitude signals, such as those originating from deep brain regions.

Another method for increasing data diversity involves injecting random matrices into the raw data, typically sampled from Gaussian distributions (Okafor et al., 2017). Gaussian noise injection applies a randomly generated matrix from a Gaussian distribution to the original data as a form of DA. While these methods are straightforward and intuitive, they can sometimes exacerbate model overfitting due to the high similarity between the original and augmented data. In particular, several studies have augmented EMG signals by adding Gaussian noise to the original dataset and adjusting the SNR (Atzori et al., 2016; Zhengyi et al., 2017; Tsinganos et al., 2018).

Another study uses injecting random Gaussian noise generated based on the statistical properties of the data. The mean value of trials for the target class is computed; then, Gaussian noise with a zero mean and a standard deviation equal to the class mean (c_{mean} in Table 1) is generated. This noise is added to randomly selected trials to create artificial frames. This simple yet effective method preserves the original waveform characteristics while introducing slight numerical variations across trials (George et al., 2022).

In other studies, DA has proven effective in addressing the challenge of limited learning caused by small training sets in EEGNet, leading to significant improvements in classification accuracy. As a result, the data were expanded by a factor of three, and the standard deviation of the added Gaussian noise was set to 0.1 (Cai et al., 2024).

The modality-wise approach was proposed in Lopez et al. (2023), where the Gaussian noise signal with zero mean is added to each sample, with its standard deviation computed modality-wise (MW in Table 1), ensuring that the augmented signal achieves a signal-to-noise ratio (SNR) of 5dB.

In addition to Gaussian noise, various types of colored noise can also be present in EEG signals due to physiological and environmental factors. These noise types typically manifest as interference, distorting the true brain activity and complicating accurate analysis and interpretation. Below are some examples of how different types of colored noise may appear in EEG signals of brain activity:

Pink noise (1/f noise) is characterized by greater power at lower frequencies, with a gradual decrease in power as the frequency increases. This type of noise can naturally arise from brain activity, particularly during resting states, or be introduced by background physiological processes such as muscle activity or skin potentials. Pink noise can dominate low-frequency bands, potentially masking slow-wave oscillations that are crucial for sleep studies or resting-state EEG analysis.

Brown (red) noise displays even more power at lower frequencies than pink noise, with a steeper decline as the frequency increases. It can arise from long-term drift in electrode potentials or baseline shifts in the EEG signal, often caused by environmental factors that affect the EEG setup. This results in large, slow oscillations that can dominate the EEG trace, potentially masking lower-frequency brain rhythms. While Gaussian (white) noise is frequently applied, the specific use of brown noise has not been widely explored in the literature, but exploring brown noise injection could potentially offer new avenues for enhancing EEG data augmentation techniques.

Blue noise is characterized by an emphasis on high frequencies, manifesting as rapid, small-amplitude fluctuations in the signal. It can originate from high-frequency environmental interference, such as electronic devices or power lines, or from muscle activity, including micro-movements of the scalp or jaw. This type of noise can mask high-frequency neural signals, such as gamma rhythms (30–100 Hz), and may lead to false-positive detections in high-frequency analyses.

Violet noise is an extreme form of high-frequency noise, with a stronger emphasis on higher frequencies than blue noise. It can be caused by electronic interference within the EEG system, such as sudden changes in electrode contact, such as detachment or movement. This noise can introduce sharp spikes or rapid fluctuations that resemble artifacts, potentially disrupting the analysis of high-frequency components, such as event-related potentials (ERPs).

In some studies, several types of noises (in addition to white Gaussian noise) were investigated (Tangermann et al., 2012; Sun et al., 2024). To increase the number of training samples and address the variability and randomness of EEG signals, several noise DA strategies were implemented (Sun et al., 2024). Specifically, the noise DA strategies were adopted to enhance EEG data by simulating various noise sources that may be encountered in real-world environments. The types of noise applied were: (1) uniform noise, (2) Gaussian noise, (3) pink noise, (4) impulse noise, and (5) power-line noise. These noise types were randomly incorporated into the processed clean EEG signals at different proportions (ranging from 10% to 70% of the average amplitude of the EEG signal), thus generating a greater number of training samples. These DA strategies not only enhance the model's robustness to existing noise in the original signals but also improve the model's generalization capabilities in the presence of unknown noises. The introduction of noise through DA strategies has a positive effect on model training, particularly with Gaussian and pink noise. This suggests that such disturbances are prevalent in real EEG data as the noise-augmented strategies enhance the diversity of the samples and the generalization ability of the model. Overall, as the intensity of the added noise increases, both pink noise and Gaussian noise initially decrease and then increase the model prediction error. The optimal results are achieved when noise is added at 30% of the average signal intensity.

In the field of DA for EEG, the use of random shifts has been explored to some extent. However, dataset shift (where the data distribution during inference differs from that during training) is common in real biosignal-based applications. To enhance robustness, probabilistic models with uncertainty quantification are adapted to assess the reliability of predictions. Despite this, evaluating the quality of the estimated uncertainty remains a challenge. Recently, the framework was proposed to assess the

ability of estimated uncertainty to capture various types of biosignal dataset shifts with different magnitudes (Xia et al., 2022). Specifically, three classification tasks were used that were based on respiratory sounds and electrocardiography signals to benchmark five representative uncertainty quantification methods. Extensive experiments reveal that, while Ensemble and Bayesian models provide relatively better uncertainty estimates under dataset shifts, all the tested models fall short in offering trustworthy predictions and proper model calibration. In another study, time-axis shifts of EEG trials were applied to generate artificial signals for DA purposes (Sakai et al., 2017). Again, the effectiveness of such geometric transformations is debated. Given the non-stationary nature of EEG signals, transformations like shifting may interfere with inherent features, potentially corrupting the data (Kalashami et al., 2022). Thus, while random shifts have been used in DA for EEG, their effectiveness continues to be a subject of ongoing research and discussion.

Another approach to applying DA for EEG involves noise injection through the inclusion of neighboring regions and other manipulations with data. A recent study utilized such DA strategies to address the challenge of small sample sizes. Specifically, translations and vertical flip operations were employed to capture a broader range of temporal information. The data were extracted from 0 to 500 ms after stimulation and then translated. Five time points within the first 200 ms after stimulus onset were randomly selected, and data from 500 ms later were collected. This method increased the dataset size 6-fold. Subsequently, the data were flipped by taking the opposite value of the augmented data, further expanding the dataset to 12 times its original size (Gou et al., 2022).

Similarly, other research efforts explore different data augmentation strategies, including Generative Adversarial Networks (GANs) and Variational Autoencoders (VAEs), to generate synthetic EEG data for training (Habashi et al., 2023; Ibrahim et al., 2024).

GANs, initially introduced for image generation, have also shown promise as a potential DA solution for EEG. GANs and their variants generate artificial data by training two competing networks: a generative network and a discriminative network. The generative network takes random noise from a predefined distribution (e.g., Gaussian) and attempts to create synthetic data that resemble real samples, while the discriminative network is trained to differentiate between real and synthetic data. Through adversarial training, the generative network progressively improves, ultimately producing highly realistic EEG signals (Zhang et al., 2021; Bao et al., 2021; Carrle et al., 2023; Ibrahim et al., 2024).

VAEs offer another approach to generating synthetic EEG data. Like a conventional autoencoder, a VAE consists of an encoder that transforms raw data into a latent representation and a decoder that reconstructs the data from this latent space. To generate new samples, the VAE randomly samples points from the learned latent distribution and passes them through the decoder, which reconstructs them into novel data. Both GANs and VAEs generate new samples indirectly by learning meaningful latent representations of the original data (Bao et al., 2021; Sun and Mou, 2023).

The proposed study contributes to investigation of novel approaches for noise-based DA for EEG classification with emphasis on influence of adding the randomly generated artificial noise and the natural noise created by inclusion of neighboring EEG data segments. This exploration is crucial as it could reveal and compare how artificial and natural noise DA can impact EEG classification performance for various noise DA parameters, for example, with increased sample size, varied offsets, etc. It is especially important for lightweight DNN architectures, designed for Edge Intelligence setups, to ensure efficient EEG processing with minimal computational resources, advancing biologically relevant and computationally efficient DA methods.

For effective application of noise-based DA methods, a clear understanding of the characteristics and sources of these noise types in real-world scenarios is necessary. That is why this study is limited to the simplest noise types that can be intuitively understandable and potentially interpreted. This study aims to provide a thorough understanding of noise-based DA by Gaussian noise injection to mimic random fluctuations evenly distributed across all frequencies in the EEG signal that can be caused by the environment.

The methods of statistical analysis and detrended fluctuation analysis (DFA) are widely used to investigate the fluctuation properties of the measured metrics and calculate the correspondent Hurst exponents (Hurst, 1956). For this purpose, the relatively small DNN [that was described and analyzed in details in Gordienko et al. (2021c)] with components of FCNs and CNNs was considered to classify physical activities (namely, hand manipulations) from the grasp-and-lift (GAL) dataset (Luciw et al., 2014; Kaggle, 2020). The special attention was paid to the analysis of the previous, mid- and post-action segments of the corresponding brain activity to anticipate them before the start of the action.

Finally, this study is targeted on investigation of EEG data collected by BCI to resolve classification problem for some physical activities (namely, hand manipulations) by the relatively simple DNN. The DNN was applied for analysis of preliminary (prior-activity), current (in-activity), and following (post-activity) parts of the relevant brain EEG signals. This problem is very important in the view of complex practical conditions where EEG activity can be disturbed by other physiological activities and, especially, external environmental noise. On the one hand, such disturbances can worsen the classification performance but, on the other hand, in reverse can improve it if it will be used during training as data augmentation (DA) technique.

2 Materials and methods

In this section, several important experimental aspects are explained: the dataset with EEG brain activities for six types of physical activities, structure of the model, metrics, workflow, and data augmentation techniques.

2.1 Dataset

In this study, the open "grasp-and-lift" (GAL) dataset is used that contains information about brain activity of 12 persons (Luciw et al., 2014; Kaggle, 2020): more than 3,900 trials (monitored and measured by the sampling rate of 500 Hz) in 32 channels of the recorded EEG signals. The person tries to perform six types of

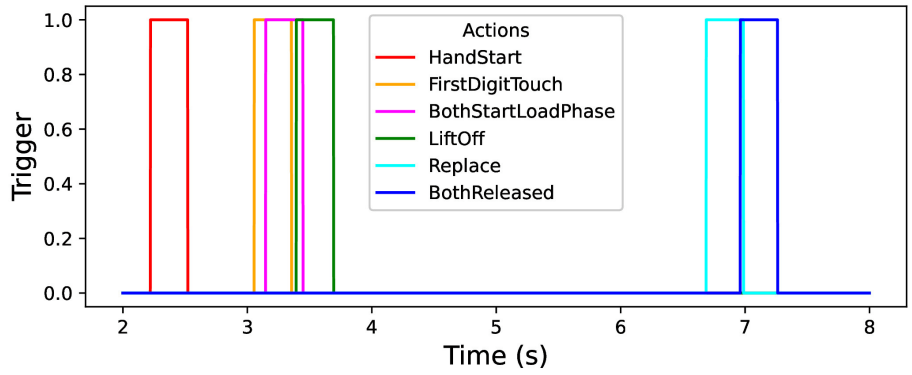

FIGURE 1
Timeline of physical actions: trigger channel vs. time.

physical activities, namely: "HandStart"—moves hand to an object (for example, some gadget), "FirstDigitTouch"—touches the object by finger (for example, press a button), "BothStartLoadPhase"—takes ("grasps") the object by fingers, LiftOff—raises ("lifts") the object by fingers, Replace—returns the object by fingers back, BothReleased–releases fingers. The data from GAL dataset were previously processed in a standard way (Kostiukevych et al., 2021; Gordienko et al., 2021c) with taking into account the correspondent time position of physical actions (actually hand movements here) and their duration (Figure 1).

It should be emphasized that these kinds of physical activity can be naively divided in three parts depending on the feasibility of their classification: the easiest (HandStart), medium (LiftOff, Replace, and BothReleased), and hardest (BothStartLoadPhase and FirstDigitTouch) classification. But BothStartLoadPhase and FirstDigitTouch activities strongly overlap in this experiment and that is why hardly can be recognized as separate activities (this is planned to be fixed by collection of the original data in the same fashion in our future research).

As a part of an explanatory data analysis (EDA), visualizing and analyzing the experimental EEG data from GAL dataset (Gramfort et al., 2013) was performed by means of MNE open-source Python (Gramfort et al., 2013). For example, all EEG data measured by the BCI-sensors with their predefined spatial position can be plotted as subtopomaps of an evoked potential trough timeline (Figure 2).

2.2 Models

From subtopomaps of an evoked potential trough timeline (Figure 2), one can evidently see the complex distribution of EEG sifgnals over scalp. As far as EEG signals interfere with each other due to their electromagnetic nature (Figure 2), the combinations of the data channels can be effectively used for their processing on the basis of FCN, CNN, and RNN like it was demonstrated in our previous studies (Gordienko et al., 2021c; Kostiukevych et al., 2021). In this research, the relatively small "vanilla" DNN (Gordienko et al., 2021c) was used here. The main motive for the usage of CNNs was to use convolution operations inside an EEG time sequence of each EEG channel where all 32 EEG channels were considered to be independent ones. Then, the workflows from 32 EEG channels were combined in fully connected dense layers and then transmitted to the classification layer. The idea is to use 1D convolution operations across all 32 EEG channels for each time step. The mentioned "vanilla" DNN contains three convolutional layers [with 32 filters and kernel (3,1); 64 filters and kernel (5,1); 128 filters and kernel (7,1)] followed by batch normalization and max pooling layers with pool kernel (2,1) with dropout (0.1) and FCN layers.

2.3 Metrics

Several standard metrics were used such as accuracy and loss that were calculated during validation phase of the model learning with checkpointing states for the minimal value and maximal value of loss and accuracy, respectively. In addition, the area under curve (AUC) was measured for receiver operating characteristic (ROC) with their micro and macro versions, and their mean and standard deviation values. It is important because for the given threshold, the accuracy measures the percentage of objects correctly classified, regardless of which class they belong to. As far as AUC is threshold-invariant, AUC can allow us to measure the quality of the models considered here independently from the selected classification threshold. The AUC can consider various possible thresholds and can provide the wider range of the classifier performance. During validation phase, the models with the best accuracy and loss values were saved for the testing phase. For smooth line fitting by locally weighted polynomial regression method (LOWESS) (Cleveland et al., 2017) using weighted least squares, giving more weight to points near the point whose response is being estimated and less weight to points further away.

To investigate the high level of the fluctuations of the measured metrics, that was observed in our previous studies, DFA (detrended fluctuation analysis) was applied here. DFA was proposed to study some memory effects in sequences of the complex biological structures (Peng et al., 1993). During the last decades, it was successfully used in investigation of sequences by means of

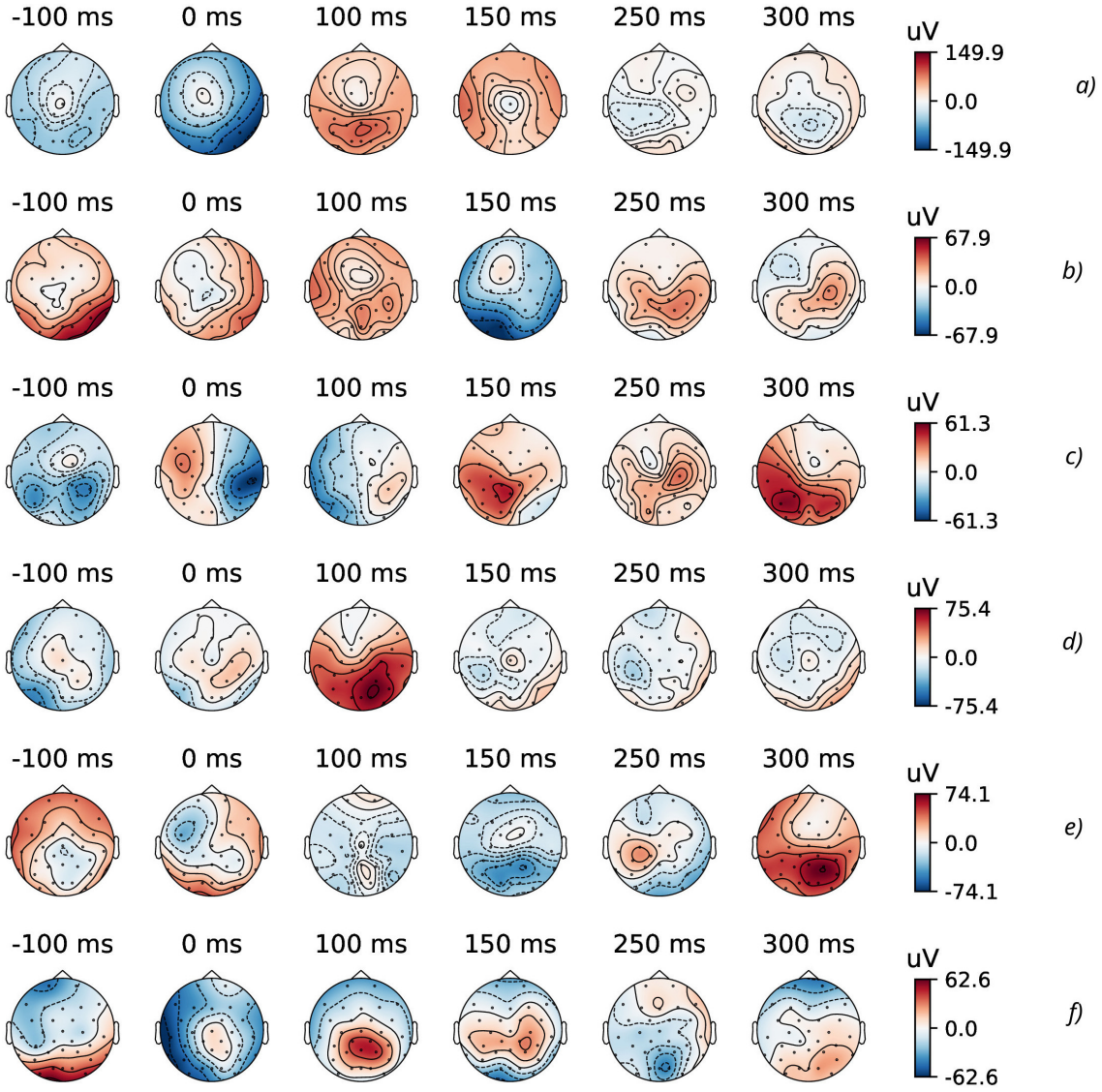

FIGURE 2
Topographic maps of specific time points of evoked data (from 32 EEG channels) for the considered physical actions: **(A)** HandStart, **(B)** FirstDigitTouch, **(C)** BothStartLoadPhase, **(D)** LiftOff, **(E)** Replace, and **(F)** BothReleased actions.

the scaling properties of the fluctuation function $F(n)$ of non-overlapping time intervals of length n. $F(n)$ is expected to scale as n^H, where H is the Hurst exponent (Hurst, 1956).

2.4 Workflow and data augmentation

The training, validation, and testing stages of the whole workflow (Figure 3) for the proposed simple DNN model were applied for the single epoch only, because the main aim was not the highest possible performance, but feasibility analysis of reliable classification under induced noise. The introduced noise was of two kinds: (i) natural NDA by inclusion of noise EEG data from neighboring regions by the different offset values (see details below) and (ii) synthetic NDA by adding the generated Gaussian noise.

During each training iteration, the callbacks were organized to save the best models (with the highest accuracy and lowest loss) for the subsequent testing stage. The number of signal samples (N) in each Input EEG time Sequence (IS) was in the range from 100 to 2,000. These ISs were collected in a random way from the whole timeline of the experimental EEG data.

To mimic the natural NDA, the labels of physical activities for each IS were defined by ground truth (GT) values in the following three locations: at the beginning, medium, and end moment inside IS. These positions were denoted by the offset values, for example, if offset = 0, then label (IS) = GT (beginning); if offset = 0.5, then label (IS) = GT (medium); if offset = 1, then label (IS) = GT (end). Actually, it allowed us to get the GT labeling without neighboring regions without the correspondent physical action (offset = 0.5), GT labeling with some neighboring regions after the correspondent physical action (offset = 0), and GT labeling

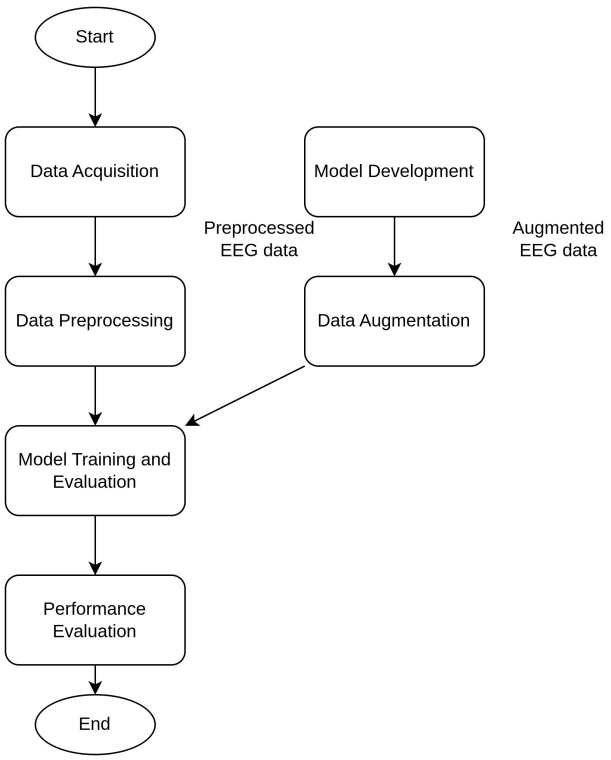

FIGURE 3
Main stages of the whole workflow.

with some neighboring regions before the correspondent physical action (offset = 1). Actually, GT labeling with offset = 0 and offset = 1 provides inclusion of some natural EEG noise after and before the actual physical action. Of course, EEG activity related to the physical action signal (PAS) can take place before and after the actual physical action, but the increase of the number of signal samples (N) can lead to the PAS-to-noise ratio (PAS-NR) decrease and imitate the higher influence of the natural noise.

Under these conditions, the training, validation, and testing stages were independently done in an iterative way for 20 values of N with the step of 100. Finally, N values were obtained in the range from 100 to 2,000 that resulted in 20 iterations of training, validation, and testing phases. For each instance of N, the dataset was distributed in approximate proportion of 82% ($\approx$ 300 examples)/9% ($\approx$ 300 examples)/9% ($\approx$ 300 examples) for training/validation/testing sets, respectively. As a result, 20 trained models were obtained for each iteration (one model per each input sequence with N values); then, 20 sets of metrics, including AUC, and its micro and macro versions, were calculated and plots of these metrics vs. N were constructed (see below).

3 Experimental

3.1 DNN training/validation/testing stages

During EDA stage, the GAL data were preprocessed in the standard way described in details in our previous studies (Gordienko et al., 2021c; Kostiukevych et al., 2021). In Figure 2, the topographic maps of specific time points of evoked data (from 32 EEG channels) for some physical actions (FirstDigitTouch and LiftOff) are shown. Here, the most characteristic parts of EEG signals and their spatial distributions over a scalp are shown for the better understanding the very complex details of EEG brain activity.

As it was demonstrated before (Gordienko et al., 2021c; Kostiukevych et al., 2021), some physical actions (such as HandStart) are followed by very pronounced patterns with the local minimums and maximums, while many others (such as BothStartLoadPhase, LiftOff, Replace) are hardly recognizable by unique patterns. In addition, it should be noted for several actions (such as HandStart, and especially Replace and BothReleased) that significant brain activity is started some milliseconds before the correspondent movements, but it is quite dubious to make the same statement about other actions in the view of the unrecognizable different patterns. The main idea of this study is based on our previous studies (Gordienko et al., 2021c; Kostiukevych et al., 2021) and consists in the hypothesis that relatively small DNNs even can classify the EEG patterns of the currently undergoing physical actions in the presence of some induced noise even, but the additional aspects include the investigation of impact induced by natural and synthetic kinds of noise.

At testing stage, AUC values were measured (dotted lines in Figure 4) and their smoothed fits were obtained by LOWESS-method (solid lines in Figure 4). For various actions and offsets, AUC values (Figure 4) demonstrate the high intensity of fluctuations with increase of N that can be explained by the influence of the non-relevant (to the current physical activity) regions of the increased time sequence under investigation (imitating the natural noise addition).

3.2 Noise data augmentation

The effect of the natural noise addition (by offsets 0 and 1 with various levels by increasing N) can be observed by calculation of the correspondent macro AUC (Figure 5A) and micro AUC (Figure 5B) values. It is evident that offsets 0 and 1 lead to the lower micro and macro AUC values in comparison with the GT labeling by offset = 0.5, and the AUC decrease is higher for the higher N values.

To investigate stability of the results obtained, the additional artificial "synthetic" NDA as the values generated with mean = 0 and different standard deviations σ_{synth} (such as 0.001, 0.01, 0.1, and 0.2) was applied to the original normalized data (Figure 6).

Calculation of maximal (Figure 7), mean (Figure 8), minimal, and range (Figure 9), and standard deviation (Figure 10) of AUC values was performed for the different offset values and synthetic noise σ_{synth} values.

From the results obtained, the similar tendency can be observed for all actions: maximal AUC values (Figure 7) are higher for offset = 0.5 than for other offset values (0 and 1) and significantly bigger than standard deviation values. The maximal AUC values for offset = 0 are slightly higher than for offset = 1, but these differences cannot be considered as statistically significant and they are in the limits of standard deviation values.

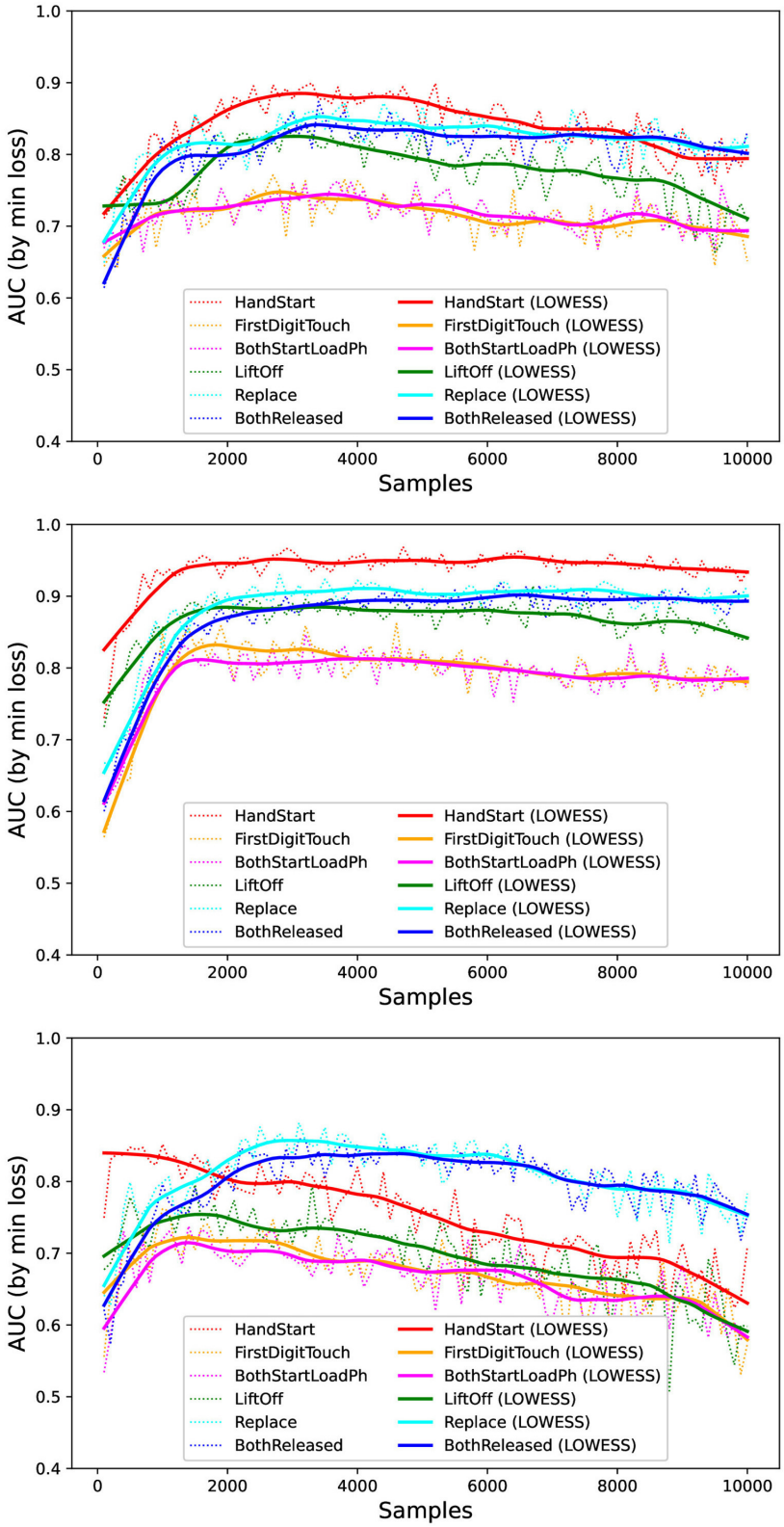

FIGURE 4
Comparison of AUC values as a function of the number of samples for the different physical actions (dotted lines) and their smoothed fits by LOWESS-method (solid lines) for the offsets imitating the natural noise addition: **(A)** 0, **(B)** 0.5, and **(C)** 1.

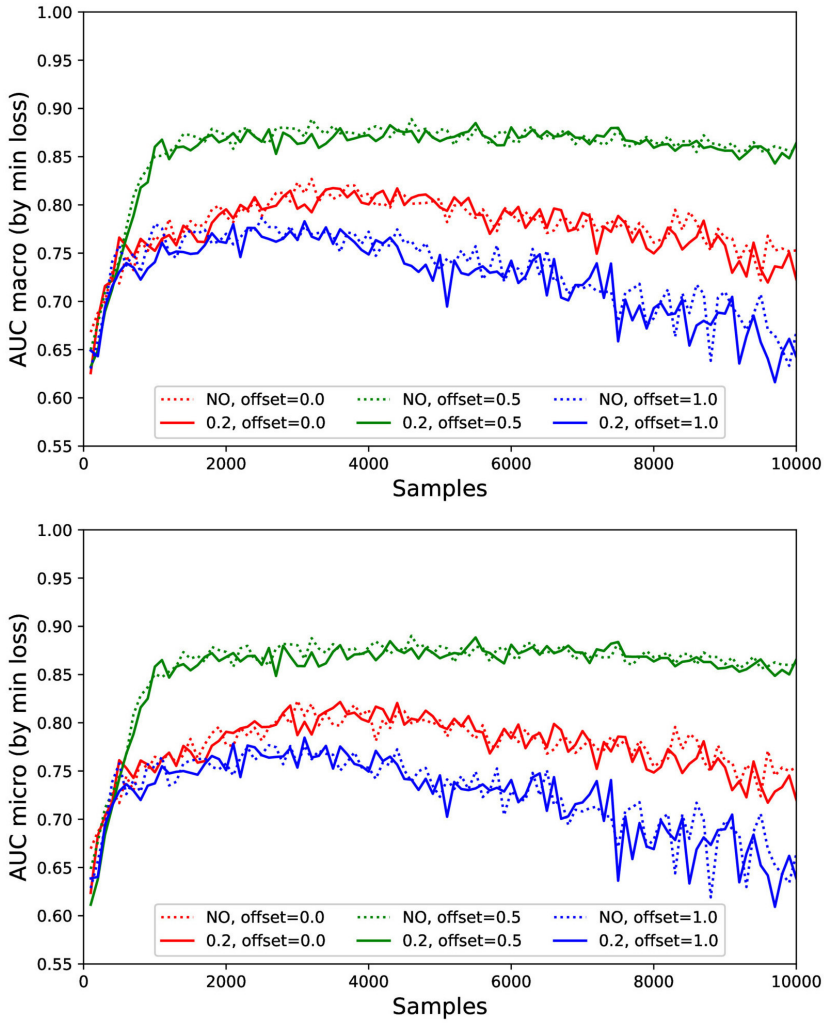

FIGURE 5
Comparison of macro **(A)** and micro **(B)** AUC values as a function of the number of samples for the different offset values (colors) without the synthetic noise (dotted lines) and with the synthetic noise $\sigma_{synth} = 0.2$ (solid lines).

The mean AUC values (Figure 8) are even more higher for offset = 0.5 than for other offset values (0 and 1) and significantly bigger than standard deviation values also. The mean AUC values for offset = 0 are even more higher than for offset = 1, but again these differences cannot be considered as statistically significant and they are in the limits of standard deviation values.

On the contrary, the range AUC values (Figure 9), which are differences between maximal and minimal AUC values, are lower for offset = 0.5 than for other offset values (0 and 1), and these differences are significantly bigger than standard deviation values. Similarly, the range AUC values for offset = 0 are lower than for offset = 1, and these differences are also statistically significant and beyond the limits of standard deviation values.

As it was seen from the previous Figure 9, the standard deviation AUC values (Figure 9) are significantly lower for offset = 0.5 than for other offset values (0 and 1). Similarly, the standard deviation AUC values for offset = 0 are significantly lower than for offset = 1.

To analyze the metrics for the steady region for N in the range from 1,000 to 10,000 samples, AUC (mean ± stdev) values were calculated (Table 2) along with the other metrics such as maximal AUC values and ranges (differences between maximal and minimal AUC values) (Table 3). The bold font in Table 3 denotes the highest values for the same level of σ_{synth}, and the italic font does the lowest ones. HandStart action demonstrates the highest AUC values, and FirstDigitTouch and BothStartLoadPhase demonstrates the lowest ones. The important aspect is that for different actions, implication of the natural noise (presented by offsets) leads to the different consequences. For example, Replace and BothReleased actions have the lowest AUC decrease and highest AUC values for offset 0. As a possible explanation for these results, Replace and BothReleased actions can have the higher PAS-NR (in comparison with other actions) for offset 0 because of the more EEG activity for "after" (post-process) part of the relevant sampling. At the same time, mediocre performance for FirstDigitTouch and BothStartLoadPhase can be explained by their

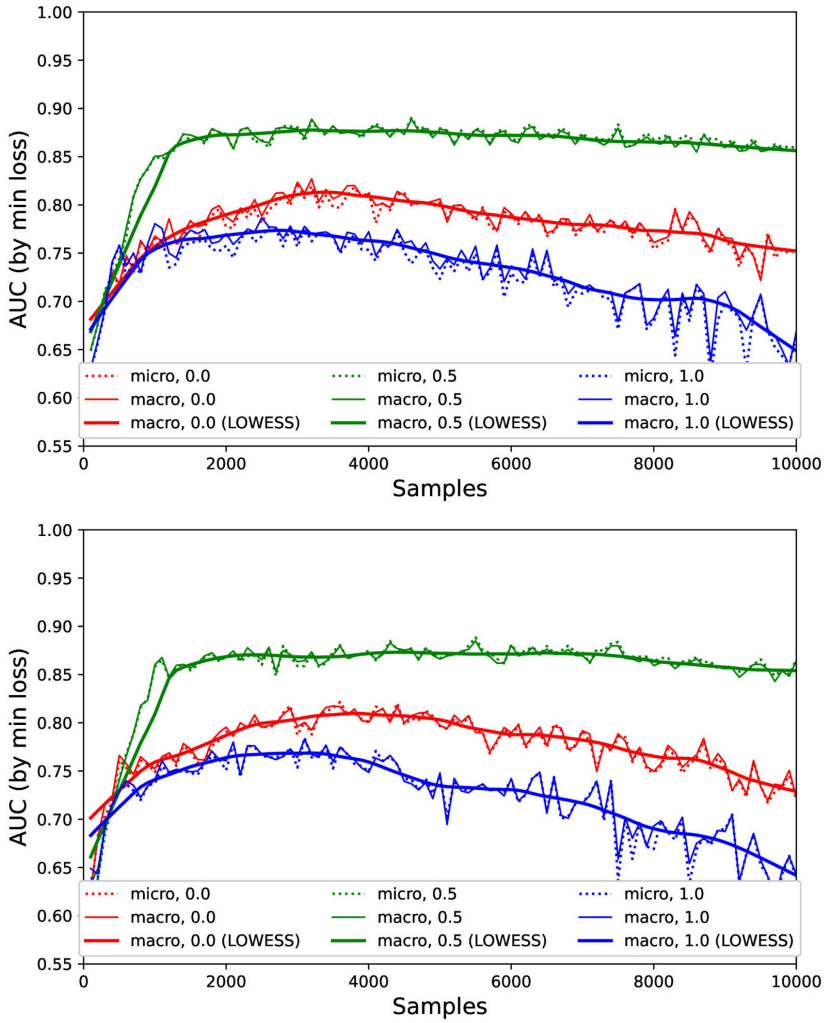

FIGURE 6
Comparison AUC values as a function of the number of samples for the different offset values (colors) without the synthetic noise **(A)** and with the synthetic noise $\sigma_{synth} = 0.2$ **(B)**.

coincidence in time (see Figure 1) that is the real drawback of the GAL dataset used.

3.3 Detrended fluctuation analysis

Detrended Fluctuation Analysis (DFA) (Peng et al., 1993, 1995; Bianchi, 2020) was applied to analyze fluctuations of AUC values and the correspondent Hurst exponent values after eliminating the temporal trend (Figure 13). For the time sequences, the Hurst exponent value (H) can indicate whether a process is persistent or anti-persistent, but here the Hurst exponent is used for the other purpose, namely, for quantitative estimation of fluctuations svariability.

In general, the Hurst exponent, H, is intrinsically related to the fractal dimension, which quantifies the "roughness" or variability of a time series (Hurst, 1956). Specifically, the value of H provides insight into the degree of smoothness in the data: Sequences that exhibit greater variability and are more irregular (i.e., more jagged) are associated with lower values of H, approaching zero. Conversely, smoother sequences yield values of H closer to one. This relationship between H and the fractal dimension is instrumental in characterizing the long-term dependence and self-similarity in stochastic processes. The Hurst exponent can also characterize a process (Bianchi, 2020) depending on the range of the measured values: H in the range [0.0, 0.5) corresponds to a very noisy process; the value $H = 0.5$ relates to uncorrelated process; H in the range (0.5, 1.0] relates to persistency where long-range correlations and relatively little noise can be observed; and $H > 1.0$ characterizes a non-stationary process with stronger long-range correlations. The correspondent open-source Python package "fathon" was used for DFA and further analysis of metric fluctuations (Bianchi, 2020).

4 Discussion

The results obtained show that different actions can be classified with the quite different reliability. The different kinds of physical activity take the different level of physical activation and the

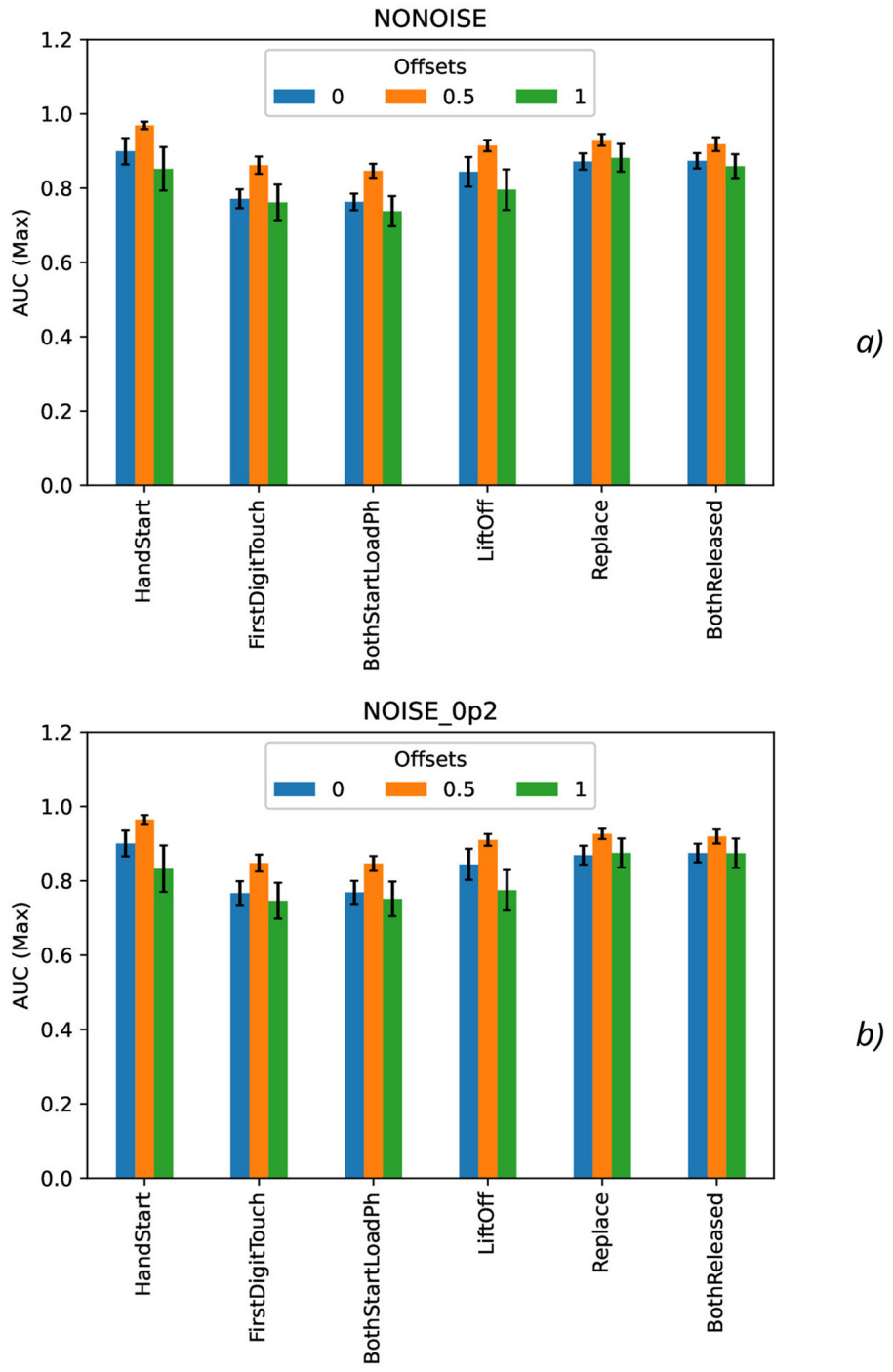

FIGURE 7
Comparison of maximal AUC values as a function of the number of samples for the different offset values (colors) without the synthetic noise **(A)** and with the synthetic noise $\sigma_{synth} = 0.2$ **(B)**. The error bars denote the standard deviation values.

correspondent EEG activity, for example, HandStart (fingers, palm, forearm, and shoulder are activated) includes involvement of more limbs than LiftOff (fingers, palm, and forearm) and Replace (fingers, palm, and forearm), and even more than BothReleased (several fingers and palm), BothStartLoadPhase (two fingers), and FirstDigitTouch (one finger). It should be noted that the observed performance of classification demonstrates some correlation where the higher performance by AUC (Figure 4) corresponds to the more pronounced physical activity in the following order from the highest AUC values to the lowest ones: HandStart → LiftOff → Replace → BothReleased → BothStartLoadPhase → FirstDigitTouch (Figure 4).

In addition, for N values in the range [100, 1,500], HandStart action demonstrates the asymmetric behavior with regard to the

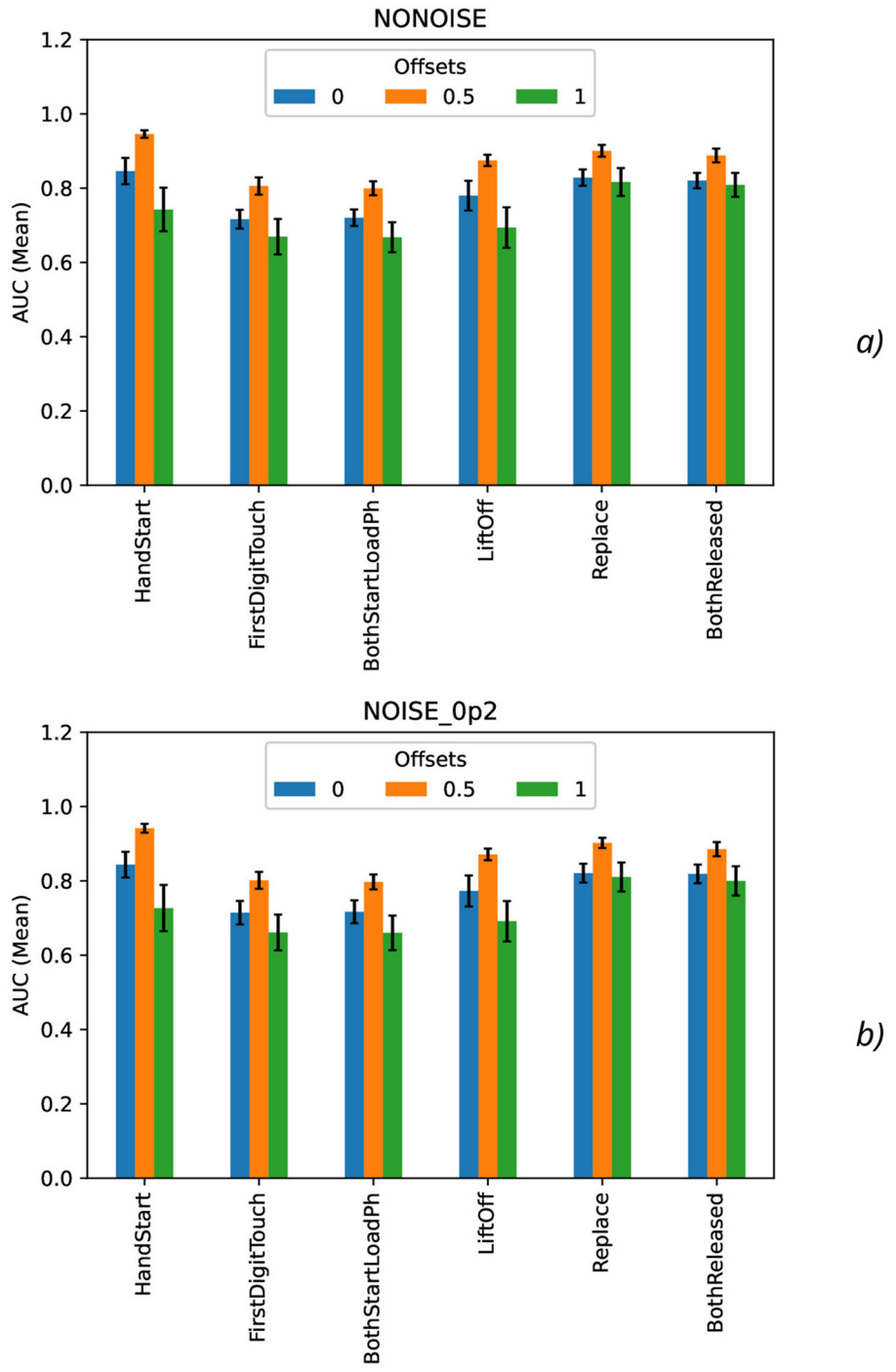

FIGURE 8
Comparison of mean AUC values as a function of the number of samples for the different offset values (colors) without the synthetic noise **(A)** and with the synthetic noise $\sigma_{synth} = 0.2$ **(B)**. The error bars denote the standard deviation values.

offset values 0 and 1 (Figure 4C), namely: AUC values grows much faster with N for offset = 1 (the dotted and smoothed red lines in Figure 4A) than for offset = 0 (the dotted and smoothed red lines in Figure 4C). It means that the related brain activity measured as "before" (pre-process) part of the correspondent EEG time sequences is more pronounced than "after" (post-process) part. As a result, this phenomenon allows us to classify HandStart before the actual physical action even as it was assumed in our previous studies (Gordienko et al., 2021c,b; Kostiukevych et al., 2021). It is in contrary to the kinds of activities that demonstrate similar behavior: similar growth of AUC values for N values in the range [100, 1,500] the offset values 0 and 1, and decay for $N > 1500$.

In general, AUC values are higher for the offset value 0.5 (in comparison with the offset values 0 and 1), steadily for N values in

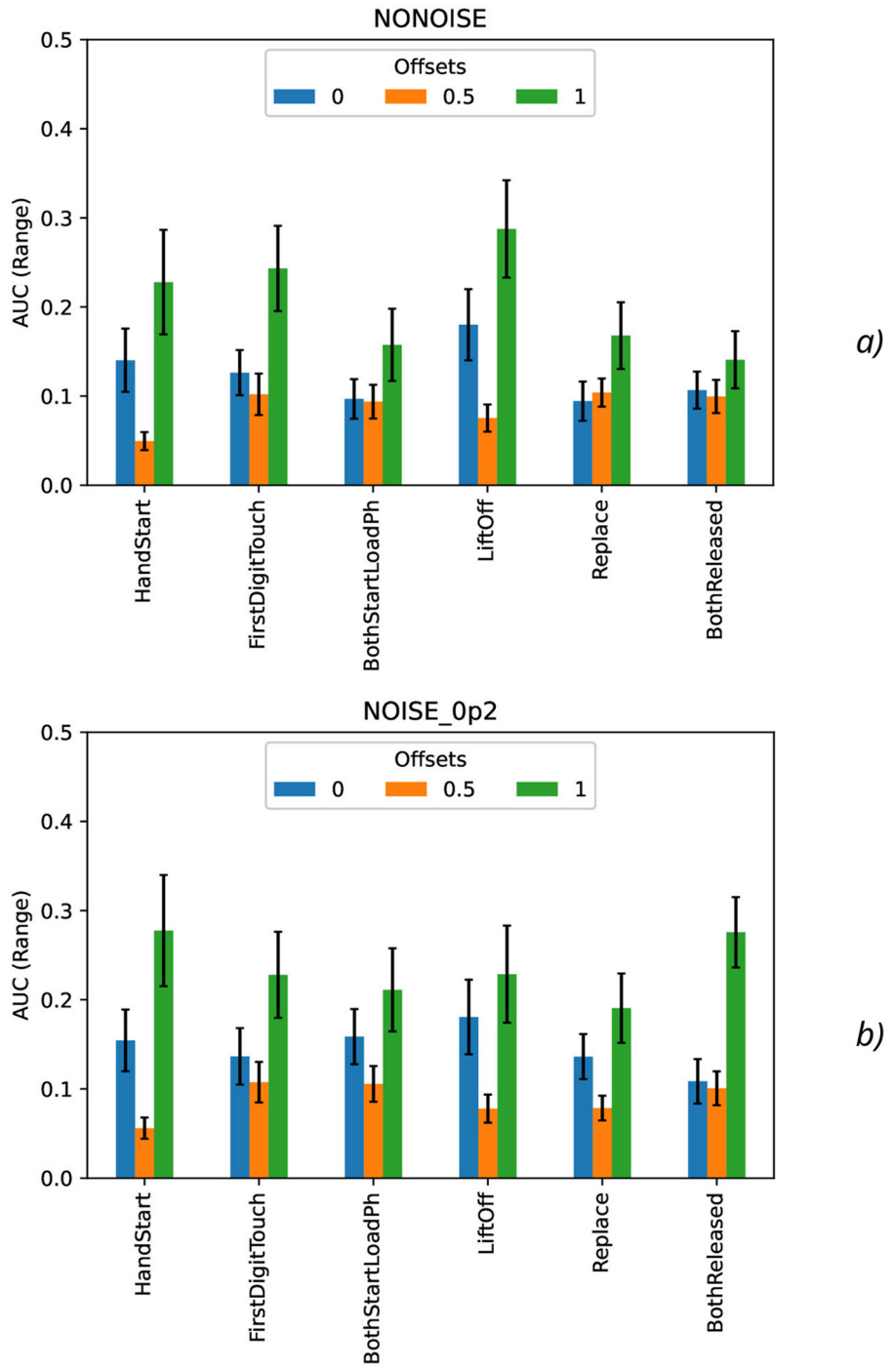

FIGURE 9
Comparison of range AUC values as a function of the number of samples for the different offset values (colors) without the synthetic noise **(A)** and with the synthetic noise $\sigma_{synth} = 0.2$ **(B)**. The error bars denote the standard deviation values.

the range [100, 1,500] and nearly constant for $N > 1,500$ for all kinds of activities (Figure 4B) as it was also shown in our previous studies (Gordienko et al., 2021c; Kostiukevych et al., 2021). That is why labeling by the offset of 0.5 seems to be the more significant for the classification problem. It should be noted that the uncertainty of AUC values estimated as their standard deviations decreases with an increase of N up to $N = 2,000$ for offset = 0.5 and up to $N = 3,000$ for offset = 0 and offset = 1. It should be noted the visually very pronounced fluctuations of all these metrics with N can be explained by the influence of the non-relevant (to the current physical activity) regions of the increased time sequence under investigation.

It should be noted that application of the natural NDA by increasing N leads to the better micro and macro AUC values for

TABLE 2 AUC (mean ± stdev) (Figures 8, 10) values for the steady region (Figure 4) from 1,000 to 10,000 samples.

	offset = 0			
Noise (σ_{synth})	0	0.01	0.1	0.2
HandStart	**0.845** ± 0.036	**0.845** ± 0.033	**0.850** ± 0.034	**0.844** ± 0.035
FirstDigitTouch	*0.716* ± 0.025	*0.719* ± 0.029	*0.719* ± 0.033	*0.714* ± 0.032
BothStartLoadPhase	*0.720* ± 0.022	*0.720* ± 0.026	*0.719* ± 0.029	*0.717* ± 0.031
LiftOff	0.780 ± 0.040	0.781 ± 0.038	0.778 ± 0.044	0.773 ± 0.042
Replace	0.828 ± 0.022	0.824 ± 0.023	0.827 ± 0.019	0.821 ± 0.025
BothReleased	0.820 ± 0.021	0.820 ± 0.022	0.819 ± 0.026	0.819 ± 0.025
	offset = 0.5			
Noise (σ_{synth})	0	0.01	0.1	0.2
HandStart	**0.946** ± 0.011	**0.945** ± 0.011	**0.945** ± 0.013	**0.942** ± 0.012
FirstDigitTouch	*0.806* ± 0.023	*0.804* ± 0.023	*0.802* ± 0.022	*0.801* ± 0.023
BothStartLoadPhase	*0.800* ± 0.019	*0.801* ± 0.019	*0.801* ± 0.019	*0.797* ± 0.020
LiftOff	0.875 ± 0.015	0.875 ± 0.016	0.878 ± 0.016	0.871 ± 0.016
Replace	0.900 ± 0.016	0.902 ± 0.014	0.900 ± 0.016	0.902 ± 0.014
BothReleased	0.888 ± 0.019	0.888 ± 0.018	0.886 ± 0.016	0.885 ± 0.019
	offset = 1			
Noise (σ_{synth})	0	0.01	0.1	0.2
HandStart	0.743 ± 0.059	0.741 ± 0.062	0.736 ± 0.062	0.727 ± 0.062
FirstDigitTouch	*0.669* ± 0.048	*0.673* ± 0.042	*0.671* ± 0.046	*0.661* ± 0.048
BothStartLoadPhase	*0.668* ± 0.041	*0.668* ± 0.043	*0.670* ± 0.040	*0.660* ± 0.047
LiftOff	0.694 ± 0.055	0.700 ± 0.051	0.698 ± 0.060	0.691 ± 0.054
Replace	**0.816** ± 0.037	**0.822** ± 0.037	**0.813** ± 0.038	**0.810** ± 0.039
BothReleased	**0.809** ± 0.032	**0.806** ± 0.035	**0.805** ± 0.032	**0.800** ± 0.039

The bold font denotes the highest values for the same level of the noise, and the italic font does the lowest ones.

N values beyond the physical action duration which is $\sim$ 0.3 s (that is equal to $\sim$ N=150 samples, see Figure 1) and up to ~3 s (N = 1,500) for offset = 0.5. For example, micro and macro AUC values are equal to $\sim$ 0.65 for sampling length N = 200 samples (that corresponds to $\sim$ 0.4 s), and increase of N up to N = 1,500 leads to the better micro and macro AUC values equal to $\sim$ 0.87 (Figures 5, 6). But to the moment it is unclear whether this improvement caused by the availability of EEG signals relevant to the physical action beyond action itself or by natural NDA. The additional interesting aspect is that micro and macro AUC values are much lower for the offset 0 and 1 (in comparison with offset = 0.5), but AUC values are improving with N (Figures 5, 6) up to ~6–7 s (N = 3,000) for offset = 0 and offset = 1. It means that heavy bias of labeling is not useful because it leads to distortion of PAS-NR due to the lower signal and higher noise values. Application of the synthetic NDA (Figures 5, 6) in the wide range of noise levels (σ_{synth} from 0.001 up to 0.2) demonstrates the general stability of the DNN used for classification of all activities with the similar micro and macro AUC values in the limits of their fluctuations.

AUC fluctuations caused by the added synthetic NDA, shown in Figures 11, 12, are not significant in comparison with AUC fluctuations without synthetic NDA due to increase of sampling size N.

To characterize AUC fluctuations (Figures 11, 12) with regard to the added synthetic NDA, the DFA was applied and analyzed for original (non-added noise) EEG time sequences (Figure 13A) and ones with NDA (Figure 13B). From DFA point of view, some very intensive actions (such as HandStart and LiftOff) demonstrate the very high stability to noise data augmentation with negligible changes of fluctuation amplitudes measured like differences (Figure 13) between the correspondent AUC fluctuation values for original (without added noise) (Figure 13A) and noise-augmented EEG time sequences (Figure 13B).

For FirstDigitTouch, BothStartLoadPhase, and Replace activities, the synthetic NDA actually lead to decrease of the AUC fluctuations (Figure 13C) with slow decay of this improvement with increase of N (due to above mentioned non-relevant noisy neighboring regions, i.e., the natural NDA). In contrary, for HandStart and BothReleased activities, the synthetic NDA actually lead to increase of the AUC fluctuations (Figure 13C) with slow decay also. Liftoff activity does not demonstrate any significant changes.

The measurements of the Hurst exponent values H_{full} (the full range of window scales with $n < 10,000$, time < 20 s), H_{low} (the low window scales with $n < 1,000$, time < 2 s), and H_{high} (the bigger window scales with $n > 1,000$, time > 2 s) were performed

TABLE 3 Maximal and range AUC values for the steady region from 1,000 to 10,000 samples (Figures 4, 11, 12).

	offset = 0							
	AUC (max)				AUC (range)			
Noise (σ_{synth})	0	0.01	0.1	0.2	0	0.01	0.1	0.2
HandStart	**0.899**	**0.909**	**0.908**	**0.901**	0.140	0.146	0.150	0.154
FirstDigitTouch	0.771	0.787	0.795	0.767	0.126	0.131	0.143	0.137
BothStartLoadPh	0.763	0.767	0.781	0.769	0.097	0.115	0.126	0.159
LiftOff	0.844	0.861	0.848	0.844	**0.180**	**0.186**	**0.245**	**0.181**
Replace	0.872	0.873	0.867	0.869	0.094	0.101	0.094	0.136
BothReleased	0.874	0.876	0.871	0.875	0.107	0.112	0.132	0.109
	offset = 0.5							
	AUC (max)				AUC (range)			
Noise (σ_{synth})	0	0.01	0.1	0.2	0	0.01	0.1	0.2
HandStart	**0.969**	**0.967**	**0.972**	**0.965**	0.050	0.054	0.058	0.056
FirstDigitTouch	0.862	0.855	0.850	0.848	**0.102**	**0.122**	**0.100**	**0.108**
BothStartLoadPh	0.847	0.842	0.839	0.847	0.094	0.082	0.087	**0.106**
LiftOff	0.915	0.913	0.916	0.910	0.075	0.076	0.086	0.078
Replace	0.930	0.932	0.932	0.926	**0.104**	0.080	0.091	0.079
BothReleased	0.918	0.914	0.914	0.919	0.100	0.092	0.076	0.101
	offset = 1							
	AUC (max)				AUC (range)			
Noise (σ_{synth})	0	0.01	0.1	0.2	0	0.01	0.1	0.2
HandStart	0.852	0.842	0.841	0.833	0.228	0.238	0.249	**0.278**
FirstDigitTouch	0.762	0.758	0.749	0.747	0.243	0.183	0.193	0.228
BothStartLoadPh	0.738	0.749	0.740	0.751	0.158	0.221	0.223	0.211
LiftOff	0.796	0.809	0.791	0.775	**0.288**	**0.289**	**0.261**	0.229
Replace	**0.882**	**0.886**	**0.883**	**0.875**	0.168	0.158	0.167	0.191
BothReleased	0.859	0.870	0.853	0.874	0.141	0.168	0.143	**0.276**

The bold font denotes the highest values for the same level of the noise, and the italic font does the lowest ones.

for various actions and levels (standard deviations $\sigma_{synth} = 0$) of the synthetic noise (Table 4). H values are rounded to 2 decimal digits in Table 4 because the bigger number of significant digits seems to be statistically insignificant.

The general tendency is that for the low window scales ($n < 1,000$, time < 2 s), H_{low} values are higher in comparison with H_{high} values for the bigger window scales ($n > 1,000$, time > 2 s) that can be seen from the slope of curves in Figure 13 and Table 4. It means that EEG fragments with the duration of scale $n < 1,000$ (time < 2 s) demonstrate the scaling behavior of the higher complexity than the fragments $n > 1,000$ (time > 2 s), i.e., $H_{low} > H_{high}$ (Table 4). It should be noted that step-like increases in the middle and in the end of all curves in Figure 13 can be explained by overlapping with the next portion of PAS data related to the other trial of recorded physical activities which are contained in the whole timeline of the experimental EEG data.

Despite the previously mentioned findings, the study has several limitations that should be taken into account in future works. First, the use of a single epoch for training (which was observed to be enough for saturation of the training process of the relatively small DNN with the quite small capacity) may limit the model's overall performance. In future research, the multiple training epochs for the more complex DNN should be employed to potentially improve model performance and generalization with attention to the impact of hyperparameter tuning (e.g., learning rate, batch size) on model performance and convergence. Second, the focus on feasibility analysis rather than maximizing performance might have constrained the exploration of more complex DNN architectures. In the next stage of the investigation, the more complex DNN architectures (such as deeper CNNs, recurrent neural networks, and transformer models) should be performed with a more comprehensive hyperparameter search to optimize model performance to potentially achieve higher classification accuracy. Third, the study relies mainly on the GAL dataset, which may not fully capture the variability and complexity of real–world EEG signals. In the extended version, this study should include investigation of the model's performance on other publicly available EEG datasets with different characteristics in

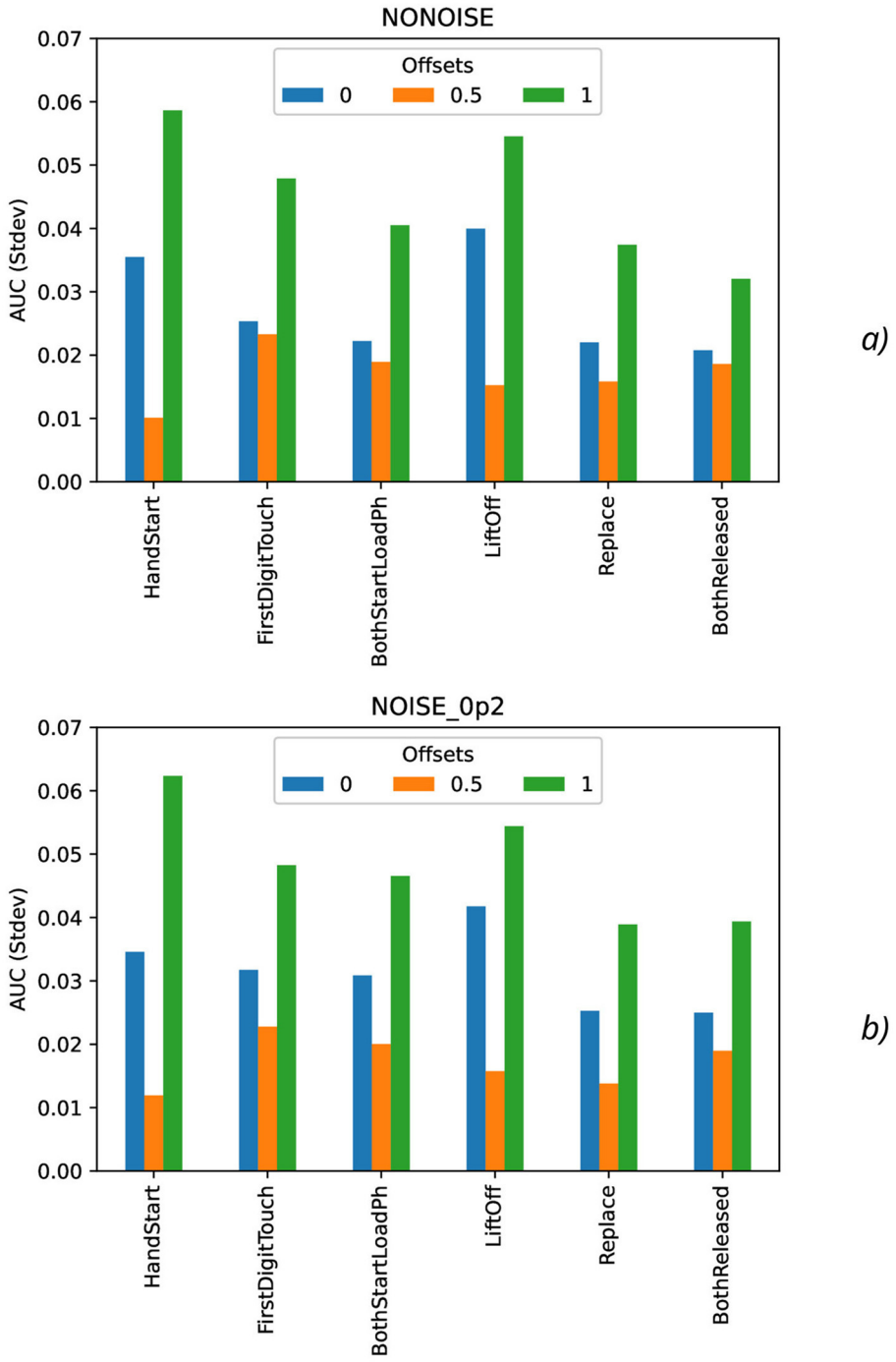

FIGURE 10
Comparison of standard deviation AUC values as a function of the number of samples for the different offset values (colors) without the synthetic noise **(A)** and with the synthetic noise $\sigma_{synth} = 0.2$ **(B)**.

the other controlled and realistic environment to improve the generalizability of the findings. Fourth, the analysis is limited to a specific set of NDA techniques, and the impact of other noise sources or more sophisticated DA methods should be also explored. Moreover, the impact of other NDA techniques (mentioned in the introductory part of the study, such as generative training and others) will be necessary to improve model robustness and explore the impact of physiological noise (e.g., muscle artifacts, eye blinks) and environmental noise on model performance. In addition, assessing the additional metrics particularly with regard to Structural Similarity Index (SSIM) and Peak Signal-to-Noise Ratio (PSNR) in future research stages will be highly intriguing and valuable. SSIM could provide insights into the structural similarity between original and noise-augmented EEG

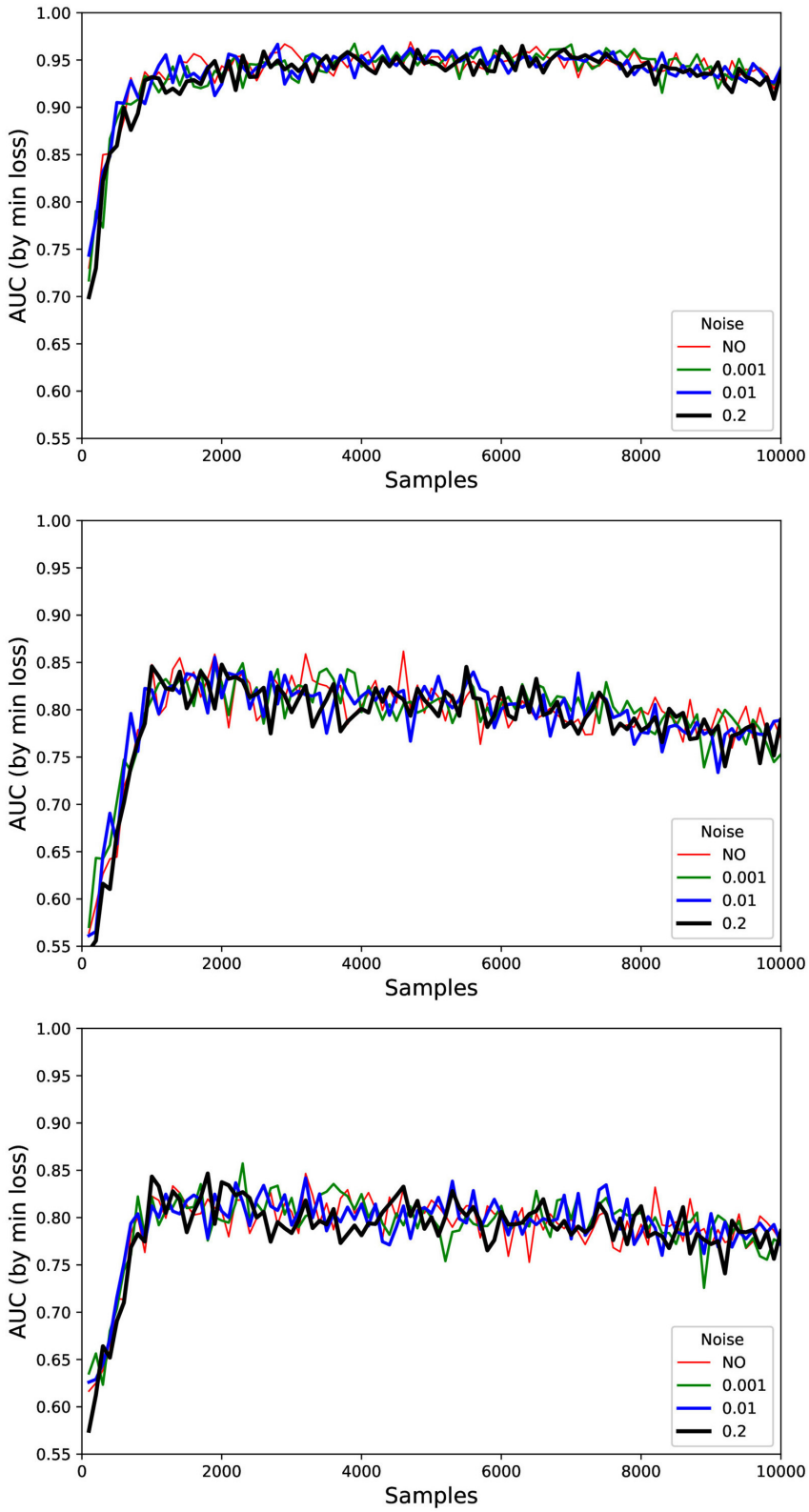

FIGURE 11
Noise influence on AUC values for offset = 0.5: **(A)** HandStart, **(B)** FirstDigitTouch, and **(C)** BothStartLoadPhase.

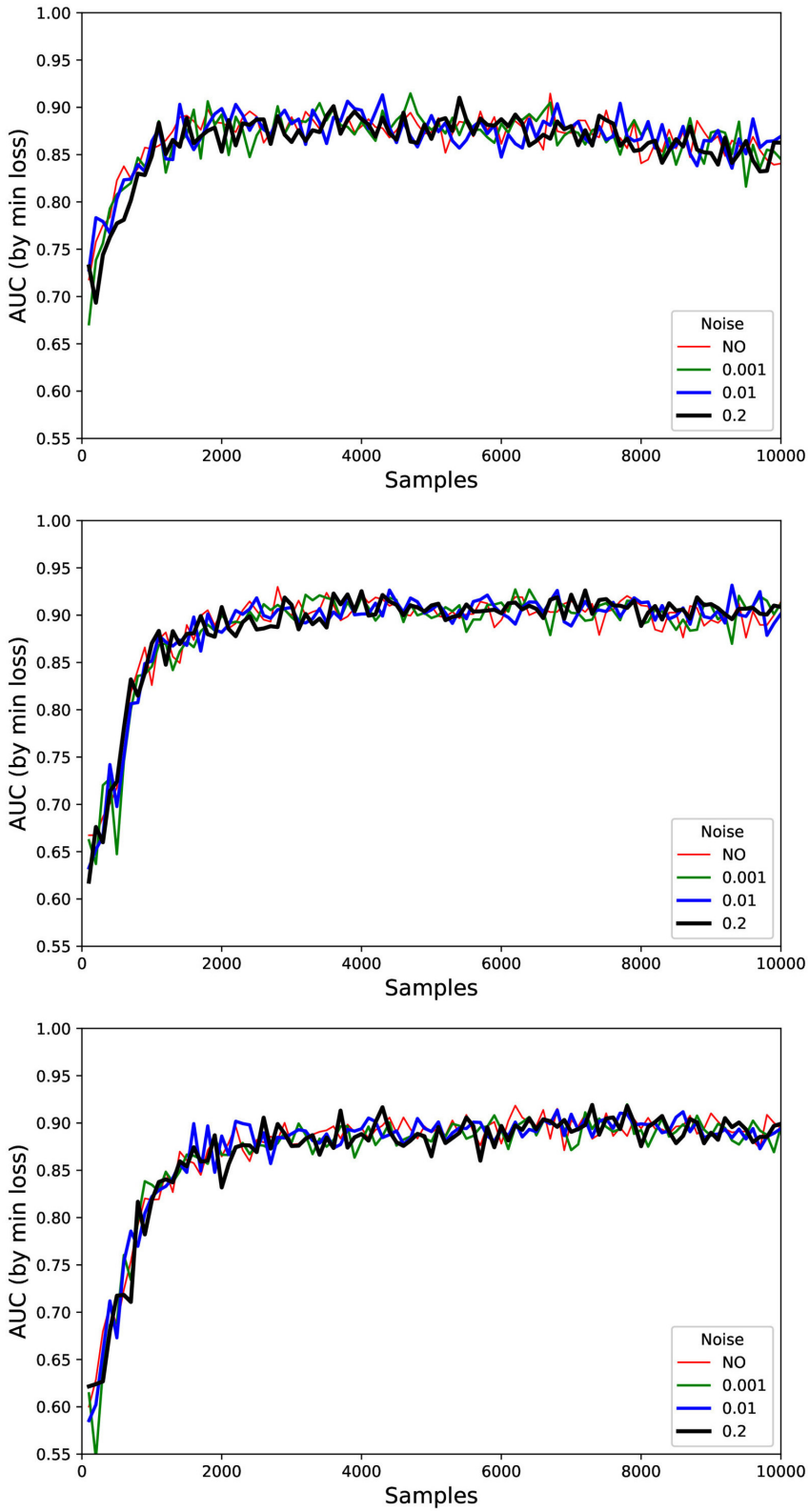

FIGURE 12
Noise influence on AUC values for offset=0.5 (continued from Figure 11): **(A)** LiftOff, **(B)** replace, **(C)** BothReleased.

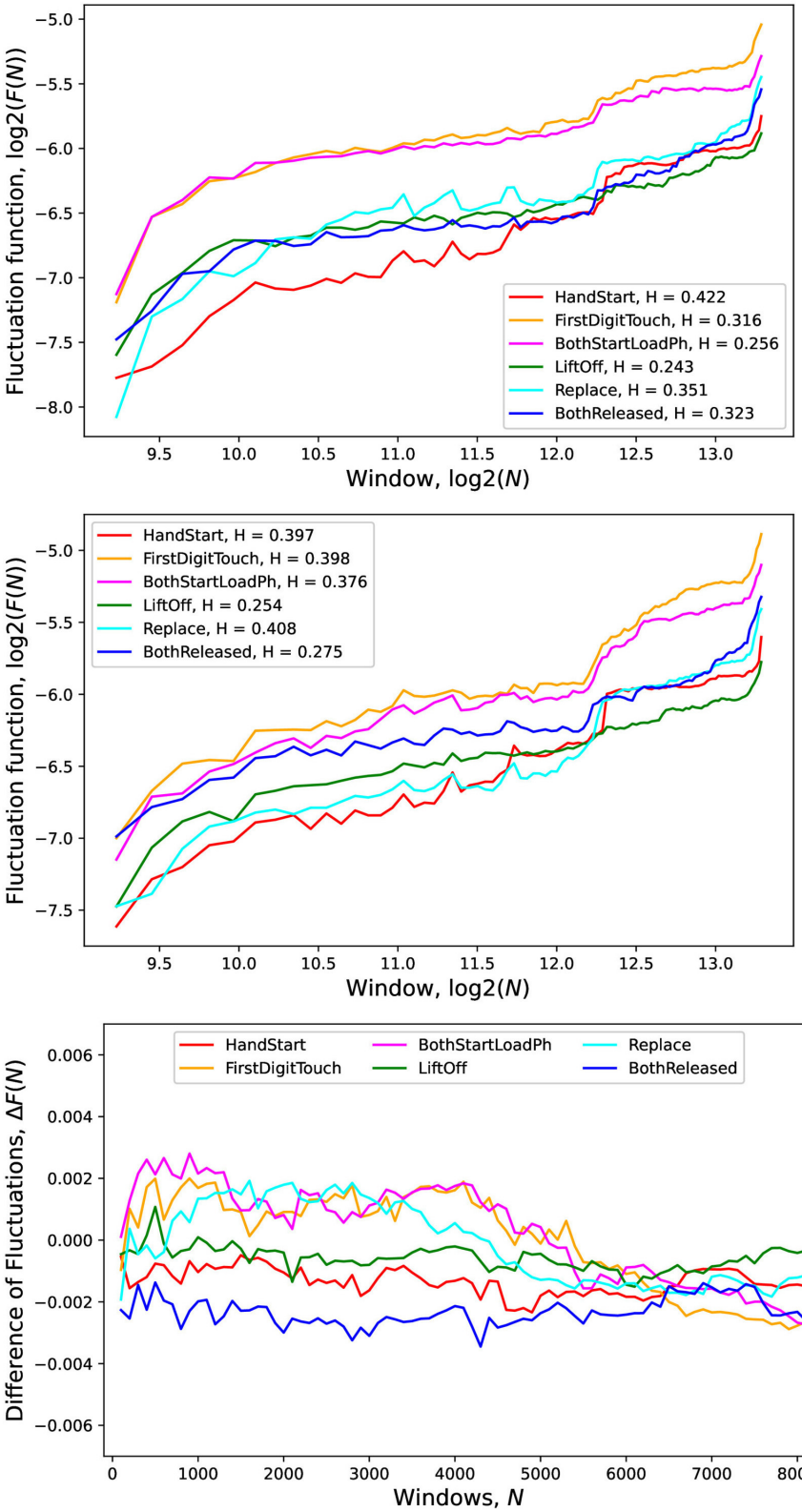

FIGURE 13
Fluctuations vs. the number of samples (N) in the input for various actions and levels (standard deviations) of the synthetic noise: **(A)** $\sigma_{synth} = 0$ (no noise), **(B)** $\sigma_{synth} = 0.2$, **(C)** difference of fluctuations from previous regimes without and with noise. The legends contain Hurst exponent values.

TABLE 4 Hurst exponents H_{full}, H_{low}, and H_{high} (rounded to 2 decimal digits) for various actions and levels (by standard deviations σ_{synth}) of the synthetic noise.

Hurst exponent	$\sigma_{synth} = 0$ (no noise)			$\sigma_{synth} = 0.2$ (noise)		
	H_{full}	H_{low}	H_{high}	H_{full}	H_{low}	H_{high}
HandStart	0.42	0.78	0.43	0.40	0.67	0.41
FirstDigitTouch	0.32	0.92	0.29	0.40	0.64	0.40
BothStartLoadPhase	0.26	0.92	0.23	0.38	0.67	0.37
LiftOff	0.24	0.87	0.21	0.25	0.67	0.22
Replace	0.35	1.07	0.28	0.41	0.72	0.42
BothReleased	0.32	0.77	0.30	0.28	0.50	0.24

signals, helping evaluate how natural noise preserves critical signal features. Meanwhile, PSNR could serve as a measure of distortion, indicating how much the augmented signals deviate from the original ones, which is crucial for maintaining signal integrity in classification tasks.

5 Conclusion

This research contributes to the field of EEG-based BCI by investigating the impact of different types of noise on the classification of physical activities by the following main novel aspects and contributions: systematic investigation of natural noise, quantitative analysis of noise impact, and analysis of offset effects. The study introduces the concept of "natural noise" by considering EEG data from neighboring regions, simulating real-world scenarios with varying levels of background EEG activity. The researchers utilize metrics such as AUC and DFA to quantitatively assess the impact of both natural and synthetic noise on classification performance, providing valuable insights into the model's robustness. By analyzing the impact of different label offsets (0, 0.5, 1), the study provides valuable insights into the optimal time window for EEG signal analysis and classification. These novel aspects contribute to a better understanding of the challenges and limitations of EEG-based BCI systems in real-world scenarios and provide valuable guidance for future research in this area.

The following key aspects of the methodology contribute to achieving the goal: DA by natural NDA and synthetic NDA, varying NDA parameters including input sequence length, and thorough performance evaluation including DFA Analysis. The introduction of both natural and synthetic noise during DA helps the model to become more robust and generalize better to real-world scenarios with varying levels of noise. As to the natural NDA by including EEG data from neighboring regions, the model learns to handle variations in EEG signals due to temporal shifts and contextual influences. As to the synthetic NDA, adding Gaussian noise increases the model's tolerance to random fluctuations and noise in the EEG data. The use of input sequences with varying lengths (N) allows the model to assess its performance under different levels of "natural noise" introduced by the inclusion of irrelevant EEG data. This helps to understand how the model's performance is affected by the amount of surrounding EEG data. For performance evaluation, the use of multiple metrics, including AUC (micro and macro), accuracy, and loss, provides a comprehensive evaluation of the model's performance. For DFA, analysis helps to quantify the variability and complexity of the AUC fluctuations, providing insights into the model's behavior under different noise conditions. By incorporating these techniques, the authors aim to understand the feasibility and limitations of classifying EEG signals related to physical activities in the presence of noise, which is crucial for the practical application of BCI systems in real-world settings.

The results obtained allow us to conclude that the relatively simple DNN with components of FCN and CNN even can be effectively used to classify physical activities (namely, hand manipulations) from the GAL dataset. Application of natural and synthetic noises imitates the possible influence from environment. It should be noted that synthetic noise influence (due to Gaussian NDA with higher σ values) has the lower impact on the general ability to provide the better reliable classification of physical activities than natural noise influence (due to increase of the sampling size N) that can significantly improve the performance with reaching the stable metric values after some noise increase.

AUC fluctuations caused by the added synthetic NDA are not significant in comparison with AUC fluctuations without synthetic NDA due to increase of sampling size N. It should be emphasized that application of the natural NDA by increasing N leads to the better micro and macro AUC values for N values beyond the action duration which is $\sim$ 0.3 s and up to $\sim$ 3 s (N = 1,500) for offset = 0.5. But to the moment the open question is whether this improvement caused by the availability of EEG signals relevant to the physical action beyond action itself or by natural NDA. This aspect should be resolved by further investigations and on other open EEG datasets.

Application of the synthetic NDA in the wide range of noise levels (σ_{synth} from 0.001 up to 0.2) demonstrates the general stability of the DNN used for classification of all activities with the similar micro and macro AUC values in the limits of their fluctuations.

DFA allows us to investigate the fluctuation properties and calculate the correspondent Hurst exponents for the quantitative characterization of their variability. As a result of this research, some PAs can be divided in separate groups of actions that can be characterized by complexity and the feasibility of their classification: the easiest (HandStart), medium (LiftOff, Replace, and BothReleased), and hardest (BothStartLoadPhase and FirstDigitTouch) classification.

A general trend is observed in the behavior of the Hurst exponent H across varying time window scales in EEG data. Specifically, for shorter time window scales (i.e., < 2 s), the values of H_{low} tend to be significantly higher than those for longer time window scales (i.e., $>$ 2 s), denoted as H_{high}. This suggests that EEG segments with durations shorter than 2 s exhibit greater scaling complexity than those of longer durations. In particular, H_{low} can exceed H_{high} by a factor of 2 to 3 during certain physical actions, indicating a marked increase in complexity for these shorter time-scale fragments.

In general, this approach of adding natural noise by extending sampling size for small DNNs can be used during porting such models to Edge Computing infrastructures on devices with the very limited computational resources because the statistically reliable results were obtained by the relatively small DNN with the low resource requirements (Kochura et al., 2019; Gordienko et al., 2020, 2021a). The additional possible improvement can be obtained due to analysis of the optimal configuration for training and inference stages of the whole workflow that is especially important for distributed infrastructures (Kochura et al., 2017b; Taran et al., 2017; Gordienko et al., 2021a; Kochura et al., 2017a). Similar research could be also useful for classification of GAL-like and any other PAs before their actual start when some prediction with PA classification can be performed on the EEG activity before PA even. By this approach, the human EEG activity can be estimated with some proactive feedback such as continuation of PAs which were initiated by brain only, but unfortunately the PAs were not continued due to fatigue or some limited physical abilities, but the future detailed investigation should be performed to take into account the more various kinds of PAs.

Data availability statement

The original contributions presented in the study are included in the article/supplementary material, further inquiries can be directed to the corresponding author.

Author contributions

YG: Conceptualization, Data curation, Formal analysis, Investigation, Methodology, Software, Validation, Visualization, Writing – original draft, Writing – review & editing. NG: Investigation, Methodology, Software, Visualization, Writing – original draft, Writing – review & editing. VT: Investigation, Software, Writing – original draft, Writing – review & editing. AR: Writing – original draft, Writing – review & editing. ST: Conceptualization, Funding acquisition, Project administration, Writing – original draft, Writing – review & editing. SS: Conceptualization, Funding acquisition, Investigation, Methodology, Resources, Supervision, Validation, Writing – original draft, Writing – review & editing.

Funding

The author(s) declare financial support was received for the research, authorship, and/or publication of this article. The work was partially supported by the Knowledge At the Tip of Your Fingers: Clinical Knowledge for Humanity (KATY) project funded by the European Union's Horizon 2020 research and innovation program under grant agreement No. 101017453 in the part of research on the new neural network architectures and by the Development of hybrid models of artificial intelligence for the analysis of multimodal medical data project (K-I-144) funded by the Ministry of Education and Science of Ukraine in the part of multimodality research for medical applications.

Acknowledgments

The authors extend their appreciation to Cracow University of Technology (Cracow, Poland) and Université Paris 8 (Paris, France) that aided the efforts of the authors.

Conflict of interest

The authors declare that the research was conducted in the absence of any commercial or financial relationships that could be construed as a potential conflict of interest.

Generative AI statement

The author(s) declare that no Gen AI was used in the creation of this manuscript.

Publisher's note

References

Aggarwal, S., and Chugh, N. (2022). Review of machine learning techniques for EEG based brain computer interface. *Arch. Comput. Methods Eng.* 29, 3001–3020. doi: 10.1007/s11831-021-09684-6

An, J., and Cho, S. (2016). "Hand motion identification of grasp-and-lift task from electroencephalography recordings using recurrent neural networks," in *2016 International Conference on Big Data and Smart Computing (BigComp)* (IEEE), 427–429. doi: 10.1109/BIGCOMP.2016.7425963

Andrzejak, R. G., Lehnertz, K., Mormann, F., Rieke, C., David, P., and Elger, C. E. (2001). Indications of nonlinear deterministic and finite-dimensional structures in time

series of brain electrical activity: dependence on recording region and brain state. *Phys. Rev. E* 64:061907. doi: 10.1103/PhysRevE.64.061907

Aricó, P., Borghini, G., Di Flumeri, G., Colosimo, A., Bonelli, S., Golfetti, A., et al. (2016a). Adaptive automation triggered by EEG-based mental workload index: a passive brain-computer interface application in realistic air traffic control environment. *Front. Hum. Neurosci.* 10:539. doi: 10.3389/fnhum.2016.00539

Aricó, P., Borghini, G., Di Flumeri, G., Colosimo, A., Pozzi, S., and Babiloni, F. (2016b). A passive brain-computer interface application for the mental workload assessment on professional air traffic controllers during realistic air traffic control tasks. *Prog. Brain Res.* 228, 295–328. doi: 10.1016/bs.pbr.2016.04.021

Ashfaq, N., Khan, M. H., and Nisar, M. A. (2024). Identification of optimal data augmentation techniques for multimodal time-series sensory data: a framework. *Information* 15:343. doi: 10.3390/info15060343

Atzori, M., Cognolato, M., and Müller, H. (2016). Deep learning with convolutional neural networks applied to electromyography data: A resource for the classification of movements for prosthetic hands. *Front. Neurorobot.* 10:9. doi: 10.3389/fnbot.2016.00009

Aznan, N. K. N., Atapour-Abarghouei, A., Bonner, S., Connolly, J. D., Al Moubayed, N., and Breckon, T. P. (2019). "Simulating brain signals: creating synthetic EEG data via neural-based generative models for improved ssvep classification," in *2019 International Joint Conference on Neural Networks (IJCNN)* (IEEE), 1–8. doi: 10.1109/IJCNN.2019.8852227

Bao, G., Yan, B., Tong, L., Shu, J., Wang, L., Yang, K., et al. (2021). Data augmentation for EEG-based emotion recognition using generative adversarial networks. *Front. Comput. Neurosci.* 15:723843. doi: 10.3389/fncom.2021.723843

Behncke, J., Schirrmeister, R. T., Burgard, W., and Ball, T. (2018). "The signature of robot action success in EEG signals of a human observer: decoding and visualization using deep convolutional neural networks," in *2018 6th International Conference on Brain-Computer Interface (BCI)* (IEEE), 1–6. doi: 10.1109/IWW-BCI.2018.8311531

Belo, J., Clerc, M., and Schön, D. (2021). EEG-based auditory attention detection and its possible future applications for passive BCI. *Front. Comput. Sci.* 3:661178. doi: 10.3389/fcomp.2021.661178

Bianchi, S. (2020). FATHON: a python package for a fast computation of detrendend fluctuation analysis and related algorithms. *J. Open Source Softw.* 5:1828. doi: 10.21105/joss.01828

Borra, D., Paissan, F., and Ravanelli, M. (2024). Speechbrain-moabb: An open-source python library for benchmarking deep neural networks applied to EEG signals. *Comput. Biol. Med.* 182:109097. doi: 10.1016/j.compbiomed.2024.109097

Brunner, C., Leeb, R., Müller-Putz, G., Schlögl, A., and Pfurtscheller, G. (2008). *BCI competition 2008-graz data set a*. Institute for knowledge discovery (laboratory of brain-computer interfaces), Graz University of Technology, 1–6.

Cai, Q., Liu, C., and Chen, A. (2024). Classification of motor imagery tasks derived from unilateral upper limb based on a weight-optimized learning model. *J. Integr. Neurosci.* 23:106. doi: 10.31083/j.jin2305106

Carrle, F. P., Hollenbenders, Y., and Reichenbach, A. (2023). Generation of synthetic EEG data for training algorithms supporting the diagnosis of major depressive disorder. *Front. Neurosci.* 17:1219133. doi: 10.3389/fnins.2023.1219133

Cattan, G. (2021). The use of brain-computer interfaces in games is not ready for the general public. *Front. Comput. Sci.* 3:628773. doi: 10.3389/fcomp.2021.628773

Cecotti, H., Marathe, A. R., and Ries, A. J. (2015). Optimization of single-trial detection of event-related potentials through artificial trials. *IEEE Trans. Biomed. Eng.* 62, 2170–2176. doi: 10.1109/TBME.2015.2417054

Chen, X., Li, C., Liu, A., McKeown, M. J., Qian, R., and Wang, Z. J. (2022). Toward open-world electroencephalogram decoding via deep learning: a comprehensive survey. *IEEE Signal Process. Mag.* 39, 117–134. doi: 10.1109/MSP.2021.3134629

Chen, Y.-W., and Jain, L. C. (2020). *Deep Learning in Healthcare*. Cham: Springer. doi: 10.1007/978-3-030-32606-7

Cho, H., Ahn, M., Ahn, S., Kwon, M., and Jun, S. (2017a). Supporting data for "EEG datasets for motor imagery brain computer interface." *GigaScience Datab.* 10:100295.

Cho, H., Ahn, M., Ahn, S., Kwon, M., and Jun, S. C. (2017b). EEG datasets for motor imagery brain-computer interface. *GigaScience* 6:gix034. doi: 10.1093/gigascience/gix034

Cleveland, W. S., Grosse, E., and Shyu, W. M. (2017). "Local regression models," in *Statistical Models in S* (Routledge), 309–376. doi: 10.1201/9780203738535-8

Collazos-Huertas, D. F., Álvarez-Meza, A. M., Cárdenas-Peña, D. A., Castaño-Duque, G. A., and Castellanos-Domínguez, C. G. (2023). Posthoc interpretability of neural responses by grouping subject motor imagery skills using cnn-based connectivity. *Sensors* 23:2750. doi: 10.3390/s23052750

Di Flumeri, G., De Crescenzio, F., Berberian, B., Ohneiser, O., Kramer, J., Aricò, P., et al. (2019). Brain-computer interface-based adaptive automation to prevent out-of-the-loop phenomenon in air traffic controllers dealing with highly automated systems. *Front. Hum. Neurosci.* 13:296. doi: 10.3389/fnhum.2019.00296

Esteva, A., Robicquet, A., Ramsundar, B., Kuleshov, V., DePristo, M., Chou, K., et al. (2019). A guide to deep learning in healthcare. *Nat. Med.* 25, 24–29. doi: 10.1038/s41591-018-0316-z

Fahimi, F., Dosen, S., Ang, K. K., Mrachacz-Kersting, N., and Guan, C. (2020). Generative adversarial networks-based data augmentation for brain-computer interface. *IEEE Trans. Neural Netw. Learn. Syst.* 32, 4039–4051. doi: 10.1109/TNNLS.2020.3016666

Falaschetti, L., Biagetti, G., Alessandrini, M., Turchetti, C., Luzzi, S., and Crippa, P. (2024). Multi-class detection of neurodegenerative diseases from EEG signals using lightweight lstm neural networks. *Sensors* 24:6721. doi: 10.3390/s24206721

Freer, D., and Yang, G.-Z. (2020). Data augmentation for self-paced motor imagery classification with c-lstm. *J. Neural Eng.* 17:016041. doi: 10.1088/1741-2552/ab57c0

Gang, P., Hui, J., Stirenko, S., Gordienko, Y., Shemsedinov, T., Alienin, O., et al. (2018). "User-driven intelligent interface on the basis of multimodal augmented reality and brain-computer interaction for people with functional disabilities," in *Future of Information and Communication Conference* (Cham: Springer), 612–631. doi: 10.1007/978-3-030-03402-3_43

Gatti, R., Atum, Y., Schiaffino, L., Jochumsen, M., and Manresa, J. B. (2019). Prediction of hand movement speed and force from single-trial EEG with convolutional neural networks. *bioRxiv*, 492660. doi: 10.1101/492660

George, O., Smith, R., Madiraju, P., Yahyasoltani, N., and Ahamed, S. I. (2022). Data augmentation strategies for EEG-based motor imagery decoding. *Heliyon* 8:e10240. doi: 10.1016/j.heliyon.2022.e10240

Gordienko, Y., Kochura, Y., Taran, V., Gordienko, N., Rokovyi, A., Alienin, O., et al. (2020). "Scaling analysis of specialized tensor processing architectures for deep learning models," in *Deep Learning: Concepts and Architectures* (Cham: Springer), 65–99. doi: 10.1007/978-3-030-31756-0_3

Gordienko, Y., Kochura, Y., Taran, V., Gordienko, N., Rokovyi, O., Alienin, O., et al. (2021a). "last mile" optimization of edge computing ecosystem with deep learning models and specialized tensor processing architectures. *Adv. Comput.* 122, 303–341. doi: 10.1016/bs.adcom.2020.10.003

Gordienko, Y., Kostiukevych, K., Gordienko, N., Rokovyi, O., Alienin, O., and Stirenko, S. (2021b). "Deep learning for grasp-and-lift movement forecasting based on electroencephalography by brain-computer interface," in *International Conference on Artificial Intelligence and Logistics Engineering* (Cham: Springer), 3–12. doi: 10.1007/978-3-030-80475-6_1

Gordienko, Y., Kostiukevych, K., Gordienko, N., Rokovyi, O., Alienin, O., and Stirenko, S. (2021c). "Deep learning with noise data augmentation and detrended fluctuation analysis for physical action classification by brain-computer interface," in *2021 8th International Conference on Soft Computing Machine Intelligence (ISCMI)* (IEEE), 176–180. doi: 10.1109/ISCMI53840.2021.9654829

Gou, H., Piao, Y., Ren, J., Zhao, Q., Chen, Y., Liu, C., et al. (2022). A solution to supervised motor imagery task in the bci controlled robot contest in world robot contest. *Brain Sci. Adv.* 8, 153–161. doi: 10.26599/BSA.2022.9050014

Gramfort, A., Luessi, M., Larson, E., Engemann, D. A., Strohmeier, D., Brodbeck, C., et al. (2013). MEG and EEG data analysis with Mne-python. *Front. Neurosci.* 7:267. doi: 10.3389/fnins.2013.00267

Gu, X., Cao, Z., Jolfaei, A., Xu, P., Wu, D., Jung, T.-P., et al. (2021). EEG-based brain-computer interfaces (BCIS): a survey of recent studies on signal sensing technologies and computational intelligence approaches and their applications. *IEEE/ACM Trans. Comput. Biol. Bioinform.* 18, 1645–1666. doi: 10.1109/TCBB.2021.3052811

Habashi, A. G., Azab, A. M., Eldawlatly, S., and Aly, G. M. (2023). Generative adversarial networks in EEG analysis: an overview. *J. Neuroeng. Rehabil.* 20:40. doi: 10.1186/s12984-023-01169-w

He, K., Zhang, X., Ren, S., and Sun, J. (2016). "Deep residual learning for image recognition," in *Proceedings of the IEEE conference on Computer Vision and Pattern Recognition* 770–778. doi: 10.1109/CVPR.2016.90

Hurst, H. E. (1956). The problem of long-term storage in reservoirs. *Hydrol. Sci. J.* 1, 13–27. doi: 10.1080/02626665609493644

Ibrahim, M., Khalil, Y. A., Amirrajab, S., Sun, C., Breeuwer, M., Pluim, J., et al. (2024). Generative ai for synthetic data across multiple medical modalities: a systematic review of recent developments and challenges. *arXiv preprint arXiv:2407.00116*.

Jayaram, V., and Barachant, A. (2018). Moabb: trustworthy algorithm benchmarking for bcis. *J. Neural Eng.* 15:066011. doi: 10.1088/1741-2552/aadea0

Jeong, J.-H., Cho, J.-H., Lee, Y.-E., Lee, S.-H., Shin, G.-H., Kweon, Y.-S., et al. (2022). 2020 international brain-computer interface competition: a review. *Front. Hum. Neurosci.* 16:898300. doi: 10.3389/fnhum.2022.898300

Kaggle (2020). *Grasp-and-lift EEG detection*. Available at: https://www.kaggle.com/competitions/grasp-and-lift-eeg-detection (accessed October 14, 2020).

Kalashami, M. P., Pedram, M. M., and Sadr, H. (2022). EEG feature extraction and data augmentation in emotion recognition. *Comput. Intell. Neurosci.* 2022:7028517. doi: 10.1155/2022/7028517

Kaya, M., Binli, M. K., Ozbay, E., Yanar, H., and Mishchenko, Y. (2018). A large electroencephalographic motor imagery dataset for electroencephalographic brain computer interfaces. *Sci. Data* 5, 1–16. doi: 10.1038/sdata.2018.211

Kemp, B., Zwinderman, A. H., Tuk, B., Kamphuisen, H. A., and Oberye, J. J. (2000). Analysis of a sleep-dependent neuronal feedback loop: the slow-wave microcontinuity of the EEG. *IEEE Trans. Biomed. Eng.* 47, 1185–1194. doi: 10.1109/10.867928

Kerous, B., Skola, F., and Liarokapis, F. (2018). EEG-based bci and video games: a progress report. *Virtual Real.* 22, 119–135. doi: 10.1007/s10055-017-0328-x

Ko, W., Jeon, E., Jeong, S., Phyo, J., and Suk, H.-I. (2021). A survey on deep learning-based short/zero-calibration approaches for EEG-based brain-computer interfaces. *Front. Hum. Neurosci.* 15:643386. doi: 10.3389/fnhum.2021.643386

Kochura, Y., Gordienko, Y., Taran, V., Gordienko, N., Rokovyi, A., Alienin, O., et al. (2019). "Batch size influence on performance of graphic and tensor processing units during training and inference phases," in *International Conference on Computer Science, Engineering and Education Applications* (Cham: Springer), 658–668. doi: 10.1007/978-3-030-16621-2_61

Kochura, Y., Stirenko, S., Alienin, O., Novotarskiy, M., and Gordienko, Y. (2017a). "Comparative analysis of open source frameworks for machine learning with use case in single-threaded and multi-threaded modes," in *12th Int. Scientific and Technical Conf. on Computer Sciences and Information Technologies (CSIT)* (IEEE), 373–376. doi: 10.1109/STC-CSIT.2017.8098808

Kochura, Y., Stirenko, S., Alienin, O., Novotarskiy, M., and Gordienko, Y. (2017b). "Performance analysis of open source machine learning frameworks for various parameters in single-threaded and multi-threaded modes," in *Conference on Computer Science and Information Technologies* (Cham: Springer), 243–256. doi: 10.1007/978-3-319-70581-1_17

Koelstra, S., Muhl, C., Soleymani, M., Lee, J.-S., Yazdani, A., Ebrahimi, T., et al. (2011). Deap: a database for emotion analysis; using physiological signals. *IEEE Trans. Affect. Comput.* 3, 18–31. doi: 10.1109/T-AFFC.2011.15

Kostiukevych, K., Stirenko, S., Gordienko, N., Rokovyi, O., Alienin, O., and Gordienko, Y. (2021). "Convolutional and recurrent neural networks for physical action forecasting by brain-computer interface," in *2021 11th IEEE International Conference on Intelligent Data Acquisition and Advanced Computing Systems: Technology and Applications (IDAACS)* (IEEE), 973–978. doi: 10.1109/IDAACS53288.2021.9660880

Kotowski, K., Stapor, K., and Ochab, J. (2020). "Deep learning methods in electroencephalography," in *Machine Learning Paradigms* (Cham: Springer), 191–212. doi: 10.1007/978-3-030-49724-8_8

Lashgari, E., Liang, D., and Maoz, U. (2020). Data augmentation for deep-learning-based electroencephalography. *J. Neurosci. Methods* 346:108885. doi: 10.1016/j.jneumeth.2020.108885

Lashgari, E., Ott, J., Connelly, A., Baldi, P., and Maoz, U. (2021). An end-to-end cnn with attentional mechanism applied to raw EEG in a bci classification task. *J. Neural Eng.* 18:0460e03. doi: 10.1088/1741-2552/ac1ade

Lawhern, V. J., Solon, A. J., Waytowich, N. R., Gordon, S. M., Hung, C. P., and Lance, B. J. (2018). EEGnet: a compact convolutional neural network for EEG-based brain-computer interfaces. *J. Neural Eng.* 15:056013. doi: 10.1088/1741-2552/aace8c

LeCun, Y., Bengio, Y., and Hinton, G. (2015). Deep learning. *Nature* 521, 436–444. doi: 10.1038/nature14539

Lee, B.-H., Cho, J.-H., Kwon, B.-H., Lee, M., and Lee, S.-W. (2024). Iteratively calibratable network for reliable EEG-based robotic arm control. *IEEE Trans. Neural Syst. Rehabil. Eng.* 32:2793–2804. doi: 10.1109/TNSRE.2024.3434983

Lee, M.-H., Kwon, O.-Y., Kim, Y.-J., Kim, H.-K., Lee, Y.-E., Williamson, J., et al. (2019). EEG dataset and openbmi toolbox for three bci paradigms: an investigation into bci illiteracy. *GigaScience* 8:giz002. doi: 10.1093/gigascience/giz002

Leeb, R., Brunner, C., Müller-Putz, G., Schlögl, A., and Pfurtscheller, G. (2008). BCI competition 2008-graz data set b. *Graz Univ. Technol.* 16, 1–6. Available at: https://www.researchgate.net/publication/238115253_BCI_Competition_2008_Graz_data_set_B

Li, G., Lee, C. H., Jung, J. J., Youn, Y. C., and Camacho, D. (2020). Deep learning for EEG data analytics: a survey. *Concurr. Comput.* 32:e5199. doi: 10.1002/cpe.5199

Li, Y., Zhang, X.-R., Zhang, B., Lei, M.-Y., Cui, W.-G., and Guo, Y.-Z. (2019). A channel-projection mixed-scale convolutional neural network for motor imagery EEG decoding. *IEEE Trans. Neural Syst. Rehabilit. Eng.* 27, 1170–1180. doi: 10.1109/TNSRE.2019.2915621

Lin, B., Deng, S., Gao, H., and Yin, J. (2020). A multi-scale activity transition network for data translation in EEG signals decoding. *IEEE/ACM Trans. Comput. Biol. Bioinform.* 18, 1699–1709. doi: 10.1109/TCBB.2020.3024228

Lopez, E., Chiarantano, E., Grassucci, E., and Comminiello, D. (2023). "Hypercomplex multimodal emotion recognition from EEG and peripheral physiological signals," in *2023 IEEE International Conference on Acoustics, Speech, and Signal Processing Workshops (ICASSPW)* (IEEE), 1–5. doi: 10.1109/ICASSPW59220.2023.10193329

Luciw, M. D., Jarocka, E., and Edin, B. B. (2014). Multi-channel EEG recordings during 3,936 grasp and lift trials with varying weight and friction. *Sci. Data* 1, 1–11. doi: 10.1038/sdata.2014.47

Micucci, D., Mobilio, M., and Napoletano, P. (2017). Unimib shar: a dataset for human activity recognition using acceleration data from smartphones. *Appl. Sci.* 7:1101. doi: 10.3390/app7101101

Nisar, M. A., Shirahama, K., Li, F., Huang, X., and Grzegorzek, M. (2020). Rank pooling approach for wearable sensor-based adls recognition. *Sensors* 20:3463. doi: 10.3390/s20123463

Okafor, E., Smit, R., Schomaker, L., and Wiering, M. (2017). "Operational data augmentation in classifying single aerial images of animals," in *2017 IEEE International Conference on INnovations in Intelligent SysTems and Applications (INISTA)* (IEEE), 354–360. doi: 10.1109/INISTA.2017.8001185

Ouyang, J., Wu, M., Li, X., Deng, H., and Wu, D. (2024). Briedge: EEG-adaptive edge ai for multi-brain to multi-robot interaction. *arXiv preprint arXiv:2403.15432*.

Pancholi, S., Giri, A., Jain, A., Kumar, L., and Roy, S. (2021). Source aware deep learning framework for hand kinematic reconstruction using EEG signal. *arXiv preprint arXiv:2103.13862*.

Parvan, M., Ghiasi, A. R., Rezaii, T. Y., and Farzamnia, A. (2019). "Transfer learning based motor imagery classification using convolutional neural networks," in *2019 27th Iranian Conference on Electrical Engineering (ICEE)* (IEEE), 1825–1828. doi: 10.1109/IranianCEE.2019.8786636

Peng, C.-K., Buldyrev, S., Goldberger, A., Havlin, S., Simons, M., and Stanley, H. (1993). Finite-size effects on long-range correlations: implications for analyzing dna sequences. *Phys. Rev. E* 47:3730. doi: 10.1103/PhysRevE.47.3730

Peng, C.-K., Havlin, S., Stanley, H. E., and Goldberger, A. L. (1995). Quantification of scaling exponents and crossover phenomena in nonstationary heartbeat time series. *Chaos* 5, 82–87. doi: 10.1063/1.166141

Pizzolato, S., Tagliapietra, L., Cognolato, M., Reggiani, M., Müller, H., and Atzori, M. (2017). Comparison of six electromyography acquisition setups on hand movement classification tasks. *PLoS ONE* 12:e0186132. doi: 10.1371/journal.pone.0186132

Rommel, C., Paillard, J., Moreau, T., and Gramfort, A. (2022). Data augmentation for learning predictive models on EEG: a systematic comparison. *arXiv preprint arXiv:2206.14483*.

Roy, Y., Banville, H., Albuquerque, I., Gramfort, A., Falk, T. H., and Faubert, J. (2019). Deep learning-based electroencephalography analysis: a systematic review. *J. Neural Eng.* 16:051001. doi: 10.1088/1741-2552/ab260c

Sakai, A., Minoda, Y., and Morikawa, K. (2017). "Data augmentation methods for machine-learning-based classification of bio-signals," in *2017 10th Biomedical Engineering International Conference (BMEiCON)* (IEEE), 1–4. doi: 10.1109/BMEiCON.2017.8229109

Simonyan, K., and Zisserman, A. (2014). Very deep convolutional networks for large-scale image recognition. *arXiv preprint arXiv:1409.1556*.

Soleymani, M., Lichtenauer, J., Pun, T., and Pantic, M. (2011). A multimodal database for affect recognition and implicit tagging. *IEEE Trans. Affect. Comput.* 3, 42–55. doi: 10.1109/T-AFFC.2011.25

Sun, C., and Mou, C. (2023). Survey on the research direction of EEG-based signal processing. *Front. Neurosci.* 17:1203059. doi: 10.3389/fnins.2023.1203059

Sun, J., Shen, A., Sun, Y., Chen, X., Li, Y., Gao, X., et al. (2024). Adaptive spatiotemporal encoding network for cognitive assessment using resting state EEG. *NPJ Digital Med.* 7:375. doi: 10.1038/s41746-024-01384-2

Talavera, E., Iglesias, G., González-Prieto, Á., Mozo, A., and Gómez-Canaval, S. (2022). Data augmentation techniques in time series domain: A survey and taxonomy. *arXiv preprint arXiv:2206.13508*.

Tangermann, M., Müller, K.-R., Aertsen, A., Birbaumer, N., Braun, C., Brunner, C., et al. (2012). Review of the bci competition IV. *Front. Neurosci.* 6:55. doi: 10.3389/fnins.2012.00055

Taran, V., Alienin, O., Stirenko, S., Gordienko, Y., and Rojbi, A. (2017). "Performance evaluation of distributed computing environments with hadoop and spark frameworks," in *2017 IEEE Int. Young Scientists Forum on Applied Physics and Engineering (YSF)* (IEEE), 80–83. doi: 10.1109/YSF.2017.8126655

Tsinganos, P., Cornelis, B., Cornelis, J., Jansen, B., and Skodras, A. (2018). "Deep learning in emg-based gesture recognition," in *PhyCS*, 107–114. doi: 10.5220/0006960201070114

Tunnell, M., Chung, H., and Chang, Y. (2022). "A novel convolutional neural network for emotion recognition using neurophysiological signals," in *2022 International Conference on Robotics and Automation (ICRA)* (IEEE), 792–797. doi: 10.1109/ICRA46639.2022.9811868

Vahid, A., Mückschel, M., Stober, S., Stock, A.-K., and Beste, C. (2020). Applying deep learning to single-trial EEG data provides evidence for complementary theories on action control. *Commun. Biol.* 3, 1–11. doi: 10.1038/s42003-020-0846-z

Vasiljevic, G. A. M., and de Miranda, L. C. (2020). Brain-computer interface games based on consumer-grade EEG devices: a systematic literature review. *Int. J. Hum. Comput. Interact.* 36, 105–142. doi: 10.1080/10447318.2019.1612213

Wan, X., Zhang, K., Ramkumar, S., Deny, J., Emayavaramban, G., Ramkumar, M. S., et al. (2019). A review on electroencephalogram based brain computer interface for elderly disabled. *IEEE Access* 7, 36380–36387. doi: 10.1109/ACCESS.2019.2903235

Wang, F., Zhong, S.-,h., Peng, J., Jiang, J., and Liu, Y. (2018a). "Data augmentation for EEG-based emotion recognition with deep convolutional neural networks," in *MultiMedia Modeling: 24th International Conference, MMM 2018, Bangkok, Thailand, February 5–7, 2018, Proceedings, Part II 24* (Springer), 82–93. doi: 10.1007/978-3-319-73600-6_8

Wang, I.-N., Lee, C.-H., Kim, H., and Kim, D.-J. (2024). Negative-sample-free contrastive self-supervised learning for electroencephalogram-based motor imagery classification. *IEEE Access*. 12, 132714–132728. doi: 10.1109/ACCESS.2024.3459866

Wang, N., Farhadi, A., Rao, R., and Brunton, B. (2018b). "Ajile movement prediction: Multimodal deep learning for natural human neural recordings and video," in *Proceedings of the AAAI Conference on Artificial Intelligence*, 2524–2531. doi: 10.1609/aaai.v32i1.11889

Wei, M., and Lin, F. (2020). A novel multi-dimensional features fusion algorithm for the EEG signal recognition of brain's sensorimotor region activated tasks. *Int. J. Intell. Comput. Cybern*. 13, 239–260. doi: 10.1108/IJICC-02-2020-0019

Wu, D., Li, S., Yang, J., and Sawan, M. (2022). neuro2vec: masked fourier spectrum prediction for neurophysiological representation learning. *arXiv preprint arXiv:2204.12440*.

Xia, T., Han, J., and Mascolo, C. (2022). "Benchmarking uncertainty quantification on biosignal classification tasks under dataset shift," in *Multimodal AI in Healthcare: A Paradigm Shift in Health Intelligence* (Springer), 347–359. doi: 10.1007/978-3-031-14771-5_25

Xu, J., and Zhong, B. (2018). Review on portable EEG technology in educational research. *Comput. Human Behav*. 81, 340–349. doi: 10.1016/j.chb.2017.12.037

Zabcikova, M., Koudelkova, Z., Jasek, R., and Lorenzo Navarro, J. J. (2022). Recent advances and current trends in brain-computer interface research and their applications. *Int. J. Dev. Neurosci*. 82, 107–123. doi: 10.1002/jdn.10166

Zhang, K., Xu, G., Han, Z., Ma, K., Zheng, X., Chen, L., et al. (2020). Data augmentation for motor imagery signal classification based on a hybrid neural network. *Sensors* 20:4485. doi: 10.3390/s20164485

Zhang, Q., and Liu, Y. (2018). Improving brain computer interface performance by data augmentation with conditional deep convolutional generative adversarial networks. *arXiv preprint arXiv:1806.07108*.

Zhang, Y., Liao, Y., Zhang, Y., and Huang, L. (2021). Emergency braking intention detect system based on k-order propagation number algorithm: a network perspective. *Brain Sci*. 11:1424. doi: 10.3390/brainsci11111424

Zhang, Z., Huang, Y., Chen, S., Qu, J., Pan, X., Yu, T., et al. (2017). An intention-driven semi-autonomous intelligent robotic system for drinking. *Front. Neurorobot*. 11:48. doi: 10.3389/fnbot.2017.00048

Zhengyi, L., Hui, Z., Dandan, Y., and Shuiqing, X. (2017). "Multimodal deep learning network based hand adls tasks classification for prosthetics control," in *2017 International Conference on Progress in Informatics and Computing (PIC)* (IEEE), 91–95. doi: 10.1109/PIC.2017.8359521

frontiers | Frontiers in Neurology

TYPE Original Research
PUBLISHED 28 February 2025
DOI 10.3389/fneur.2025.1521001

OPEN ACCESS

EDITED BY
Jisu Elsa Jacob,
Sree Chitra Thirunal College of Engineering, India

REVIEWED BY
Colette Williams,
University of California, Davis, United States
Noor Kamal Al-Qazzaz,
University of Baghdad, Iraq
Yan Huang,
University of Texas Health Science Center at Houston, United States

*CORRESPONDENCE
Hunmin Kim
✉ hunminkim@snubh.org

†These authors have contributed equally to this work

RECEIVED 01 November 2024
ACCEPTED 17 February 2025
PUBLISHED 28 February 2025

CITATION
Chung YG, Cho J, Kim YH, Kim HW, Kim H, Koo YS, Lee S-Y and Shon Y-M (2025) Data transformation of unstructured electroencephalography reports by natural language processing: improving data usability for large-scale epilepsy studies. *Front. Neurol.* 16:1521001. doi: 10.3389/fneur.2025.1521001

Data transformation of unstructured electroencephalography reports by natural language processing: improving data usability for large-scale epilepsy studies

Yoon Gi Chung[1†], Jaeso Cho[1†], Young Ho Kim[1], Hyun Woo Kim[1], Hunmin Kim[1,2*], Yong Seo Koo[3], Seo-Young Lee[4,5] and Young-Min Shon[6]

[1]Department of Pediatrics, Seoul National University Bundang Hospital, Seoul National University College of Medicine, Seongnam-si, Gyeonggi-do, Republic of Korea, [2]Department of Pediatrics, Seoul National University College of Medicine, Seoul, Republic of Korea, [3]Department of Neurology, Asan Medical Center, University of Ulsan College of Medicine, Seoul, Republic of Korea, [4]Department of Neurology, Kangwon National University School of Medicine, Chuncheon-si, Republic of Korea, [5]Interdisciplinary Graduate Program in Medical Bigdata Convergence, Kangwon National University, Chuncheon-si, Republic of Korea, [6]Department of Neurology, Samsung Medical Center, Sungkyunkwan University School of Medicine, Seoul, Republic of Korea

Introduction: Electroencephalography (EEG) is a popular technique that provides neurologists with electrographic insights and clinical interpretations. However, these insights are predominantly presented in unstructured textual formats, which complicates data extraction and analysis. In this study, we introduce a hierarchical algorithm aimed at transforming unstructured EEG reports from pediatric patients diagnosed with epilepsy into structured data using natural language processing (NLP) techniques.

Methods: The proposed algorithm consists of two distinct phases: a deep learning-based text classification followed by a series of rule-based keyword extraction procedures. First, we categorized the EEG reports into two primary groups: normal and abnormal. Thereafter, we systematically identified the key indicators of cerebral dysfunction or seizures, distinguishing between focal and generalized seizures, as well as identifying the epileptiform discharges and their specific anatomical locations. For this study, we retrospectively analyzed a dataset comprising 17,172 EEG reports from 3,423 pediatric patients. Among them, we selected 6,173 normal and 6,173 abnormal reports confirmed by neurologists for algorithm development.

Results: The developed algorithm successfully classified EEG reports into 1,000 normal and 1,000 abnormal reports, and effectively identified the presence of cerebral dysfunction or seizures within these reports. Furthermore, our findings revealed that the algorithm translated abnormal reports into structured tabular data with an accuracy surpassing 98.5% when determining the type of seizures (focal or generalized). Additionally, the accuracy for detecting epileptiform discharges and their respective locations exceeded 88.5%. These outcomes were validated through both internal and external assessments involving 800 reports from two different medical institutions.

Discussion: Our primary focus was to convert EEG reports into structured datasets, diverging from the traditional methods of formulating clinical notes or discharge summaries. We developed a hierarchical and streamlined approach leveraging keyword selections guided by neurologists, which contributed to the exceptional performance of our algorithm. Overall, this methodology enhances data accessibility as well as improves the potential for further research and clinical applications in the field of pediatric epilepsy management.

KEYWORDS

natural language processing, electroencephalography, epilepsy, deep learning, keyword extraction

1 Introduction

Electroencephalography (EEG) is a noninvasive diagnostic modality that is specifically designed to record neuronal activity within the brain. This technique has demonstrated considerable efficacy in identifying clinically significant cortical electrophysiological markers in individuals suffering from neurological disorders. As such, EEG assessments serve as preliminary diagnostic measures for neurological conditions, especially epilepsy (1–3).

Typically, EEG reports are composed of unstructured data formatted as free-text, which varies in stylistic presentation depending on the individual neurologist. This variability necessitates that neurologists must manually scrutinize each report to aggregate the data into a cohesive database—a process that is both time-consuming and labor-intensive. Consequently, the potential for large-scale data analysis and related clinical applications utilizing EEG reports has been significantly curtailed. Despite these reports containing valuable clinical insights vital for the interpretation of patient EEG recordings, no systematic efforts have been achieved to convert this information into structured, tabulated datasets. In response to these challenges, recent advancements in natural language processing (NLP) techniques have emerged as promising solutions for managing unstructured data in electronic medical records (EMR) and identifying information from text-heavy EEG reports of epilepsy patients (4). Various methodologies involving rule-based systems, machine learning algorithms, and deep learning approaches have been implemented for a spectrum of tasks such as information extraction, text classification, and summarization (4–6). These innovations offer the potential to revolutionize the handling of EEG reports, thereby enhancing their utility in clinical and research settings.

Despite the significant advancements in information extraction and text classification, the majority of existing studies have primarily focused on clinical notes and discharge summaries instead of EEG reports. Researchers have utilized both rule-based and deep learning methodologies to extract epilepsy- and seizure-related variables from these free-text documents. The key variables include epilepsy phenotypes (7, 8), seizure onsets (9), seizure frequency (8, 10, 11), seizure types (8, 10, 12), and EEG patterns (13). Additionally, certain studies have focused on classifying patients based on their seizure-free status (11, 12). However, the extensive array of target variables for keyword extraction from clinical notes and summaries presents challenges in data selection strategies when applying NLP techniques. In contrast, EEG reports typically offer more concise and focused information, particularly regarding the electrographic findings of patients. This structured format allows for effective analysis in a time-sequenced manner when processed sequentially.

Therefore, in the present study, we propose a hierarchical algorithm designed to transform unstructured EEG reports from pediatric patients diagnosed with epilepsy into structured data that is clinically relevant, leveraging advanced NLP techniques. This algorithm was designed to achieve the following objectives: (1) convert large volumes of free-text EEG reports into tabular data using deep learning and simplified rule-based methods with high accuracy and (2) ensure easy adaptability to various EEG report formats through external validation.

2 Methods

2.1 Dataset

We retrospectively compiled 17,172 reports from 3,423 pediatric patients (mean age: 10.8 ± 6.0 years) diagnosed with epilepsy. These reports were sourced from the clinical data warehouse of Seoul National University Bundang Hospital (SNUBH), situated in Seongnam, Republic of Korea. Two neurologists, identified as H.K. and J.C., meticulously reviewed all the EEG reports to categorize them as either normal or abnormal. A report was deemed normal if it revealed no abnormal findings, whereas an abnormal report was characterized by the presence of at least one abnormal finding. Based on the annotations of the neurologists, we identified 6,173 reports as normal and 10,822 as abnormal. To facilitate a balanced dataset, we randomly selected 6,173 abnormal reports to match a 1:1 ratio of normal to abnormal cases. For the purposes of developing our classification algorithm, we further narrowed our selection to 5,173 reports from both the normal and abnormal categories. The remaining 1,000 reports from each category were reserved for the evaluation of our classification models and internal validation.

Additionally, we conducted a retrospective collection of 400 EEG reports from 229 pediatric patients (age: 9.3 ± 7.8 years) with epilepsy, sourced from the clinical data warehouse of Seoul National University Children's Hospital (SNUCH), which is an independent tertiary facility located in Seoul, Republic of Korea. The same neurologists, H.K. and J.C., reviewed these 400 reports and confirmed that they were 200 normal and 200 abnormal reports. All EEG reports from SNUCH were employed for the external validation. The overall study process is illustrated in Figure 1.

This research was granted approval by the Institutional Review Board at Seoul National University Bundang Hospital (Approval No.

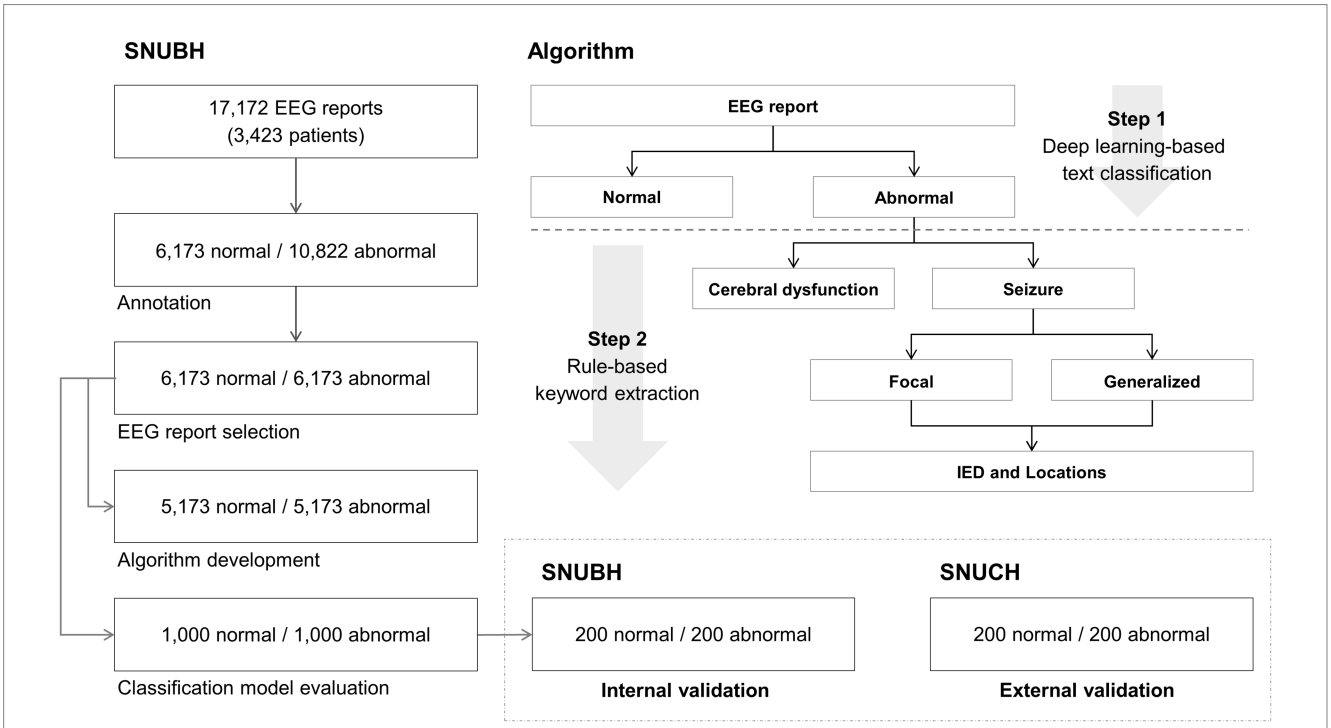

FIGURE 1
Overall process of this study. Normal and abnormal electroencephalography (EEG) reports (5,173 each) from the Seoul National University Bundang Hospital (SNUBH), located in Seongnam, Republic of Korea, were used for algorithm development. Normal and abnormal reports (1,000 each) of SNUBH were used for classification model evaluation. Among the 1,000 normal and 1,000 abnormal reports, randomly selected 200 normal and 200 abnormal reports were used for internal validation. Normal and abnormal reports (200 each) from an independent tertiary hospital in Korea (Seoul National University Children's Hospital (SNUCH), Seoul, Republic of Korea) were used for external validation. IED denotes interictal epileptiform discharge.

B-2312-873-107). Due to the retrospective nature of the study, the requirement for informed consent was waived. The research adhered to the ethical principles outlined in the Declaration of Helsinki.

2.2 Algorithm development

We executed a two-step process to transform the free-text EEG reports into structured tabular data. The first step involved classifying the EEG reports into two categories: normal and abnormal, using a deep learning-based model. The primary aim of this classification was to identify the abnormal EEG reports, which encapsulate critical findings from neurologists concerning various abnormalities. The second step focused on extracting specific keywords from the identified abnormal EEG reports using rule-based methodologies. The main goal of this keyword extraction was to pinpoint significant abnormal findings that could provide insights into the condition of patients diagnosed with epilepsy. This second step comprised three sequential procedures for keyword extraction. Below, we provide a comprehensive overview of our hierarchical algorithm:

(1) Step 1: Classification of normal and abnormal reports.

EEG reports were categorized as either normal or abnormal through the application of a deep learning-based classification model. Reports classified as normal did not proceed to further analysis. Conversely, those identified as abnormal prompted the execution of the second phase, as detailed below. Note that abnormal reports may include keywords that suggest both *normal* and *abnormal* conditions (e.g., "*This is a normal waking and moderately abnormal stage I-II…*"). In cases where a report contained solely *abnormal* keywords, it was categorized as abnormal irrespective of the model's output.

(2) Step 2: Keyword extraction.

The extraction of specific keywords from the abnormal EEG reports was performed using rule-based methods that relied on regular expressions and the spaCy library in Python. This method facilitated the identification of relevant keywords that denote significant abnormal findings. All abnormal reports were structured into two distinct sections: impression and clinical correlation. Initially, each abnormal report was divided into these two sections, and one section was selected based on the targeted keywords. The extraction of keywords was conducted through a series of three hierarchical procedures, detailed as follows:

A Extraction of keywords related to *dysfunction* or *seizure* from the clinical correlation section: In instances where an abnormal report indicated *dysfunction*, it was inferred that the corresponding background EEG activity was abnormal (e.g., *cerebral dysfunction* or *occipital lobe dysfunction*). Conversely, if the report identified *seizure* activity, it was determined that the corresponding EEG exhibited characteristics indicative of

a seizure. Both keywords, *dysfunction* and *seizure*, were systematically extracted.

B Extraction of *focal* (or *partial*) or *generalized* seizure information from the clinical correlation section: This procedure was specifically applied to abnormal reports identified in the previous procedure (A) that indicated *seizure* activity. If the report contained references to *focal* (or *partial*) seizures, the corresponding seizure type was classified as focal; if it referenced *generalized* seizures, the classification was adjusted accordingly to generalized. Both keywords were extracted to ensure comprehensive categorization.

C Extraction of keywords associated with interictal epileptiform discharges (IEDs) and their respective locations from the impression section: This procedure was applied to the abnormal reports identified in the earlier step (A) that contained *seizure* activity. We defined keywords relating to IEDs as any phrases incorporating the terms *spike*, *discharge*, *wave*, *sharp*, or all possible combinations of these four terms (such as *spike discharge* or *sharp wave discharge*). The keywords related to the locations of IEDs were defined as phrases with one or all possible combinations of the names of the 19 channels according to the international 10–20 system (e.g., *Fp1* or *F3F7*).

2.3 Deep learning model

In the first phase of our algorithm development, we established deep learning-based binary classification models aimed at categorizing EEG reports as either normal or abnormal. For this purpose, we employed two publicly available language models from the Hugging Face repository: Bidirectional Encoder Representations from Transformers (BERT) and Clinical BERT. BERT is a transformer-based deep learning model pretrained on extensive datasets such as BooksCorpus and Wikipedia. In contrast, Clinical BERT is a specialized variant of BERT, pretrained on clinical text corpora, which includes clinical notes extracted from the MIMIC-III database (14–17).

We selected the BERT-base model from Hugging Face, characterized by 12 transformer layers, hidden size of 768, 12 self-attention heads, and a total parameter count of 110 million, which aligns with the specifications of Clinical BERT. Both the BERT and Clinical BERT models were fine-tuned using an equal dataset composed of 5,173 normal reports and 5,173 abnormal reports to optimize their performance in classification tasks. Each report was tokenized with a maximum length limit of 128 tokens before feeding to the input layer of the model. No additional preprocessing was applied to the reports. AutoTokenizer from Hugging Face tokenized all the reports yielding input IDs, token type IDs, and attention mask value sets for each report. We used zero padding to the maximum length of tokens and truncation to provide data sets for the input layer. Supplementary Table 1 shows an example of a tokenized EEG report.

To augment the capability of the model in sentence recognition, we concatenated each model with long short-term memory (LSTM) networks with both BERT and Clinical BERT, resulting in two enhanced architectures: BERT with LSTM and Clinical BERT with LSTM. In these configurations, the output generated from the final hidden layer of each model was subsequently directed into the input layer of the LSTM, thereby creating a cohesive model that leverages the strengths of both deep learning frameworks for improved classification outcomes. Supplementary Figure 1 shows our model architectures.

We used 64 LSTM units, a dropout rate of 0.1, and a sigmoid activation function, which yielded a probability score between 0 and 1. Specifically, an input report was classified as normal if the output was less than 0.5 and as abnormal if it was equal to or greater than 0.5. We used adaptive moment estimation as an optimizer with a learning rate of 1×10^{-5}, a binary cross entropy loss function, a batch size of 32, and 5 epochs for model training. All algorithmic processes were executed using Python 3.8 and Tensorflow 2.10, facilitated by an NVIDIA 3080Ti graphics processing unit with 12GB of memory, in conjunction with the Compute Unified Device Architecture (CUDA) version 11.4 programming interface.

2.4 Performance evaluation

The performance of our algorithm was rigorously assessed through three key methodologies: (1) model evaluation, (2) internal validation, and (3) external validation. During the model evaluation phase, we examined the performance of our two deep learning models in classifying reports as normal or abnormal, using a dataset comprising 1,000 normal and 1,000 abnormal EEG reports sourced from SNUBH. The evaluation metrics included sensitivity, specificity, accuracy, and the area under the receiver operating characteristic curve (AUC). Internal and external validations were subsequently conducted to ascertain the applicability of the algorithm within a clinical setting, where EEG reports were systematically converted into structured tabular data from a clinical perspective. For the internal validation, we randomly selected 200 normal and 200 abnormal reports from the previously mentioned model evaluation dataset. In contrast, the external validation utilized a separate set of 200 normal and 200 abnormal reports from SNUCH. Two neurologists (H.K. and J.K.) compared 400 reports from SNUBH and 400 reports of SNUCH with their corresponding algorithm outputs in terms of all hierarchical procedures for internal and external validations, respectively. We adopted the Clinical BERT with LSTM model for normal and abnormal classifications in the internal and external validations. For the performance of the Clinical BERT with LSTM model, we additionally performed 6-fold cross-validation using the EEG reports from SNUBH. 1,000 normal and 1,000 abnormal reports were used for evaluation and the remaining ones were used for model training in each round.

3 Results

3.1 Model evaluation

In our evaluation of the classification models for distinguishing between normal and abnormal EEG reports from SNUBH, both the BERT with LSTM and Clinical BERT with LSTM models demonstrated impressive performance metrics: sensitivity of 100%, specificity of 99.90%, accuracy of 99.95%, and an AUC of 100%. Notably, each model produced one false-positive result. The outputs of the models, when averaged over 1,000 normal reports, were

recorded as 0.173 ± 2.410% for the BERT with LSTM and 0.175 ± 3.137% for the Clinical BERT with LSTM. In contrast, the model outputs averaged over 1,000 abnormal reports were significantly higher, with the BERT with LSTM yielding 99.854 ± 0.175% and the Clinical BERT with LSTM achieving 99.870 ± 0.656%. Additionally, our Supplementary Table 2 includes detailed outputs from the Clinical BERT with LSTM model alongside the corresponding keyword extraction results for both 1,000 normal and 1,000 abnormal EEG reports. Supplementary Table 3 shows confusion matrices over 6-fold cross-validation of the Clinical BERT with LSTM model with the average sensitivity, specificity, accuracy, and AUC of 99.88, 99.98, 99.93, and 100%, respectively.

3.2 Internal validation

During the internal validation using the EEG reports from SNUBH, we attained a perfect accuracy of 100% in Step 1 for the classification of normal and abnormal EEG reports. Furthermore, in Step 2, the accuracy rates for the keyword extraction processes were also commendable, with 100% accuracy for classification A (*dysfunction* or *seizure*), 98.50% for classification B (*focal* or *generalized*), and 97.50% for classification C (IEDs and locations). Among the 200 abnormal EEG reports, we failed to extract the *generalized* information because the relevant keyword did not exist in the clinical correlation part in two reports, and in one report, the keyword was misspelled. Furthermore, we encountered challenges in extracting the locations of IEDs, because these characteristics were not specified as channel names in four different reports. Conversely, the model mistakenly identified a channel name that referred to locations of abnormal background activities in one of the reports.

3.3 External validation

During the external validation process utilizing EEG reports from the SNUCH, we achieved a perfect accuracy rate of 100% in Step 1 for classifying EEG reports as normal or abnormal. In Step 2, we recorded accuracy rates of 100, 100, and 88.50% for our keyword extraction procedures labeled A, B, and C, respectively. Among the 200 abnormal EEG reports analyzed from SNUCH, we were unable to extract the locations of IEDs in six reports due to the absence of channel name representation. Additionally, we erroneously extracted channel names indicative of abnormal background activities in 16 reports. In one instance, we mistakenly classified *delta waves*, described in a phrase concerning background activity, as an IED.

The detailed results from both internal and external validations are presented in Table 1. Furthermore, Tables 2, 3 show representative abnormal EEG reports from the SNUBH and SNUCH, respectively, highlighting both the successful and erroneous conversions into structured data during our validation process.

TABLE 1 Detailed results of the internal and external validations using the electroencephalography (EEG) reports from Seoul National University Bundang Hospital (SNUBH) and an independent tertiary hospital (SNUCH), respectively.

		Step 1	Step 2		
			A	B	C
SNUBH	I. Normal	200	-	-	-
	II. Abnormal	200	200	197	195
	Accuracy (%)	100	100	98.50	97.50
SNUCH	I. Normal	200	-	-	-
	II. Abnormal	200	200	200	177
	Accuracy (%)	100	100	100	88.50

A, B, and C in Step 2 denote the keyword extraction procedures for *dysfunction* or *seizure*, *focal (partial)* or *generalized* seizure, and the existence of interictal epileptiform discharges and their locations, respectively. I and II in the second column represent the number of EEG reports that are correctly converted to structured data for the Step 1 and Step 2.

4 Discussion

The present findings confirm that the NLP-based hierarchical algorithm we developed effectively classified free-text EEG reports from pediatric patients diagnosed with epilepsy as either normal or abnormal. The algorithm demonstrated its capability to identify the presence of cerebral dysfunction or seizures within the abnormal reports. We demonstrated that our algorithm converted abnormal reports to tabular data with an accuracy higher than 98.5% for the determination of focal or generalized seizures and higher than 88.5% for the identification of IEDs and their locations. Neurologists identified a set of clinical keywords essential for the diagnosis of epilepsy prior to the analysis. Following this, we systematically extracted keywords from abnormal reports through a series of methodical procedures. Accordingly, we successfully developed structured datasets that accurately correspond to the EEG reports obtained from two distinct medical institutions.

4.1 Normal and abnormal classification

In Step 1 of our algorithm, we implemented a deep learning-based classification model designed specifically to identify abnormal EEG reports for subsequent keyword extraction tasks. Previous studies have demonstrated that BERT-based classification models perform exceptionally well in text classification across various medical domains (11, 18–20). Therefore, we were optimistic that we could apply our detailed rules for keyword extraction exclusively to the abnormal reports once we amassed a sufficient quantity of these datasets. Additionally, in the deep learning-based classification, we expected to avoid two situations: skipping required rules due to misspelled *abnormal*, or executing unnecessary rules due to misspelled *normal* in the reports. If we had utilized only the rule-based classification approach in Step 1, we would have faced a considerable risk of misclassifying reports, as misspellings in both *abnormal* and *normal* reports could easily lead to false recognition, and thus, erroneous classification of normal and abnormal reports.

As most normal EEG reports contain general words describing waking and sleep states, our BERT and Clinical BERT models had no additional domain-specific fine-tuning, unlike previous studies (11, 20, 21). We fine-tuned our models for the binary classification of normal and abnormal reports. Both BERT and Clinical BERT models exhibited high performance for binary classification, probably because the properties of normal and abnormal reports were highly different from each other in that the abnormal reports contained a significantly

10.3389/fneur.2025.1521001

TABLE 2 Representative electroencephalography (EEG) reports from Seoul National University Bundang Hospital (top three rows) and an independent tertiary hospital (bottom three rows) that are correctly converted to structured data evaluated by two neurologists in the internal and external validations, respectively.

EEG report	Step 1	Step 2				Model output
		A	B	C		
(Impression) This is a normal waking and mildly abnormal stage N1-2 sleep record due to a few low-voltage spike discharges from O2O1, during sleep. Clinical correlation: this recording is suggestive of focal seizure (subtle axial myoclonus without EEG changes was noted).	Abnormal	Seizure	Focal	Spike discharges	O2O1	0.9991
(Impression) This is a moderately abnormal waking and stage I-II sleep record due to: (1) Poorly regulated posterior rhythm for age. (2) High amplitude irregular 1.5–2 Hz delta slowing on both posterior head region. (3) Frequent spike discharge from C3P3T3 or F8T4 activated by sleep. Clinical correlation: This record is indicative of diffuse cerebral dysfunction and consistent with partial seizure.	Abnormal	Dysfunction, seizure	Partial	Spike discharge	C3P3T3 or F8T4	0.9991
(Impression) This is a mildly abnormal sedated sleep record due to intermittent medium to high amplitude 2.5–3 Hz delta activities on the anterior head region. Clinical correlation: This recording is indicative of anterior cerebral dysfunction.	Abnormal	Dysfunction				0.9990
This is a mildly abnormal Stage II sleep record due to a few low voltage spike discharges from F3C3P3 or P4T4. Clinical correlation: this recording is consistent with focal seizure.	Abnormal	Seizure	Focal	Spike discharges	F3C3P3 or P4T4	0.9992
This is a moderately abnormal Stage II sleep record due to: (1) Frequent generalized polyspike wave discharges or paroxysmal fast activities. (2) Frequent spike discharges form C3T3 or C4T4. Clinical correlation: this recording is consistent with focal and generalized seizure.	Abnormal	Seizure	Focal and generalized	Polyspike wave discharges, spike discharges	C3T3 or C4T4	0.9991
This is a moderately abnormal drowsy and sleep record due to: (1) Intermittent delta activities on the anterior head region. (2) Frequent low to medium voltage spike or spike wave discharges from Fp1F3F7 and Fp2F4F8. Clinical correlation: this recording is suggestive of diffuse cerebral dysfunction and consistent with focal seizure.	Abnormal	Dysfunction, seizure	Focal	Spike or spike wave discharges	Fp1F3F7 and Fp2F4F8	0.9991

A, B, and C in Step 2 denote the keyword extraction procedures for *dysfunction* or *seizure*, *focal (partial)* or *generalized* seizure, and the existence of interictal epileptiform discharges and their locations, respectively. The model output represents the probability from 0 to 1 that its corresponding report is determined as a normal one if the model output <0.5 and as an abnormal one if the model output ≥0.5.

higher frequency of epilepsy-related terminology when compared to their normal counterparts. Another reason of the similar performance of the two models to each other may have been arisen from the data sources of the Clinical BERT. The MIMIC-III database contained a large number of clinical text data across various diseases. However, its knowledge in the field of epilepsy could be possibly weak because it handled less amount of data for neurological diseases and EEG examinations (22). During our evaluation, we encountered a single false positive for both models, an occurrence linked to the unique sentence structure of the report in question. This structure deviated substantially from that of typical normal reports, as it included enumerated numerical values regarding background activity rather than descriptive sentences detailing the state of normal EEG recordings.

Notably, we observed that the output scores from the Clinical BERT model were marginally higher than those from the BERT model for abnormal reports. Although this difference did not reach statistical significance, we hypothesized that the Clinical BERT model might inherently be predisposed to assign higher probabilities to abnormal reports than the BERT model. This observation prompts the necessity for further research to validate our hypothesis. Based on these findings, we opted to utilize the Clinical BERT model for Step 1 in both our internal and external validation processes.

TABLE 3 Representative electroencephalography (EEG) reports from Seoul National University Bundang Hospital (top four rows) and Seoul National University Children's Hospital (bottom three rows) that are incorrectly converted to structured data evaluated by two neurologists in the internal and external validations, respectively.

EEG report	Step 1	Step 2				Model output
		A	B	C		
(Impression) This is a moderately abnormal waking and stage I-II sleep record due to: (1) Frequent episodes of generalized rhythmic 3 Hz spike wave discharges with videographic evidence of dialeptic seizure. (2) Occasional generalized spike wave discharges Clinical correlation: this recording is diagnostic of electroclinical absence seizure.	Abnormal	Seizure		Spike wave discharges (2)		0.9990
(Impression) This is a mildly abnormal waking and normal stage I-II sleep record due to two episodes of brief, rhythmic, bifrontal, 3 Hz, rhythmic delta activities (which cannot be discriminated from typical 3 Hz spike wave discharges - video is not available.) Clinical correlation: this recording is suggestive of generalized seizure.	Abnormal	Seizure		Spike wave discharges		0.9990
(Impression) This is a moderately abnormal sedated sleep record due to: (1) Diffuse high amplitude irregular pleomorphic 1.5–2.0 Hz delta activities. (2) Frequent spike discharges from the left or right centro-temporal area. Clinical correlation; this record is indicative of diffuse cerebral dysfunction and consistent with partial seizure (modified hypoarrythmia).	Abnormal	Dysfunction, seizure	Partial	Spike discharges		0.9991
(Impression) This is a mildly abnormal waking and normal stage N1-2 sleep record due to brief, intermittent, high amplitude, 2–3 Hz rhythmic delta activities from both posterior head region or P4O2, during and after hyperventilation. Clinical correlation: this recording is suggestive of both posterior cerebral dysfunction worse on the right hemisphere.	Abnormal	Dysfunction			P4O2	0.9990
This is a moderately abnormal drowsy and Stage I-II sleep record due to: (1) Intermittent delta activities on T6O2 during drowsiness. (2) A few or occasional spike discharges from T4T6 Clinical correlation: this recording is suggestive of left temporo-occipital cerebral dysfunction and consistent with focal seizure	Abnormal	Dysfunction, seizure	Focal	Spike discharges	T6O2, T4T6	0.9991
This is a mildly abnormal sleep record due to a few atypical spike discharges from the right or left frontocentral areas. Clinical correlation: this recording is suggestive of focal seizure	Abnormal	Seizure	Focal	Spike discharges		0.9991
This is a moderately abnormal record due to: (1) Medium to high delta waves in right hemisphere. (2) Slowing in both hemisphere. Clinical correlation: this recording is indicative of diffuse cerebral dysfunction.	Abnormal	Dysfunction		Waves		0.9986

A, B, and C in the Step 2 denote the keyword extraction procedures for *dysfunction* or *seizure*, *focal (partial)* or *generalized* seizure, and the existence of interictal epileptiform discharges and their locations, respectively. The model output represents the probability from 0 to 1 that its corresponding report is determined as a normal one if the model output <0.5 and as an abnormal one if the model output ≥0.5.

4.2 Keyword extraction

In Step 2 of our algorithm, we systematically implemented a series of rules to extract specific keywords from abnormal EEG reports. We argue that a rule-based approach to keyword extraction is justified, as a finite set of key terms can effectively capture the defining features of abnormal EEG reports. This assertion is supported by prior research that examined the limitations of BERT in this context (23). Moreover,

TABLE 4 Comparison of performance metrics of our work and recent natural language processing studies in the field of epilepsy.

Study	Method	Objective	Result
This study	Rule-based and BERT	To convert EEG reports into tabular data by classification and keyword extraction	• Internal: accuracy = 0.985 (focal or generalized seizure), accuracy = 0.975 (identification of IEDs and locations) • External: accuracy = 1.0 (focal or generalized seizure), accuracy = 0.885 (identification of IEDs and locations)
Beaulieu-Jones et al. (28)	Clinical-longformer	To predict seizure recurrence after an initial seizure-like event	• Additional domain-specific and location-specific pretraining: F1-score = 0.826, AUC = 0.897 • No pretraining: F1-score = 0.739, AUC = 0.846
Tao et al. (9)	Rule-based	To extract temporal information of seizure onset from discharge summaries	Precision = 0.750, recall = 0.651, and F1-score = 0.697
Xie et al. (11)	BERT	To extract clinical information (seizure frequency, seizure freedom) from clinical notes	• Median accuracy for classification: 0.837 (BioClinical BERT), 0.747 (RoBERTa) • Median F1 score for text extraction: 0.845 and 0.834 (RoBERTa)
Decker et al. (10)	Rule-based	To extract seizure data (seizures and frequency) from clinical notes	• Internal test: recall = 0.70, precision = 0.95, and F1-score = 0.82 • External test: recall = 0.22, precision = 0.73, and F1-score = 0.40
Rawal and Varatharajah (12)	Rule-based and BERT	To extract attributes for organized reporting from EEG reports	• Seizure classification: F1-scores = 0.92 • Epilepsy classification: F1-scores = 0.82 • Normal and abnormal classification: F1-scores = 0.97
Fonferko-Shadrach et al. (8)	Rule-based	To extract detailed clinical information from epilepsy clinic letters	Precision = 0.914, recall = 0.814, and F1-score = 0.861
Cui et al. (7)	Rule-based	To extract epilepsy phenotypes and anatomical locations from clinical discharge summaries	• Epilepsy phenotypes: micro-averaged precision = 0.924, recall = 0.931, and F1-score = 0.927 • Correlated phenotypes and anatomical locations: precision = 0.852, recall = 0.859, and F1-score = 0.856
Cui et al. (13)	Rule-based	To extract seizure-related clinical free text from discharge summaries	Precision = 0.936, recall = 0.840, and F1-score = 0.885

we aimed to enhance the transparency of the keyword extraction process in Step 2 by utilizing explicit rules, which aligns with the previous studies that underscored concerns regarding reproducibility in machine learning models (4, 24).

Rule-based techniques enable an accurate extraction of keywords from sentences without manipulating statistical scores, barring any typographical errors. Drawing on neurologists' prior identification of significant clinical keywords, we established a sequential keyword extraction process tailored to abnormal reports. This hierarchical framework serves to streamline our algorithm by minimizing the scope of target variables within the reports. We contend that the reduced complexity of our algorithm is conducive to achieving high performance, particularly in the detection of cerebral dysfunction, focal or generalized seizures, and the identification of IEDs.

However, during internal validation, we encountered a limitation: the keyword of *generalized* was not extracted from the two abnormal EEG reports of patients diagnosed with absence seizures. The generalized 3 Hz spike-and-wave complexes represent the typical electrographic signatures of absence seizures (25, 26). Consequently, although the clinical correlations observed in the abnormal reports of patients with absence seizures are not universally applicable, these reports strongly suggest the presence of generalized seizures based on their signatures. To address this challenge, it may be beneficial to implement deep learning techniques aimed at analyzing the reports at the sentence level, or to introduce supplementary rules to accurately identify the type of seizure. To overcome this issue, we may need to utilize specific deep learning-based models to automatically match a variety of regional terminologies for their corresponding channel names.

A significant number of failures were recorded during the final step of Step 2, particularly regarding the localization of IEDs in the abnormal reports from both medical institutions. The present algorithm struggled to detect channel names as the locations of IEDs were frequently described using regional terminologies, such as "*centro-temporal*" or "*fronto-central*," in 10 abnormal reports (4 from SNUBH and 6 from SNUCH). Thus, these regional terms need to be included as target keywords; however, we are concerned about the vast array of potential combinations of these regional names.

Additionally, our algorithm erroneously identified the channel names that referred to background activities, such as "*delta activities from P4O2*," in 17 abnormal reports (1 from SNUBH and 16 from SNUCH). Abnormal reports can contain both background activities and IEDs simultaneously. Therefore, it is crucial to develop precise rules for determining channel names after categorizing the data into distinct domains, such as background activity or IEDs. This approach is reminiscent of a previous study by (27), which demonstrated an

effective two-level keyword extraction approach from clinical notes. Typographical errors and inappropriate words constituted critical issues that require resolution in our keyword extraction procedures, such as misspelled *generalized* and *delta waves* instead of *delta activities* in the abnormal reports from SNUBH and SNUCH. In the rule-based keyword extraction, it may be highly challenging to overcome those troubles due to the necessity of additional complicated rules for searching replaceable words based on the detection of every possible types of typos or approximate string matching.

During the internal and external validation procedures, typographical errors and improper word usage could have led to both false negatives and false positives. For example, EEG reports that misspelled the term *generalized* have been mistakenly classified as lacking generalized seizure characteristics. Similarly, reports noting *delta waves* as background activity could have been erroneously interpreted as containing IEDs simply due to the appearance of the word *waves*. However, because these observations were drawn from only a few instances, it remains difficult to make broad generalizations based solely on these examples. Moving forward, we plan to build large-scale databases comprising numerous EEG reports to more thoroughly investigate and address such errors, ultimately improving the reliability and accuracy of automated EEG report analysis.

4.3 Applications and limitations

A multitude of studies leveraging NLP techniques have focused on the analysis of unstructured data related to epilepsy. Rule-based methodologies have been effectively employed to extract various seizure-related parameters (8–11, 13), as well as patient clinical information (8) and distinct epilepsy phenotypes (7) from clinical notes and discharge summaries. Additionally, BERT-based models have been implemented to categorize clinical notes based on seizure occurrence, achieving a notable median accuracy of 83.7% (11). These models have also been applied to classify publicly available clinical reports with respect to epilepsy and related abnormalities, resulting in impressive F1 scores of 82 and 97%, respectively (12).

In a recent advancement, a transformer-based large language model known as clinical-longformer, pre-trained on publicly accessible clinical notes, was utilized to predict seizure recurrence in EMR data, achieving an F1 score of 82.6% (28). Note that, to date, no NLP-focused studies have successfully developed a method for transforming unstructured EEG reports into structured clinical components. We posit that our hierarchical algorithm could serve a critical function in the establishment of specialized databases, facilitating the organization and analysis of a significant number of EEG reports from patients diagnosed with epilepsy. Unlike the visual interface based on discharge summaries reported in a previous study (13), our structured outcomes in a tabular format required specific keywords solely from EEG reports. Table 4 presents a comparative overview of the performance metrics for our method alongside those reported in the aforementioned NLP studies. While these comparisons can provide useful insights, making direct parallels is challenging due to the distinct objectives and methodologies employed in each investigation. Importantly, the novelty of our work lies in the development of structured datasets derived from EEG reports—an underutilized resource in clinical research—that extend beyond conventional NLP techniques. By focusing on this unique data source, our approach has the potential to enhance clinical databases in ways that previous studies have not fully explored, thereby paving the way for more comprehensive and clinically relevant analyses. By integrating NLP techniques with large-scale medical records—such as discharge summaries and clinical notes—researchers and clinicians can enhance diagnostic processes for complex conditions, including rare and previously undiagnosed diseases. These approaches enable the automated extraction and analysis of relevant clinical information, potentially improving both the speed and accuracy of identifying elusive disorders that often pose significant challenges to traditional diagnostic methods (29). It could also potentially aid with tailored treatment and diagnosis of clinical diseases with text-heavy clinical notes such as headache patients (30).

Thus, our methodology presents an innovative NLP-driven framework aimed at extracting pertinent information from unstructured text within medical reports, specifically targeting EEG reports. We customized our algorithm to align with the unique formatting of these reports, facilitating the extraction of key variables of interest. Nevertheless, this study acknowledges several notable limitations. First, the internal and external validation phases were conducted using a relatively small sample of EEG reports, which may impact the robustness of our findings. Additionally, the EEG reports utilized in the external validation phase bore a close resemblance to those in the internal validation, thereby limiting the diversity of our dataset. To enhance the validity and generalizability of our findings, we strongly advocate for extensive multi-institutional studies that can address these concerns regarding sample size and diversity. Our study was constrained by the use of internal and external datasets that were relatively similar, which may have limited the generalizability of our findings. To address this issue and improve the robustness of our text classification models, we could incorporate EEG reports from multiple institutions representing various reporting formats and clinical settings. By doing so, we anticipate not only enhancing the performance of our classifiers but also developing more targeted keyword extraction strategies tailored to each institution's unique report structure, ultimately leading to more accurate and widely applicable analysis of EEG data in the future studies. In terms of ethical concerns and data security, it is highly required to ensure that all the reports have no patients' personal and sensitive medical records keeping them safe in their corresponding institutions. In terms of data access, federated learning can be suggested for deep learning and NLP tasks through multi-institutional collaborations (31). Also, future research should consider exploring state-of-the-art large language models beyond the present rule-based methods for tackling complex tasks such as handling typographical errors, inappropriate words, and regional terminologies by automated correction techniques (32, 33).

5 Conclusion

This study introduces a hierarchical algorithm designed to transform unstructured EEG reports from pediatric epilepsy patients into structured data presented in a tabular format through the application of NLP techniques. Utilizing BERT-based deep learning models for text classification, we subsequently applied a series of rule-based procedures for the extraction of relevant keywords. Given that

neurologists pre-select specific clinical keywords, we crafted a hierarchical structure that streamlines the process, enhancing the ability of the algorithm to manage the nuances of free-text EEG reports and produce standardized tables. We believe that our approach holds significant promise for the creation of specialized databases focused on EEG reports, thereby advancing healthcare research and clinical applications.

Data availability statement

The original contributions presented in the study are included in the article/Supplementary material, further inquiries can be directed to the corresponding author.

Ethics statement

The studies involving humans were approved by the Institutional Review Board at Seoul National University Bundang Hospital (Approval Number: B-2312-873-107). The studies were conducted in accordance with the local legislation and institutional requirements. The ethics committee/institutional review board waived the requirement of written informed consent for participation from the participants or the participants' legal guardians/next of kin due to the retrospective nature of the study.

Author contributions

YGC: Formal analysis, Methodology, Software, Writing – original draft, Writing – review & editing. JC: Data curation, Investigation, Methodology, Validation, Writing – original draft, Writing – review & editing. YHK: Data curation, Investigation, Writing – review & editing. HWK: Formal analysis, Software, Writing – review & editing. HK: Conceptualization, Data curation, Funding acquisition, Investigation, Methodology, Project administration, Validation, Writing – original draft, Writing – review & editing. YSK: Conceptualization, Writing – review & editing. S-YL: Conceptualization, Writing – review & editing. Y-MS: Conceptualization, Funding acquisition, Writing – review & editing.

Funding

The author(s) declare that financial support was received for the research, authorship, and/or publication of this article. This research was supported by a grant from the Korea Health Technology R&D Project through the Korea Health Industry Development Institute (KHIDI), funded by the Ministry of Health and Welfare, Republic of Korea (grant number: HI23C1532).

Conflict of interest

The authors declare that the research was conducted in the absence of any commercial or financial relationships that could be construed as a potential conflict of interest.

Generative AI statement

The authors declare that no Gen AI was used in the creation of this manuscript.

Publisher's note

Supplementary material

The Supplementary material for this article can be found online at: https://www.frontiersin.org/articles/10.3389/fneur.2025.1521001/full#supplementary-material

References

1. Kim H, Hwang H. Resting-state electroencephalography (EEG) functional connectivity analysis. *Ann Child Neurol.* (2018) 26:129–34. doi: 10.26815/jkcns.2018.26.3.129

2. Morris H, Kaplan PW, Kane N. Electroencephalography in encephalopathy and encephalitis. *Pract Neurol.* (2024) 24:2–10. doi: 10.1136/pn-2023-003798

3. Noachtar S, Remi J. The role of EEG in epilepsy: a critical review. *Epilepsy Behav.* (2009) 15:22–33. doi: 10.1016/j.yebeh.2009.02.035

4. Yew ANJ, Schraagen M, Otte WM, Van Diessen E. Transforming epilepsy research: a systematic review on natural language processing applications. *Epilepsia.* (2023) 64:292–305. doi: 10.1111/epi.17474

5. Fu S, Chen D, He H, Liu S, Moon S, Peterson KJ, et al. Clinical concept extraction: a methodology review. *J Biomed Inform.* (2020) 109:103526. doi: 10.1016/j.jbi.2020.103526

6. Li I, Pan J, Goldwasser J, Verma N, Wong WP, Nuzumlali MY, et al. Neural natural language processing for unstructured data in electronic health records: a review. *Comput Sci Rev.* (2022) 46:100511. doi: 10.1016/j.cosrev.2022.100511

7. Cui L, Sahoo SS, Lhatoo SD, Garg G, Rai P, Bozorgi A, et al. Complex epilepsy phenotype extraction from narrative clinical discharge summaries. *J Biomed Inform.* (2014) 51:272–9. doi: 10.1016/j.jbi.2014.06.006

8. Fonferko-Shadrach B, Lacey AS, Roberts A, Akbari A, Thompson S, Ford DV, et al. Using natural language processing to extract structured epilepsy data from unstructured clinic letters: development and validation of the ExECT (extraction of epilepsy clinical text) system. *BMJ Open.* (2019) 9:e023232. doi: 10.1136/bmjopen-2018-023232

9. Tao S, Abeysinghe R, De La Esperanza BT, Lhatoo S, Zhang GQ, Cui L. Extracting temporal expressions of first seizure onset from epilepsy patient discharge summaries. *AMIA Jt Summits Transl Sci Proc.* (2023) 2023:515–24.

10. Decker BM, Turco A, Xu J, Terman SW, Kosaraju N, Jamil A, et al. Development of a natural language processing algorithm to extract seizure types and frequencies from the electronic health record. *Seizure.* (2022) 101:48–51. doi: 10.1016/j.seizure.2022.07.010

11. Xie K, Gallagher RS, Conrad EC, Garrick CO, Baldassano SN, Bernabei JM, et al. Extracting seizure frequency from epilepsy clinic notes: a machine reading approach to natural language processing. *J Am Med Inform Assoc.* (2022) 29:873–81. doi: 10.1093/jamia/ocac018

12. Rawal S., Varatharajah Y. (2021). "SCORE-IT: A machine learning framework for automatic standardization of EEG reports", in: IEEE signal processing in medicine and biology symposium. (Philadelphia, PA, USA: IEEE).

13. Cui L, Bozorgi A, Lhatoo SD, Zhang GQ, Sahoo SS. EpiDEA: extracting structured epilepsy and seizure information from patient discharge summaries for cohort identification. *AMIA Annu Symp Proc*. (2012) 2012:1191–200.

14. Alsentzer E., Murphy J.R., Boag W., Weng W.-H., Jin D., Naumann T., et al. (2019). "Publicly available clinical BERT embeddings". Available online at: https://arxiv.org/abs/1904.03323 (Accessed September 27, 2023).

15. Crema C, Attardi G, Sartiano D, Redolfi A. Natural language processing in clinical neuroscience and psychiatry: a review. *Front Psych*. (2022) 13:946387. doi: 10.3389/fpsyt.2022.946387

16. Devlin J., Chang M.-W., Lee K., Toutanova K. (2019). "BERT: pre-training of deep bidirectional transformers for language understanding". Available online at: https://arxiv.org/abs/1810.04805 (Accessed September 27, 2023).

17. Huang K., Altosaar J., Ranganath R. (2020). "ClinicalBERT: modeling clinical notes and predicting hospital readmission", In ACM conference on health, inference, and learning; workshop track. Toronto, ON: Association for Computing Machinery.

18. Han S, Zhang RF, Shi L, Richie R, Liu H, Tseng A, et al. Classifying social determinants of health from unstructured electronic health records using deep learning-based natural language processing. *J Biomed Inform*. (2022) 127:103984. doi: 10.1016/j.jbi.2021.103984

19. Miller MI, Orfanoudaki A, Cronin M, Saglam H, Yeon S, Kim I, et al. Natural language processing of radiology reports to detect complications of ischemic stroke. *Neurocrit Care*. (2022) 37:291–302. doi: 10.1007/s12028-022-01513-3

20. Nishigaki D, Suzuki Y, Wataya T, Kita K, Yamagata K, Sato J, et al. BERT-based transfer learning in sentence-level anatomic classification of free-text radiology reports. *Radiol Artif Intell*. (2023) 5:e220097. doi: 10.1148/ryai.220097

21. Zhou S, Wang N, Wang L, Liu H, Zhang R. CancerBERT: a cancer domain-specific language model for extracting breast cancer phenotypes from electronic health records. *J Am Med Inform Assoc*. (2022) 29:1208–16. doi: 10.1093/jamia/ocac040

22. Johnson AE, Pollard TJ, Shen L, Lehman LW, Feng M, Ghassemi M, et al. MIMIC-III, a freely accessible critical care database. *Sci Data*. (2016) 3:160035. doi: 10.1038/sdata.2016.35

23. Gao S, Alawad M, Young MT, Gounley J, Schaefferkoetter N, Yoon HJ, et al. Limitations of transformers on clinical text classification. *IEEE J Biomed Health Inform*. (2021) 25:3596–607. doi: 10.1109/JBHI.2021.3062322

24. Beam AL, Manrai AK, Ghassemi M. Challenges to the reproducibility of machine learning models in health care. *JAMA*. (2020) 323:305–6. doi: 10.1001/jama.2019.20866

25. Bai X, Vestal M, Berman R, Negishi M, Spann M, Vega C, et al. Dynamic time course of typical childhood absence seizures: EEG, behavior, and functional magnetic resonance imaging. *J Neurosci*. (2010) 30:5884–93. doi: 10.1523/JNEUROSCI.5101-09.2010

26. Hughes JR. Absence seizures: a review of recent reports with new concepts. *Epilepsy Behav*. (2009) 15:404–12. doi: 10.1016/j.yebeh.2009.06.007

27. Lituiev DS, Lacar B, Pak S, Abramowitsch PL, De Marchis EH, Peterson TA. Automatic extraction of social determinants of health from medical notes of chronic lower back pain patients. *J Am Med Inform Assoc*. (2023) 30:1438–47. doi: 10.1093/jamia/ocad054

28. Beaulieu-Jones BK, Villamar MF, Scordis P, Bartmann AP, Ali W, Wissel BD, et al. Predicting seizure recurrence after an initial seizure-like episode from routine clinical notes using large language models: a retrospective cohort study. *Lancet Digit Health*. (2023) 5:e882–94. doi: 10.1016/S2589-7500(23)00179-6

29. Cho J, Joo YS, Yoon JG, Lee SB, Kim SY, Chae JH, et al. Characterizing families of pediatric patients with rare diseases and their diagnostic odysseys: a comprehensive survey analysis from a single tertiary center in Korea. *Ann Child Neurol*. (2024) 32:167–75. doi: 10.26815/acn.2024.00472

30. Cho J, Han JY, Cho A, Yoo S, Lee HY, Kim H. Enhancing clinical history taking through the implementation of a streamlined electronic questionnaire system at a pediatric headache clinic: development and evaluation study. *JMIR Med Inform*. (2024) 12:e54415. doi: 10.2196/54415

31. Peng L, Luo G, Zhou S, Chen J, Xu Z, Sun J, et al. An in-depth evaluation of federated learning on biomedical natural language processing for information extraction. *NPJ Digit Med*. (2024) 7:127. doi: 10.1038/s41746-024-01126-4

32. Bedi S, Liu Y, Orr-Ewing L, Dash D, Koyejo S, Callahan A, et al. Testing and evaluation of health care applications of large language models: a systematic review. *JAMA*. (2025) 333:319–28. doi: 10.1001/jama.2024.21700

33. Pais C, Liu J, Voigt R, Gupta V, Wade E, Bayati M. Large language models for preventing medication direction errors in online pharmacies. *Nat Med*. (2024) 30:1574–82. doi: 10.1038/s41591-024-02933-8

frontiers | Frontiers in Neuroinformatics

TYPE Original Research
PUBLISHED 28 February 2025
DOI 10.3389/fninf.2025.1519391

OPEN ACCESS

EDITED BY
A. Amalin Prince,
Birla Institute of Technology and Science, India

REVIEWED BY
Vignayanandam Ravindernath Muddapu, Ecole Polytechnique Fédérale de Lausanne (EPFL), Switzerland
Xin Wang, Chinese Academy of Sciences, China
Sreejith Chandrasekharan Nair, Delft University of Technology, Netherlands

*CORRESPONDENCE
Christopher Ivan Hernandez
christopher.hernandez@ucf.edu
Waldemar Karwowski
wkar@ucf.edu

RECEIVED 29 October 2024
ACCEPTED 13 February 2025
PUBLISHED 28 February 2025

CITATION
Hernandez CI, Afek N, Gawłowska M, Oświęcimka P, Fafrowicz M, Slowik A, Wnuk M, Marona M, Nowak K, Zur-Wyrozumska K, Amon MJ, Hancock PA, Marek T and Karwowski W (2025) Impact of interferon-β and dimethyl fumarate on nonlinear dynamical characteristics of electroencephalogram signatures in patients with multiple sclerosis.
Front. Neuroinform. 19:1519391.
doi: 10.3389/fninf.2025.1519391

Impact of interferon-β and dimethyl fumarate on nonlinear dynamical characteristics of electroencephalogram signatures in patients with multiple sclerosis

Christopher Ivan Hernandez[1]*, Natalia Afek[2], Magda Gawłowska[3], Paweł Oświęcimka[4,5], Magdalena Fafrowicz[3], Agnieszka Slowik[6,7], Marcin Wnuk[6,7], Monika Marona[6,7], Klaudia Nowak[6,7], Kamila Zur-Wyrozumska[8], Mary Jean Amon[9], P. A. Hancock[10,11], Tadeusz Marek[12] and Waldemar Karwowski[1]*

[1]Computational Neuroergonomics Laboratory, Department of Industrial Engineering and Management Systems, University of Central Florida, Orlando, FL, United States, [2]Doctoral School in the Social Sciences, Jagiellonian University, Kraków, Poland, [3]Department of Cognitive Neuroscience and Neuroergonomics, Jagiellonian University, Kraków, Poland, [4]Complex Systems Theory Department, Institute of Nuclear Physics, Polish Academy of Sciences, Kraków, Poland, [5]Mark Kac Centre for Complex Systems Research, Jagiellonian University, Kraków, Poland, [6]Department of Neurology, Jagiellonian University Medical College, Kraków, Poland, [7]Department of Neurology, University Hospital in Krakow, Kraków, Poland, [8]Centre for Innovative Medical Education, Jagiellonian University Medical College, Kraków, Poland, [9]Department of Informatics, Luddy School of Informatics, Computing, and Engineering, Indiana University Bloomington, Bloomington, IN, United States, [10]Department of Psychology, University of Central Florida, Orlando, FL, United States, [11]Institute for Simulation and Training, University of Central Florida, Orlando, FL, United States, [12]Faculty of Psychology, SWPS University, Katowice, Poland

Introduction: Multiple sclerosis (MS) is an intricate neurological condition that affects many individuals worldwide, and there is a considerable amount of research into understanding the pathology and treatment development. Nonlinear analysis has been increasingly utilized in analyzing electroencephalography (EEG) signals from patients with various neurological disorders, including MS, and it has been proven to be an effective tool for comprehending the complex nature exhibited by the brain.

Methods: This study seeks to investigate the impact of Interferon-β (IFN-β) and dimethyl fumarate (DMF) on MS patients using sample entropy (SampEn) and Higuchi's fractal dimension (HFD) on collected EEG signals. The data were collected at Jagiellonian University in Krakow, Poland. In this study, a total of 175 subjects were included across the groups: IFN-β (n = 39), DMF (n = 53), and healthy controls (n = 83).

Results: The analysis indicated that each treatment group exhibited more complex EEG signals than the control group. SampEn had demonstrated significant sensitivity to the effects of each treatment compared to HFD, while HFD showed more sensitivity to changes over time, particularly in the DMF group.

Discussion: These findings enhance our understanding of the complex nature of MS, support treatment development, and demonstrate the effectiveness of nonlinear analysis methods.

KEYWORDS

electroencephalogram, complexity, nonlinear dynamics, sample entropy, Higuchi's fractal dimension, multiple sclerosis

1 Introduction

Multiple sclerosis (MS) is a chronic inflammatory disease of the central nervous system (CNS). It is defined by the spread of demyelinating lesions in the CNS over space and time (Siffrin et al., 2010). Neuronal injury occurs early in the disease and is linked to inflammatory activity. The remaining stages of neuronal damage after focal axonal lesions include axon degeneration and atrophy of neuronal cell bodies and dendrites (Siffrin et al., 2010). Atrophy and long-term disability in patients with MS can be attributed to the loss of neurons and their processes. Since inflammation is one of the leading causes of neurodegeneration, a combination of neuroprotective agents and anti-inflammatory treatments are encouraged early on Siffrin et al. (2010).

There are several treatments for multiple sclerosis; however, this paper will focus on two treatments widely used in managing this disease: Interferon-β (IFN-β) and dimethyl fumarate (DMF) (Reick et al., 2014). There are three main types of Interferon: Interferon-alpha, Interferon-beta, and Interferon-gamma (Jakimovski et al., 2018). Interferon-β treats different types of MS by reducing inflammation and regulating the immune response. This drug is administered via injection, and common side effects include flu-like symptoms, injection-site reactions, myalgia, depression, and increased liver enzymes (Jakimovski et al., 2018). Dimethyl fumarate is branded as Tecfidera®. Also known as B-12, it is an oral medication that regulates the immune system and prevents stress and inflammation by activating the nuclear factor erythroid 2-related pathway. Some side effects include gastrointestinal issues, flushing, and lymphopenia (Linker and Haghikia, 2016; Mills et al., 2018).

It is important to note that Sattarnezhad et al. (2022) recognized that patients on IFN-β experienced a higher occurrence of relapses and a higher number of magnetic resonance imaging (MRI) lesions. In contrast, those on dimethyl fumarate experienced a lower occurrence of relapses and a lower number of lesions (Sattarnezhad et al., 2022). D'Amico et al. (2021) also observed fewer relapses in dimethyl fumarate compared to IFN-β (D'Amico et al., 2021). To further back this up, Lorscheider et al. (2021) demonstrated that dimethyl fumarate had similar efficacy compared to another drug, fingolimod, and Cohen et al. (2010) proved fingolimod had a better performance than IFN-β (Lorscheider et al., 2021; Cohen et al., 2010). Table 1 shows a summary of the characteristics of IFN-β and DMF outlined in several studies (Cohen et al., 2010; D'Amico et al., 2021; Linker and Haghikia, 2016; Lorscheider et al., 2021; Mills et al., 2018; Jakimovski et al., 2018; Sattarnezhad et al., 2022).

TABLE 1 Summary of interferon-β vs. dimethyl fumarate.

Interferon-β (IFN-β)	Dimethyl fumarate (DMF)
Injection	Oral
Helps reduce inflammation and regulates the immune response	Regulates the immune system and prevents stress and inflammation
Side effects: flu-like symptoms, injection site reactions, myalgia, depression, and an increase in liver enzymes	Side effects: gastrointestinal issues, flushing, and lymphopenia
Higher occurrence of relapses	Lower occurrence of relapses
Higher number of MRI lesions	Lower number of MRI lesions

Many illnesses exhibit irregular brain wave activity, including MS, which can be detected and analyzed by electroencephalography (EEG) (Sanei and Chambers, 2007). Structural changes observed in the brain wave activity of MS patients can be identified by EEG analysis, as opposed to imaging methods, such as MRI (Carrubba et al., 2012). Despite appearing random, EEG signals exhibit complex characteristics with intricate temporal organization and are fundamentally deterministic (Rodriguez-Bermudez and Garcia-Laencina, 2015; Pritchard and Duke, 1995). Nonlinear analysis methods have successfully captured the complexities and nonlinearities in EEG signals, as opposed to conventional linear methods, such as autocorrelation (Rodriguez-Bermudez and Garcia-Laencina, 2015; Pritchard and Duke, 1995; Kargarnovin et al., 2023). Sample entropy (SampEn) and fractal dimension analysis are both commonly used to analyze the complexity or irregularity of a signal, particularly in nonlinear contexts, and we opted to use both sample entropy and Higuchi's fractal dimension (HFD) in our study (Kargarnovin et al., 2023; Hernandez et al., 2023).

Among the algorithms used for entropy estimation, particularly concerning EEG data, SampEn has been successfully employed (Bruce et al., 2009; Cuesta-Frau et al., 2017; Zhang et al., 2021). Created to reduce the bias of approximate entropy (ApEn), SampEn quantifies time series data regardless of the signal length, providing insights into complexity, irregularity, and rate at which new information is produced, making it especially valuable in analyzing noisy signals (Duran et al., 2013; Richman and Moorman, 2000). Studies have analyzed EEG signatures using SampEn, and a couple to note are studies conducted by Mohseni and Moghaddasi (2022) and Shalbaf et al. (2012). In Mohseni and Moghaddasi (2022), SampEn was used to develop a diagnostic tool for MS, and their tool attained significantly higher diagnostic activity compared to other MS diagnostic methods (Mohseni and Moghaddasi, 2022). Shalbaf et al. (2012) used SampEn to measure the effects of sevoflurane on electroencephalogram, and they concluded it outperformed response entropy (RE) (Shalbaf et al., 2012).

Fractal dimension (FD) is a common measure of time series regularity, widely used to quantify long-range correlation and power law dependencies by determining the scaling exponent. FD has demonstrated its ability to differentiate between healthy and pathological brains, indicating its strength in examining the maturation and degeneration of brain function (Marino et al., 2019; Smits et al., 2016; Zappasodi et al., 2014; Zappasodi et al., 2015). Marino et al. (2019) noted that changes in FD can reflect an alteration in the complexity of the dynamical nature of the brain, and it could be potentially tied to cognitive or perceptual impairment, as seen in studies investigating dementia and Alzheimer's symptoms (Zappasodi et al., 2015; Marino et al., 2019; Ahmadlou et al., 2011; Smits et al., 2016). Higuchi's fractal dimension (HFD) is the most accurate in estimating FD compared to other FD methods (Esteller et al., 2001; Raghavendra et al., 2009; Kesić and Spasić, 2016). It has been a prominent method in analyzing neuronal data, such as EEG and electrocorticography (ECoG), because it holds advantages over linear and spectral analysis methods due to its speed, accuracy, and computational cost (Paramanathan and Uthayakumar, 2008; Spasic et al., 2011; Chouvarda et al., 2011; Arle and Simon, 1990). In some cases, HFD produces better results when combined with other linear and nonlinear methods (Kesić and Spasić, 2016).

Thus, a research gap lies in investigating the nonlinear dynamics in EEG signals from multiple sclerosis patients under different drug treatments, such as IFN-β and DMF. This study aims to compare the nonlinear dynamics of EEG signals between MS patients treated with IFN-β and DMF. The following research questions were developed prior to the study:

- RQ1: Does the EEG of patients with MS exhibit increased complexity compared to the control group?
- RQ2: How do the complexity characteristics of EEG signals differ between MS patients undergoing treatment with IFN-β and those treated with DMF?
- RQ3: Which complexity measure is most sensitive to the effects of IFN-β or DMF treatment on EEG dynamics in MS patients?
- RQ4: Can the observed changes in complexity characteristics of EEG signals be used as potential biomarkers for monitoring the effectiveness of IFN-β or DMF treatment in MS patients?

In response to each research question, we hypothesize the following:

1 EEG data collected from patients with MS demonstrates an increase in complexity when compared to healthy participants, as reflected via sample entropy and Higuchi's fractal dimension.
2 Sample entropy and Higuchi's fractal dimension, will illustrate distinguishable alterations between patients treated with IFN-β, patients treated with DMF, and the control group (healthy participants). Patients treated with DMF will exhibit significant differences in nonlinear characteristics compared to patients treated with IFN-β and the control group.
3 Sample entropy will demonstrate the highest sensitivity and the greatest predicted value in evaluating the effects of IFN-β or DMF treatment on MS compared to the control group.
4 Nonlinear analysis of EEG signals via sample entropy and Higuchi's fractal dimension will reveal significant and consistent changes over time in MS patients undergoing IFN-β and DMF treatments relative to the control group of healthy patients. This will serve as definitive biomarkers for assessing treatment effectiveness and disease progression.

2 Methodology

2.1 Location of data collection and participants

The data were collected at Jagiellonian University in Krakow, Poland. The study included two groups of subjects: patients with early onset relapsing–remitting multiple sclerosis (RRMS) and healthy subjects. In the group of MS patients, there were two subgroups: those treated with IFN-β and those treated with DMF. The total number of participants for this analysis is 175. To further break it down, 39 patients were on IFN-β, 53 were on DMF, and there were 83 healthy controls. The IFN-β group consisted of participants between 22 and 63 years old ($M = 39.15$, SD = 7.909), and there were 24 females (61.5%) and 15 males (38.5%). The DMF group contained participants between 18 and 54 years old ($M = 32.11$, SD = 7.250). This group had 33 females (62.3%) and 20 males (37.7%). The participants in the control group were between 21 and 61 years old ($M = 36.22$, SD = 8.498). There were 53 females (63.9%) and 30 males (36.1%). There were two rounds of data collection (first measurement and second measurement). The data for the second measurement were obtained 1 year after the data for the first measurement were collected. MS patients' Expanded Disability Status Scale (EDSS) scores (Kurtzke, 1983) ranged from 1 to 4 in the first measurement and from 1 to 4.5 in the second measurement. The number of relapses in the year prior to each measurement ranged from 0 to 2. A Wilcoxon signed-rank test indicated that there was no significant difference between EDSS scores in the first and second measurements, $z = -0.958$, $p = 0.338$. The median EDSS score was 1 in both the first and second measurements. Similarly, there was no significant difference in the number of relapses in the year prior to each measurement between the first and second measurements, $z = -0.915$, $p = 0.360$. The median number of relapses in the year prior was 0 in both the first and second measurements. The control group did not undergo a second round of data collection because there should not be significant changes in resting state EEG in healthy subjects within 1 year (Kondacs and Szabó, 1999).

2.2 Experimental protocol

For this study, data were collected during a resting state task. The resting state task included a six-minute procedure without any stimuli. In the first 3 minutes, subjects were asked to have their eyes open while focusing on a fixation point, and they had to keep their eyes closed in the last 3 minutes. Commands were pre-recorded and played by speakers. A 256-channel dense array EEG system (HydroCel Geodesic Sensor Net, EGI System 300; Electrical Geodesic Inc., OR, USA) was used to collect the data. The researchers decided to remove channels located on the cheeks (E225, E226, E227, E228, E229, E230, E231, E232, E233, E234, E235, E236, E237, E238, E239, E240, E241, E242, E243, E244, E245, E246, E247, E248, E249, E250, E251, E252, E253, E254, E255, and E256) due to many artifacts of low interest in the signal.

2.3 Pre-processing

The EEG data underwent pre-processing using MATLAB's EEGLAB software to ensure data quality and integrity (Delorme and Makeig, 2004). The initial pre-processing stage involved discarding 5 seconds of data that followed sound commands—eliminating these potential artifacts or confounding effects because the experimental instruction allowed for a more precise analysis of the EEG signals. A high pass filter was employed to exclude any signals below the frequency of 0.5 Hz. Adding on, a notch filter to remove power line interference and its harmonics was integrated to reject 50 Hz and its multiplicities from the signal. Independent component analysis (ICA) was conducted. Fifty principal components were used for the analysis to identify and reject artifact components, such as components related to eye movements, muscle activity, or other sources of artifact. Every removed channel was interpolated to estimate the missing values based on surrounding electrodes and provide comprehensive coverage

of all channels. Each subject had a sampling rate of 250 Hz for this study.

2.4 Autocorrelation

A commonly used linear analysis with applications in neurophysiological data, lag-1 autocorrelation (AC1), was carried out to validate the use of nonlinear analysis (Meisel et al., 2017; Scheffer et al., 2009). AC1 is a reliable measure of the rate at which the autocorrelation function decays (Huang et al., 2018). The autocorrelation function (ACF) is defined in Equation 1, where $x(t)$ represents the envelope signals, N is the length, μ is the mean, and v is the variance:

$$ACF(s) = \sum_{t=1}^{N-s} \frac{(x(t)-\mu)(x(t+s)-\mu)}{v}, s = 1,\ldots,\frac{N}{2} \quad (1)$$

To obtain lag-1 autocorrelation, we set $s = 1$ (Meisel et al., 2017). Higher AC1 values indicate greater predictability in the signal, whereas lower AC1 values suggest less predictability (Huang et al., 2018).

2.5 Sample entropy

Sample entropy (SampEn), initially developed by Richman and Moorman (2000) to measure regularity, was used to analyze the EEG signals across all groups (Duran et al., 2013; Richman and Moorman, 2000). Greater entropy values indicate that the system is complex, irregular, and unpredictable, often associated with a healthy system. Conversely, low entropy values indicate a more deterministic and predictable system, meaning the EEG signals show more regular patterns and less complexity (Duran et al., 2013; Pincus, 2006; Delgado-Bonal and Marshak, 2019). Two notable parameters are used in calculating SampEn: m and r. The parameter m represents the length of the subseries, and r represents the similarity criterion (Ramdani et al., 2009). Following the guidance of Costa et al. (2005) and Duran et al. (2013) selected $m = 2$ and $r = 0.15$ as the parameters, and it was noted that the selection of the parameters does not negatively impact the overall pattern of the results (Costa et al., 2005; Duran et al., 2013). Thus, others typically default to the parameters Duran et al. (2013) used, as they are considered standard and, therefore, were deemed appropriate for this study. Following the guidance outlined by Ramdani et al. (2009), the equation for sample entropy is as follows (Richman and Moorman, 2000; Ramdani et al., 2009):

With time series $x_1, x_2, \ldots x_N$, subsequences of length m are first defined in Equation 2:

$$y_i(m) = (x_i, x_{i+1}, \ldots, x_{i+m-1}), where\ i = 1,2,\ldots,N-m+1 \quad (2)$$

After, the quantity is calculated by the following:

$$B_i^m(r) = \frac{1}{N-m-1} \sum_{j=1, j\neq i}^{N-m} \Theta(r - \| y_j(m) - y_i(m) \| \infty) \quad (3)$$

The Heaviside function is defined by Θ, and $\|\bullet\| \infty$ represents the maximum norm, which is $y_j(m) - y_i(m)\infty = \max_{0\le k\le m-1} |X_{j+k} - X_{i+k}|$. To explain, Equation 3 calculates the sum of the quantity of vectors, $y_j(m)$, that are within the radius, r, from $y_i(m)$ that exist in the reconstructed phase space. Identical matches are excluded and are represented by $j \neq i$. Also, $N - m$ represents the total amount of vectors in the $(m + 1)$ dimensional state space.

Equation 4 calculates the density:

$$B^m(r) = \frac{1}{N-m} \sum_{N-m}^{N-m} B_i^m(r) \quad (4)$$

Calculations in the $(m + 1)$ space to extend the template matching process are as follows:

$$A_i^m(r) = \frac{1}{N-m-1} \sum_{j=1, j\neq i}^{N-m} \Theta(r - \| y_j(m+1) - y_i(m+1) \| \infty) \quad (5)$$

$$A^m(r) = \frac{1}{N-m} \sum_{N-m}^{N-m} A_i^m(r) \quad (6)$$

In Equation 5, the number of sequences $y_j(m+1)$ within radius r of $y_i(m+1)$ is calculated, with the term $y_j(m+1) - y_i(m+1)$ representing the maximum difference between the two subsequences. After calculating the individual template matches $A_i^m(r)$, they are all averaged across all vectors to give $A^m(r)$, as shown in Equation 6. Then, the total amount of template matches in a m-dimensional and $m + 1$ dimensional phase space with r is represented by Equations 7 and 8:

$$B(r) = \frac{1}{2}(N-m-1)(N-m)B^m(r) \quad (7)$$

$$A(r) = \frac{1}{2}(N-m-1)(N-m)A^m(r) \quad (8)$$

The sample entropy can then be calculated as follows in Equation 9:

$$SampEn(m,r,N) = -\log\left(\frac{A(r)}{B(r)}\right) \quad (9)$$

The sample entropy MATLAB script provided by Richman and Moorman (2000) was used in conjunction with an unpublished modified script from Amon (2021) to conduct the analysis (Richman and Moorman, 2000; Amon, 2021).

2.6 Higuchi's fractal dimension

Higuchi's fractal dimension (HFD) was also employed to analyze the EEG signals. It is another method frequently used in

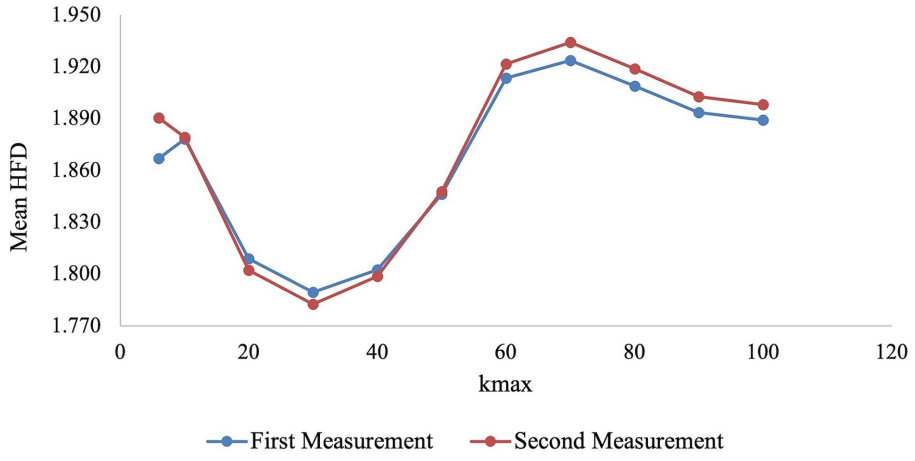

FIGURE 1
The mean Higuchi's fractal dimension of the first and second measurements is plotted for each k_{max} to assess where it approaches a local maximum or asymptote.

nonlinear analysis, and it details the time series' complexity and self-similarity (Accardo et al., 1997). Following the outline of the computation summarized in Hernandez et al. (2023), the calculation of HFD involves analyzing a time series data sequence, denoted as $X(1)$, $X(2)$, …, $X(N)$, where N represents the total number of samples (Hernandez et al., 2023). The selection of a scale factor, m, begins the process. This scale factor, m, defines the length of the subseries under investigation. The selection of k is also necessary to commence the process, as this is the index of the subseries. The cumulative length, $L(m, k)$, is calculated by comparing the absolute differences between adjacent data points within the subseries, as shown in Equation 10 (Porcaro et al., 2020):

$$L_m(k) = \frac{1}{k}\left[\sum_{i=1,\mathrm{int}\left(\frac{N-m}{k}\right)} \left|X(m+ik) - X(m+(i-1)k)\right| \cdot \frac{N-1}{\mathrm{int}\left(\frac{N-m}{k}\right)}\right] \quad (10)$$

N is the length of the original time series X and $\frac{N-1}{\mathrm{int}\left(\frac{N-m}{k}\right)}$ normalizes the function. The average cumulative length across all subseries is calculated to acquire $L(k)$, the average length for the given scale factor, as represented in Equation 11:

$$L(k) = \frac{\sum_{m=1}^{k} L_m(k)}{k} \quad (11)$$

The Higuchi's fractal dimension is then computed by taking the logarithm of $L(k)$, as defined in Equation 12:

$$FD = \frac{\ln(L(k))}{\ln(1/k)} \; for \; k = 1,2,\ldots,k_{\max} \quad (12)$$

The resulting fractal dimension value represents the fractal dimension of the time series, providing insight into its complexity (Porcaro et al., 2020). The method for calculating Higuchi's fractal dimension was adopted from Jesús Monge-Álvarez[1].

Typically, the fractal dimension ranges between 1 and 2, where higher HFD values indicate greater complexity and lower values suggest reduced complexity (Accardo et al., 1997; Scarpa et al., 2017).

Currently, no standard method is used to select the most appropriate value for the k_{max} parameter (Kesić and Spasić, 2016). The method selected in this paper is a common method used by Doyle et al. (2004) and Wajnsztejn et al. (2016). They considered the most appropriate k_{max} parameter to be where HFD approaches a local maximum or asymptote (saturation point) (Wanliss et al., 2021; Doyle et al., 2004; Wajnsztejn et al., 2016). According to Figure 1, the data reaches a local maximum at $k_{max} = 70$. Therefore, $k_{max} = 70$ was the parameter chosen for this study.

2.7 Windowing

For the analysis, each participant's EEG signal was divided into short 15-s time windows with 50% overlap. This was decided after following the advice of several articles that have opted to divide EEG signals into short time windows for computational efficiency (Mohseni and Moghaddasi, 2022; Ramanand et al., 2004; Er et al., 2021; Kesić and Spasić, 2016). The 50% overlap was chosen to prevent any discontinuity at the frame's beginning or end (Er et al., 2021).

2.8 Statistical analysis

Several statistical analysis techniques were used to understand the data and answer the research questions comprehensively. Descriptive statistics provided a summary of the data. Levene's and

1 https://www.mathworks.com/matlabcentral/fileexchange/50290-higuchi-and-katz-fractal-dimension-measures

Mauchly's tests were conducted to test for homogeneity and sphericity. Although homogeneity was violated in most cases, it was not violated in the second measurement of AC1. There was no indication of a violation of sphericity. Given the sample size ($n > 30$) and following guidance from Hair et al. (2010) and Byrne (2010), parametric tests were utilized, as skewness (between −2 and + 2) and kurtosis (between −7 and + 7) were within acceptable ranges (Hair et al., 2010; Byrne, 2010). A paired samples t-test was used to compare the means within subjects, and mixed analysis of variance (ANOVA) was used to investigate the main effects of time and group. Welch's ANOVA was employed to analyze the means between subjects to address the violation of homogeneity, and standard ANOVA was used to evaluate the means between subjects in the second measurement of AC1, where homogeneity was not violated. Games-Howell *post hoc* test was completed to identify which groups demonstrated significant differences. An alpha level of 0.05 was used as the threshold for determining the effect's significance.

3 Results

3.1 Assessment of linearity

Lag-1 autocorrelation (AC1) was carried out to assess the linearity of the dataset. The mean AC1 value of the IFN-β group was 0.800 (SD = 0.044) in the first measurement and 0.815 (SD = 0.042) in the second measurement. For the DMF group, the mean AC1 value was 0.812 (SD = 0.052) in the first measurement and 0.805 (SD = 0.050) in the second measurement. The mean AC1 of the control group was 0.806 (SD = 0.034). Paired samples t-test revealed no significant differences in the means within the IFN-β group ($t(38) = -1.676$, $p = 0.102$) and DMF group ($t(52) = 0.901$, $p = 0.372$). According to the mixed factorial ANOVA, time did not have a significant effect, $F(1, 172) = 0.727$, $p = 0.395$. However, a significant interaction effect of time and group was reported $F(2, 172) = 3.396$, $p = 0.036$, highlighting a significant change in the pattern over time across groups. Due to the violation of homogeneity in the first measurement, $F(2, 172) = 3.344$, $p = 0.038$, Welch's ANOVA was conducted for between-subjects comparison. No significant differences were reported in the first measurement, $F(2, 82.498) = 0.651$, $p = 0.524$. Since the data in the second measurement, $F(2, 172) = 1.636$, $p = 0.198$, did not violate homogeneity, standard ANOVA was carried out. Like in the first measurement, no significant differences were reported, $F(2, 172) = 0.728$, $p = 0.484$.

3.2 Assessment of nonlinearity

To assess the complexity of the EEG data, box plots with 95% confidence intervals were created to understand the distribution and central tendency of the SampEn and HFD values across different groups and measurements (Figure 2). Referring to the point plots in Figure 3, both treatment groups at each measurement had recorded relatively high mean SampEn values and HFD values compared to the control group. Summary statistics are shown in Table 2. A paired samples *t*-test was employed to evaluate the significance of the difference within each treatment group.

3.2.1 Variations and trends in sample entropy across groups

The median, interquartile range (IQR), and potential outliers of SampEn are shown in Figure 2 for both time measurements across groups. For the IFN-β group, the median SampEn at the initial measurement was reported as 1.687 (IQR 1.561–1.754), and the median SampEn at the second measurement slightly decreased to 1.640 (IQR 1.516–1.685). Similarly, for the DMF group, the median SampEn at the first measurement was 1.640 (IQR 1.515–1.721), and a slight decrease in median SampEn was observed in the second measurement at 1.635 (IQR 1.578–1.731). The median SampEn for the control group for the first measurement was 1.544 (IQR 1.201–1.699). The presence of outliers confirms the violation of homogeneity.

Referring to Figure 3, only a slight increase in mean SampEn was observed from the first measurement to the second measurement in the IFN-β and DMF groups. Results indicate that the increase in the mean SampEn of the IFN-β treatment group observed in the second measurement ($M = 1.614$, SD = 0.138) was not significant compared

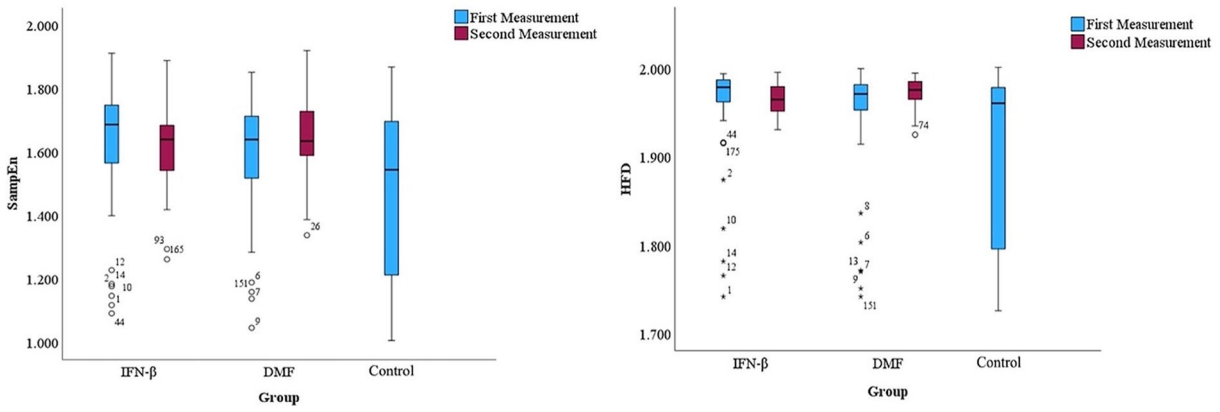

FIGURE 2
Box plots represent the distribution of SampEn and HFD values across groups.

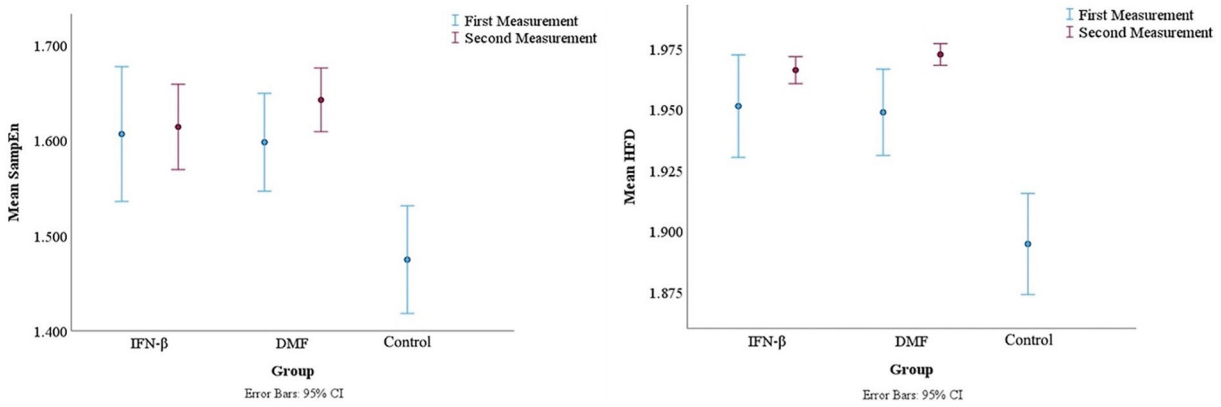

FIGURE 3
Mean SampEn and HFD for each group with associated error bars.

TABLE 2 Descriptive statistics for SampEn and HFD across groups.

Measurement	Group	N	Mean	SD	Median	IQR	Min	Max
SampEn first measurement	Control	83	1.475	0.259	1.544	0.499	1.005	1.869
	IFN-β	39	1.607	0.219	1.687	0.193	1.090	1.912
	DMF	53	1.598	0.187	1.640	0.206	1.045	1.852
SampEn second measurement	Control	-	-	-	-	-	-	-
	IFN-β	39	1.614	0.138	1.640	0.169	1.261	1.889
	DMF	53	1.643	0.121	1.635	0.154	1.337	1.920
HFD first measurement	Control	83	1.895	0.095	1.960	0.185	1.726	2.001
	IFN-β	39	1.951	0.065	1.979	0.027	1.741	1.994
	DMF	53	1.949	0.064	1.971	0.030	1.742	2.000
HFD second measurement	Control	-	-	-	-	-	-	-
	IFN-β	39	1.966	0.017	1.965	0.028	1.931	1.996
	DMF	53	1.973	0.016	1.976	0.021	1.925	1.995

to the mean SampEn of its initial measurement ($M = 1.607$, SD = 0.219), $t(38) = -0.186$, $p = 0.854$. For DMF, the mean SampEn of its second measurement (M = 1.643, SD = 0.121) did not differ significantly from its initial measurement ($M = 1.598$, SD = 0.187), $t(52) = -1.687$, $p = 0.098$. The mean SampEn value for the control group was 1.475 (SD = 0.259).

3.2.2 Variations and trends in Higuchi's fractal dimension across groups

Figure 2 shows the median, interquartile range (IQR), and potential outliers for both measurements across groups for HFD. The median HFD value in the first measurement of the IFN-β group was high at 1.979 (IQR 1.961–1.988), and it saw a minor decrease in the second measurement with a value of 1.965 (IQR 1.951–1.980). In the DMF group, the median HFD value was also high at 1.971 (IQR 1.952–1.982), and an increase in HFD was reported in the second measurement with a value of 1.976 (IQR 1.965–1.986). For the control group, the median HFD value was 1.960 (IQR 1.794–1.979). Like in SampEn, the presence of outliers confirms the violation of homogeneity.

Small increases in mean HFD measurements were observed between measurements in both treatment groups (Figure 3). The mean HFD value in the second measurement of the IFN-β group ($M = 1.966$, SD = 0.017) slightly increased when compared to the first measurement ($M = 1.951$, SD = 0.065); however, it was not significant, $t(38) = -1.372$, $p = 0.178$. On the other hand, the second measurement of the DMF group ($M = 1.973$, SD = 0.016) significantly increased when compared to the first measurement ($M = 1.949$, SD = 0.064), $t(52) = -2.760$, $p = 0.008$. The significant results are shown in Table 3. The mean HFD value for the control group was 1.895 (SD = 0.095).

3.3 Longitudinal analysis and interaction effects

A mixed factorial ANOVA was conducted for SampEn and HFD to observe the main effects of time and group (control, IFN-β, or DMF). An interaction plot was created to visualize the effects.

3.3.1 Interaction effects of time and treatment on sample entropy

Time did not have a significant effect, $F(1, 172) = 1.905$, $p = 0.169$, and an insignificant interaction effect of time and group was reported

TABLE 3 Paired samples *T*-test for HFD in the DMF treatment group.

Group	*t*	df1	Two-sided *p*
DMF	−2.760	52	0.008

$F(2, 172) = 1.336$, $p = 0.266$. The results indicate that SampEn did not significantly change between the first- and second-time measurements across all groups, and the pattern of change over time was insignificant across all groups. Although the interaction plot (Figure 4) shows some level of interaction between IFN-β and DMF, the graph alone does not confirm any statistically significant interaction. Neither of the treatment groups intersected with the control group, indicating their trend is different from the control group. Accordingly, the results confirm no significance was reported when comparing the pattern of change in both treatment groups between measurements 1 and 2.

3.3.2 Interaction effects of time and treatment on Higuchi's fractal dimension

The mixed factorial ANOVA highlighted the main effects of time and group (control, IFN-β, or DMF). It yielded a significant effect for time $F(1, 172) = 12.008$, $p < 0.001$ and the interaction effect of time and group $F(2, 172) = 4.384$, $p = 0.014$. The results indicate that HFD significantly changed between the first- and second-time measurements across the treatment groups, and the pattern of change over time was significantly different. The detailed results are displayed in Table 4. The interaction plot (Figure 5) illustrates these findings. Both treatment groups saw an increase in their mean HFD in the second measurement, while the control group remained stable. The lines representing the two treatment groups did intersect, demonstrating some level of interaction. No interaction between either of the treatment group and the control group was observed. Hence, this also confirms the significance of the pattern of change in both treatment groups between measurements 1 and 2.

3.4 Diagnostic potential of complexity metrics

Due to the violation of homogeneity, Welch's ANOVA was performed for the between-subjects effect at the first and second measurements for both SampEn and HFD. A Games-Howell *post hoc* test was conducted to identify significant differences between groups.

3.4.1 Between-subjects effects of treatment on sample entropy

Welch's ANOVA was conducted following the Levene's test, which indicated a violation of homogeneity in the first measurement, $F(2, 172) = 12.206$, $p < 0.001$, and in the second measurement, $F(2, 172) = 49.377$, $p < 0.001$. The summary of the results is displayed in Table 5. Welch's ANOVA revealed a significant effect of treatment in the first measurement, $F(2, 97.945) = 6.446$, $p = 0.002$, and the second measurement, $F(2,104.188) = 13.059$, $p < 0.001$. Games-Howell *post hoc* test (Table 6) revealed that IFN-β ($M = 1.607$, $SD = 0.219$) and DMF ($M = 1.598$, $SD = 0.187$) had significantly higher sample entropy values in the first measurement compared to the control group ($M = 1.475$, $SD = 0.259$). Specifically, the mean difference between IFN-β and the control group was −0.132, 95% CI [−0.240, −0.025], $p = 0.012$. DMF's mean difference with the control group was −0.123, 95% CI [−0.214,

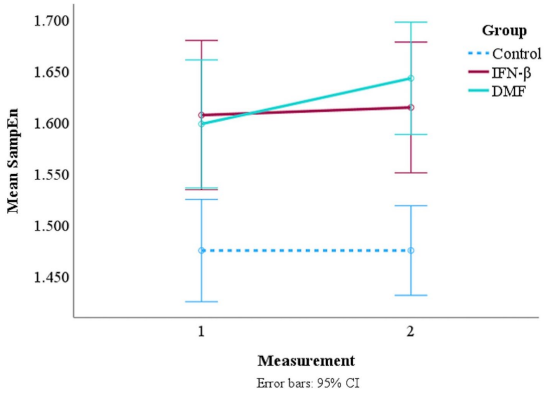

FIGURE 4
Interaction plot of mean SampEn over time across the treatment groups and the control group. *A second measurement for the control group was not collected. However, since no significant changes in resting-state EEG are expected in healthy subjects within 1 year, the control group is represented as constant in the interaction plot (Kondacs and Szabó, 1999).

TABLE 4 Mixed ANOVA table results for HFD across groups and time measurements.

Source	Sum of squares	df	Mean square	*F*	*p*
Time	0.013	1	0.013	12.008	<0.001
Time*Group	0.010	2	0.005	4.384	0.014
Error(Time)	0.188	172	0.001	-	-

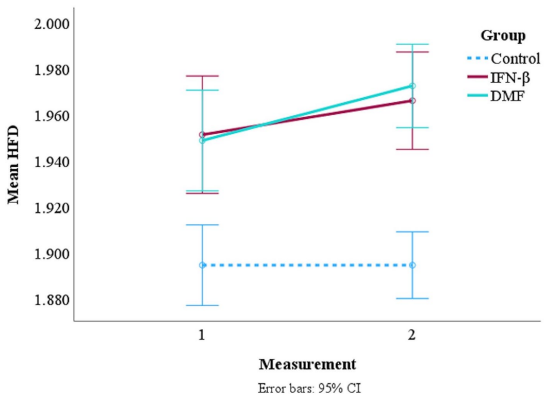

FIGURE 5
Interaction plot of mean HFD over time across the treatment groups and the control group. *A second measurement for the control group was not collected. However, since no significant changes in resting-state EEG are expected in healthy subjects within 1 year, the control group is represented as constant in the interaction plot (Kondacs and Szabó, 1999).

TABLE 5 Welch's ANOVA for the effect of treatment group on sample entropy.

Measurement	Statistic	df1	df2	*p*
First measurement	6.446	2	97.945	0.002
Second measurement	13.059	2	104.188	<0.001

TABLE 6 Games-Howell *post hoc* comparisons for differences in sample entropy across treatment groups.

Dependent variable	(I) Group	(J) Group	Mean difference (I-J)	Std. Error	Sig.	95% Confidence Interval	
						Lower bound	Upper bound
SampEn first measurement	Control	IFN-β	−0.132	0.045	0.012	−0.240	−0.025
		DMF	−0.123	0.038	0.005	−0.214	−0.033
	IFN-β	Control	0.132	0.045	0.012	0.025	0.240
		DMF	0.009	0.043	0.978	−0.095	0.112
	DMF	Control	0.123	0.038	0.005	0.033	0.214
		IFN-β	−0.009	0.043	0.978	−0.112	0.095
SampEn second measurement	Control	IFN-β	−0.140	0.036	0.001	−0.225	−0.054
		DMF	−0.168	0.033	<0.001	−0.246	−0.090
	IFN-β	Control	0.140	0.036	0.001	0.054	0.225
		DMF	−0.028	0.028	0.563	−0.095	0.038
	DMF	Control	0.168	0.033	<0.001	0.090	0.246
		IFN-β	0.028	0.028	0.563	−0.038	0.095

−0.033], $p = 0.005$. There was no significant difference when comparing IFN-β and DMF in the first measurement ($p = 0.978$).

For the second measurement, the Games-Howell *post hoc* test demonstrated that IFN-β (M = 1.614, SD = 0.138) and DMF ($M = 1.643$, SD = 0.121) had significantly higher sample entropy values in the second measurement compared to the control group ($M = 1.475$, SD = 0.259). In this measurement, the mean difference between IFN-β and the control group was −0.140, 95% CI [−0.225, −0.054], $p = 0.001$, and the mean difference between DMF and the control group was −0.168, 95% CI [−0.246, −0.090], $p < 0.001$. Like in the first measurement, there was no significant difference when comparing IFN-β and DMF in the first measurement ($p = 0.563$).

3.4.2 Between-subjects effects of treatment on Higuchi's fractal dimension

Like in SampEn, the Levene's test confirmed a violation of homogeneity in the first measurement, $F(2, 172) = 34.473$, $p < 0.001$, and in the second measurement, $F(2, 172) = 387.564$, $p < 0.001$. Therefore, Welch's ANOVA was conducted to determine the between-subjects effect in HFD values. A significant effect of treatment was observed in the first measurement, $F(2, 103.306) = 9.799$, $p < 0.001$, and in the second measurement, $F(2,107.471) = 26.777$, $p < 0.001$ was observed. A breakdown of the results is outlined in Table 7. The Games-Howell *post hoc* test (Table 8) was performed to identify where the significance lay. IFN-β ($M = 1.951$, SD = 0.065) and DMF ($M = 1.949$, SD = 0.064) had significantly larger HFD values in the first measurement compared to the control group ($M = 1.895$, SD =0 0.095). The mean difference between IFN-β and the control group was −0.057, 95% CI [−0.092, −0.022], $p = 0.001$. DMF's mean difference with the control group was −0.054, 95% CI [−0.087, −0.022], $p < 0.001$. There was no significant difference when comparing IFN-β and DMF in the first measurement ($p = 0.981$).

Like the first measurement, the Games-Howell *post hoc* test demonstrated that IFN-β ($M = 1.966$, SD = 0.017) and DMF ($M = 1.973$, SD = 0.016) had significantly larger HFD values in the second measurement compared to the control group ($M = 1.895$, SD = 0.095). In this measurement, the mean difference between IFN-β and the control group was −0.072, 95% CI [−0.097, −0.046], $p < 0.001$, and the mean difference between DMF and the control group was −0.0780, 95% CI [−0.103, −0.052], $p < 0.001$. No significant difference was reported when comparing IFN-β and DMF in the first measurement ($p = 0.170$).

TABLE 7 Welch's ANOVA for the effect of treatment group on Higuchi's fractal dimension.

Measurement	Statistic	df1	df2	*p*
First measurement	9.799	2	103.306	<0.001
Second measurement	26.777	2	107.471	<0.001

4 Discussion

Multiple sclerosis is a complex and progressive disease that is mostly diagnosed in young women. It impacts the central nervous system and causes various symptoms, such as deficits in complex attention, long-term memory, and processing speed (Chiaravalloti and DeLuca, 2008; Dobson and Giovannoni, 2019). It also reduces the brain's ability to compensate for damage and cognitive reserve. It has been historically treated with immunosuppressant or immunomodulatory treatments, which must be ongoing to reduce inflammation (Dobson and Giovannoni, 2019). In line with Pritchard and Duke (1995), the high AC1 values highlight the deterministic nature of the EEG signals (Pritchard and Duke, 1995). Although a significant interaction between time and group was observed in the AC1 values, no other significant results were reported. This demonstrates that linear measures, such as AC1, capture only limited information regarding the complexity of EEG signals, emphasizing the need for nonlinear analyses. Thus, nonlinear analyses have been proven to be effective in the analysis of EEG data of MS patients (Hernandez et al., 2023). So, this study provides novel insights into pharmaceutical treatments' effects on MS patients' brain dynamics, as measured by sample entropy and Higuchi's fractal dimension.

TABLE 8 Games-Howell *post hoc* comparisons for differences in Higuchi's fractal dimension across treatment groups.

Dependent variable	(I) Group	(J) Group	Mean difference (I-J)	Std. Error	Sig.	95% Confidence Interval	
						Lower bound	Upper bound
HFD first measurement	Control	IFN-β	−0.057	0.015	0.001	−0.092	−0.022
		DMF	−0.054	0.014	<0.001	−0.087	−0.022
	IFN-β	Control	0.057	0.015	0.001	0.022	0.092
		DMF	0.003	0.014	0.981	−0.030	0.035
	DMF	Control	0.054	0.014	<0.001	0.022	0.087
		IFN-β	−0.003	0.014	0.981	−0.035	0.030
HFD second measurement	Control	IFN-β	−0.072	0.011	<0.001	−0.097	−0.046
		DMF	−0.078	0.011	<0.001	−0.103	−0.052
	IFN-β	Control	0.072	0.011	<0.001	0.046	0.097
		DMF	−0.006	0.004	0.170	−0.015	0.002
	DMF	Control	0.078	0.011	<0.001	0.052	0.103
		IFN-β	0.006	0.004	0.170	−0.002	0.015

4.1 Evidence of complexity in MS EEG: sample entropy and Higuchi's fractal dimension analysis

As mentioned, higher entropy values indicate that a system is complex, irregular, and unpredictable, often linked to a healthy system. On the other hand, lower entropy values indicate a more predictable and deterministic system (Duran et al., 2013; Pincus, 2006; Delgado-Bonal and Marshak, 2019). As for HFD, greater values indicate more complexity in the signal (Scarpa et al., 2017). Treatment was expected to have some level of impact on the complexity of the signal (Shalbaf et al., 2012; Thomasson et al., 2000).

In the study, the control, Interferon-β, and dimethyl fumarate groups displayed high SampEn and HFD values at each time measurement, supporting the hypothesis that an increase of complexity was observed. It is shown that both treatment groups displayed higher SampEn and HFD values when compared to the control group, suggesting that the MS patients were found to have a greater number of nonlinear segments. These findings were similar to those of Pezard et al. (2001), who reported higher entropy values compared to the control group when investigating Parkinson's disease (Pezard et al., 2001). This further reveals MS patients treated with IFN-β and DMF have less predictable and more complex electrical activity compared to the controls (Pezard et al., 2001). The high nonlinearity can also be tied to the dimensionality of the electrical activity. Lachaux et al. (1997) described how dimensionality decreases if nonlinearity increases (Lachaux et al., 1997). This indicates that the MS patients treated with both treatments may have brain dynamics of a lower dimension (Pezard et al., 2001; Stam et al., 1994). Additionally, it has been noted that the increase in the complexity of EEG signals for MS patients is linked to the brain's compensatory mechanisms and is indicative of the brain's structural complexity (Wątorek et al., 2024). We can hypothesize that the higher complexity reported in the treatment groups could also be due to the brain's adaptive response to the effects of the treatments, as they are responsible for the regulation of the immune system and reduction in inflammation (Jakimovski et al., 2018; Linker and Haghikia, 2016; Mills et al., 2018).

4.2 Distinct EEG patterns in MS treatments and sensitivity of complexity measures

There were no significant differences reported in the complexity characteristics of EEG signals between MS patients undergoing treatment with IFN-β and DMF at the first and second measurements, which rejects the hypothesis that patients treated with DMF will exhibit significant differences in complexity characteristics compared to patients treated with IFN-β. However, the second hypothesis was partially supported because the complexity characteristics (SampEn and HFD) of each treatment group differed significantly compared to the control group at each time measurement, as confirmed by Welch's ANOVA and the Games-Howell *post hoc* test. These findings are backed by other studies that have concluded that nonlinear EEG measures can be sensitive to treatments (Pezard et al., 1998; Pezard et al., 2001; Wackermann et al., 1993).

In particular, as seen in Tables 6, 8, the mean differences in SampEn between each treatment group and the control group at the first and second measurements were higher than the mean differences observed in the same scenario for HFD. This indicates that SampEn demonstrated the highest sensitivity and the greatest predicted value in evaluating the effects of each treatment group compared to the control group, supporting our third hypothesis. These results suggest that treatments, such as IFN-β and DMF, impact the overall brain dynamics, as reflected by the higher sample entropy and Higuchi fractal dimension values.

4.3 Complexity EEG metrics as biomarkers for MS treatment effectiveness

Several studies (Hossain et al., 2022; Di Ieva et al., 2015) have investigated using nonlinear analysis in recognizing biomarkers in individuals with MS and healthy controls (Hernandez et al., 2023). Both entropy and fractal dimension have been used to

either distinguish between conditions or differentiate between healthy and pathological brains in previous research (Marino et al., 2019; Smits et al., 2016; Zappasodi et al., 2014; Zappasodi et al., 2015; Bauer et al., 2011; Pezard et al., 2001). In this study, we aimed to explore whether sample entropy and HFD are reliable indicators for the progression of MS. We initially hypothesized that MS patients treated with IFN-β and DMF treatments would reveal significant and consistent changes over time relative to the control group.

Referencing Figure 2, it was observed that the initial measurements of SampEn and HFD demonstrated more dispersion compared to the second set of measurements. This observation could indicate the progression of MS over time, leading to more consistency in the results. Nevertheless, we determined that the hypothesis could only be partially supported because time and the interaction between time and treatment group significantly impacted only HFD and not SampEn. However, a significant increase from the first measurement to the second measurement was only observed in HFD values of the DMF group. Hence, an increase in signal complexity and positive neurophysiological changes can be attributed to DMF, which is reflected only in HFD. This finding is supported by Viglietta et al. (2015) and Vermersch et al. (2022). Viglietta et al. (2015) concluded that DMF reduces new and enlarging T2 lesions, gadolinium-enhancing lesions activity, and the number of new non-enhancing T2 lesions (Viglietta et al., 2015). Similarly, Vermersch et al. (2022) reported that more pediatric patients treated with DMF did not develop new or newly enlarging T2 lesions compared to those treated with IFN-β (Vermersch et al., 2022). These findings demonstrate the effectiveness of DMF in reducing disease activity and may explain the increase in EEG complexity over time compared to IFN-β. Although SampEn demonstrated the highest sensitivity and greatest predicted value, its responsiveness was limited when time was factored in. This finding signifies how HFD may be more responsive to temporal changes in EEG dynamics than SampEn.

4.4 Limitations and future research

There are a few limitations and opportunities for future research to note in this study. The first limitation is centered on the selection of the kmax parameter. Different methods of kmax parameter selection have been employed previously, but researchers have yet to agree on a universal method (Kesić and Spasić, 2016). Different parameter selection methods could alter the results. However, one of the most common methods was chosen in this study. This method was carried out by selecting the parameter where HFD reached a maximum or asymptote (Wanliss et al., 2021; Doyle et al., 2004; Wajnsztejn et al., 2016). Another possible limitation is the sample size of each treatment group. Increasing the sample size could have enhanced the results reported in this experiment. More specifically, the IFN-β treatment group had the lowest number of participants, and an increase in the number of MS patients on IFN-β could have highlighted clinically significant differences between the treatment groups.

There are several opportunities for future research. First, future studies could expand and balance the sample sizes for each treatment and collect longitudinal EEG data from the control group to strengthen the analysis and validate these findings. The next step in the study could be to analyze the EEG time series using multifractal methodology. This method helps quantify the data's correlation structure through the set of scaling exponents, providing a deeper understanding of the data's complexity (Wątorek et al., 2024). Furthermore, there are several methods to characterize complexity. One method is detrended fluctuation analysis (DFA), which is used to evaluate the Hurst exponent and can then be recalculated to determine the fractal dimension (Márton et al., 2014). Another method is the Lyapunov exponent, which is employed to identify chaotic behavior in the data and can be used to quantify data complexity (Yakovleva et al., 2020). The presented study investigates the effects of two immunomodulatory treatments; however, they aren't the only treatments for multiple sclerosis. MS treatments include immunosuppressants (i.e., fingolimod), immunomodulatory therapies (i.e., IFN-β and DMF), and immune reconstitution therapies (i.e., alemtuzumab and cladribine) (Dobson and Giovannoni, 2019). Future studies could investigate the effects of immunosuppressants and immune reconstitution therapies on the brain's dynamics via nonlinear analysis. These studies could use nonlinear analysis to investigate how these different treatment groups compare.

As reported by Hernandez et al. (2023), several articles have used machine learning algorithms in studying MS (Ahmadi and Pechenizkiy, 2016; Torabi et al., 2017; Kotan et al., 2019; Raeisi et al., 2020; Karaca et al., 2021; Karacan et al., 2022; Mohseni and Moghaddasi, 2022). Methods include feature extraction, feature selection, and feature classification, and these methods could allow researchers to swiftly search and analyze large datasets for potential biomarkers (Hernandez et al., 2023; Hossain et al., 2022). In future studies, researchers could build on this study's approach by developing machine-learning methods that integrate MRI and functional magnetic resonance imaging (fMRI) to compare the efficacy of different MS treatments. This could further enhance the analysis by identifying trends and possible biomarkers more efficiently.

5 Conclusion

After demonstrating the limitations associated with lag-1 autocorrelation, we employed sample entropy and Higuchi's fractal dimension to analyze the nonlinearity in electroencephalogram signatures of MS patients treated with Interferon-β and dimethyl fumarate. We have shown that patients undergoing each treatment exhibited more complex and less predictable brain activity when compared to the control group. SampEn demonstrated the highest sensitivity to treatment effects, whereas HFD revealed greater sensitivity when considering the effect of time.

Thus, these results have provided insights into how the effects of each treatment have a different impact on brain activity. They have furthered our understanding of the brain's mechanics associated with MS. With the knowledge gathered here and on future investigations, current treatment strategies could be improved, and any benefits or limitations associated with these treatments could be disclosed. Thus, our study expands the scope of the analysis of EEG signatures of MS patients and paves the way for an alternative approach to analyzing treatment effectiveness.

Data availability statement

The raw data supporting the conclusions of this article will be made available by the authors, without undue reservation.

Ethics statement

The studies involving humans were approved by Institute of Applied Psychology Ethics Committee of the Jagiellonian University. The studies were conducted in accordance with the local legislation and institutional requirements. The participants provided their written informed consent to participate in this study.

Author contributions

CH: Conceptualization, Formal analysis, Methodology, Visualization, Writing – original draft, Writing – review & editing, Software. NA: Conceptualization, Data curation, Investigation, Writing – review & editing, Writing – original draft, Formal analysis, Methodology. MG: Writing – review & editing, Conceptualization, Data curation, Investigation, Writing – original draft, Formal analysis, Methodology. PO: Writing – review & editing, Writing – original draft, Conceptualization, Formal analysis, Methodology. MF: Writing – original draft, Writing – review & editing, Conceptualization, Formal analysis, Methodology. AS: Writing – review & editing, Data curation, Investigation. MW: Writing – review & editing, Data curation, Investigation. MM: Writing – review & editing, Data curation, Investigation. KN: Writing – review & editing, Data curation, Investigation. KZ-W: Writing – review & editing, Data curation, Investigation. MA: Writing – original draft, Writing – review & editing, Formal analysis. PH: Writing – original draft, Writing – review & editing, Formal analysis. TM: Writing – original draft, Writing – review & editing, Conceptualization, Formal analysis, Methodology. WK: Conceptualization, Formal analysis, Methodology, Supervision, Writing – original draft, Writing – review & editing.

Funding

The author(s) declare that financial support was received for the research, authorship, and/or publication of this article. The data collection was funded by the Foundation for Polish Science cofinanced by the European Union under the European Regional Development Fund in the POIR.04.04.00-00-14DE/18-00 project carried out within the Team-Net programme. The research for this publication has been supported by a grant from the Priority Research Area DigiWorld under the Strategic Programme Excellence Initiative at Jagiellonian University.

Conflict of interest

The authors declare that the research was conducted in the absence of any commercial or financial relationships that could be construed as a potential conflict of interest.

The author(s) declared that they were an editorial board member of Frontiers, at the time of submission. This had no impact on the peer review process and the final decision.

Generative AI statement

The authors declare that no Gen AI was used in the creation of this manuscript.

Publisher's note

References

Accardo, A., Affinito, M., Carrozzi, M., and Bouquet, F. (1997). Use of the fractal dimension for the analysis of electroencephalographic time series. *Biol. Cybern.* 77, 339–350. doi: 10.1007/s004220050394

Ahmadi, N., and Pechenizkiy, M. (2016) Application of horizontal visibility graph as a robust measure of neurophysiological signals synchrony. IEEE 29th international symposium on computer-based medical systems (CBMS), IEEE: Piscataway 273–278.

Ahmadlou, M., Adeli, H., and Adeli, A. (2011). Fractality and a wavelet-chaos-methodology for EEG-based diagnosis of Alzheimer disease. *Alzheimer Dis. Assoc. Disord.* 25, 85–92. doi: 10.1097/WAD.0b013e3181ed1160

Amon, M. J. (2021). SampEnRun [MATLAB]. In Unpublished script.

Arle, J. E., and Simon, R. H. (1990). An application of fractal dimension to the detection of transients in the electroencephalogram. *Electroencephalogr. Clin. Neurophysiol.* 75, 296–305. doi: 10.1016/0013-4694(90)90108-V

Bauer, M., Glenn, T., Alda, M., Grof, P., Sagduyu, K., Bauer, R., et al. (2011). Comparison of pre-episode and pre-remission states using mood ratings from patients with bipolar disorder. *Pharmacopsychiatry* 44, S49–S53. doi: 10.1055/s-0031-1273765

Bruce, E. N., Bruce, M. C., and Vennelaganti, S. (2009). Sample entropy tracks changes in electroencephalogram power spectrum with sleep state and aging. *J. Clin. Neurophysiol.* 26, 257–266. doi: 10.1097/WNP.0b013e3181b2f1e3

Byrne, B. M. (2010). Structural equation modeling with AMOS: basic concepts, applications, and programming (multivariate applications series). New York: Taylor & Francis Group.

Carrubba, S., Minagar, A., Chesson, A. L. Jr., Frilot, C. 2nd, and Marino, A. A. (2012). Increased determinism in brain electrical activity occurs in association with multiple sclerosis. *Neurol. Res.* 34, 286–290. doi: 10.1179/1743132812Y.0000000010

Chiaravalloti, N. D., and DeLuca, J. (2008). Cognitive impairment in multiple sclerosis. *Lancet Neurol.* 7, 1139–1151. doi: 10.1016/S1474-4422(08)70259-X

Chouvarda, I., Rosso, V., Mendez, M. O., Bianchi, A. M., Parrino, L., Grassi, A., et al. (2011). Assessment of the EEG complexity during activations from sleep. *Comput. Methods Prog. Biomed.* 104, e16–e28. doi: 10.1016/j.cmpb.2010.11.005

Cohen, J. A., Barkhof, F., Comi, G., Hartung, H.-P., Khatri, B. O., Montalban, X., et al. (2010). Oral fingolimod or intramuscular interferon for relapsing multiple sclerosis. *N. Engl. J. Med.* 362, 402–415. doi: 10.1056/NEJMoa0907839

Costa, M., Goldberger, A. L., and Peng, C.-K. (2005). Multiscale entropy analysis of biological signals. *Phys. Rev. E Stat. Nonlin. Soft Matter Phys.* 71:021906. doi: 10.1103/PhysRevE.71.021906

Cuesta-Frau, D., Miró-Martínez, P., Jordán Núñez, J., Oltra-Crespo, S., and Molina Picó, A. (2017). Noisy EEG signals classification based on entropy metrics. Performance assessment using first and second generation statistics. *Comput. Biol. Med.* 87, 141–151. doi: 10.1016/j.compbiomed.2017.05.028

D'Amico, E., Zanghì, A., Romeo, M., Cocco, E., Maniscalco, G. T., Brescia Morra, V., et al. (2021). Injectable versus oral first-line disease-modifying therapies: results from the Italian MS register. *Neurotherapeutics* 18, 905–919. doi: 10.1007/s13311-020-01001-6

Delgado-Bonal, A., and Marshak, A. (2019). Approximate entropy and sample entropy: a comprehensive tutorial. *Entropy* 21:541. doi: 10.3390/e21060541

Delorme, A., and Makeig, S. (2004). EEGLAB: an open source toolbox for analysis of single-trial EEG dynamics including independent component analysis. *J. Neurosci. Methods* 134, 9–21. doi: 10.1016/j.jneumeth.2003.10.009

Di Ieva, A., Esteban, F. J., Grizzi, F., Klonowski, W., and Martín-Landrove, M. (2015). Fractals in the neurosciences, part II: clinical applications and future perspectives. *Neuroscientist* 21, 30–43. doi: 10.1177/1073858413513928

Dobson, R., and Giovannoni, G. (2019). Multiple sclerosis–a review. *Eur. J. Neurol.* 26, 27–40. doi: 10.1111/ene.13819

Doyle, T. L., Dugan, E. L., Humphries, B., and Newton, R. U. (2004). Discriminating between elderly and young using a fractal dimension analysis of Centre of pressure. *Int. J. Med. Sci.* 1, 11–20. doi: 10.7150/ijms.1.11

Duran, N. D., Dale, R., Kello, C. T., Street, C. N., and Richardson, D. C. (2013). Exploring the movement dynamics of deception. *Front. Psychol.* 4:140. doi: 10.3389/fpsyg.2013.00140

Er, M. B., Çiğ, H., and Aydilek, I. B. (2021). A new approach to recognition of human emotions using brain signals and music stimuli. *Appl. Acoust.* 175:107840. doi: 10.1016/j.apacoust.2020.107840

Esteller, R., Vachtsevanos, G., Echauz, J., and Litt, B. (2001). A comparison of waveform fractal dimension algorithms. *IEEE Trans. Circuits Syst. I* 48, 177–183. doi: 10.1109/81.904882

Hair, J., Black, W., Babin, B., Anderson, R., and Tatham, R. (2010). Multivariate data analysis. Upper Saddle River, NJ: Prentice-Hall.

Hernandez, C. I., Kargarnovin, S., Hejazi, S., and Karwowski, W. (2023). Examining electroencephalogram signatures of people with multiple sclerosis using a nonlinear dynamics approach: a systematic review and bibliographic analysis. *Front. Comput. Neurosci.* 17:7067. doi: 10.3389/fncom.2023.1207067

Hossain, M. Z., Daskalaki, E., Brüstle, A., Desborough, J., Lueck, C. J., and Suominen, H. (2022). The role of machine learning in developing non-magnetic resonance imaging based biomarkers for multiple sclerosis: a systematic review. *BMC Med. Inform. Decis. Mak.* 22:242. doi: 10.1186/s12911-022-01985-5

Huang, Z., Liu, X., Mashour, G. A., and Hudetz, A. G. (2018). Timescales of intrinsic BOLD signal dynamics and functional connectivity in pharmacologic and neuropathologic states of unconsciousness. *J. Neurosci.* 38, 2304–2317. doi: 10.1523/JNEUROSCI.2545-17.2018

Jakimovski, D., Kolb, C., Ramanathan, M., Zivadinov, R., and Weinstock-Guttman, B. (2018). Interferon β for multiple sclerosis. *Cold Spring Harb. Perspect. Med.* 8:32003. doi: 10.1101/cshperspect.a032003

Karaca, B. K., Akşahin, M. F., and Öcal, R. (2021). Detection of multiple sclerosis from photic stimulation EEG signals. *Biomed. Signal Process. Control* 67:102571. doi: 10.1016/j.bspc.2021.102571

Karacan, S. Ş., Saraoğlu, H. M., Kabay, S. C., Akdağ, G., Keskinkılıç, C., and Tosun, M. (2022). EEG based environment classification during cognitive task of multiple sclerosis patients. International congress on human-computer interaction, Optimization and Robotic Applications (HORA). IEEE, Ankara, Türkiye. 01–04.

Kargarnovin, S., Hernandez, C., Farahani, F. V., and Karwowski, W. (2023). Evidence of Chaos in electroencephalogram signatures of human performance: a systematic review. *Brain Sci.* 13:813. doi: 10.3390/brainsci13050813

Kesić, S., and Spasić, S. Z. (2016). Application of Higuchi's fractal dimension from basic to clinical neurophysiology: a review. *Comput. Methods Prog. Biomed.* 133, 55–70. doi: 10.1016/j.cmpb.2016.05.014

Kondacs, A., and Szabó, M. (1999). Long-term intra-individual variability of the background EEG in normals. *Clin. Neurophysiol.* 110, 1708–1716. doi: 10.1016/S1388-2457(99)00122-4

Kotan, S., Van Schependom, J., Nagels, G., and Akan, A. (2019). Comparison of IMF selection methods in classification of multiple sclerosis EEG data. In 2019 medical technologies congress (TIPTEKNO). Izmir: IEEE, 1–4.

Kurtzke, J. F. (1983). Rating neurologic impairment in multiple sclerosis: an expanded disability status scale (EDSS). *Neurology* 33:1444. doi: 10.1212/WNL.33.11.1444

Lachaux, J. P., Pezard, L., Garnero, L., Pelte, C., Renault, B., Varela, F. J., et al. (1997). Spatial extension of brain activity fools the single-channel reconstruction of EEG dynamics. *Hum. Brain Mapp.* 5, 26–47. doi: 10.1002/(SICI)1097-0193(1997)5:1<26::AID-HBM4>3.0.CO;2-P

Linker, R. A., and Haghikia, A. (2016). Dimethyl fumarate in multiple sclerosis: latest developments, evidence and place in therapy. *Ther. Adv. Chronic Dis.* 7, 198–207. doi: 10.1177/2040622316653307

Lorscheider, J., Benkert, P., Lienert, C., Hänni, P., Derfuss, T., Kuhle, J., et al. (2021). Comparative analysis of dimethyl fumarate and Fingolimod in relapsing–remitting multiple sclerosis. *J. Neurol.* 268, 941–949. doi: 10.1007/s00415-020-10226-6

Marino, M., Liu, Q., Samogin, J., Tecchio, F., Cottone, C., Mantini, D., et al. (2019). Neuronal dynamics enable the functional differentiation of resting state networks in the human brain. *Hum. Brain Mapp.* 40, 1445–1457. doi: 10.1002/hbm.24458

Márton, L., Brassai, S. T., Bakó, L., and Losonczi, L. (2014). Detrended fluctuation analysis of EEG signals. *Proc. Technol.* 12, 125–132. doi: 10.1016/j.protcy.2013.12.465

Meisel, C., Bailey, K., Achermann, P., and Plenz, D. (2017). Decline of long-range temporal correlations in the human brain during sustained wakefulness. *Sci. Rep.* 7:11825. doi: 10.1038/s41598-017-12140-w

Mills, E. A., Ogrodnik, M. A., Plave, A., and Mao-Draayer, Y. (2018). Emerging understanding of the mechanism of action for dimethyl fumarate in the treatment of multiple sclerosis. *Front. Neurol.* 9:5. doi: 10.3389/fneur.2018.00005

Mohseni, E., and Moghaddasi, S. M. (2022). A hybrid approach for MS diagnosis through nonlinear EEG descriptors and metaheuristic optimized classification learning. *Comput. Intell. Neurosci.* 2022, 1–14. doi: 10.1155/2022/5430528

Paramanathan, P., and Uthayakumar, R. (2008). Application of fractal theory in analysis of human electroencephalographic signals. *Comput. Biol. Med.* 38, 372–378. doi: 10.1016/j.compbiomed.2007.12.004

Pezard, L., Jech, R., and Růžička, E. (2001). Investigation of non-linear properties of multichannel EEG in the early stages of Parkinson's disease. *Clin. Neurophysiol.* 112, 38–45. doi: 10.1016/S1388-2457(00)00512-5

Pezard, L., Martinerie, J., Varela, F., Bouchet, F., Derouesné, C., and Renault, B. (1998). Brain entropy maps quantify drug dosage on Alzheimer's disease. *Neurosci. Lett.* 253, 5–8. doi: 10.1016/S0304-3940(98)00603-X

Pincus, S. M. (2006). Approximate entropy as a measure of irregularity for psychiatric serial metrics. *Bipolar Disord.* 8, 430–440. doi: 10.1111/j.1399-5618.2006.00375.x

Porcaro, C., Mayhew, S. D., Marino, M., Mantini, D., and Bagshaw, A. P. (2020). Characterisation of haemodynamic activity in resting state networks by fractal analysis. *Int. J. Neural Syst.* 30:2050061. doi: 10.1142/S0129065720500616

Pritchard, W. S., and Duke, D. W. (1995). Measuring Chaos in the brain - a tutorial review of EEG dimension estimation. *Brain Cogn.* 27, 353–397. doi: 10.1006/brcg.1995.1027

Raeisi, K., Mohebbi, M., Khazaei, M., Seraji, M., and Yoonessi, A. (2020). Phase-synchrony evaluation of EEG signals for multiple sclerosis diagnosis based on bivariate empirical mode decomposition during a visual task. *Comput. Biol. Med.* 117:103596. doi: 10.1016/j.compbiomed.2019.103596

Raghavendra, B., Dutt, D. N., Halahalli, H. N., and John, J. P. (2009). Complexity analysis of EEG in patients with schizophrenia using fractal dimension. *Physiol. Meas.* 30, 795–808. doi: 10.1088/0967-3334/30/8/005

Ramanand, P., Nampoori, V., and Sreenivasan, R. (2004). Complexity quantification of dense array EEG using sample entropy analysis. *J. Integr. Neurosci.* 3, 343–358. doi: 10.1142/S0219635204000567

Ramdani, S., Seigle, B., Lagarde, J., Bouchara, F., and Bernard, P. L. (2009). On the use of sample entropy to analyze human postural sway data. *Med. Eng. Phys.* 31, 1023–1031. doi: 10.1016/j.medengphy.2009.06.004

Reick, C., Ellrichmann, G., Thöne, J., Scannevin, R. H., Saft, C., Linker, R. A., et al. (2014). Neuroprotective dimethyl fumarate synergizes with immunomodulatory interferon beta to provide enhanced axon protection in autoimmune neuroinflammation. *Exp. Neurol.* 257, 50–56. doi: 10.1016/j.expneurol.2014.04.003

Richman, J. S., and Moorman, J. R. (2000). Physiological time-series analysis using approximate entropy and sample entropy. *Am. J. Phys. Heart Circ. Phys.* 278, H2039–H2049. doi: 10.1152/ajpheart.2000.278.6.H2039

Rodriguez-Bermudez, G., and Garcia-Laencina, P. J. (2015). Analysis of EEG signals using nonlinear dynamics and chaos: a review. *Appl. Math. Inf. Sci.* 9:2309. doi: 10.12785/amis/090512

Sanei, S., and Chambers, J. A. (2007). EEG signal processing. New York: Wiley, 1–34.

Sattarnezhad, N., Healy, B. C., Baharnoori, M., Diaz-Cruz, C., Stankiewicz, J., Weiner, H. L., et al. (2022). Comparison of dimethyl fumarate and interferon outcomes in an MS cohort. *BMC Neurol.* 22, 1–8. doi: 10.1186/s12883-022-02761-8

Scarpa, F., Rubega, M., Zanon, M., Finotello, F., Sejling, A.-S., and Sparacino, G. (2017). Hypoglycemia-induced EEG complexity changes in type 1 diabetes assessed by fractal analysis algorithm. *Biomed. Signal Process. Control* 38, 168–173. doi: 10.1016/j.bspc.2017.06.004

Scheffer, M., Bascompte, J., Brock, W. A., Brovkin, V., Carpenter, S. R., Dakos, V., et al. (2009). Early-warning signals for critical transitions. *Nature* 461, 53–59. doi: 10.1038/nature08227

Shalbaf, R., Behnam, H., Sleigh, J., and Voss, L. (2012). Measuring the effects of sevoflurane on electroencephalogram using sample entropy. *Acta Anaesthesiol. Scand.* 56, 880–889. doi: 10.1111/j.1399-6576.2012.02676.x

Siffrin, V., Vogt, J., Radbruch, H., Nitsch, R., and Zipp, F. (2010). Multiple sclerosis–candidate mechanisms underlying CNS atrophy. *Trends Neurosci.* 33, 202–210. doi: 10.1016/j.tins.2010.01.002

Smits, F. M., Porcaro, C., Cottone, C., Cancelli, A., Rossini, P. M., and Tecchio, F. (2016). Electroencephalographic fractal dimension in healthy ageing and Alzheimer's disease. *PLoS One* 11:e0149587. doi: 10.1371/journal.pone.0149587

Spasic, S., Kalauzi, A., Kesic, S., Obradovic, M., and Saponjic, J. (2011). Surrogate data modeling the relationship between high frequency amplitudes and Higuchi fractal dimension of EEG signals in anesthetized rats. *J. Theor. Biol.* 289, 160–166. doi: 10.1016/j.jtbi.2011.08.037

Stam, K. J., Tavy, D. L., Jelles, B., Achtereekte, H. A., Slaets, J. P., and Keunen, R. W. (1994). Non-linear dynamical analysis of multichannel EEG: clinical applications in dementia and Parkinson's disease. *Brain Topogr.* 7, 141–150. doi: 10.1007/BF01186772

Thomasson, N., Pezard, L., Allilaire, J.-F., Renault, B., and Martinerie, J. (2000). Nonlinear EEG changes associated with clinical improvement in depressed patients. *Nonlinear Dynamics Psychol. Life Sci.* 4, 203–218. doi: 10.1023/A:1009580427443

Torabi, A., Daliri, M. R., and Sabzposhan, S. H. (2017). Diagnosis of multiple sclerosis from EEG signals using nonlinear methods. *Australas. Phys. Eng. Sci. Med.* 40, 785–797. doi: 10.1007/s13246-017-0584-9

Vermersch, P., Scaramozza, M., Levin, S., Alroughani, R., Deiva, K., Pozzilli, C., et al. (2022). Effect of dimethyl fumarate vs interferon β-1a in patients with pediatric-onset multiple sclerosis: the CONNECT randomized clinical trial. *JAMA Netw. Open* 5:e2230439. doi: 10.1001/jamanetworkopen.2022.30439

Viglietta, V., Miller, D., Bar-Or, A., Phillips, J. T., Arnold, D. L., Selmaj, K., et al. (2015). Efficacy of delayed-release dimethyl fumarate in relapsing-remitting multiple sclerosis: integrated analysis of the phase 3 trials. *Ann. Clin. Transl. Neurol.* 2, 103–118. doi: 10.1002/acn3.148

Wackermann, J., Lehmann, D., Dvorak, I., and Michel, C. M. (1993). Global dimensional complexity of multi-channel EEG indicates change of human brain functional state after a single dose of a nootropic drug. *Electroencephalogr. Clin. Neurophysiol.* 86, 193–198. doi: 10.1016/0013-4694(93)90007-I

Wajnsztejn, R., De Carvalho, T. D., Garner, D. M., Raimundo, R. D., Vanderlei, L. C. M., Godoy, M. F., et al. (2016). Higuchi fractal dimension applied to rr intervals in children with attention defi cit hyperactivity disorder. *J. Hum. Growth Dev.* 26, 147–153. doi: 10.7322/jhgd.119256

Wanliss, J., Arriaza, R. H., Wanliss, G., and Gordon, S. (2021). Optimization of the Higuchi method. *Int. J. Res. Granthaalayah* 9, 202–213. doi: 10.29121/granthaalayah.v9.i11.2021.4393

Wątorek, M., Tomczyk, W., Gawłowska, M., Golonka-Afek, N., Żyrkowska, A., Marona, M., et al. (2024). Multifractal organization of EEG signals in multiple sclerosis. *Biomed. Signal Process. Control* 91:105916. doi: 10.1016/j.bspc.2023.105916

Yakovleva, T. V., Kutepov, I. E., Karas, A. Y., Yakovlev, N. M., Dobriyan, V. V., Papkova, I. V., et al. (2020). EEG analysis in structural focal epilepsy using the methods of nonlinear dynamics (Lyapunov exponents, Lempel–Ziv complexity, and multiscale entropy). *Sci. World J.* 2020, 1–13. doi: 10.1155/2020/8407872

Zappasodi, F., Marzetti, L., Olejarczyk, E., Tecchio, F., and Pizzella, V. (2015). Age-related changes in electroencephalographic signal complexity. *PLoS One* 10:e0141995. doi: 10.1371/journal.pone.0141995

Zappasodi, F., Olejarczyk, E., Marzetti, L., Assenza, G., Pizzella, V., and Tecchio, F. (2014). Fractal dimension of EEG activity senses neuronal impairment in acute stroke. *PLoS One* 9:e100199. doi: 10.1371/journal.pone.0100199

Zhang, Q., Ding, J., Kong, W., Liu, Y., Wang, Q., and Jiang, T. (2021). Epilepsy prediction through optimized multidimensional sample entropy and bi-LSTM. *Biomed. Signal Process. Control* 64:102293. doi: 10.1016/j.bspc.2020.102293

frontiers | Frontiers in Neuroinformatics

TYPE Original Research
PUBLISHED 09 April 2025
DOI 10.3389/fninf.2025.1559335

OPEN ACCESS

EDITED BY
Saadullah Farooq Abbasi,
University of Birmingham, United Kingdom

REVIEWED BY
Muhammad Farrukh Qureshi,
Namal College, Pakistan
Hafza Ayesha Siddiqa,
Fudan University, China

*CORRESPONDENCE
Jie Zhou
✉ sxuj_zhou@163.com

RECEIVED 12 January 2025
ACCEPTED 06 March 2025
PUBLISHED 09 April 2025

CITATION
Jiang Z, Hu K, Qu J, Bian Z, Yu D and Zhou J (2025) Recognition of MI-EEG signals using extended-LSR-based inductive transfer learning.
Front. Neuroinform. 19:1559335.
doi: 10.3389/fninf.2025.1559335

Recognition of MI-EEG signals using extended-LSR-based inductive transfer learning

Zhibin Jiang[1,2], Keli Hu[1,3], Jia Qu[4], Zekang Bian[5,6], Donghua Yu[1,2] and Jie Zhou[1,2]*

[1]Department of Computer Science and Engineering, Shaoxing University, Shaoxing, China, [2]Institute of Artificial Intelligence, Shaoxing University, Shaoxing, China, [3]Information Technology R&D Innovation Center of Peking University, Shaoxing, China, [4]Department of Computer Science and Artificial Intelligence, Changzhou University, Changzhou, China, [5]Department of AI & Computer Science, Jiangnan University, Wuxi, China, [6]Department of Taihu Jiangsu Key Construction Lab of IoT Application Technologies, Wuxi, China

Introduction: Motor imagery electroencephalographic (MI-EEG) signal recognition is used in various brain–computer interface (BCI) systems. In most existing BCI systems, this identification relies on classification algorithms. However, generally, a large amount of subject-specific labeled training data is required to reliably calibrate the classification algorithm for each new subject. To address this challenge, an effective strategy is to integrate transfer learning into the construction of intelligent models, allowing knowledge to be transferred from the source domain to enhance the performance of models trained in the target domain. Although transfer learning has been implemented in EEG signal recognition, many existing methods are designed specifically for certain intelligent models, limiting their application and generalization.

Methods: To broaden application and generalization, an extended-LSR-based inductive transfer learning method is proposed to facilitate transfer learning across various classical intelligent models, including neural networks, Takagi-SugenoKang (TSK) fuzzy systems, and kernel methods.

Results and discussion: The proposed method not only promotes the transfer of valuable knowledge from the source domain to improve learning performance in the target domain when target domain training data are insufficient but also enhances application and generalization by incorporating multiple classic base models. The experimental results demonstrate the effectiveness of the proposed method in MI-EEG signal recognition.

KEYWORDS

motor imagery, EEG, brain-computer interface, LSR, inductive transfer learning

1 Introduction

A brain–computer interface (BCI) is a technology that establishes connections between the brain and external devices, facilitating information exchange between them (Edelman et al., 2024). BCIs collect and analyze electrical signals generated by brain activity, transforming these signals into instructions that can be used to control external devices such as computers, prosthetics, and wheelchairs. As such, BCIs can assist, enhance, and repair human sensory and motor functions, improving human–computer interaction capabilities. BCIs do not rely on the peripheral nervous system or muscles, providing a new method for people who have lost their mobility due to illness or disability to communicate with the external environment and operate devices. BCIs not only open new possibilities for people with disabilities but also

advance our understanding of the brain, ushering in a new era of human–computer interaction.

1.1 Motivation

Motor imagery electroencephalographic (MI-EEG) (Mohammadi et al., 2022) signal recognition is an important mechanism for brain-computer interfaces (BCIs). Moreover, with the advancement of machine learning, numerous classification methods based on machine learning have been proposed for MI-EEG signal recognition in the literature (Abbas et al., 2021; Ko et al., 2021; Zhang et al., 2024; Ghumman et al., 2021; Cover and Hart, 1967; Aldea et al., 2014; Kohavi, 1996; Wang and Zhang, 2016; Fisher, 1936; Li et al., 2022; Bennett and Demiriz, 1999; Fouad et al., 2020; Siddiqa et al., 2024; Siddiqa et al., 2023; Qureshi et al., 2022; Qureshi et al., 2023), including neural networks (NNs) (Abbas et al., 2021; Ko et al., 2021), fuzzy logic systems (FLSs) (Zhang et al., 2024; Ghumman et al., 2021), k-nearest neighbors (kNNs) (Cover and Hart, 1967; Aldea et al., 2014), naïve Bayes (NB) (Kohavi, 1996; Wang and Zhang, 2016), linear discriminant analysis (LDA) (Fisher, 1936; Li et al., 2022), support vector machines (SVMs) (Bennett and Demiriz, 1999; Fouad et al., 2020), and more. Although these methods have demonstrated varying degrees of success, they typically require a large amount of subject-specific training data to adjust their parameters. However, this data acquisition process can be time-consuming and not user-friendly. When calibration data is insufficient, the classification performance of these algorithms can significantly deteriorate. As highlighted in BCI Competition III (Blankertz et al., 2006), "*a challenge is that more expectations of training a model with a good classification accuracy are becoming urgent in the case that only a small number of training samples are available.*" Therefore, it is essential to develop advanced machine-learning methods for MI-EEG that perform effectively with small calibration datasets.

Transfer learning is a promising method for addressing the above problem. It can be used to transfer useful information from related scenes (i.e., source domains) to the current scene (i.e., target domain), which typically has limited training data (Pan and Yang, 2010). As a result, transfer learning is particularly effective in improving classification performance during the early stages of model training when there is not enough subject-specific training data. Figure 1 shows the differences

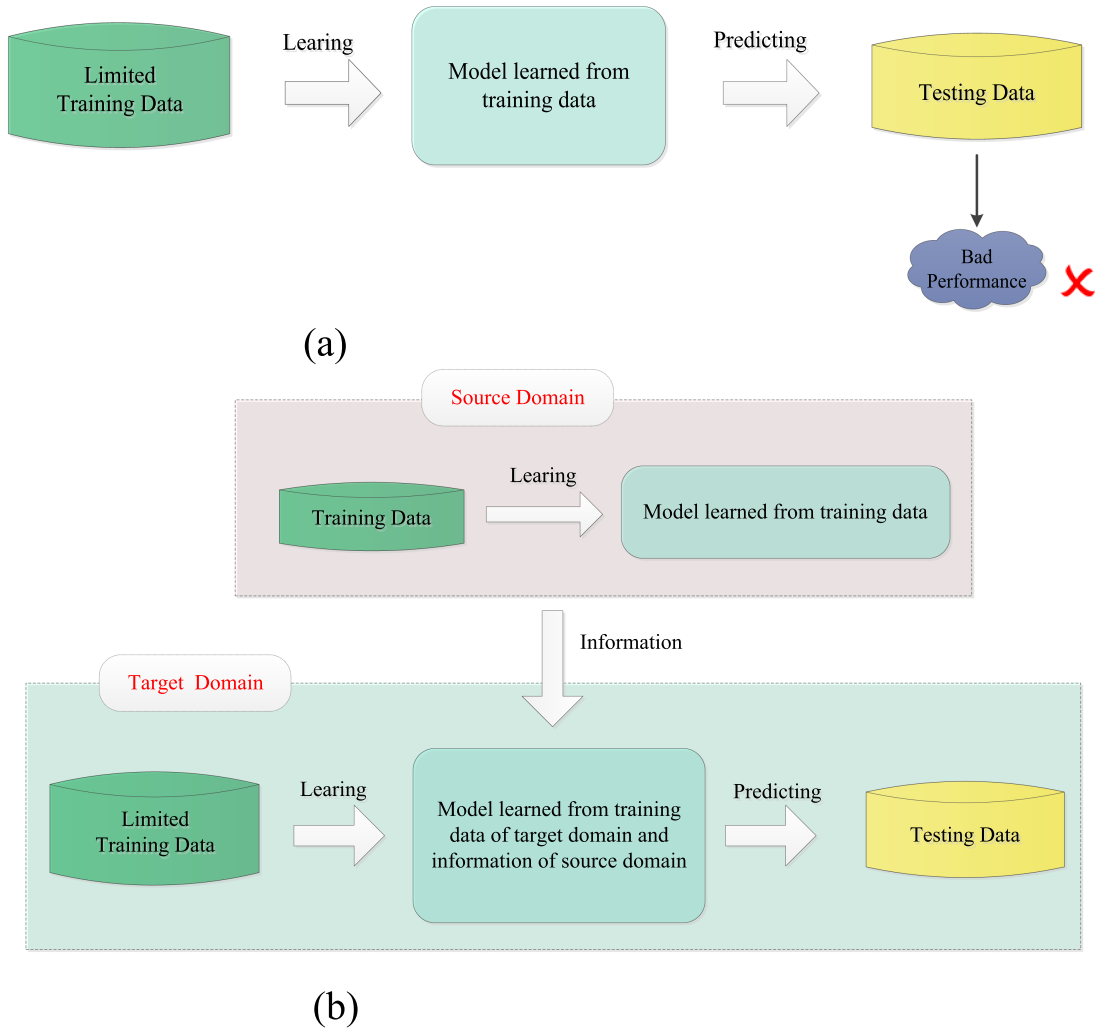

FIGURE 1
Differences between traditional machine learning **(a)** and transfer learning **(b)**.

between traditional machine learning and transfer learning. Since its introduction in 1995, transfer learning has been successfully applied in classification, clustering, and regression, with classification being the most extensively researched area. Some representative studies can be found in Zhang et al. (2022), Jiang et al. (2019), Xie et al. (2018), Pan et al. (2011), Wan et al. (2021), Li et al., 2019). Existing transfer learning methods can be categorized into three types: inductive transfer learning methods (Zhang et al., 2022; Jiang et al., 2019), which consider both supervised source and target domains; transductive transfer learning methods (Xie et al., 2018; Pan et al., 2011), which involve supervised source domains and unsupervised target domains; and unsupervised transfer learning methods, which account for both unsupervised source and target domains (Wan et al., 2021; Li et al., 2019). In MI-EEG signal recognition, when labeled MI-EEG samples in the target domain are insufficient, inductive transfer learning methods naturally become the preferred choice. Furthermore, since MI-EEG signals involve personal privacy information, inspired by Jiang et al. (2019), we investigate a knowledge-based inductive transfer learning method to ensure security without directly utilizing samples from the source domain.

Inductive transfer learning has recently attracted widespread attention and demonstrated strong performance in MI-EEG signal recognition. However, most existing inductive transfer learning methods are tailored to specific base models, rendering them inapplicable to other base models. As a result, they demonstrate poor performance in terms of application and generalization. To address this limitation, we propose an extended-LSR-based inductive transfer learning framework (ELSR-TL) that integrates neural networks, Takagi-Sugeno-Kang (TSK) fuzzy systems, and kernel methods. Figure 2 shows the framework of ELSR-TL.

1.2 Contributions

The main contributions of this study can be highlighted as follows:

1 ELSR-TL has an inductive transfer learning mechanism that can be used to transfer useful knowledge from the source domain to enhance learning performance in the target domain when the training data in the target domain are insufficient.
2 ELSR-TL enhances LSR by integrating multiple classic base models, such as neural networks, TSK fuzzy systems, and kernel methods. As such, ELSR-TL is not only suited for a specific model but also demonstrates improved applicability and generalization.
3 Experimental studies were conducted to validate the applicability of the proposed method for MI-EEG signal identification.

The remainder of this paper is organized as follows: Section II describes related work, including studies on existing MI-EEG feature extraction and pattern recognition methods. Section III details the proposed extended-LSR-based inductive transfer learning method. Section IV provides the experimental results and analysis. Finally, Section VI presents the conclusions drawn.

2 Backgrounds

This section states the backgrounds underlying the proposed MI-EEG recognition method. It describes the datasets used to evaluate

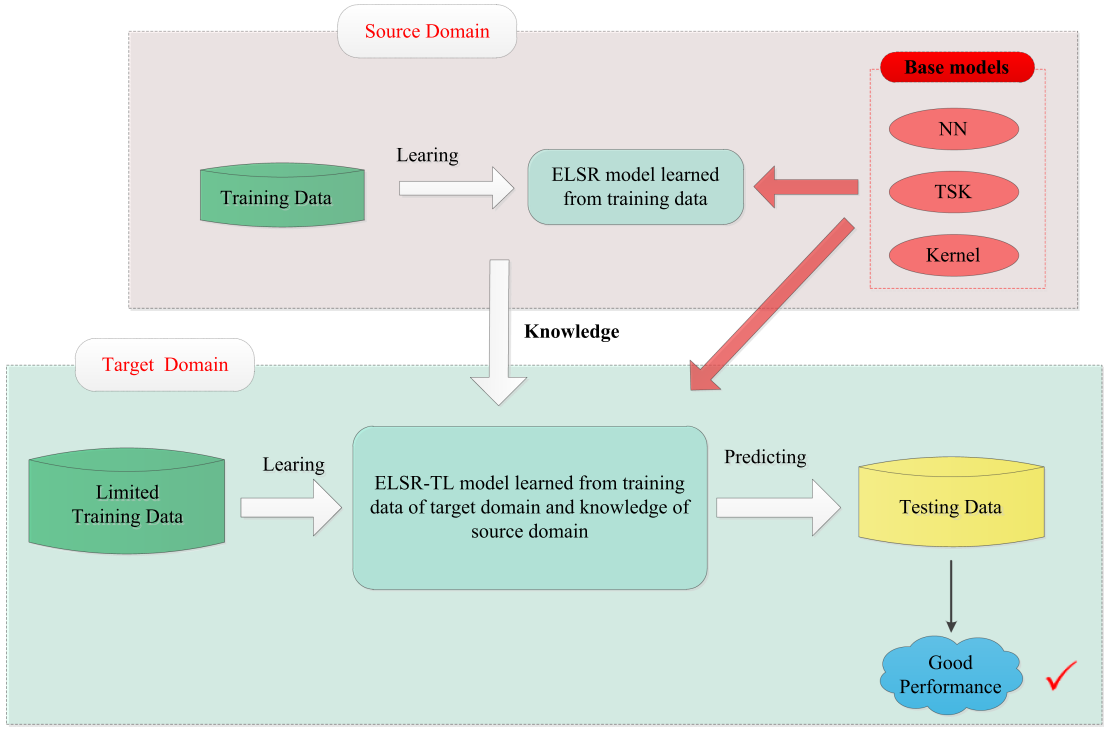

FIGURE 2
Framework of ELSR-TL.

the method and reviews several classical feature extraction and pattern recognition methods.

2.1 Datasets

We used BCI Competition Data Set IVa, provided by Fraunhofer FIRST and Charité University Medicine Berlin. A detailed description of this dataset can be found in (Blankertz et al., 2006).

This MI-EEG dataset contains five subsets corresponding to five healthy testers (aa, al, av., aw, and ay). Each subset contains 280 EEG trials, which have 128 electrodes and a trial length of 3.5 s. Each subset was partitioned into a training set and a test set, as shown in Figure 3. Figure 4 shows the representative MI-EEG signals in the five subsets.

2.2 Feature extraction methods

EEG signals are complex, nonlinear, and non-stationary. Effective feature extraction is critical to pattern recognition performance. Some of the most representative feature extraction methods have been proposed to manage raw MI-EEG signals. Typically, feature extraction methods can be classified into four main categories: time-domain analysis, frequency-domain analysis, time-frequency analysis, and space-domain analysis.

In time domain analysis, EEG signal features are analyzed in the time domain. Characteristics of the waveforms, such as mean, variance, amplitude, and kurtosis, can be used to extract features of MI-EEG signals (Greene et al., 2008).

In frequency domain analysis, the features of EEG signals are analyzed by investigating the relationship between their frequency and energy. The short-time Fourier transform (Schafer and Rabiner, 1973) is a classical power spectrum analysis method, and adaptive autoregression (Pfurtscheller et al., 1998) is an improved frequency domain analysis method.

In time-frequency analysis (Blanco et al., 1997), the features of EEG signals are extracted using the joint distribution information of the time and frequency domains. Wavelet transform analysis (Antonini et al., 1992) is the most representative method in this category.

In space-domain analysis, the features of EEG signals are extracted by analyzing the electrical activity of neurons in different brain spaces. Common spatial pattern (CSP) (Lotte and Guan, 2011) is a commonly used method in this category. In this method, labeled trials are used to produce a transformation that maximizes the variance of one class while minimizing the variance of the other.

2.3 Pattern recognition methods

Pattern recognition utilizes the extracted EEG features for classification. Some of the most representative pattern recognition methods include the following: (1) NNs (Abbas et al., 2021; Ko et al., 2021), which simulate the mechanism of the human nervous system. Feedforward NNs are the most commonly used in EEG classification. (2) FLSs (Zhang et al., 2024; Ghumman et al., 2021), which emulate the human reasoning process and excel at managing numerical and linguistic uncertainties. (3) kNNs (Cover and Hart, 1967; Aldea et al., 2014), which determine the class of a new sample by considering its k nearest neighbors. (4) NB (Kohavi, 1996; Wang and Zhang, 2016), a simple and efficient classification algorithm based on probability. By utilizing known conditional probability and *a priori* probability, NB calculates the posterior probability of each class and assigns the test sample to the class with the highest a posteriori probability. (5) LDA (Fisher, 1936; Li et al., 2022), which applies the Fisher criterion to find the optimal projective vector that maximizes the largest scatter between classes while minimizing the scatter within each class. (6) SVMs (Bennett and Demiriz, 1999; Fouad et al., 2020), which aim to maximize the margins between different classes.

Although existing MI-EEG classification methods have demonstrated their effectiveness in various applications, they all require a substantial amount of subject-specific training data. In

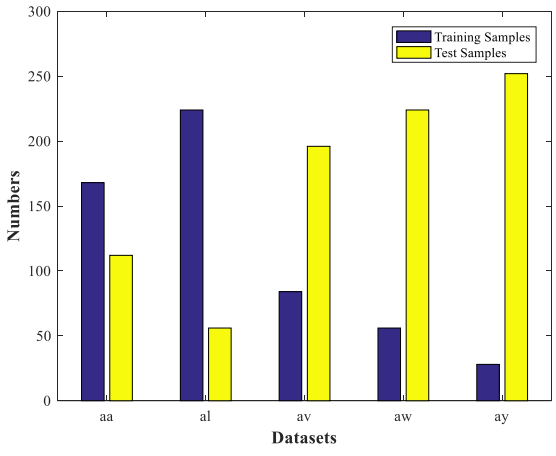

FIGURE 3
Distribution of each subset from the BCI Competition Data Set IVa.

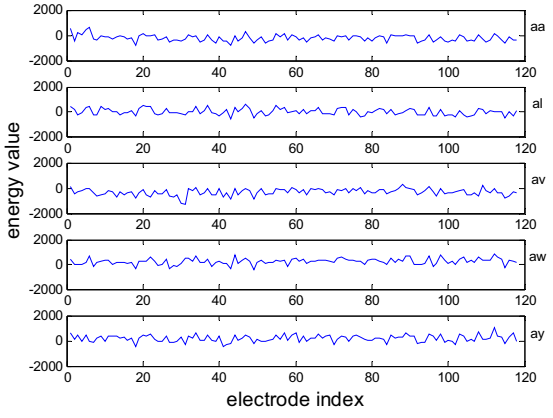

FIGURE 4
Representative MI-EEG signals for each subset of the BCI Competition Data Set IVa.

practice, such training data may not be easy to obtain, and the classification accuracy of existing methods may drop significantly. To address this challenge, we use an inductive transfer learning-based MI-EEG classification method.

3 Extended-LSR-based inductive transfer learning

In this section, we provide a detailed description of the proposed extended-LSR-based inductive transfer learning (ELSR-TL) method. First, we extend LSR (Naseem et al., 2010) to its extended version, ELSR, by merging neural networks, TSK fuzzy systems, and kernel methods. Then, we develop the proposed ELSR-TL. Finally, we present the learning algorithm and theoretical analysis of ELSR-TL.

3.1 ELSR

3.1.1 Objective function of ELSR

ELSR is an extension of the basic LSR (Naseem et al., 2010). Given n d-dimensional samples $\{(\mathbf{x}_i, y_i)\}_{i=1}^{N}$, where $\mathbf{x}_i \in \mathbb{R}^d, y_i \in \{-1; +1\}$, the objective function of ELSR can be expressed as follows:

$$\min_{\mathbf{w}} \frac{1}{2}\left\|\mathbf{X}_\rho \mathbf{w} - \mathbf{y}\right\|^2 + \frac{\lambda}{2}\|\mathbf{w}\|^2 \tag{1}$$

where the matrix $\mathbf{X}_\rho = \left[\rho(\mathbf{x}_1), \cdots, \rho(\mathbf{x}_N)\right]^T \in \mathbb{R}^{N \times d_\rho}$ denotes all the given training samples, and $\rho(\mathbf{x}) \in \mathbb{R}^{d_\rho}$ is the hidden mapping function in the hidden mapping space. $\mathbf{w}$ represents the mapping matrix, λ is the given regularization parameter, and $\mathbf{y}$ is the corresponding label matrix.

The decision-making function of ELSR can be expressed as follows:

$$y = f(\mathbf{x}) = \rho(\mathbf{x})^T \mathbf{w} \tag{2}$$

Using different mapping functions $\rho(\mathbf{x})$, we can integrate multiple models, such as neural networks, TSK fuzzy systems, and kernel methods, into the proposed ELSR framework. In other words, ELSR can be developed for different base models, which improves its generalization and adaptability. We will describe its relationships with several base models next.

3.1.1.1 The relationship between ELSR and feedforward NNs

A multiple hidden layer feedforward network (MHFN) has an input layer, M hidden layers, and an output layer. The multiple hidden layers can be treated as a single complex hidden layer, allowing the overall activation function of these hidden layers to be represented by a single complex function. Therefore, an MHFN can be viewed as a generalized single hidden layer feedforward network (SHFN) with a more complex activation function. The output of a generalized SHFN can be expressed as follows:

$$y = f(\mathbf{x}) = \sum_{i=1}^{N_M} g_i(\mathbf{x}, \theta_i)^T w_i \tag{3}$$

where N_M is the number of nodes in the last hidden layer of an MHFN. As demonstrated in Huang et al. (2006), if the activation function $g_i(\mathbf{x}, \theta_i)$ is piecewise continuous, then the hidden nodes can be randomly generated independently of the training data, and the corresponding NN still maintains its universal approximation capability. Let the hidden mapping function $\rho(\mathbf{x})$ as Equation 4:

$$\rho(\mathbf{x}) = \left[g_1(\mathbf{x}, \theta_1), \cdots, g_{N_M}(\mathbf{x}, \theta_{N_M})\right]^T \tag{4}$$

Then, Equation 3 can be expressed as follows:

$$y = f(\mathbf{x}) = \rho(\mathbf{x})^T \mathbf{w} \tag{5}$$

Comparing Equation 5 with Equation 2, we can see that Equation 5 is a special case of Equation 2, so Equation 1 can be used to optimize the corresponding MHFN.

3.1.1.2 The relationship between ELSR and TSK fuzzy systems

The Takagi–Sugeno–Kang fuzzy system (Gu et al., 2024; Bian et al., 2024) is the most widely used FLS due to its simplicity and flexibility. The rules in a TSK fuzzy system are typically represented as Equation 6:

TSK Fuzzy Rule R^k:

$$\begin{aligned} &\text{IF } x_1 \text{ is } A_1^k \wedge x_2 \text{ is } A_2^k \wedge \cdots \wedge x_d \text{ is } A_d^k \\ &\text{Then } f^k(\mathbf{x}) = p_0^k + p_1^k x_1 + \cdots + p_d^k x_d \; k = 1, \cdots, K \end{aligned} \tag{6}$$

Here, A_i^k is a fuzzy set for the ith input variable in the kth rule, K is the number of fuzzy rules, and $\wedge$ is a fuzzy conjunction operator. The output of the TSK fuzzy system is computed as Equation 7:

$$y = f(\mathbf{x}) = \sum_{k=1}^{K} \frac{\mu^k(\mathbf{x})}{\sum_{k'=1}^{K} \mu^{k'}(\mathbf{x})} \cdot f^k(\mathbf{x}) = \sum_{k=1}^{K} \tilde{\mu}^k(\mathbf{x}) \cdot f^k(\mathbf{x}) \tag{7}$$

where $\mu^k(\mathbf{x})$ is the firing level of Rule R^k, and $\tilde{\mu}^k(\mathbf{x})$ is the normalized $\mu^k(\mathbf{x})$, i.e., Equation 8:

$$\mu^k(\mathbf{x}) = \prod_{i=1}^{d} \mu_{A_i^k}(x_i) \tag{8a}$$

$$\tilde{\mu}^k(\mathbf{x}) = \mu^k(\mathbf{x}) / \sum_{k'=1}^{K} \mu^{k'}(\mathbf{x}) \tag{8b}$$

The parameters of the antecedent fuzzy sets are usually derived from clustering. The output of the TSK fuzzy system can subsequently be expressed as as Equations 9, 10:

$$y = f(\mathbf{x}) = \rho(\mathbf{x})^T \mathbf{w} \tag{9}$$

where

$$\rho(\mathbf{x}) = \left[\begin{pmatrix} \tilde{1} \\ \mathbf{x} \end{pmatrix}^T, \begin{pmatrix} \tilde{2} \\ \mathbf{x} \end{pmatrix}^T, \cdots, \begin{pmatrix} \tilde{K} \\ \mathbf{x} \end{pmatrix}^T \right]^T \tag{10a}$$

$$\tilde{\mathbf{x}}^k = \tilde{\mu}^k(\mathbf{x}) \mathbf{x}_e \tag{10b}$$

$$\mathbf{x}_e = \left(1, \mathbf{x}^T\right)^T \tag{10c}$$

$$\mathbf{w} = \left[\left(\mathbf{p}^1\right)^T, \left(\mathbf{p}^2\right)^T, \cdots, \left(\mathbf{p}^K\right)^T \right]^T \tag{10d}$$

$$\mathbf{p}^k = \left(p_0^k, p_1^k, \cdots, p_d^k\right)^T \tag{10e}$$

Equation 9 suggests that training the TSK fuzzy system can also be treated as a special case of ELSR, and thus, it can be addressed using Equation 1.

3.1.1.3 The relationship between ELSR and kernel methods

A kernel linear regression model is expressed as follows:

$$y = \rho(\mathbf{x})^T \mathbf{w} \tag{11}$$

The hidden mapping $\rho(\mathbf{x})$ can be viewed as a kernel function; thus, Equation 11 can also be solved using Equation 1. In this case, ELSR also corresponds to the classical kernel ridge regression (Saunders et al., 1998).

3.1.2 Solution of ELSR

Depending on the condition of the hidden mapping, the objective function of ELSR in Equation 1 can be efficiently solved in various ways $\rho(\mathbf{x})$. Here, we discuss the different cases as follows:

Case 1: $\rho(\mathbf{x})$ *is known*: In this case, we can obtain explicit values of the data $\rho(\mathbf{x})$ in the hidden mapping space.

Let $J(\mathbf{w}) = \min_{\mathbf{w}} \frac{1}{2}\|\mathbf{X}_\rho \mathbf{w} - \mathbf{y}\|^2 + \frac{\lambda}{2}\|\mathbf{w}\|^2$; according to the optimization theory (Qu et al., 2023a; Qu et al., 2023b), the solution for the model parameter $\mathbf{w}$ can then be obtained by taking the derivatives of Equation 1 and equating them to zero. That is,

$$\begin{aligned} &\frac{\partial J(\mathbf{w})}{\partial \mathbf{w}} = \mathbf{0} \\ &\Rightarrow \mathbf{X}_\rho^T \mathbf{X}_\rho \mathbf{w} - \mathbf{X}_\rho^T \mathbf{y} + \lambda \mathbf{w} = \mathbf{0} \\ &\Rightarrow \mathbf{w} = \left(\mathbf{X}_\rho^T \mathbf{X}_\rho + \lambda \mathbf{I}_{d_\rho}\right)^{-1} \mathbf{X}_\rho^T \mathbf{y} \end{aligned} \tag{12}$$

The final decision function $f(\mathbf{x})$ can then be expressed as Equation 13:

$$y = f(\mathbf{x}) = \rho(\mathbf{x})^T \mathbf{w} \tag{13}$$

with $\mathbf{w}$ obtained in Equation 12.

Case 2: $\rho(\mathbf{x})$ *is unknown:* In this case, the explicit formulation of the data $\rho(\mathbf{x})$ in the hidden mapping space cannot be obtained, meaning that $\mathbf{w}$ cannot be specified explicitly. Therefore, the kernel trick is necessary to determine the final decision function $f(\mathbf{x})$. Although introducing the kernel trick into the solution strategy in Equation 12 is challenging, Equation 14, identity can be adopted to address this issue:

$$\left(\mathbf{P}^{-1} + \mathbf{Q}^T \mathbf{U}^{-1} \mathbf{Q}\right)^{-1} \mathbf{Q}^T \mathbf{U}^{-1} = \mathbf{P}\mathbf{Q}^T \left(\mathbf{Q}\mathbf{P}\mathbf{Q}^T + \mathbf{U}\right)^{-1} \tag{14}$$

In Equation 14, $\mathbf{P}$, $\mathbf{Q}$, and $\mathbf{U}$ are three matrices. Let $\mathbf{P} = \frac{1}{\lambda}\mathbf{I}_{d_\rho}$, $\mathbf{Q} = \mathbf{X}_\rho$, and $\mathbf{U} = \mathbf{I}_N$. With the identity of Equation 14, the solution in Equation 12 can then be expressed as follows:

$$\mathbf{w} = \left(\mathbf{X}_\rho^T \mathbf{X}_\rho + \lambda \mathbf{I}_{d_\rho}\right)^{-1} \mathbf{X}_\rho^T \mathbf{y} = \mathbf{X}_\rho^T \left(\mathbf{X}_\rho \mathbf{X}_\rho^T + \lambda \mathbf{I}_N\right)^{-1} \mathbf{y} \tag{15}$$

Define a Mercer kernel matrix as Equation 16:

$$\Omega = \mathbf{X}_\rho \mathbf{X}_\rho^T \in \mathbb{R}^{N \times N}, \tag{16}$$

where $\Omega_{i,j} = \rho(\mathbf{x}_i)^T \rho(\mathbf{x}_j) = K(\mathbf{x}_i, \mathbf{x}_j)$, and $K(\cdot)$ is a kernel function.

The final decision function $f(\mathbf{x})$ can then be expressed as follows:

$$\begin{aligned} y = f(\mathbf{x}) = \rho(\mathbf{x})^T \mathbf{w} = \rho(\mathbf{x})^T \mathbf{X}_\rho^T \left(\mathbf{X}_\rho \mathbf{X}_\rho^T + \lambda \mathbf{I}_N\right)^{-1} \\ \mathbf{y} = \begin{bmatrix} K(\mathbf{x}, \mathbf{x}_1) \\ \vdots \\ K(\mathbf{x}, \mathbf{x}_N) \end{bmatrix} (\Omega + \lambda \mathbf{I}_N)^{-1} \mathbf{y} \end{aligned} \tag{17}$$

3.2 ELSR-TL

3.2.1 Objective function of ELSR-TL

ELSR-TL integrates transfer learning and ELSR. Its objective function can be expressed as follows:

$$\min_{\mathbf{w}_t} \frac{1}{2}\left\|\mathbf{X}_{\rho,t}\mathbf{w}_t-\mathbf{y}\right\|^2+\frac{\lambda}{2}\left\|\mathbf{w}\right\|_t^2+\frac{\beta}{2}\left\|\mathbf{w}_t-\mathbf{w}_s\right\|^2 \tag{18}$$

where $\mathbf{X}_{\rho,t}\in\mathbb{R}^{N_t\times d_\rho}$ represents N_t training samples of d_ρ dimensions in the target domain. $\mathbf{w}_t$ and $\mathbf{w}_s$ represent the mapping matrices of the target domain and source domain, respectively. λ and β are the given regularization parameters, and $\mathbf{y}$ is the corresponding label matrix of the target domain.

In Equation 18, the first two terms are inherited directly from ELSR for learning from the target domain data, while the third term is used to leverage knowledge from the source domain. In other words, ELSR-TL generalizes ELSR from the perspective of transfer learning.

Moreover, as a regularization parameter, β can be used to adjust the role of transfer learning. When β is large, it indicates that transfer learning has a significant impact, indicating that the knowledge obtained from the source domain has a significant positive effect on the target domain. In contrast, when β is very small, it indicates that its role in learning of the target domain is relatively small. In extreme cases, when $\beta=0$, it means that β has no effect on the learning of the target domain. In other words, we can control the effectiveness of transfer learning by making adjustments, thus effectively avoiding negative transfer.

3.2.2 Solution of ELSR-TL

ELSR-TL is solved differently in different scenarios:

Case 1: $\rho(\mathbf{x})$ *is known*: In this case, we can obtain explicit values of the data $\rho(\mathbf{x})$ in the hidden mapping space. The solution for the model parameter $\mathbf{w}_t$ can then be obtained in a similar form as that shown in Equation 12, that is

$$\begin{aligned}&\frac{\partial J(\mathbf{w}_t)}{\partial \mathbf{w}_t}=\mathbf{0}\\&\Rightarrow \mathbf{X}_{\rho,t}^T\mathbf{X}_{\rho,t}\mathbf{w}_t-\mathbf{X}_{\rho,t}^T\mathbf{y}+\lambda\mathbf{w}_t+\beta(\mathbf{w}_t-\mathbf{w}_s)=\mathbf{0}\\&\Rightarrow \mathbf{w}_t=\left(\mathbf{X}_{\rho,t}^T\mathbf{X}_{\rho,t}+(\lambda+\beta)\mathbf{I}_{d_\rho}\right)^{-1}\left(\mathbf{X}_{\rho,t}^T\mathbf{y}+\beta\mathbf{w}_s\right)\end{aligned} \tag{19}$$

The final output of the proposed ELSR-TL is expressed as follows:

$$y=f(\mathbf{x})=\rho(\mathbf{x})^T\mathbf{w}_t \tag{20}$$

with $\mathbf{w}_t$ obtained in Equation 19.

Case 2: $\rho(\mathbf{x})$ *is unknown:* In this case, the explicit formulation of the data $\rho(\mathbf{x})$ in the hidden mapping space cannot be obtained, and thus, $\mathbf{w}_t$ cannot be specified explicitly. Similar to the form shown in Equation 17, the output of the proposed ELSR-TL can be calculated using the kernel trick. From Equation 15, we know that $\mathbf{w}_s$ can be expressed as Equation 21:

$$\mathbf{w}_s=\mathbf{X}_{\rho,s}^T\left(\mathbf{X}_{\rho,s}\mathbf{X}_{\rho,s}^T+\lambda_s\mathbf{I}_{N_s}\right)^{-1}\mathbf{y}_s \tag{21}$$

Here, $\mathbf{w}_s$ is the parameter of ELSR in the source domain. For a similar scenario, let

$$\alpha_s=\left(\mathbf{X}_{\rho,s}\mathbf{X}_{\rho,s}^T+\lambda_s\mathbf{I}_{N_s}\right)^{-1}\mathbf{y}_s \tag{22}$$

A Mercer kernel matrix is defined, and Equation 22 can then be re-expressed as Equation 23:

$$\alpha_s=\left(\Omega_s+\lambda_s\mathbf{I}_{N_s}\right)^{-1}\mathbf{y}_s \tag{23}$$

where $\Omega_s=\mathbf{X}_{\rho,s}\mathbf{X}_{\rho,s}^T=\left[K\left(\mathbf{x}_{i,s},\mathbf{x}_{j,s}\right)\right]_{N_s\times N_s}$, in which $K\left(\mathbf{x}_{i,s},\mathbf{x}_{j,s}\right)$is the kernel function.

$\mathbf{w}_s$ can then be written as follows:

$$\mathbf{w}_s=\mathbf{X}_{\rho,s}^T\alpha_s \tag{24}$$

From Equation 19, we obtain the following:

$$\begin{aligned}\mathbf{w}_t=&\frac{\beta}{\lambda+\beta}\mathbf{w}_s\\&+\frac{1}{\lambda+\beta}\mathbf{X}_{\rho,t}^T\left(\mathbf{X}_{\rho,t}\mathbf{X}_{\rho,t}^T+(\lambda+\beta)\mathbf{I}_{N_t}\right)^{-1}\left(\mathbf{y}-\frac{\beta}{\lambda+\beta}\mathbf{X}_{\rho,t}\mathbf{w}_s\right)\end{aligned} \tag{25}$$

Substituting Equation 24 into Equation 25 and defining a Mercer kernel matrix, the equation above can then be rewritten as follows:

$$\begin{aligned}\mathbf{w}_t=&\frac{\beta}{\lambda+\beta}\mathbf{w}_s+\frac{1}{\lambda+\beta}\mathbf{X}_{\rho,t}^T\\&\left(\mathbf{X}_{\rho,t}\mathbf{X}_{\rho,t}^T+(\lambda+\beta)\mathbf{I}_{N_t}\right)^{-1}\left(\mathbf{y}-\frac{\beta}{\lambda+\beta}\mathbf{X}_{\rho,t}\mathbf{w}_s\right)\\=&\frac{\beta}{\lambda+\beta}\mathbf{X}_{\rho,s}^T\boldsymbol{\alpha}_s+\frac{1}{\lambda+\beta}\mathbf{X}_{\rho,t}^T\\&\left(\Omega_t+(\lambda+\beta)\mathbf{I}_{N_t}\right)^{-1}\left(\mathbf{y}-\frac{\beta}{\lambda+\beta}\Omega_{t,s}\boldsymbol{\alpha}_s\right)\end{aligned} \tag{26}$$

where $\Omega_t=\mathbf{X}_{\rho,t}\mathbf{X}_{\rho,t}^T=\left[K\left(\mathbf{x}_{i,t},\mathbf{x}_{j,t}\right)\right]_{N_t\times N_t}$, $\Omega_{t,s}=\mathbf{X}_{\rho,t}\mathbf{X}_{\rho,s}^T=\left[K\left(\mathbf{x}_{i,t},\mathbf{x}_{j,s}\right)\right]_{N_t\times N_s}$

Finally, by using $\mathbf{w}_t$ obtained in Equation 26, the decision function of the proposed ELSR-TL can be expressed as follows:

$$
\begin{aligned}
f(\mathbf{x}) &= \rho(\mathbf{x})^T \mathbf{w}_t \\
&= \rho(\mathbf{x})^T \left[\frac{\beta}{\lambda+\beta} \mathbf{X}_{\rho,s}^T \alpha_s + \frac{1}{\lambda+\beta} \mathbf{X}_{\rho,t}^T \left(\Omega_t + (\lambda+\beta)\mathbf{I}_{N_t} \right)^{-1} \left(\mathbf{y} - \frac{\beta}{\lambda+\beta} \Omega_{t,s} \alpha_s \right) \right] \\
&= \frac{\beta}{\lambda+\beta} \begin{bmatrix} K(\mathbf{x}_{1,s}, \mathbf{x}) \\ \vdots \\ K(\mathbf{x}_{N_s,s}, \mathbf{x}) \end{bmatrix}^T \alpha_s + \frac{1}{\lambda+\beta} \begin{bmatrix} K(\mathbf{x}_{1,t}, \mathbf{x}) \\ \vdots \\ K(\mathbf{x}_{N_t,t}, \mathbf{x}) \end{bmatrix}^T \left(\Omega_t + (\lambda+\beta)\mathbf{I}_{N_t} \right)^{-1} \left(\mathbf{y} - \frac{\beta}{\lambda+\beta} \Omega_{t,s} \alpha_s \right)
\end{aligned} \tag{27}
$$

3.3 Learning algorithm of ELSR-TL

Considering the above discussion, we summarize the learning algorithm of ELSR-TL in Algorithm 1. Below, we provide some remarks on ELSR-TL.

3.3.1 Remark 1

For the proposed ELSR-TL, if the hidden mapping is known and the amount of training data exceeds the dimensionality of the hidden mapping features (i.e., $(N_t \gg d_{\rho,t})$, obtaining the solution using Equation 25 is more efficient than that using Equation 19, due to the computational complexity of matrix; otherwise, Equation 19 is more efficient.

3.3.2 Remark 2

When the hidden mapping is known, only the knowledge $\mathbf{w}_s$ is used for transfer learning, and the data in the source domain are not required. This means that the proposed method provides good privacy protection. However, if the hidden feature mapping is unknown, the data in the source are also required, as shown in Equations 26, 27, to effectively implement transfer learning. In this case, the proposed method can no longer protect the privacy of the data in the source domain.

3.3.3 Computational Complexity

In this section, we discussed the computational complexity of Algorithm 1 as follows:

When the hidden mapping is known, the complexity of computing step 1 is about$O\left(d_{\rho,s}^3 + d_{\rho,s}^2 N_s\right)$, where $d_{\rho,s}$is the dimension of samples and $N_s$is the number of samples in the source domain. The complexity of computing the target domain model parameters $\mathbf{w}_t$ in step 2 is about $O\left(d_{\rho,t}^3 + d_{\rho,t}^2 N_t\right)$, where $d_{\rho,t}$is the dimension of samples and $N_t$is the number of samples in the target domain. In this case, the computational complexity of Algorithm 1 is about $O\left(d_{\rho,s}^3 + d_{\rho,s}^2 N_s + d_{\rho,t}^3 + d_{\rho,t}^2 N_t\right)$. When the hidden mapping is unknown, the computational complexity of Algorithm 1 is about $O\left(N_s^3 + N_t^3\right)$.

4 Experiments

In this section, we adopted a real MI-EEG dataset to evaluate the performance of the proposed ELSR-TL method. Moreover, we compared it with seven non-transfer learning methods—LSR (Naseem et al., 2010), KNN (Cover and Hart, 1967), SVM (Bennett and Demiriz, 1999), NB (Kohavi, 1996), CNN (Zhang et al., 2019), ELSR (NN), ELSR (TSK), and ELSR (Ker)—alongside two transfer learning methods—Au-SVM (Wu and Dietterich, 2004) and Tr-Adaboost (Dai et al., 2007). The comparison was conducted in terms of both average classification accuracy and standard deviation for 10 runs. The details of the experimental settings and the MI-EEG recognition results are provided as follows.

Input: The set of training samples in target domain $\mathbf{X} = \left[\mathbf{x}_1, \mathbf{x}_2, \ldots, \mathbf{x}_{N_t}\right] \in \mathbb{R}^{N_t \times d}$, and their corresponding class labels $y_i \in \{-1, +1\} (i = 1, 2, \ldots, N_t)$, where $\mathbf{x}_i \in \mathbb{R}^d (i = 1, 2, \ldots, N_t)$.

Output: The mapping $\mathbf{w}_t$ matrix for target domain.

Procedure:

Case 1: The hidden mapping function is known

Step 1: Obtain the source domain knowledge, i.e., the model parameters $\mathbf{w}_s$ and the related parameters of the hidden nodes of the source domain.

Step 2: Calculate the target domain model parameters $\mathbf{w}_t$ by using (19).

Step 3: Use (20) to calculate the output of the test set.

Case 2: The hidden mapping function is unknown

Step 1: Obtain the knowledge and data from the source domain, i.e., $\boldsymbol{\alpha}_s$, and $D_s = \{\mathbf{x}_{i,s}\}$.

Step 2: Use (27) to calculate the output of the test set.

ALGORITHM 1
The ELSR-TL.

4.1 Data preparation and feature extraction

4.1.1 Configurations of source and target domains

To match the transfer learning task, we constructed 20 different transfer learning datasets by subject-to-subject transferring. Table 1 shows the 20 different configurations of source and target domains. All source domains have the same number of training data, but the target domains do not. Please note that in our experiments, non-transfer learning methods are only used on the target domain.

4.1.2 Feature extraction

As mentioned in the background section, effective feature extraction is critical to pattern recognition performance. Based on (Lotte and Guan, 2011), we primarily used the Tikhonov regularization-based common spatial pattern (TR-CSP) (Lotte and Guan, 2011) for feature extraction. Furthermore, we conducted simple experiments using two other feature extraction methods, namely Composite CSP (C-CSP) and Filter Bank CSP (FB-CSP), to compare with TR-CSP. The three feature extraction methods are briefly introduced as follows:

1 TR-CSP: It introduces a quadratic regularization into the CSP objective function and replaces the feature matrix of the new data with the prior knowledge matrix. This regularization prefers filters with smaller norms, reducing the influence of noise.

2 C-CSP: It aims to perform subject-to-subject transfer by regularizing the covariance matrices using data from other subjects. Within the framework of this study, it relies only on the βhyperparameter and defines the generic covariance matrices according to the covariance matrices of other subjects.

FB-CSP: This is a feature extraction method used for motor imagery classification in BCI. It improves the accuracy of motion imagery classification by combining CSP and filter bank techniques, optimizing the subject-specific frequency band for CSP.

We extracted features from the time segment between 0.5 and 2.5 s after the cue instructing the subject to perform MI. Each trial is bandpass filtered in the 8–30 Hz range using a fifth-order Butterworth filter. For TR-CSP, we applied three pairs of filters, as recommended in (Lotte and Guan, 2011). Some examples of features extracted from subset aa are shown in Figure 5.

TABLE 1 Settings of the source domain and target domain.

Source domain		Target domain		
Datasets	Size	Datasets	Size	
			Training	Test
al	280	aa	168	112
av	280	aa		
aw	280	aa		
ay	280	aa		
aa	280	al	224	56
av	280	al		
aw	280	al		
ay	280	al		
aa	280	av	86	196
al	280	av		
aw	280	av		
ay	280	av		
aa	280	aw	56	224
al	280	aw		
av	280	aw		
ay	280	aw		
aa	280	ay	28	252
al	280	ay		
av	280	ay		
aw	280	ay		

4.2 Adopted methods and parameters settings

All the adopted methods (without CNN) are listed in Table 2. Based on the guidelines in (Jiang et al., 2019; Xie et al., 2018; Zhang X. et al., 2023) and our experiments, we employ a grid search strategy to identify the appropriate parameters for all the adopted methods. Table 2 also includes a list of the grid search ranges for each parameter related to all the adopted methods.

4.3 Performance indices

The classification accuracy defined Equation 28 is used to evaluate the performances of different methods:

$$Accuracy = \frac{(TP + TN)}{(TP + TN + FP + FN)} \tag{28}$$

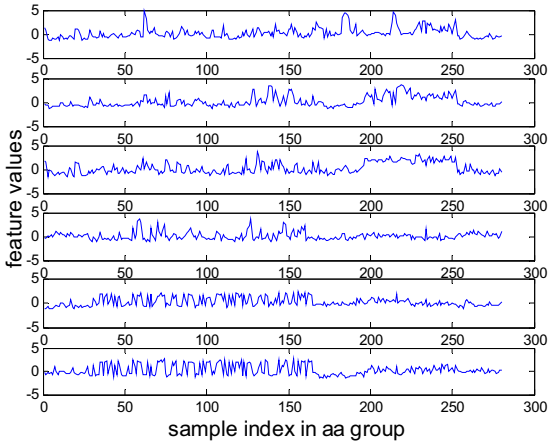

FIGURE 5
Features extracted from subset aa by TR-CSP.

TABLE 2 The parameter setting of different methods.

Methods	Parameter settings for grid search
LSR (Naseem et al., 2010): Learns a linear regression model by using each class of training samples with the ℓ_2-norm regularization.	The regularization parameter $\lambda \in \{10^{-6}, 10^{-5}, \ldots, 10^{5}, 10^{6}\}$
kNN (Cover and Hart, 1967): A classical supervised learning model and has been widely used for classification and regression analysis.	The number of nearest points: $k \in \{1, 3, 5, 7, 9\}$.
SVM (Bennett and Demiriz, 1999): A classical classification method based on kernel trick and margin maximization.	The tradeoff parameter $C \in \{2^{-6}, 2^{-5}, \cdots, 2^{0}, 2^{1}, \cdots, 2^{5}, 2^{6}\}$; the width in the Gaussian kernel function $\sigma \in \{2^{-6}, 2^{-5}, \cdots, 2^{0}, 2^{1}, \cdots, 2^{5}, 2^{6}\}$
NB (Kohavi, 1996): A classification method based on Bayes' theorem and independent assumption of feature conditions.	The tradeoff parameter $\alpha \in \{10^{-5}, 10^{-4}, 10^{-3}, 10^{-2}, 10^{-1}, 10^{0}\}$
ELSR (NN): Applying the proposed ELSR for signal layer neural networks.	The number of hidden nodes $P \in \{10, 20, 30, 40, 50, 75, 100, 150, 200\}$, the parameters of the sigmoid function: $\kappa \in \{2^{-6}, 2^{-5}, \cdots, 2^{0}, 2^{1}, \cdots, 2^{5}, 2^{6}\}$, and the regularization parameters: $\lambda \in \{10^{-6}, 10^{-5}, \ldots, 10^{5}, 10^{6}\}$
ELSR (TSK): Applying the proposed ELSR for TSK.	The number of fuzzy rules: $M \in \{5, 10, 15, 20, 25, 30, 40, 50, 80, 100\}$; the regularization parameter: $\tau \in \{10^{-6}, 10^{-5}, \ldots, 10^{5}, 10^{6}\}$, the regularization parameters: $\lambda \in \{10^{-6}, 10^{-5}, \ldots, 10^{5}, 10^{6}\}$.
ELSR (Ker): Applying the proposed ELSR for the kernel method.	The width in the Gaussian kernel function $\sigma \in \{2^{-6}, 2^{-5}, \cdots, 2^{0}, 2^{1}, \cdots, 2^{5}, 2^{6}\}$ and the regularization parameters: $\lambda \in \{10^{-6}, 10^{-5}, \ldots, 10^{5}, 10^{6}\}$.
Au-SVM (Wu and Dietterich, 2004): an inductive transfer learning method based on the linear programming support vector machine with the RBF-type kernel function by using the auxiliary data.	The tradeoff parameter $C \in \{2^{-6}, 2^{-5}, \cdots, 2^{0}, 2^{1}, \cdots, 2^{5}, 2^{6}\}$; the width in RBF kernel function $\sigma \in \{2^{-6}, 2^{-5}, \cdots, 2^{0}, 2^{1}, \ldots, 2^{5}, 2^{6}\}$
Tr-Adaboost (Dai et al., 2007): an inductive transfer learning method based on the LS-SVM learner with the RBF-type kernel function for classification.	The tradeoff parameter $C \in \{2^{-6}, 2^{-5}, \cdots, 2^{0}, 2^{1}, \cdots, 2^{5}, 2^{6}\}$; the width in RBF kernel function $\sigma \in \{2^{-6}, 2^{-5}, \cdots, 2^{0}, 2^{1}, \ldots, 2^{5}, 2^{6}\}$
ELSR-TL (NN): Applying the proposed method for transfer learning of signal layer neural networks.	The number of the hidden nodes: $P \in \{10, 20, 30, 40, 50, 75, 100, 150, 200\}$, the parameters of sigmoid function: $\kappa \in \{2^{-6}, 2^{-5}, \cdots, 2^{0}, 2^{1}, \cdots, 2^{5}, 2^{6}\}$, the regularization parameters: $\lambda \in \{10^{-6}, 10^{-5}, \ldots, 10^{5}, 10^{6}\}$, $\lambda \in \{10^{-6}, 10^{-5}, \ldots, 10^{5}, 10^{6}\}$.
ELSR-TL (TSK): Applying the proposed method for transfer learning of TSK.	The number of fuzzy rules: $M \in \{5, 10, 15, 20, 25, 30, 40, 50, 80, 100\}$; the regularization parameters: $\tau \in \{10^{-6}, 10^{-5}, \ldots, 10^{5}, 10^{6}\}$, $\lambda \in \{10^{-6}, 10^{-5}, \ldots, 10^{5}, 10^{6}\}$, $\lambda \in \{10^{-6}, 10^{-5}, \ldots, 10^{5}, 10^{6}\}$.
ELSR-TL (Ker): Applying the proposed method for transfer learning of the kernel method.	The width in the Gaussian kernel function $\sigma \in \{2^{-6}, 2^{-5}, \cdots, 2^{0}, 2^{1}, \cdots, 2^{5}, 2^{6}\}$, the regularization parameters: $\lambda \in \{10^{-6}, 10^{-5}, \ldots, 10^{5}, 10^{6}\}$, $\lambda \in \{10^{-6}, 10^{-5}, \ldots, 10^{5}, 10^{6}\}$.

4.4 Results and discussions

In all the experiments, each comparison method is implemented for 10 runs to report the average classification performance. The experimental results are shown in Tables 3, 4 and Figure 6. Please note that the feature extraction method used for these results is TR-CSP. We can make the following observations:

i In general, the performance of the proposed ELSR-TL-based methods significantly surpasses that of the other methods used, whether they are non-transfer learning methods such as LSR, kNN, SVM, NB, CNN, and ELSR-based methods, or transfer learning methods such as Au-SVM and Tr-Adaboost. This provides experimental evidence that ELSR-TL effectively enhances MI-EEG recognition through knowledge transfer from the source domain to the target domain.

ii Comparing the performances of the seven non-transfer learning methods, we can see that the performance of ELSR (TSK) is the best, while the performance of NB is inferior. Moreover, each method obtains significant performance differences on different datasets. Specifically, seven non-transfer learning methods obtain the best performance on dataset *al* but poor performance on datasets *aw* and *ay*. This is because these methods require a large amount of training samples to achieve satisfactory performance, while their performance decreases when there are few training samples.

iii Table 4 shows the performances of five transfer learning methods, showing that ELSR-TL (TSK) performs the best while Tr-Adaboost performs the worst. Furthermore, each method achieves similar

TABLE 3 Classification accuracies of the non-transfer learning method.

Datasets	LSR	kNN	SVM	NB	CNN	ELSR (NN)	ELSR (TSK)	ELSR (Ker)
aa	0.6673 (0.0133)	0.5982 (0.0148)	0.6518 **(0.0071)**	0.6696 (0.0101)	0.6041 (0.0136)	0.6664 (0.0106)	0.6693 (0.0110)	**0.6708** (0.0107)
al	**1(0)**	**1(0)**	0.9821 (0.0031)	**1(0)**	0.5450 (0.0029)	**1(0)**	**1(0)**	**1(0)**
av	0.5416 (0.0115)	**0.5663** (0.0132)	0.5561 **(0.0064)**	0.5510 (0.0124)	0.5459 (0.0028)	0.5612 (0.0127)	0.5658 (0.0122)	0.5508 (0.0103)
aw	0.7122 (0.0139)	0.7277 (0.0129)	0.7143 (0.0158)	0.7009 (0.0125)	0.5556 (0.0072)	0.7188 **(0.0103)**	**0.7366** (0.0109)	0.7054 (0.0128)
ay	0.7019 (0.0142)	0.7302 (0.0172)	**0.7698** (0.0145)	0.5873 (0.0129)	0.5137 (0.0107)	0.7143 (0.0120)	0.7063 (0.0117)	0.7262 **(0.0114)**
Avg.Acc	0.7246	0.7245	0.7348	0.7018	0.5527	0.7321	**0.7356**	0.7306
Avg.Std	0.0106	0.0116	0.0094	0.0096	0.0074	0.0091	0.0092	**0.0090**

The best results are highlited in this table.

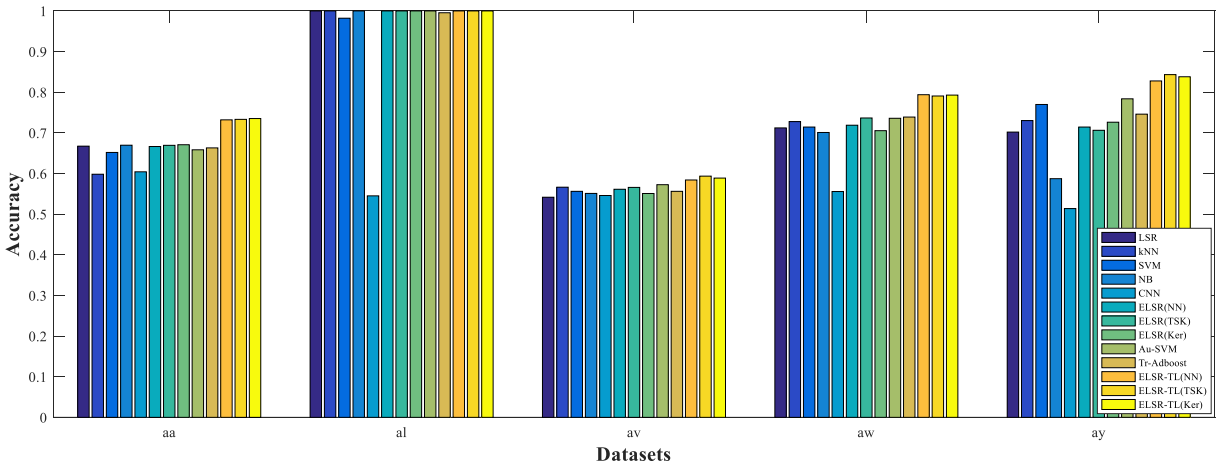

FIGURE 6
Classification accuracies of 13 different methods, where the accuracies of the transfer learning methods represent the average accuracies across four different source domains with a fixed target domain.

TABLE 4 Average accuracies of four different source domains for the transfer learning methods.

Target domain	Au-SVM	Tr-Adaboost	ELSR-TL (NN)	ELSR-TL (TSK)	ELSR-TL (Ker)
aa	0.6583(0.0165)	0.6630(0.0242)	0.7320(0.0116)	0.7332(0.0108)	**0.7352(0.0108)**
al	**1(0)**	0.9955(0.0002)	**1(0)**	**1(0)**	**1(0)**
av	0.5725(0.0180)	0.5561(0.0146)	0.5840(**0.0101**)	**0.5935**(0.0114)	0.5887(0.0113)
aw	0.7359(0.0179)	0.7389(0.0117)	**0.7939**(0.0108)	0.7907(0.0117)	0.7929(**0.0100**)
ay	0.7838(0.0184)	0.7460(0.0173)	0.8277(0.0111)	**0.8433(0.0110)**	0.8380(0.0110)
Avg.Acc	0.7501	0.7399	0.7875	**0.7921**	0.7910
Avg.Std	0.0142	0.0136	0.0087	0.0090	**0.0086**

The best results are highlited in this table.

performances for each target subject, regardless of the auxiliary subject chosen as the source domain. Additionally, for a fixed configuration of the source and target domains, the three ELSR-TL-based methods yield similar classification accuracies.

iv Comparing the performances of transfer learning methods (i.e., Au-SVM and ELSR-TL-based methods) with their corresponding non-transfer learning methods (i.e., SVM and ELSR-based methods), we can see that the transfer learning methods outperform the others. Therefore, transfer learning strategies are effective for MI-EEG signal recognition. Impressively, even the least effective transfer learning methods still perform better than or are comparable to the non-transfer learning methods.

v When datasets *aa*, *al*, and *av* are used in the target domain, the performance improvements achieved by the ELSR-TL-based methods are not very significant. This is because the target domain contains sufficient data to train a good model; therefore, the knowledge from the source domain is not critical. However, when datasets *aw* and *ay* are used in the target domain, the ELSR-TL-based methods significantly outperform the other methods due to the limited training data available in the target domain.

vi To visually compare the performances of all methods, Figure 6 illustrates the performance of each method across all datasets for visual comparison. Please note that, for transfer learning methods, we report the average performance of four different source domains with fixed target domains in Figure 6. For each dataset, the ELSR-TL-based methods achieve either the best accuracy or performance comparable to that of the other methods.

In summary, we show that ELSR-TL-based methods can outperform other methods, especially when the number of training samples in the target domain is limited.

4.5 On different feature extraction

In this section, we compare the effectiveness of three feature extraction methods. Figure 7 illustrates the classification results of these methods when using the same classification method. Specifically, we use ELSR-TL (TSK) as the classification method.

4.6 On running time

In this section, we compared the average running times of all adopted methods (without CNN) over ten trials. Table 5 lists the average time (in seconds) for each method across all datasets. It is evident that LSR has the shortest computational time. However, among all transfer learning methods, the computational time of ELSR-TL (NN) is less than that of the other two transfer learning methods. Nevertheless, the running time of the proposed ELSR-TL is still not particularly small. Therefore, determining how to accelerate the proposed method for large-scale data remains an open problem that we should explore in the future.

4.7 Statistical analysis

A nonparametric Friedman test (Zhang Y. et al., 2023) is used to validate whether the performance differences among different algorithms are statistically significant. This test uses the rankings of different algorithms in multiple comparisons. First, we calculate the sum ranking and average ranking of the accuracy of each algorithm (without CNN), as shown in Table 6, and find the best one. We then perform *post hoc* hypothesis testing.

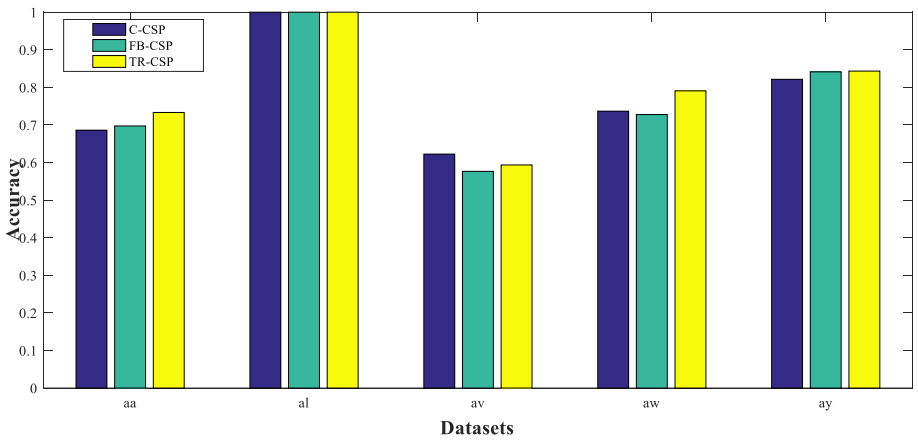

FIGURE 7
Classification results of three feature extraction methods.

TABLE 5 Running time (Seconds) for all adopted methods on all datasets.

Datasets	LSR	kNN	SVM	NB	ELSR(NN)	ELSR(TSK)	ELSR(Ker)	Au-SVM	Tr-Adaboost	ELSR-TL (NN)	ELSR-TL (TSK)	ELSR-TL (Ker)
aa	0.2715	0.3014	83.9542	0.3058	84.5401	85.0113	86.7844	823.7881	325.6131	269.3713	274.3649	298.0787
al	0.2646	0.3001	83.0776	0.3022	84.5932	84.9688	85.0619	819.3875	325.2478	269.0109	271.3828	293.1613
av	0.2503	0.2953	82.5644	0.2759	82.9663	83.6533	83.9803	818.7702	310.2496	260.4783	270.5006	289.3647
aw	0.2382	0.2922	82.1311	0.2801	80.6762	81.4226	82.2949	803.2313	298.1549	252.3586	266.1136	279.5312
ay	0.2344	0.2887	79.6846	0.2794	78.4760	78.6811	79.1756	801.4153	296.9221	249.3428	258.9078	268.5438

TABLE 6 Rankings of the 12 algorithms (Friedman test).

Algorithm	aa	al	av	aw	ay	Sum Ranking	Average Ranking
LSR	7	5.5	12	10	11	45.5	9.1
kNN	12	5.5	5	7	7	36.5	7.3
SVM	11	12	8.5	9	5	45.5	9.1
NB	5	5.5	10	12	12	44.5	8.9
ELSR(NN)	8	5.5	7	8	9	37.5	7.5
ELSR(TSK)	6	5.5	6	5	10	32.5	6.5
ELSR(Ker)	4	5.5	11	11	8	39.5	7.9
Au-SVM	10	5.5	4	6	4	29.5	5.9
Tr-Adaboost	9	11	8.5	4	6	38.5	7.7
ELSR-TL(NN)	3	5.5	3	1	3	15.5	3.1
ELSR-TL(TSK)	2	5.5	1	3	1	12.5	2.5
ELSR-TL(Ker)	1	5.5	2	2	2	12.5	2.5

TABLE 7 The *post-hoc* comparison for $\alpha = 0.05$ (Friedman).

i	Algorithm	*z*	*p*	Holm	Hypothesis
11	LSR	2.894291	0.0038	0.004545	Reject
10	SVM	2.894291	0.0038	0.005	Reject
9	NB	2.806586	0.005007	0.005556	Reject
8	ELSR(Ker)	2.368057	0.017882	0.00625	Reject
7	Tr-Adaboost	2.280351	0.022587	0.007143	Accept
6	ELSR(NN)	2.192645	0.028333	0.008333	Accept
5	kNN	2.104939	0.035297	0.01	Accept
4	ELSR(TSK)	1.754116	0.079411	0.0125	Accept
3	Au-SVM	1.490999	0.135962	0.016667	Accept
2	ELSR-TL(NN)	0.263117	0.79246	0.025	Accept
1	ELSR-TL(Ker)	0	1	0.05	Accept

The Friedman test statistics are as Equation 29:

$$Q = \frac{12}{kn(n+1)}\sum_{i=1}^{k}\left(R_i - \frac{k(n+1)^2}{2}\right) = \frac{12}{kn(n+1)}\sum_{i=1}^{k}R_i^2 - 3k(n+1) \quad (29)$$

where R_i is the sum ranking of each algorithm, n is the number of algorithms, and $k$is the number of datasets.

From Table 6, we have $Q = 26.25$, and the corresponding p-value is 0.005964. This suggests that the performance differences among the 12 methods are statistically significant, with ELSR-TL (TSK) performing the best. To further evaluate the performance differences between ELSR-TL (TSK) and the other 11 methods, we also conduct post hoc multiple comparison tests:

$$z = \frac{\left|\bar{R}_0 - \bar{R}_i\right|}{SE} \text{ with } SE = \sqrt{\frac{n^*(n+1)}{6^*k}}$$

where z is subject to the standard normal distribution that will be used further to calculate the value of P.

Table 7 shows the *post hoc* comparison results for $\alpha = 0.05$ (Friedman). The null hypothesis is rejected when $p \le 0.00625$ because $p \le Holm$. In summary, we conclude that there are significant performance differences between ELSR-TL (TSK) and other methods, confirming that transfer learning is effective in boosting classification accuracy.

In addition, Figure 8 shows the specific differences between ELSR-TL (TSK) and other methods. Clearly, it is consistent with the above conclusion that there are significant performance differences between ELSR-TL (TSK) and the other methods.

4.8 Sensitivity analysis

We also conduct experiments to study the sensitivity of ELSR-TL to various parameters. Below, we use the AW dataset as an example of sensitivity analysis. Figure 9 illustrates how accuracy varies with different values of four parameters while the others remain fixed, based on the grid search detailed in section 4.2. Please note that, due to the limitations of this paper, we only use ELSR-TL (TSK) for the sensitivity analysis.

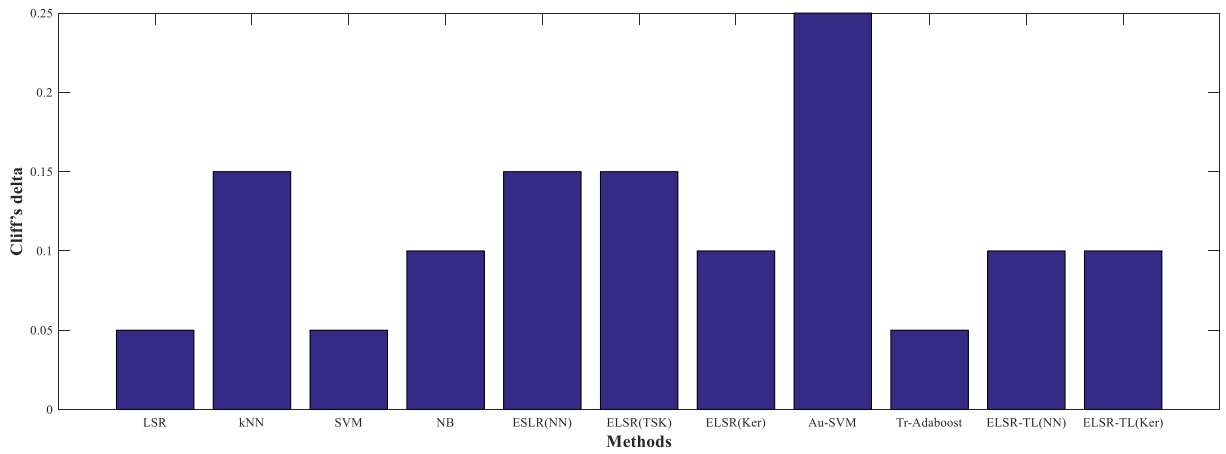

FIGURE 8
Specific differences of ELSR-TL (TSK) compared to other methods.

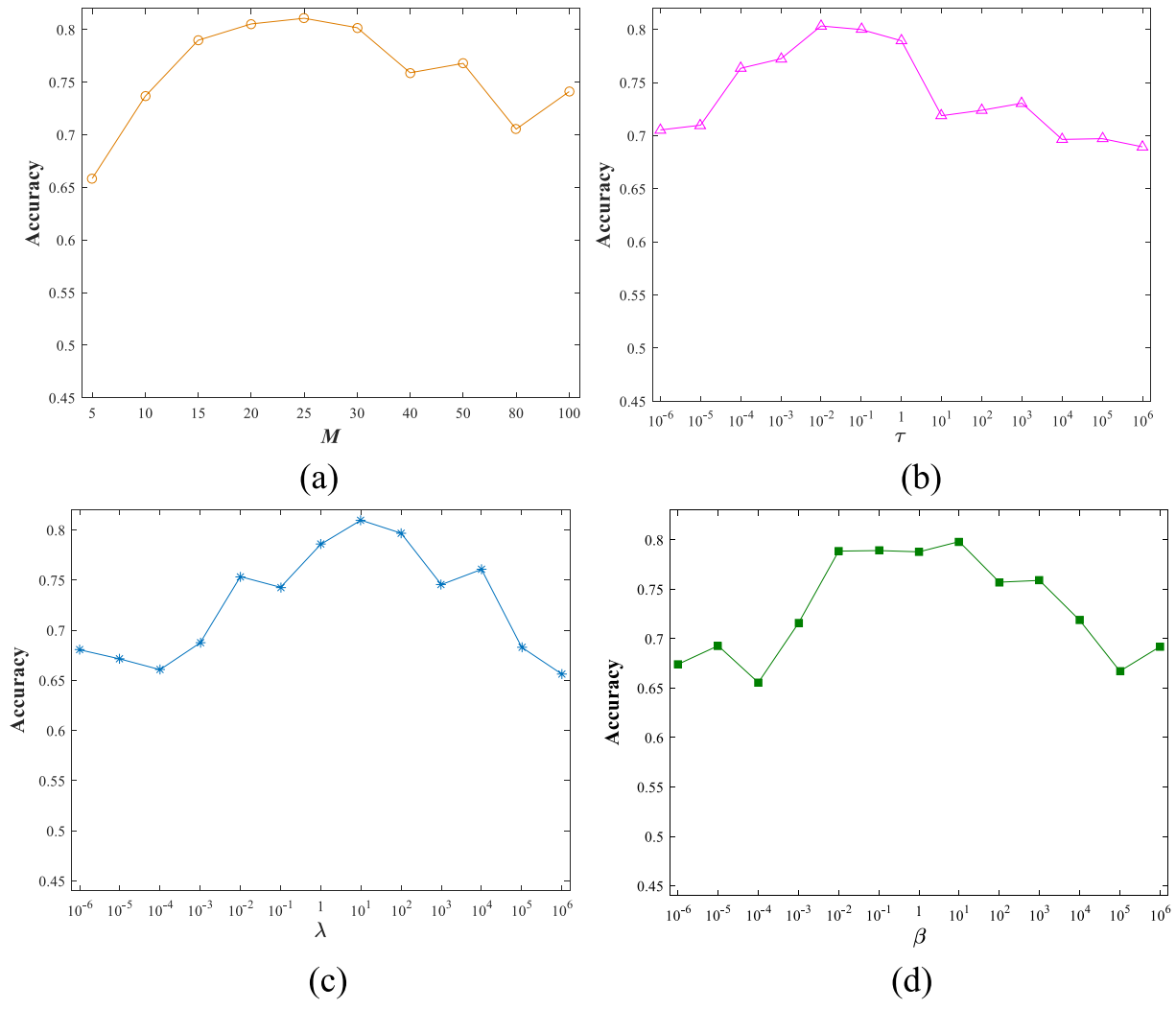

FIGURE 9
Accuracy changes with different values of four parameters: **(a)** M, **(b)** τ, **(c)** λ, **(d)** β.

4.9 Limitations

Although the proposed ELSR-TL demonstrates effectiveness in these experiments, it still has some limitations. For example, there are four hyperparameters in the proposed method, and the hyperparameter optimization procedure based on grid searching and cross-validation is computationally expensive. The running time of the proposed method is significant, especially compared to traditional simple methods, making it unsuitable for real-time scenarios. The proposed ELSR-TL operates offline and cannot be used in online scenarios. The datasets used in this paper contain only five subjects on a small scale, and the effectiveness of the proposed method needs to be validated on more extensive and larger datasets in future studies. In addition, it is also worth further investigating how to provide more theoretical justifications for knowledge transfer and how to avoid negative transfer. We primarily focused on binary MI tasks in this study; therefore, exploring how to extend the proposed ELSR-TL to multi-class MI tasks, multimodal integration, and cross-dataset transfers is worth studying.

5 Conclusion

In this study, an extended LSR-based inductive transfer learning method was proposed to facilitate transfer learning for several classical intelligent models, including neural networks, TSK fuzzy systems, and kernel methods. We applied this method to MI-EEG signal recognition in BCIs. ELSR-TL provides three distinctive advantages: (1) It features an inductive transfer learning mechanism that allows for the transfer of useful knowledge from the source domain to enhance learning performance in the target domain when the training data in the target domain are insufficient. (2) It enhances application and generalization by extending LSR while integrating multiple classic base models such as neural networks, TSK fuzzy systems, and kernel methods. (3) It uses knowledge extracted from the source domain to train the classification model in the target domain, ensuring security for MI-EEG signal recognition. Experimental studies indicate the effectiveness of the proposed method in MI-EEG signal recognition. Although the proposed ELSR-TL demonstrates effectiveness in these experiments, there is still room for further research. For example, the hyperparameter optimization procedure based on grid searching and cross-validation is computationally expensive, so future research should focus on addressing this issue. The proposed ELSR-TL operates offline and cannot be applied in real-time scenarios. The datasets used in this study are relatively small in scale; thus, the effectiveness of the proposed method needs validation on more extensive datasets in future studies. Additionally, it is also worth further examining how to provide more theoretical justifications for knowledge transfer to avoid negative transfer. While this study primarily focuses on binary MI tasks, extending the proposed ELSR-TL to multi-class MI tasks, multimodal integration, and cross-dataset transfers is also worth studying.

Data availability statement

Publicly available datasets were analyzed in this study. This data can be found at: https://www.bbci.de/competition/iii/desc_IVa.html.

Author contributions

ZJ: Writing – original draft, Writing – review & editing. KH: Formal analysis, Writing – review & editing. JQ: Methodology, Validation, Visualization, Writing – review & editing. ZB: Data curation, Methodology, Validation, Visualization, Writing – review & editing. DY: Methodology, Validation, Visualization, Writing – review & editing. JZ: Conceptualization, Methodology, Supervision, Writing – review & editing.

Funding

The author(s) declare that financial support was received for the research and/or publication of this article. This study was partially supported by the National Natural Science Foundation of China through Grants 62206177, 62106145, 62002227, and 62306126; from the Zhejiang Provincial Natural Science Foundation of China under Grants LY23F020007, LQ22F020024, LTY22F020003, and LZ24F020006; and from the Natural Science Foundation of Jiangsu Province through Grant BK20220621.

Conflict of interest

The authors declare that the research was conducted in the absence of any commercial or financial relationships that could be construed as a potential conflict of interest.

Generative AI statement

The authors declare that no Gen AI was used in the creation of this manuscript.

Publisher's note

References

Abbas, A., Sutter, D., Zoufal, C., Lucchi, A., Figalli, A., and Woerner, S. (2021). The power of quantum neural networks. *Nat. Comput. Sci.* 1, 403–409. doi: 10.1038/s43588-021-00084-1

Aldea, R., Fira, M., and Lazăr, A. (2014). Classifications of motor imagery tasks using k-nearest neighbors. *In 12th symposium on Neural Network applications in electrical engineering (NEUREL)*, IEEE. 115–120.

Antonini, M., Barlaud, M., Mathieu, P., and Daubechies, I. (1992). Image coding using wavelet transform. *IEEE Trans. Image Process.* 1, 205–220. doi: 10.1109/83.136597

Bennett, K., and Demiriz, A. (1999). Semi-supervised support vector machines. *Adv. Neural Inf. Proces. Syst.* 11, 368–374.

Bian, Z., Qu, J., Zhou, J., Jiang, Z., and Wang, S. (2024). Weighted adaptively ensemble clustering method based on fuzzy co-association matrix. *Inform. Fusion* 103:102099. doi: 10.1016/j.inffus.2023.102099

Blanco, S., Kochen, S., Rosso, O., and Salgado, P. (1997). Applying time-frequency analysis to seizure EEG activity. *Engin. Med. Biol. Magazine IEEE* 16, 64–71. doi: 10.1109/51.566156

Blankertz, B., Müller, K., Krusienski, D., Schalk, G., Wolpaw, J. R., Schlögl, A., et al. (2006). The BCI competition III: validating alternative approaches to actual BCI problems. *IEEE Trans. Neural Syst. Rehabil. Eng.* 14, 153–159. doi: 10.1109/TNSRE.2006.875642

Cover, T., and Hart, P. (1967). Nearest neighbor pattern classification. *IEEE Trans. Inf. Theory* 13, 21–27. doi: 10.1109/TIT.1967.1053964

Dai, W., Yang, Q., Xue, G., and Yu, Y., "Boosting for transfer learning," in Proc. 24th Int. Conf. Mach. Learning, (2007), pp. 193–200.

Edelman, B. J., Zhang, S., Schalk, G., Brunner, P., Muller-Putz, G., Guan, C., et al. (2024). Non-invasive brain-computer interfaces: state of the art and trends. *IEEE Rev. Biomed. Eng.* 18, 26–49. doi: 10.1109/RBME.2024.3449790

Fisher, R. (1936). The use of multiple measurements in taxonomic problems. *Ann. Eugenics* 7, 179–188. doi: 10.1111/j.1469-1809.1936.tb02137.x

Fouad, I. A., Labib, F. E. Z. M., Mabrouk, M. S., Sharawy, A. A., and Sayed, A. Y. (2020). Improving the performance of P300 BCI system using different methods. *Network Model. Analysis Health Inform. Bioinform.* 9, 1–13. doi: 10.1007/s13721-020-00268-1

Ghumman, M. K., Singh, S., Singh, N., and Jindal, B. (2021). Optimization of parameters for improving the performance of EEG-based BCI system. *J. Reliable Intelligent Environ.* 7, 145–156. doi: 10.1007/s40860-020-00117-y

Greene, B. R., Faul, S., Marnane, W. P., Lightbody, G., Korotchikova, I., and Boylan, G. B. (2008). A comparison of quantitative EEG features for neonatal seizure detection. *Clin. Neurophysiol.* 119, 1248–1261. doi: 10.1016/j.clinph.2008.02.001

Gu, S., Chou, Y., Zhou, J., Jiang, Z., and Lu, M. (2024). Takagi–sugeno–Kang fuzzy clustering by direct fuzzy inference on fuzzy rules. *IEEE Transact. Emerg. Topics Comput. Intelligence* 8, 1264–1279. doi: 10.1109/TETCI.2023.3336537

Huang, G., Chen, L., and Siew, C. (2006). Universal approximation using incremental constructive feedforward networks with random hidden nodes. *IEEE Trans. Neural Netw.* 17, 879–892. doi: 10.1109/TNN.2006.875977

Jiang, Z., Chung, F. L., and Wang, S. (2019). Recognition of multiclass epileptic EEG signals based on knowledge and label space inductive transfer. *IEEE Trans. Neural Syst. Rehabil. Eng.* 27, 630–642. doi: 10.1109/TNSRE.2019.2904708

Ko, W., Jeon, E., Jeong, S., and Suk, H-Il. (2021). Multi-scale neural network for EEG representation learning in BCI. *IEEE Comput. Intell. Mag.* 16, 31–45. doi: 10.1109/MCI.2021.3061875

Kohavi, R. (1996). Scaling up the accuracy of naive-Bayes classifiers: a decision-tree hybrid. *KDD*. 96, 202–207.

Li, S., Jin, J., Daly, I., Liu, L., and Cichocki, A. (2022). Feature selection method based on Menger curvature and LDA theory for a P300 brain–computer interface. *J. Neural Eng.* 18:066050. doi: 10.1088/1741-2552/ac42b4

Li, J., Qiu, S., Shen, Y. Y., Liu, C. L., and He, H. (2019). Multisource transfer learning for cross-subject EEG emotion recognition. *IEEE Transact. Cybernet.* 50, 3281–3293. doi: 10.1109/TCYB.2019.2904052

Lotte, F., and Guan, C. (2011). Regularizing common spatial patterns to improve BCI designs: unified theory and new algorithms. *IEEE Trans. Biomed. Eng.* 58, 355–362. doi: 10.1109/TBME.2010.2082539

Mohammadi, E., Daneshmand, P. G., and Khorzooghi, S. M. S. M. (2022). Electroencephalography-based brain–computer interface motor imagery classification. *J. Med. Signals Sensors* 12, 40–47. doi: 10.4103/jmss.JMSS_74_20

Naseem, I., Togneri, R., and Bennamoun, M. (2010). Linear regression for face recognition. *IEEE Trans. Pattern Anal. Mach. Intell.* 32, 2106–2112. doi: 10.1109/TPAMI.2010.128

Pan, S., Tsang, I., Kwok, J., and Yang, Q. (2011). Domain adaptation via transfer component analysis. *IEEE Trans. Neural Netw.* 22, 199–210. doi: 10.1109/TNN.2010.2091281

Pan, S., and Yang, Q. (2010). A survey on transfer learning. *IEEE Trans. Knowl. Data Eng.* 22, 1345–1359.

Pfurtscheller, G., Neuper, C., Schlögl, A., and Lugger, K. (1998). Separability of EEG signals recorded during right and left motor imagery using adaptive autoregressive parameters. *IEEE Trans. Rehabil. Eng.* 6, 316–325. doi: 10.1109/86.712230

Qu, J., Song, Z., Cheng, X., Jiang, Z., and Zhou, J. (2023a). A new integrated framework for the identification of potential virus–drug associations. *Front. Microbiol.* 14:1179414. doi: 10.3389/fmicb.2023.1179414

Qu, J., Song, Z., Cheng, X., Jiang, Z., and Zhou, J. (2023b). Neighborhood-based inference and restricted Boltzmann machine for small molecule-miRNA associations prediction. *PeerJ* 11:e15889. doi: 10.7717/peerj.15889

Qureshi, M. F., Mushtaq, Z., Rehman, M. Z. U., and Kamavuako, E. N. (2022). Spectral image-based multiday surface electromyography classification of hand motions using CNN for human–computer interaction. *IEEE Sensors J.* 22, 20676–20683. doi: 10.1109/JSEN.2022.3204121

Qureshi, M. F., Mushtaq, Z., Rehman, M. Z. U., and Kamavuako, E. N. (2023). E2cnn: an efficient concatenated cnn for classification of surface emg extracted from upper limb. *IEEE Sensors J.* 23, 8989–8996. doi: 10.1109/JSEN.2023.3255408

Saunders, C., Gammerman, A., and Vovk, V., "Ridge regression learning algorithm in dual variables," (ICML-1998) Proceedings of the 15th International Conference on Machine Learning. Morgan Kaufmann, pp. 515–521 (1998)

Schafer, R., and Rabiner, L. (1973). Design and simulation of a speech analysis-synthesis system based on short-time Fourier analysis. *IEEE Trans. Audio Electroacoust.* 21, 165–174. doi: 10.1109/TAU.1973.1162474

Siddiqa, H. A., Irfan, M., Abbasi, S. F., and Chen, W. (2023). Electroencephalography (EEG) based neonatal sleep staging and detection using various classification algorithms. *Comput. Materials Continua* 77, 1759–1778. doi: 10.32604/cmc.2023.041970

Siddiqa, H. A., Tang, Z., Xu, Y., Wang, L., Irfan, M., Abbasi, S. F., et al. (2024). Single-Channel EEG data analysis using a multi-branch CNN for neonatal sleep staging. *IEEE Access* 12, 29910–29925. doi: 10.1109/ACCESS.2024.3365570

Wan, Z., Yang, R., Huang, M., Zeng, N., and Liu, X. (2021). A review on transfer learning in EEG signal analysis. *Neurocomputing* 421, 1–14. doi: 10.1016/j.neucom.2020.09.017

Wang, H., and Zhang, Y. (2016). Detection of motor imagery EEG signals employing Naïve Bayes based learning process. *Measurement* 86, 148–158. doi: 10.1016/j.measurement.2016.02.059

Wu, P., and Dietterich, T. G., "Improving SVM accuracy by training on auxiliary data sources," in Proc. 21st Int. Conf. Mach. Learning, (2004)

Xie, L., Deng, Z., Xu, P., Choi, K. S., and Wang, S. (2018). Generalized hidden-mapping transductive transfer learning for recognition of epileptic electroencephalogram signals. *IEEE Transact. Cybernet.* 49, 2200–2214. doi: 10.1109/TCYB.2018.2821764

Zhang, X., Dong, S., Shen, Q., Zhou, J., and Min, J. (2023). Deep extreme learning machine with knowledge augmentation for EEG seizure signal recognition. *Front. Neuroinform.* 17:1205529. doi: 10.3389/fninf.2023.1205529

Zhang, J., Li, Y., Liu, B., Chen, H., Zhou, J., Yu, H., et al. (2024). A dynamic broad TSK fuzzy classifier based on iterative learning on progressively rebalanced data. *Inf. Sci.* 677, 120976.

Zhang, Y., Wang, G., Huang, X., and Ding, W. (2023). TSK fuzzy system fusion at sensitivity-ensemble-level for imbalanced data classification. *Inform. Fusion* 92, 350–362. doi: 10.1016/j.inffus.2022.12.014

Zhang, Y., Xia, K., Jiang, Y., Qian, P., Cai, W., Qiu, C., et al. (2022). Multi-modality Fusion & Inductive Knowledge Transfer Underlying non-Sparse Multi-Kernel Learning and distribution adaption. *IEEE/ACM Trans. Comput. Biol. Bioinform.* 20, 2387–2397. doi: 10.1109/TCBB.2022.3142748

Zhang, L., Song, J., Gao, A., Chen, J., Bao, C., and Ma, K. "Be your own teacher: Improve the performance of convolutional neural networks via self distillation," In Proc. IEEE/CVF Int. Conf. Comput. Vis., Seoul, Korea (South), (2019), pp. 3713–3722.

frontiers | Frontiers in Neuroinformatics

TYPE Review
PUBLISHED 18 June 2025
DOI 10.3389/fninf.2025.1561401

OPEN ACCESS

EDITED BY
Changming Wang,
Capital Medical University, China

REVIEWED BY
Cancheng Li,
Beihang University, China
Maheshi Dissanayake,
University of Peradeniya, Sri Lanka
Guilherme Bastos,
Federal University of Itajubá, Brazil

*CORRESPONDENCE
Jisu Elsa Jacob
jisuelsa@sctce.ac.in

RECEIVED 15 January 2025
ACCEPTED 20 May 2025
PUBLISHED 18 June 2025

CITATION
Chandrasekharan S and Jacob JE (2025) Bridging neuroscience and AI: a survey on large language models for neurological signal interpretation.
Front. Neuroinform. 19:1561401.
doi: 10.3389/fninf.2025.1561401

Bridging neuroscience and AI: a survey on large language models for neurological signal interpretation

Sreejith Chandrasekharan [1] and Jisu Elsa Jacob [2*]

[1]Freelance Researcher, Trivandrum, Kerala, India, [2]Department of Electronics and Communication Engineering, Sree Chitra Thirunal College of Engineering, Trivandrum, Kerala, India

Electroencephalogram (EEG) signal analysis is important for the diagnosis of various neurological conditions. Traditional deep neural networks, such as convolutional networks, sequence-to-sequence networks, and hybrids of such neural networks were proven to be effective for a wide range of neurological disease classifications. However, these are limited by the requirement of a large dataset, extensive training, and hyperparameter tuning, which require expert-level machine learning knowledge. This survey paper aims to explore the ability of Large Language Models (LLMs) to transform existing systems of EEG-based disease diagnostics. LLMs have a vast background knowledge in neuroscience, disease diagnostics, and EEG signal processing techniques. Thus, these models are capable of achieving expert-level performance with minimal training data, nominal fine-tuning, and less computational overhead, leading to a shorter time to find effective solutions for diagnostics. Further, in comparison with traditional methods, LLM's capability to generate intermediate results and meaningful reasoning makes it more reliable and transparent. This paper delves into several use cases of LLM in EEG signal analysis and attempts to provide a comprehensive understanding of techniques in the domain that can be applied to different disease diagnostics. The study also strives to highlight challenges in the deployment of LLM models, ethical considerations, and bottlenecks in optimizing models due to requirements of specialized methods such as Low-Rank Adapation. In general, this survey aims to stimulate research in the area of EEG disease diagnostics by effectively using LLMs and associated techniques in machine learning pipelines.

KEYWORDS

electroencephalogram, large language model, LLM, BERT, GPT

1 Introduction

Artificial intelligence and machine learning techniques have greatly contributed to the field of EEG signal processing. The emergence of Large Language Models (LLMs) to interpret and understand complex brain activity patterns is a new era in EEG signal processing. Electroencephalography (EEG) or brain signal is one of the best techniques for measuring neural activity and provides a vast amount of temporal data that requires efficient algorithms for analysis and thereby extracting meaningful insights and information. As EEG signals are non-invasive, more portable, have greater potential for use, and apply to a wider population.

EEG analysis can be performed using different methods:

(i) **Representation learning in EEG analysis:** It is the basic step in EEG analysis that can extract relevant features from EEG signals that are useful for identifying certain states or pathologies. It is performed using self-supervised learning methods to develop biomarkers for various pathologies. This analysis technique can be applied to huge brain signal data.

(ii) **Discriminative EEG analysis:** As the name suggests, this analysis technique is employed for discrimination and for distinguishing between various groups like disease and normal, based on various patterns in EEG signals. This can be done using advanced architectures such as Foundation Models, LLMs, and Graph Neural Networks (GNNs). This architecture efficiently captures the EEG patterns, which are capable of discrimination and are crucial for learning complex neural processes.

(iii) **Generative EEG analysis:** Generative EEG analysis refers to a set of techniques that aims to understand and model the underlying processes that cause electrical activity in the brain and generate EEG signals. Unlike traditional EEG analysis, which focuses on identifying patterns or abnormalities in the recorded EEG data, generative approaches seek to explain how these signals are produced by the brain and how they relate to cognitive or neural processes. Generative methods aim to generate new modalities or signal data from EEG signals. Innovative approaches such as diffusion produce images or text from EEG data, providing novel approaches to the understanding and visualization of brain activity.

The application of LLMs to EEG interpretation addresses several critical challenges in neuroscience research and clinical practice. First, EEG data is inherently complex, containing various frequency bands, spatial relationships, and temporal patterns that cannot be completely explored by traditional analysis methods. LLMs, with their ability to process sequential data and identify long-range dependencies, offer a promising approach to understanding these intricate patterns within the EEG signal. Secondly, the medical interpretation of EEG often relies heavily on expert knowledge and pattern recognition skills developed over many years. The capacity of LLMs to learn from large datasets of annotated EEG recordings and medical reports could help bridge this expertise gap and support clinical decision making.

Furthermore, LLMs are good at understanding context and generating natural language descriptions, which makes them particularly valuable for translating complex EEG patterns into clinically relevant insights. This LLM capability can revolutionize the way EEG signals are analyzed and neurological findings are made and communicated between healthcare providers and researchers. This can potentially improve diagnostic accuracy and treatment planning. The ability of such models to process multimodal inputs also gives new possibilities for integrating EEG data with other clinical information, thereby creating a more comprehensive understanding of various neurological pathologies.

Generative Large Language Models (LLMs) often present several benefits compared to pre-trained Transformer language models (Kalajdzievski, 2024). Firstly, many generative LLMs can perform tasks without requiring explicit fine-tuning on annotated datasets, leading to considerable savings in time and resources associated with data annotation. Secondly, these models frequently overcome the limitation of a fixed maximum input length, enabling the processing of longer sequences of text. Thirdly, task-specific behavior in generative LLMs is often achieved through prompt engineering, which can be a more efficient approach than extensive hyperparameter optimization typically needed for pre-trained Transformer models.

LLMs are less susceptible to data imbalance issues due to the vast pre-training they receive, covering domain knowledge, signal analysis, and related methodologies. Fine-tuning methods in LLMs, such as PEFT, freeze base model weights, and preserve core knowledge. This approach prevents catastrophic overwriting compared to training approaches used with traditional deep learning methods. Hence, LLMs are less dependent on perfectly balanced training datasets compared to traditional models.

Recent advances in LLM architectures and training techniques have made these applications more feasible. The development of specialized attention mechanisms and temporal embedding methods has enhanced their ability to process time-series data like EEG. Additionally, the success of transfer learning in various domains suggests that pre-trained language models could be effectively utilized for neurological signal interpretation, thereby reducing the amount of labeled data required for specific applications. However, applying LLMs to EEG analysis also presents unique challenges that must be addressed. It includes the need for appropriate data representations, integration of domain-specific knowledge, and development of interpretable models that can provide clinically meaningful outputs. Understanding these challenges and potential solutions is crucial to advance the field and realize the full potential of LLM in neuroscience. This survey makes an effort to consolidate the major studies related to applying LLM in the context of EEG signal interpretation.

1.1 Understanding neural signaling

Classical research in the neurological sector is concentrated on advancements for diagnosing particular conditions, and the majority of this research is centered on handling neurological signals individually. There is a clear need to bridge the gap and pave the way toward more generalized neurological signal processing paradigms that can be applied to the broader context of neuroscience. Although early applications of LLMs focused on individual neural signals, mainly EEG and fMRI, the focus is now increasingly shifting toward unified frameworks capable of handling a wider range of neurological signals beyond these popular modalities. The following subsections give an overview of neurological signals that are considered in this study and inter-relations between them (Gentile and Barragan, 2023; Hong et al., 2018; Baghdadi et al., 2025; Chaudhary, 2025).

1.1.1 EEG signals

Electroencephalography (EEG) signals are used to record the electrical activity of the brain via electrodes placed on the scalp. This non-invasive method captures the summation of postsynaptic

potentials of numerous of neurons firing synchronously in the cerebral cortex. The resulting EEG signal reflects the ongoing electrical activity and exhibits its changes in response to various stimuli or pathological states. Small metal or silver/silver chloride electrodes are attached to the scalp for EEG recording using standard placements like the international 10–20 system. These electrodes detect minute voltage fluctuations on the scalp, which are then amplified and digitized by the EEG machine. The raw EEG data is typically formatted as a time series of voltage values for each electrode, representing the electrical potential difference between the recording electrode and a reference electrode over time. A significant strength of EEG is its high temporal resolution, as it can capture rapid changes in brain activity on the order of milliseconds, making it excellent for studying the timing of neural events. EEG also provides a direct measure of neuronal activity, offering a real-time window into brain function. Compared to other neuroimaging techniques like MEG and fMRI, EEG equipment and operational costs are generally lower, making it more accessible for research and clinical applications (Baghdadi et al., 2025). Furthermore, the non-invasive nature of EEG, with electrodes placed on the scalp surface, poses no surgical or internal risks to the subject. EEG systems can also be relatively compact and portable, allowing for recordings in various settings. However, EEG suffers from low spatial resolution because the electrical signals recorded on the scalp are blurred and attenuated as they pass through the skull and scalp, making it difficult to precisely localize the sources of neural activity within the brain. EEG signals are also highly susceptible to various artifacts originating from physiological sources (e.g., eye blinks, muscle movements, and heart activity) and external sources (e.g., electrical noise), requiring careful preprocessing. Finally, EEG is primarily sensitive to activity in the superficial layers of the cortex and has difficulty detecting activity originating from deeper brain structures.

1.1.2 MEG signals

Magnetoencephalography (MEG) is a non-invasive neuroimaging technique that measures the magnetic fields produced by electrical activity in the brain. These magnetic fields, generated by the flow of ionic currents within neurons, are extremely weak and are detected by highly sensitive superconducting quantum interference devices (SQUIDs) housed in a cryogenic dewar that does not touch the patient's head. MEG is particularly sensitive to neuronal currents that are tangential to the scalp, making it complementary to EEG which is more sensitive to radial currents. During a MEG recording, the subject sits or lies down in a magnetically shielded room to minimize external magnetic interference. The dewar containing the SQUID sensors is positioned around the head, capturing the minute magnetic field changes. Simultaneously, the subject's head position relative to the sensors is often tracked using head position indicator (HPI) coils. The raw MEG data consists of a time series of magnetic field measurements for each sensor. Similar to EEG, MEG data is susceptible to artifacts from various sources, including environmental magnetic noise, movement of the subject, and physiological signals like heartbeats and eye blinks (Cuffin and Cohen, 1979). Magnetoencephalography (MEG) measures the magnetic fields produced by the electrical activity of the brain. These magnetic fields are less distorted by the skull and scalp compared to the electrical potentials measured by EEG. Similar to EEG, MEG offers excellent temporal resolution, capable of tracking rapid neural events in the millisecond range. MEG also directly measures the electromagnetic consequences of neuronal activity, providing a real-time assessment of brain function. A key advantage of MEG over EEG is its better spatial resolution because magnetic fields are less distorted by intervening tissues, allowing for more accurate localization of neural sources. However, MEG systems are significantly more expensive to purchase, maintain (due to the need for cryogenic cooling of the sensors), and operate compared to EEG. The use of MEG is also limited to specialized facilities due to the requirement of magnetically shielded rooms to minimize interference from external magnetic fields (Baghdadi et al., 2025). Despite shielding, MEG recordings can still be affected by subtle magnetic noise from the environment or even movement of metallic objects near the scanner.

1.1.3 fMRI signals

Functional Magnetic Resonance Imaging (fMRI) is a neuroimaging technique that measures brain activity by detecting changes in blood flow and oxygenation. The underlying principle is neurovascular coupling, which posits that local neural activity is accompanied by changes in regional cerebral blood flow (rCBF) and blood oxygenation. fMRI most commonly utilizes the blood-oxygen-level-dependent (BOLD) contrast, which is sensitive to the ratio of oxygenated to deoxygenated hemoglobin in the blood. During an fMRI scan, the subject lies inside a strong magnetic field. Radio frequency pulses are applied, causing protons in the brain tissue to align and then relax, emitting signals that are detected by the MRI scanner. For fMRI, specific pulse sequences are used to make the images sensitive to the BOLD signal. A series of 3D brain volumes are acquired over time, capturing the dynamic changes in blood oxygenation related to neural activity. The raw fMRI data is a 4D dataset (3 spatial dimensions + time), where each voxel (volumetric pixel) contains a time series of signal intensity values. Functional Magnetic Resonance Imaging (fMRI) is a neuroimaging technique that measures brain activity by detecting changes in blood flow and oxygenation using a strong magnetic field. The most common method, Blood-Oxygen-Level-Dependent (BOLD) fMRI, relies on the different magnetic properties of oxygenated and deoxygenated hemoglobin. fMRI offers the highest spatial resolution among these four techniques, allowing for detailed mapping of brain activity down to the millimeter level. It also provides complete brain coverage in a single scan, offering a complete view of neural activity in different regions, and unlike EEG and fNIRS, fMRI is sensitive to activity in both the cortical and subcortical structures (deep brain) (Baghdadi et al., 2025). However, the hemodynamic response measured by fMRI is relatively slow, peaking several seconds after the onset of neural activity, which limits its ability to precisely track the timing of rapid neural events, resulting in low temporal resolution. fMRI scanners are very expensive to purchase, install, and operate, requiring specialized infrastructure and trained personnel, and they are non-portable, being large, stationary pieces of equipment.

A significant limitation of fMRI is the requirement for participants to remain very still during scans to avoid motion artifacts, which can significantly degrade the image quality, posing challenges for certain populations.

1.1.4 fNIRS signals

Functional Near-Infrared Spectroscopy (fNIRS) is a non-invasive neuroimaging technique that measures brain activity by assessing changes in the concentration of oxygenated hemoglobin (HbO) and deoxygenated hemoglobin (HbR) in the cerebral cortex. fNIRS utilizes the principle of neurovascular coupling, similar to fMRI, but uses near-infrared light to penetrate the scalp and skull. Changes in neural activity may lead to changes in blood flow and oxygen consumption, which in turn alter the absorption and scattering of the near-infrared light that passes through the brain tissue. An fNIRS system typically consists of light sources that emit near-infrared light at one or more wavelengths (typically between 700 and 900 nm) and detectors (photodiodes) placed on the scalp. The sources and detectors are arranged in optodes, which are positioned on the scalp using a cap or a custom-made holder. The light emitted by the sources travels through the head tissue and is partially absorbed and scattered before reaching the detectors. The intensity of the detected light at each wavelength is measured over time. The raw fNIRS data consists of time series of light intensity measurements for each source-detector pair (channel) and each wavelength. This raw data is then converted to changes in optical density. Functional Near-Infrared Spectroscopy (fNIRS) is an optical neuroimaging technique that measures brain activity by assessing changes in the concentration of oxygenated hemoglobin (HbO) and deoxygenated hemoglobin (HbR) in the cerebral cortex. It utilizes the principle that neural activity is coupled with changes in local blood flow. fNIRS offers the advantage of being portable, with devices that are generally lightweight and allowing for measurements in more naturalistic settings and with participants who may not be able to tolerate other imaging modalities (Hong et al., 2018). Due to its portability and tolerance to some movement, fNIRS is suitable for studying brain activity during tasks involving movement. The non-invasive nature of fNIRS, using light shone onto the scalp and detected by sensors, is another benefit, and compared to MEG and fMRI, fNIRS systems are often considered easier to set up and operate. However, fNIRS has relatively low spatial resolution compared to fMRI and even MEG, as the scattering of light in the tissue limits the precision of source localization (Gentile and Barragan, 2023). The depth penetration of near-infrared light is also limited, primarily allowing measurement of activity in the superficial layers of the cortex. As fNIRS measures brain activity indirectly through hemodynamic changes, which are slower than the direct neuronal activity measured by EEG and MEG, its temporal resolution is also limited compared to electrophysiological methods. Finally, the presence of hair and variations in scalp and skull thickness can affect the light transmission and signal quality, requiring careful consideration during setup and analysis, and a baseline scalp condition is typically needed for reliable measurements.

1.2 Overview of large language models

Advanced language models with huge parameter sizes and remarkable learning capacities are known as large language models, or LLMs. The self-attention module in Transformer (Vaswani et al., 2017) is the fundamental component of many LLMs, including GPT-3 (Floridi and Chiriatti, 2020) and GPT-4.

A crucial component of LLMs is in-context learning (Brown et al., 2020), in which the model is trained to produce text based on a specified context or prompt. As a result, LLMs can produce responses that are more logical and pertinent to the situation, which makes them appropriate for conversational and interactive applications. Another essential component of LLMs is Reinforcement Learning from Human Feedback (RLHF) (Christiano et al., 2017). By using human-generated replies as rewards, this technique fine-tunes the model, enabling it to learn from its errors and gradually enhance its performance. Prompt engineering is a popular method of communicating with LLMs in which users build and provide certain prompt messages to direct LLMs to produce the required responses or perform particular tasks (White et al., 2023; Clavié et al., 2023; Zhou et al., 2022). People can participate in dialogue interactions, which involve speaking with LLMs in natural language, or question-and-answer interactions, in which they ask the model questions and get replies. In summary, LLMs have transformed NLP and have the potential for several uses thanks to their Transformer architecture, in-context learning, and RLHF capabilities.

1.2.1 Bidirectional encoder representations from transformers

Bidirectional Encoder Representations from Transformers (BERT) introduced a deep, bidirectional, unsupervised language representation. BERT considers the entire context of a word, both preceding and succeeding, during training, unlike previous models, which process text sequentially (Koroteev, 2021). This enables the model to capture rich semantic and syntactic information, leading to significant performance improvements in various NLP tasks. This powerful understanding is further enhanced by BERT's pre-training process, which utilizes two unsupervised learning objectives. Firstly, Masked Language Modeling (MLM) forces the model to deeply understand language semantics by randomly masking words in the input and training it to predict the masked words based on the surrounding context. Secondly, Next Sentence Prediction (NSP) improves the model's ability to understand discourse by training it to predict whether two given sentences are consecutive in the original text, thereby capturing crucial sentence-level relationships.

BERT's architecture is based on the Transformer model, which utilizes self-attention mechanisms to capture complex relationships between words. It consists of multiple layers of stacked transformer blocks, each containing a Multi-Head Self-Attention and Position-wise Feed-Forward Network (FFN) (Devlin et al., 2018; Hao et al., 2019). Multi-head self-attention allows the model to attend to different parts of the input sequence simultaneously, capturing diverse relationships between words. FFN introduces non-linearity and allows the model to learn complex representations. Two

unsupervised pre-training tasks are used by BERT: Next Sentence Prediction, which asks the network to determine whether two sentences are consecutive, and Masked LM, in which some words are masked and the network infers their meaning from context.

The main limitations of BERT include high computational cost, requiring significant resources for pre-training, and difficulty in handling very long sequences due to its fixed maximum sequence length. It is challenging to fine-tune the BERT model for some specific tasks, which may require careful tuning of hyperparameters.

1.2.2 GPT-1

There has been a long history behind GPT-1 dating back to the groundbreaking paper "Attention is all you need" (Vaswani et al., 2017). According to it, the Transformer is divided into two parts: encoder and decoder, both of which perform Multi-Head Self Attention, though the encoder is able to observe information from the entire source sequence while the decoder does not. Similar to filling in the gaps, the Bert model adjusts the encoder and uses context to forecast the missing intermediate phrases when creating pre-training tasks. GPT-1 also executes masked multi-head self-attention by using a decoder, which anticipates the subsequent context based on the preceding context. Making context predictions from a huge corpus of data is the pre-training phase. The final token's embedding is fed into the prediction layer, which fits the downstream data's label distribution after the model has been trained using downstream data during the fine-tuning stage. The model's accuracy and generalization abilities improve as the number of layers increases. Zero-shot learning is a built-in feature of GPT-1 and as the model gets bigger, so does this capability, which leads to the development of later GPT models.

1.2.3 GPT-2

Based on the Transformer architecture for language modeling, GPT-2 is an improved version of GPT-1. Large amounts of unlabeled data can be used to train models with GPT-2, and fine-tuning improves model performance and optimizes it for downstream tasks. GPT-2 places more focus on the language model in a zero-shot scenario, when the model hasn't been trained or optimized for downstream tasks before being used. GPT-1 often relies on fine-tuning, and adjusting the model's parameters specifically for each downstream task. This typically involves introducing special tokens, such as start and separator symbols, to guide the model's understanding of the task at hand. In contrast, GPT-2 emphasizes zero-shot learning, aiming to perform tasks without explicit fine-tuning. This necessitates a different approach to task specification. Instead of modifying the model, GPT-2 primarily modifies the input sequences.

GPT-2 significantly scales up the Transformer architecture, boasting 48 layers and 1.5 billion parameters, compared to GPT-1's 12 layers and BERT's 24. This scaling necessitates a massive training dataset, derived from WebText after basic data cleaning. Research suggests that larger models require more data to reach their full potential, and current models, including GPT-2, are likely still under-trained (Radford et al., 2019). Unlike BERT, which employs bidirectional transformers, GPT-2 utilizes unidirectional transformers, mirroring the sequential nature of language generation. Furthermore, GPT-2 adopts a novel multi-tasking approach during pre-training. Instead of focusing on a single objective, it learns across multiple tasks simultaneously, ensuring that the model converges effectively. Notably, the core Transformer parameters are shared across these tasks, promoting efficient learning and enhancing generalization. This multi-tasking strategy, inspired by MT-DNN (Liu et al., 2020), empowers GPT-2 to achieve impressive performance even without task-specific fine-tuning.

1.2.4 GPT-3

GPT-3 primarily focuses on the idea of a universal language model excluding traditional fine-tuning. To address the computational challenges associated with its massive 175 billion parameters, GPT-3 incorporates the sparse attention mechanism from Sparse Transformers (Floridi and Chiriatti, 2020). This technique reduces computational load by selectively attending to relevant parts of the input sequence. For downstream tasks, GPT-3 employs a few-shot learning approach, demonstrating remarkable performance with just a few examples. This highlights the significant impact of model size on few-shot learning capabilities. The GPT-3 architecture is identical to the GPT 2, except the transformer layers have dense and sparse attention (Child et al., 2019; Radford et al., 2019). GPT-3 employs the gradient noise scale as in (McCandlish et al., 2018) to determine the batch size during training, demonstrating that big models may train on larger batch sizes with a lower learning rate. In general, GPT-3 raises model parameters to 175B, demonstrating that large language models improve with the scale and are competitive with the fine-tuned models.

One important feature of GPT-3 is its capacity for in-context learning. By merely supplying examples within the input sequence, in-context learning provides few-shot performance, in contrast to traditional fine-tuning, which updates model parameters based on downstream task examples. As the number of instances increases, this "prompting" strategy shows a notable performance improvement. But after eight shots, the effect of more examples decreases and, after ten rounds, is insignificant.

1.2.5 GPT-4

In comparison to GPT-3, GPT-4 has more than a trillion parameters and greatly enhances the GPT model scale and training methods. The GPT-4 model may produce text more accurately and naturally by employing a novel training method called Reinforcement Learning from Human Feedback (RLHF). To train through reinforcement learning, RLHF combines pre-training and fine-tuning techniques, having conversations with human operators. This increases GPT-4's performance on particular tasks and strengthens its understanding of context and questions (Nori et al., 2023; Wang et al., 2023). GPT-4 generally employs the same pre-training, prompting, and prediction-based training methodology as ChatGPT. Three noteworthy improvements are introduced in GPT-4: (1) Using a rule-based reward model (RBRM); (2) Including multi-modal prompt learning to

accommodate different prompts; (3) Including a chain of thought mechanism to improve overall coherence in thinking. GPT-4 is a strong multimodal model that can interpret text and image input, producing text outputs that rank among the top 10% of test takers. On conventional benchmarks, the GPT-4 language model performs better than most cutting-edge NLP systems (Liu et al., 2021; Chang et al., 2023).

1.2.6 Claude

Anthropic, a business started by former OpenAI researchers with experience in language models such as GPT-3, created the AI helper Claude (Wu et al., 2023). With a high Google investment, Anthropic seeks to develop AI that is both beneficial and safe. AnthropicLM v4-s3, their flagship model, is an autoregressive model with 52 billion parameters that was trained on enormous text datasets. Anthropic uses a novel "Constitutional AI" technique in contrast to conventional fine-tuning techniques that depend on human input (Bai et al., 2022). This novel system employs a model to direct the process of fine-tuning, guaranteeing that the AI abides by a set of principles centered on autonomy (respecting freedom of choice), beneficence (maximizing positive impact), and non-maleficence (avoiding giving harmful advice).

1.2.7 Open-source LLMs

Open Source Large Language Models (LLMs) stand in contrast to proprietary models like GPT and Claude, which are often fine-tuned to align with human preferences, enhancing their usability and safety. This alignment process, however, can be expensive in terms of computational resources and human annotation, and its lack of transparency can hinder progress in AI safety research within the wider community. Open source LLMs offer an alternative by providing researchers and developers with the ability to examine, modify, and build upon the underlying technology. This fosters innovation, allows for greater customization, and promotes a deeper understanding of these models' inner workings. Llama 2 prioritizes helpfulness and safety through specific training. Qwen modifies the Transformer architecture for efficiency and long sequence handling.

The two notable open source LLMs are Llama 2 and Qwen. Llama 2 is a family of pre-trained and fine-tuned LLMs developed by Meta AI, scaling up to 70 billion parameters. Considering to achieve the two benchmarks, helpfulness and safety, Llama 2-Chat models reportedly outperform existing open-source models on benchmarks for both these qualities and, in human evaluations, appear to be comparable to some closed-source models. Meta AI implemented several safety measures, including the use of safety-specific data for annotation and tuning, red-teaming exercises to identify vulnerabilities, and iterative evaluations to refine safety. The accompanying documentation provides a detailed account of their fine-tuning methodology and their strategies for enhancing LLM safety. A noted limitation of Llama 2, particularly its larger versions, is the longer computational time required for operation.

Qwen, short for Tongyi Qianwen, is another open-source LLM that utilizes a modified version of the Transformer architecture, inspired from the LLama model. Qwen's architecture incorporates several specific modifications. It employs a unified embedding approach, which aims to improve performance at the cost of increased memory usage. For incorporating positional information, Qwen utilizes Rotary Positional Embedding (RoPE). Additionally, biases are added to the Query, Key, and Value layers of the attention mechanism to enhance the model's ability to handle longer sequences. Qwen also replaces the traditional layer normalization technique with RMSNorm, which is reported to offer similar performance with greater efficiency. For the activation function, Qwen has chosen SwiGLU, a combination of Swish and Gated Linear Unit.

Both Llama 2 and Qwen represent significant advancements in the realm of open-source LLMs. They provide transparency and flexibility, enabling the AI community to understand and build upon these technologies. Llama 2 places a strong emphasis on safety through dedicated training and evaluation methodologies, while Qwen introduces architectural modifications aimed at improving performance and efficiency, particularly in handling longer sequences. Both models contribute to the growing landscape of accessible and powerful language models.

2 Taxonomy of AI tasks

The usage of LLMs in the context of EEG-based disease diagnostics can be classified into generative and discriminative tasks. Generative tasks help us create all new content, such as textual output showing the reasoning behind a specific decision. On the other hand, discriminative tasks are useful for the categorization of given input data into classes, such as in the case of disease classification. Utilization of both of the models is important for achieving effective disease diagnostics. Use of various key LLM models in the context of neuro signal analysis is listed in Table 1.

The block diagram shown in Figure 1 details the modules involved in a typical machine-learning pipeline using LLM for EEG-based disease diagnostics. It has got 4 stages as given below:

- Input Stage

  This stage reads the input data in the form of EEG which can optionally be multimodal inputs bringing additional information helpful for categorization or generation of data at the output.
- EEG LLM fine-tuning stage

  Fine-tuning is the key step of the pipeline and tunes the LLM for a specific context which can be a single task or multiple tasks in the same context. This stage uses various adaptation methods for tuning a given LLM for a specific task such as report generation or disease classification. Internally it makes use of techniques such as transfer learning and incremental adaptation for generative tasks, and incremental adaptation and hybrid model enhancement for discriminative tasks. It can be a mixture of both approaches and the associated techniques based on the use case that is being addressed.
- Output stage

  The output can be generated text or labels indicating the class of health condition of the patient. It can be a combination

of both for hybrid models. In case of multi tasking, the labels generated by the model can belong to different set of classes based on the task in focus.

TABLE 1 Description of key LLM models in the context of neuro signal analysis.

Research	Year	LLM	Task
Mishra et al. (2024)	2024	Llama v3, MISTRALv0.3, QWEN2.5	Generative
Tung et al. (2024)	2024	Gemini 1.5 flash, Claude 3 sonnet, GPT-4	Generative
Chen et al. (2024)	2024	Qwen2-0.5B	Generative
Wang et al. (2024a)	2024	BART	Generative
Kim et al. (2024)	2024	da Vinci GPT-3 base	Discriminative
Parani et al. (2024)	2024	pre trained Longformer	Discriminative
Jiang et al. (2024)	2024	Large Brain Model (LaBraM)	Discriminative
Zhang et al. (2023)	2023	GPT-3.5, GPT-4	Discriminative
Gijsen and Ritter (2024)	2024	EEG Language Model (ELM)	Discriminative
Lee and Chung (2024)	2024	GPT-3.5 turbo model	Discriminative
Sano et al. (2024)	2024	GPT-4, GPT-4 Vision, GPT-3.5	Discriminative
Zhang et al. (2024c)	2024	BERT	Discriminative
Wang et al. (2024b)	2024	Llama 2	Generative
Han et al. (2024)	2024	BERT	Generative
Ma et al. (2024)	2024	miniGPT-4, CLIP	Generative
Yang et al. (2024)	2024	Qwen2 1.5B	Generative
Zhang et al. (2024a)	2024	Llama 2	Generative

2.1 LLMs for generative tasks

2.1.1 Thought2Text

The goal of this approach is to evaluate efficiency of public LLMs such as LLAMA v3, MISTRALv0.3, and QWEN2.5 in translating visual thoughts from EEG signals into textual form (Mishra et al., 2024). This is achieved by a 3 step approach, involving capturing of EEG signals, encoding of these signals as token embeddings and fine-tuning of language models with these features.

For the first step, to generate embeddings, this solution makes use off a EEG encoder derived from a deep convolutional neural network model—ChannelNet—that converts EEG signals to multidimensional embeddings (Heeg). Pooled image embeddings (Hclip) are generated by a pre-trained CLIP model capable of abstracting image representations. The encoder functions by minimizing two set of losses—one which is a categorical cross-entropy loss between predicted and actual labels using EEG embeddings and secondly, the mean squared error (MSE) between EEG embeddings (Heeg) and pooled image embeddings (Hclip). In the following stage, these representations are further translated into multimodal embeddings (Hmm) by passing through a projector implementing a transformation. The LLMs learns representation in multimodal feature form generated from an image sketch filtering original image using Gaussian blur and Canny filters. In the next step, it learns the representation generated by the projector using a multichannel EEG signal that represents the response of the brain to the image shown to the subject.

On using this trained model for inference, the EEG encoder generates EEG embeddings and makes use of no images. This representation is further passed through projectors to get multimodal features for performing predictions. The embeddings from EEG signal segments are further concatenated and given to fine-tuned LLM which generates meaningful text descriptions.

2.1.2 Multi-stage LLM report generation

The objective of the proposed system here is to generate and verify EEG reports with the help of a multi-stage LLM

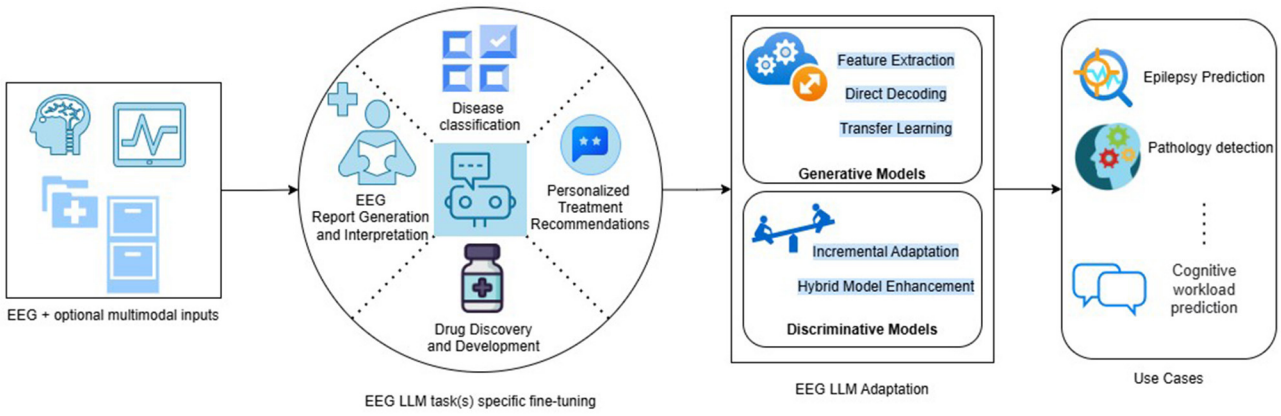

FIGURE 1
Overview of LLM solutions for EEG diagnosis use cases.

solution (Tung et al., 2024). Generation phase, which is first among the two phase approach, takes EEG features as inputs and format them to generate a structured prompt. This prompt is also given to the Google Gemini 1.5 pro API for the processing and generation of reports. In the second phase, the system uses 3 promising LLMs—Gemini 1.5 flash, Claude 3 sonnet, and GPT-4—and performs verification. This solution makes use of advanced LLM capabilities of Gemini pro to build its core language model. The model is chosen for its advanced capabilities that include long context memory, reasoning abilities, and optimized computational performance. The input of this pipeline employs a hybrid AI algorithm that generates a JSON object based on structured EEG features. This ensures capturing of important metrics such as background frequency, amplitude, symmetry, and detected anomalies. These objects are further used by the LLM along with an efficient prompt engineering method. The prompt engineering method used in this system has four parts, namely : (1) role as neurologist, (2) structure EEG features and interpretations, (3) task specifications for generation of report, and (4) outline of report. Each of the LLM model is set to assess independently and finally decision is based on majority voting. Validation of the method by generation of reports on a few hundred report showed effectiveness of the system in guiding neurologist to make infallible decisions.

2.1.3 EEG emotion copilot

EEG emotion copilot uses a lighter LLM in a local server to perform multiple tasks using EEG signals (Chen et al., 2024). The features of this system include emotion recognition, the generation of custom diagnostics, treatment recommendations, and the automatic creation of medical records for patients. It also provides an ergonomic user interface and employs strong privacy safety measures through novel data processing protocols.

The study methodology involves pre-processing EEG signals and transforming them via wavelet to shorten the signal length. The final prompt is constructed using the initial context-defining prompt, demographic data, emotional label, and treatment as training data. Qwen2-0.5B pre-trained model is used for pruning and achieving 50% reduction over the model parameters. A warm-up during the fine-tuning phase using Lora gradually increases the learning rate of the model. Finally, the RAG (Retrieval-augmented generation) technique is used to deploy the model to enhance retrieval performance and improve the interactivity through the dialogue method in the user interface.

This approach addressed the issue of data redundancy inherent in EEG signal processing. The long EEG data sequence handling was managed through efficient data compression techniques, thus improving computational efficiency and computing the real-time emotion. This study highlighted the importance of patient privacy by ensuring that the proposed model is run locally. Model pruning strategies were explored to create a lightweight version of the language model, making it feasible to deploy in environments with limited computational resources while maintaining high performance. While signal compression improves efficiency, complex scenarios still require additional channel signals for accurate analysis. The study proposed that LLMs could potentially generate dense channel signals from limited channel data, which would significantly enhance computational efficiency. This approach could revolutionize emotion analysis and streamline the overall process. This research demonstrates the potential of EEG Emotion Copilot to transform emotional recognition and treatment in clinical settings.

2.1.4 Contrastive EEG-text masked autoencoder

This research work reports a significant advancement in EEG-based language decoding through CET-MAE (Contrastive EEG-Text Masked Autoencoder) and E2T-PTR (EEG-to-Text using Pre-trained Transferable Representations) (Wang et al., 2024a). While E2T-PTR utilizes these pre-trained representations together with BART for better text generation, the CET-MAE model combines masked autoencoding with contrastive learning in an innovative manner for both single-modality and cross-modality processing. This study suggests a novel pre-trained model called Contrastive EEG-Text Masked Autoencoder (CET-MAE) to align EEG and text. CET MAE uses a specialized multi-stream encoder to combine masked signal modeling and contrastive learning. By balancing the semantic-level aligned embeddings of text tokens and text-evoked EEG features with the latent embeddings represented by self-reconstruction, it efficiently learns pre-trained representations of text and EEG. Concerning masked signal modeling, CET-MAE applies a high mask ratio (75%) to both text and EEG data, which poses a significant challenge for the model to manage more missing data during the reconstruction step.

CET-MAE integrates intra- and cross-modal SSL into a single unified system utilizing a multistream architecture: (1) Using masked modeling with a mask ratio of up to 75%, intramodality streams investigate representative embeddings that capture the inherent properties of text or EEG sequences. (2) The intermodality stream constrains the encoder to maximize semantic consistency between text and its related EEG sequences and offers dual-modal representations to improve intramodality reconstruction. E2T-PTR uses BART's capabilities to generate text from these consistent and representative features by transferring pre-trained EEG representations. Multiple experiments using ZuCo, the latest text-evoked EEG dataset, highlight the high standard of this study in both qualitative and quantitative evaluations. Other inner speech BCI data sets can also be used to study the performance of the suggested CET-MAE model, which exhibits significant potential to improve EEG-based language decoding tasks.

2.1.5 LLM analysis of fMRI language data in neurocognitive disorder

A study by Wang et al. (2024b) investigates language-related functional changes in older adults with Neurocognitive Disorders (NCD) using LLM-based fMRI encoding. This work explores the correlation between brain scores derived from fMRI encoding models and cognitive scores in subjects with NCD, in contrast to previous studies that focused on healthy young adults. This study develops an fMRI encoding model using LLaMA2, specifically for older adults with early stage NCD or at risk, in order to quantify the association between brain areas and language functions. Individuals with higher cognitive abilities were revealed to have better brain scores compared to those with lower cognitive abilities,

with maximum correlations observed in the middle temporal gyrus (r = 0.368) and the superior frontal gyrus (r = 0.289). This suggests that fMRI encoding models and brain scores have the potential to detect early functional changes in NCD patients, offering a promising avenue for developing interpretable machine learning models for early detection of NCD based on language-related fMRI signals. This study marks the beginning of applying an LLaMA2-based fMRI encoding model to study subjects with NCD.

2.1.6 Mindformer

Mindformer, introduced by Han et al. (2024), is a novel semantic alignment method for multisubject fMRI signals, designed to overcome limitations in current multisubject brain decoding techniques. MindFormer generates fMRI-conditioned feature vectors suitable for conditioning Stable Diffusion for fMRI-to-image generation and LLMs such as Bidirectional Encoder Representations from Transformers (BERT) for fMRI-to-text generation. The model incorporates two key innovations: subject-specific tokens to capture individual differences while leveraging multisubject data for training, and a feature embedding and training scheme based on the Image Prompt Adapter(IP)-Adapter to extract semantically meaningful features from fMRI signals. By effectively embedding multisubject fMRI signals using subject tokens and the IP-Adapter, MindFormer significantly outperforms existing multisubject brain decoding frameworks. This advancement provides a new framework for understanding the decoding of the brain of multiple subjects and identifying common neural patterns, effectively leveraging shared information while maintaining individual-specific accuracy. The current implementation primarily focuses on visual stimuli, and extending it to more complex cognitive and sensory experiences requires advancements in model architecture and training methodologies. However, the computational complexity associated with training on larger datasets presents a limitation.

2.1.7 LLM visual encoding model

LLM Visual Encoding Model (LLM-VEM) introduced in Ma et al. (2024) provided a new multimodal training paradigm, utilizing miniGPT-4 to enhance the encoding of fMRI activity in the visual cortex. The paradigm generates detailed textual descriptions for stimulus images using the LLM, creating a high-quality text description set. These descriptions are then processed through a pre-trained text encoder, namely Contrastive Language Image Pre-training (CLIP), to obtain text embedding features. A contrastive loss function is used to minimize the distance between image embedding features and text embedding features, aligning the stimulus image and text information. This alignment, facilitated by the LLM, improves the visual encoding model learning process, leading to higher precision. Such an effective visual encoding model helps researchers investigate and predict the brain responses to different visual stimuli.

LLM-VEM processes stimulus image features in two stages: Stage 1 utilizes a frozen image feature extractor, Explore the limits of Visual representation at scAle (EVA), for feature extraction, followed by dimensionality reduction via feature projection. To mitigate overfitting, a portion of the voxel mapping network is replaced with a Principal Component Analysis (PCA) module, reducing model parameters. Stage 2 refines the model by unfreezing specific blocks within EVA while freezing others, and incorporates the LLM-aligned loss function to further align stimulus image and text features. By extending unimodal features to multimodal features, this training paradigm improves the encoding model performance. LLM-VEM integrates stimulus images and textual descriptions, aligning them to obtain multimodal feature information and achieve strong performance.

2.1.8 NeuGPT

NeuGPT is a multimodal language generation model designed to unify the analysis of various neural recording types (EEG, MEG, ECoG, SEEG, fMRI, and fNIRS) which have traditionally been studied separately (Yang et al., 2024). The goal is to create a model that can process various neural signals and interact with speech and text, focusing on brain-to-text decoding.

The model is structured in two main stages:

- Stage 1: Neural signal tokenization: this stage focuses on converting neural signals into discrete codes. It consists of four components: an encoder that transforms raw neural signals into embeddings, a quantizer that converts these embeddings into discrete code indices, a decoder that reconstructs the neural signals from the quantized embeddings, and a discriminator that enhances the quality of the reconstructed signals.
- Stage 2: LLM fine-tuning for neural code understanding: this stage involves fine-tuning a large language model (LLM) to understand and generate neural codes, facilitating cross-modal communication between neural signals, speech, and text. QWEN2-1.5B, a relatively small but efficient LLM with a 32K context length, was chosen as the base model for this fine-tuning.

This model demonstrates the feasibility of translating neural signals into coherent speech and text, bridging the gap between brain activity and expressive communication. Highlights the benefits of a unified framework for processing various types of neural signal, overcoming the traditional compartmentalization in neural recording research. The model's flexibility in handling various sensor layouts and coordinates allows for broader application across different experimental settings. The integration of neural signals into language generation models offers insight into human brain language processing and paves the way for advanced brain-computer interfaces.

2.1.9 fNIRS and LLM for VR rehab evaluation in mild cognitive impairment

The study addresses the challenge of effectively evaluating Virtual Reality (VR) tasks designed for Mild Cognitive Impairment (MCI) rehabilitation (Zhang et al., 2024b). Traditional evaluation methods, such as post-training metrics and subjective questionnaires, do not capture the comprehensiveness and intensity of cognitive stimulation provided by VR tasks. To overcome these limitations, Zhang et al. (2024b) proposed a novel

approach that integrates functional near-infrared spectroscopy data with an LLM to evaluate and optimize VR rehabilitation tasks.

The study introduces a systematic paradigm, based on the Diagnostic and Statistical Manual of Mental Disorders (DSM-5), to assess the scope of cognitive domains stimulated by VR tasks. This paradigm enables a unified assessment of various cognitive domains, including attention, memory, executive functions, language, visuospatial skills, and psychomotor abilities. This study uses fNIRS technology to objectively measure cognitive stimulation with high time resolution. They extract graph parameters from fNIRS data to quantify brain region connectivity and efficiency during VR tasks, providing robust neural indicators of cognitive engagement.

LLM-enabled analysis: A key innovation of the study is the development of a three-stage prompt strategy to facilitate LLM-based analysis. The LLM is used to translate complex metrics derived from fNIRS and the scope of stimulated cognitive domains into easy-to-understand evaluation reports and actionable recommendations for VR task optimization. This approach aims to bridge the gap between complex neural observations and practical insights for VR task designers.

This approach exhibits the potential of integrating fNIRS data and LLMs to provide a comprehensive and objective evaluation of VR rehabilitation tasks. The proposed framework improves the design and effectiveness of VR interventions for MCI, by automating the analysis and interpretation of complex neural data.

2.1.10 MindSpeech

A novel AI model, named MindSpeech, is designed to decode imagined continuous speech using high-density functional near-infrared spectroscopy (fNIRS). The study aims to develop a non-invasive brain-AI interface that can translate imagined thoughts into text, enhancing human-AI communication.

Zhang et al. (2024a) used high-density fNIRS to record brain signals from participants engaged in an imagined speech task. They developed a "word cloud" paradigm to elicit a variety of imagined sentences across a broad semantic space. In this paradigm, participants were presented with a central topic word and surrounding keywords and instructed to imagine sentences using these words. After the imagined speech period, the participants typed the sentences, providing ground-truth data for decoder training. In addition, a continuous-wave high-density fNIRS system was used to collect neurovascular data. The fNIRS data was preprocessed through several steps, including conversion to optical density, detrending, motion artifact removal, and bandpass filtering.

The core of the MindSpeech model involves using a prompt tuning approach with the Llama2 model. This approach allows the LLM to generate text guided by the fNIRS brain signals. The process includes segmenting the imagined sentences into context input and continuation, converting both context input and fNIRS signals into embeddings, and concatenating these embeddings as input to the LLM.

A brain encoding model, using a sequence-to-sequence (Seq2Seq) neural network with transformers, maps the fNIRS data to LLM embeddings. The model is trained to predict the continuation text from the brain signal-generated embeddings and the context input embeddings. The model's performance was evaluated using natural language processing metrics to compare the generated sentences with the ground truth. The study also explored the combination of data from multiple participants to improve the decoder performance.

2.1.11 Language postdiction vs. prediction in MEG

A research study by Azizpour et al. (2024) investigated whether MEG data can reveal predictive information during natural listening, similar to findings in fMRI. The researchers examined whether pre-onset neural encoding of upcoming words could be detected in MEG signals, aligning with results from other neuro signals. They also tested whether incorporating future word embeddings, as done in fMRI studies, would enhance the alignment between MEG data and linguistic predictions. To address these questions, the study built encoding models using GPT-2 embeddings to map to MEG data recorded while participants listened to approximately 10 h of narrated stories. The results showed that the GPT-2 embeddings explain the variability in post-onset MEG signals. Critically, consistent with electrocorticography findings, pre-onset representations of upcoming words were detected up to 1 second before word onset in language-related regions. However, unlike fMRI findings, including future word embeddings did not improve MEG encoding.

The study concludes that while MEG can capture pre-onset representations similar to electrocorticography, the lack of enhancement with future word embeddings suggests that these signals might not reflect predictive processing and could be due to correlations between nearby embeddings and word co-occurrences. The findings also revealed robust evidence for postdiction. In general, the study demonstrates the value of MEG combined with LLMs for studying naturalistic language processing and emphasizes the need for more research to define evidence for prediction in this context.

2.2 LLMs for discriminative tasks

2.2.1 EEG-GPT

EEG GPT is an attempt to use a comparatively small training data set to fine-tune an LLM and achieve performance comparable to that of other classical approaches in a deep learning context, for classification of the given EEG signal segment as normal or disease. It shows that with zero-shot learning, the base LLM yields improved performance in such classification tasks (Kim et al., 2024). The pipeline used for this approach generates quantitative EEG features that are fed to a fine-tuned LLM that uses a specific private knowledge base. The dataset used here is the Temple University Hospital Abnormal Corpus, which is made up of 1140 hours of EEG data acquired from 2,993 subjects. It is balanced between normal and abnormal recordings to some extent and is further pre-split into train and evaluation sets for uniformity of evaluation over experiments.

Each of the given EEG files is segmented into non-overlapping 20-second epochs and quantitative features such as standard deviation, kurtosis power ratios, etc. are calculated for each epoch. Open AI's Completions APIs are further used to fine-tune and evaluate on da Vinci GPT-3 base LLM. The original quantitative features are converted to verbal representation with the use of prompts, making it generate normal/disease labels at the output. This solution aims to use 50 times less data, yet provides performance comparable to that of deep learning approaches such as ChronoNet, StanfordCNN, and HybridCNN. This study also highlights the reasoning ability and ability of EEG GPT to make use of specialist EEG tools on several temporal scales in a gradual and transparent way. Such a tree-of-thought reasoning approach helps generate the reasoning behind predictions in a human-readable form by making use of tools such as qEEG. By going through multiple segments until the system is confident in predicting the start and duration of a seizure or as normal, this solution helps to allow early stoppage of seizures.

2.2.2 Pretrained longformer LLM

This method utilizes a large language model for epilepsy classification by re-factoring the data for a pre-trained LLM model (Parani et al., 2024). Such an approach requires minimal retraining and still results in better performance compared to deep learning models trained from scratch.

The data preparation stage of the mode converts EEG signals that are in the form of real numbers into string tokens. Due to memory limitations, the tokenization is performed on each of the 20 EEG channels individually. The generated tokens are divided into segments corresponding to 1 second each to improve efficiency. Further, a locally deployed open-source LLM—Longformer—is utilized for learning from generated features, i.e., tokens. By using sliding window attention to process tokens within a specific window and symmetric global attention that captures relationships between pairs of tokens, LLM is trained for the given disease classification context. The training is focused on the classifier layer of Longformer with a chosen set of hyperparameters for 4 batches. The final classification result of a segment corresponding to detection or otherwise is performed by majority voting, where detection over 10 channels indicates a positive label.

The study further compares the chosen LLM solution against ViT methods having multiple stages of transformer blocks followed by a classifier stage. ViT is efficient in extracting spatial features and short-term local temporal features efficiently. However, its incapability to capture long-term temporal dependencies and correlations makes it inferior to the aforementioned LLM method of disease classification.

2.2.3 NeuroLM—multitask foundation model

Even though there are many advances in large-scale pre-training with EEG, proving significant potential for advancing brain-computer interfaces and healthcare applications, current pre-trained models typically require complete fine-tuning for each downstream task (Jiang et al., 2024). This limits their flexibility and leads to inefficient resource usage. This study develops NeuroLM, a multi-task foundation model that treats EEG signals as a foreign language, leveraging the capabilities of Large Language Models (LLMs) to enable multi-task learning and inference. NeuroLM addresses three major challenges in combining EEG processing with LLMs: the alignment of EEG and text embeddings, effective representation learning within the LLM framework, and unified multi-task learning across diverse EEG applications. This system introduces a text-aligned neural tokenizer that converts EEG signals into discrete neural tokens through vector-quantized temporal-frequency prediction. These tokens are then processed by an LLM that learns causal EEG information through multi-channel autoregression and enables the model to understand both EEG and language modalities.

The architecture of this model is remarkable for its scale and comprehensive training approach. It features 1.7B parameters which have been pre-trained on approximately 25,000 h of EEG data. The data goes into a text-aligned neural tokenizer which is trained through adversarial training. In the next step, a VQ encoder helps extract compressed embedding representations for LLM processing. Finally, multitasking instruction tuning helps to implement a vast set of downstream applications.

The dataset for the study included six different EEG datasets to evaluate NeuroLM, TUAB (Harati et al., 2015) (abnormal detection), TUEV (Zheng and Lu, 2015) (event type classification), SEED (Zheng and Lu, 2015) (emotion recognition), HMC (Alvarez-Estevez and Rijsman, 2021) (sleep stage classification), Workload (Zyma et al., 2019) (cognitive workload classification) and TUSL (von Weltin et al., 2017) (slowing event classification). The model performance is demonstrated across six different tasks, including abnormal detection, event type classification, emotion recognition, sleep stage classification, cognitive workload prediction, and slowing type classification. The use of instruction tuning for multi-task learning in EEG signal processing has shown remarkable success in this model, thus eliminating the need for individual fine-tuning while maintaining high performance across various applications.

2.2.4 Word-level neural state classification

This study makes use of LLMs that are provided by eye-tracking data and EEG measurements, for the investigation of neural responses (Zhang et al., 2023). It utilizes the Zurich Cognitive Language Processing Corpus (ZuCo), focuses on semantic inference processing and analyzes brain states during word fixation periods.

The classification pipeline consists of (i) Initial word classification where two language models evaluate sentences and words categorized into: high-relevance words (HRW) and low-relevance words (LRW), (ii) Data processing where joint selection process identifies shared HRW set, eye-gaze data is used to extract corresponding EEG signals and four feature-extraction techniques are applied to reduce signal complexity, and (iii) Classification System where three distinct classifiers implemented and follow standard brain-computer interface methodology to perform binary HRW/LRW classification. It achieved over 60% validation accuracy across 12 subjects and successfully distinguished between high and low-relevance word processing. This is the first study to classify

brain states at the word level using LLM knowledge and contributes to the understanding of human cognitive processing.

2.2.5 Zero-shot pathology detection

The study integrates clinical EEG data with language modeling and develops a novel approach for medical diagnostics and pathology detection, based on an extensive dataset of 15,000 EEGs paired with corresponding clinical reports (Gijsen and Ritter, 2024). It employs contrastive learning techniques and is one of the pioneer works in applying multimodal pre-training using natural language and functional brain data in a medical context. It seems that exposure to a range of textual material combined with contrastive learning produces the most accurate representations. In particular, retrieval performance was significantly enhanced by integrating data on the patient's medication and clinical history with EEG interpretation. Zero-shot pathology detection also proved to be possible with such multimodal models. It showed significant performance over EEG-only SSL was noted using linear probing, with the greatest improvements in situations with a limited number of annotated samples.

2.2.6 LLM for neural decoding

This study aims to employ LLM to develop a novel neural decoder for interpreting intracranial EEG (iEEG). It tried to overcome the limitations of traditional decoders, which often specialize in specific tasks and struggle to interpret complex, real-world brain activity (Lee and Chung, 2024).

This novel approach can provide more comprehensive, and faster interpretations of iEEG signals more efficiently. The GPT-3.5 turbo model was fine-tuned with preprocessed iEEG signals categorized by frequency bands [high-gamma (30–200 Hz), beta (12–30 Hz), and theta (4–8 Hz)] and by the regions of the brain. These signals were presented as prompts to the model. A Python-based system was developed to integrate neural signal processing with the LLM decoder. The authors observed frequent responses corresponding to visual and auditory stimuli. This variability in responses to identical prompts highlights a limitation, which could be addressed through more specific fine-tuning of the LLM.

2.2.7 LLM on human attention

This research applies LLMs in the context of human attention and sleep and tries to estimate the stages and quality of sleep and attention states (Sano et al., 2024). The model can generate suggestions for improving sleep and adaptive guided imagery scripts based on electroencephalogram (EEG) and data related to physical activity. This study's results show that LLMs can estimate sleep quality based on human textual behavioral features, even though it requires further training data and domain-specific knowledge. The study utilized (a) zero-shot learning: LLMs (GPT-4, GPT-4 Vision) were used without specific training, relying on their pre-trained knowledge to interpret the input data. (b) In-context learning: LLMs (GPT-4) were provided with input data and label examples within the prompts to enable them to learn from the context. (c) Fine-tuned LLMs: GPT 3.5 Turbo was fine-tuned on specific datasets for improved performance, and (d) traditional Machine Learning: XGBoost, a gradient boosting algorithm, was used as a benchmark for comparison. The study focused on using interpretable features (e.g., power spectrum density) to understand the extent to which LLM contributes to the detection and improvement of altered states of sleep.

LLMs, even with fine-tuning, showed lower accuracy in directly detecting attention states, sleep stages, and sleep quality from EEG and activity data compared to traditional machine learning models like XGBoost. This study is done with limited datasets and limited LLMs. Refining prompts and using large and diverse datasets can enhance the model's performance. More extensive training of LLM can be done with diverse physiological and behavioral data to effectively capture complex human patterns.

2.2.8 LLM on human reading comprehension

This study developed a Brain-Computer Interface (BCI) system that can predict the relevance of words during reading comprehension tasks by integrating EEG and eye-tracking data with a novel reading embedding representation. LLMs are used to guide the learning process and understand the underlying semantic relationships within the text (Zhang et al., 2024c). This study uses the pre-trained BERT model to generate word embedding that helps to learn the semantic context of every token within a given sentence. In addition, it also utilizes important eye-gaze features such as fixation duration and pupil size, as well as conditional entropy of the EEG signal at the input. In the next step, these bio-signal features are normalized and projected into a common space. The final set of processed features is passed on to an attention-based transformer encoder combining word embeddings and biosignal features resulting in effective multimodal representations. This approach provides a reliable LLM-guided labeling process.

This improvement highlights the superior performance of the transformer architecture in handling complex, multi-modal data. This representation, which combined eye-tracking and EEG biomarkers using an attention-based transformer encoder, had the highest single-subject accuracy of 71.2% and a mean 5-fold cross-validation accuracy of 68.7% across nine people using a balanced sample. This is a pioneer study in eye tracking, EEG, and LLMs to predict human reading comprehension at the word level. Without any prior information about the reading tasks, the Bidirectional Encoder Representations from Transformers (BERT) model is fine-tuned for word embedding. The model easily achieves an accuracy of 92.7% despite the lack of task-specific information.

3 Discussion

The studies considered here show the ability of LLMs to generate several meaningful features, especially proving to be promising for use cases where the available data set size is limited. This is achieved through the use of zero-shot and few-shot learning. Recent research has shown the effectiveness of LLMs in performing few shot learnings in domains ranging from seizure forecasting to EEG textual report generations. Many of these works have reported

that these transformer architectures are efficient in making use of in-context learning for zero-shot tasks, merely by utilization of information given over a textual prompt resulting in better performance for both generative and discriminative tasks.

One of the key advantages of LLMs is their ability to generate intermediate reasoning steps for the analysis of complex problems. The use of strategies such as Chain of Thought for multi-step calculations with LLM was proven to be effective due to strategic lookahead and backtracking. Moreover, LLMs are proven to be capable of using external expert tools in the analysis of EEG and then synergizing those outputs to generate more meaningful results, similar to a subject matter expert of the domain.

3.1 Ethical considerations

A serious aspect of using LLMs with neurological signal processing and analysis is its ethical considerations. The data, that is fed to the LLMs are personal physiological and behavioral data which can raise privacy concerns. The users might get worried about security and confidentiality, as the data is sent to cloud servers with the use of popular LLMs such as GPT 4, Gemini, and Claude. Transparency and effective data anonymization are essential in this regard for avoiding issues due to leakage of data from cloud platforms. Additionally, concerns are raised around the generated contents from LLMs, which potentially be harmful and inaccurate or may intend to manipulate the user. To avoid this, implementing comprehensive guidelines covering ethical and safety aspects is necessary.

A possible solution to reduce concerns around privacy and security is to run the models locally on high-end servers. However, this requires model pruning resulting in lightweight LLMs well-suited for local execution with limited resources. Such a solution often results in compromises around model's effectiveness in terms of prediction accuracy and computational time.

3.2 Limitations and future work

The need for LLM in the context of EEG analysis arises from the gaps that were identified from existing literature. One major challenge is the limited availability of EEG data. Unlike image or text data collection, acquiring EEG data is complex. Expert annotation is particularly time-consuming and results in small datasets of labeled EEGs for specific BCI tasks. Existing EEG datasets are not substantial enough to support robust LLM training required for significant model efficiency gains. Thus the questions to address are: how can we effectively utilize large-scale unlabeled EEG data, and what volume of data would be necessary for training LLMs?

Varying EEG collection configurations pose another challenge to the use of LLMs for EEG analysis. Although the international 10–20 system provides standardization guidelines for EEG testing, clinicians often use different numbers of electrodes based on their specific application requirements. This variability creates a significant research challenge in adapting various EEG data formats to align with the input specifications of the neural transformer.

An additional hurdle involves developing effective EEG representation learning approaches. The primary difficulty is the low signal-to-noise ratio (SNR) and various types of interference. Successfully balancing temporal and spatial characteristics is essential for effective learning of EEG representation. Despite the existence of various deep learning approaches for raw EEG data processing, including CNN, RNN, and GNN architectures, many researchers continue to rely on manually designed EEG features due to these inherent challenges.

Author contributions

SC: Conceptualization, Formal analysis, Methodology, Project administration, Writing – original draft, Writing – review & editing. JJ: Conceptualization, Investigation, Methodology, Project administration, Supervision, Validation, Writing – original draft, Writing – review & editing.

Funding

The author(s) declare that no financial support was received for the research and/or publication of this article.

Acknowledgments

The related biomedical research works, its computation, and this literature survey is done with the computational facilities of Innovation Centre for Biomedical Research, Sree Chitra Thirunal College of Engineering, Pappanamcode funded by Plan Fund, Government of Kerala.

Conflict of interest

The authors declare that the research was conducted in the absence of any commercial or financial relationships that could be construed as a potential conflict of interest.

Generative AI statement

The author(s) declare that no Gen AI was used in the creation of this manuscript.

Publisher's note

References

Alvarez-Estevez, D., and Rijsman, R. M. (2021). Inter-database validation of a deep learning approach for automatic sleep scoring. *PLoS ONE* 16:e0256111. doi: 10.1371/journal.pone.0256111

Azizpour, S., Westner, B. U., Szewczyk, J., Güçlü, U., and Geerligs, L. (2024). Signatures of prediction during natural listening in meg data? *arXiv preprint arXiv:2412.19622*.

Baghdadi, G., Hadaeghi, F., and Kamarajan, C. (2025). Editorial: Multimodal approaches to investigating neural dynamics in cognition and related clinical conditions: integrating EEG, MEG, and fMRI data. *Front. Syst. Neurosci.* 19:1495018. doi: 10.3389/fnsys.2025.1495018

Bai, Y., Kadavath, S., Kundu, S., Askell, A., Kernion, J., Jones, A., et al. (2022). Constitutional AI: Harmlessness from AI feedback. *arXiv:2212.08073*.

Brown, T. B., Mann, B., Ryder, N., Subbiah, M., Kaplan, J., Dhariwal, P., et al. (2020). "Language models are few-shot learners," in *Neural Information Processing Systems, abs/2005.14165*.

Chang, Y., Wang, X., Wang, J., Wu, Y., Yang, L., Zhu, K., et al. (2023). A survey on evaluation of large language models. *arXiv:2307.03109*.

Chaudhary, U. (2025). *Non-invasive Brain Signal Acquisition Techniques*. Cham: Springer Nature Switzerland, 25–80. doi: 10.1007/978-3-031-76081-5_2

Chen, H., Zeng, W., Senior, M.ember, Chen, C., Cai, L., Wang, F., Wang, L., et al. (2024). EEG emotion copilot: pruning LLMs for emotional EEG interpretation with assisted medical record generation. *arXiv:2410.00166*.

Child, R., Gray, S., Radford, A., and Sutskever, I. (2019). Generating long sequences with sparse transformers. *arXiv:1904.10509*.

Christiano, P., Leike, J., Brown, T. B., Martic, M., Legg, S., and Amodei, D. (2017). Deep reinforcement learning from human preferences. *arXiv:1706.03741*.

Clavié, B., Ciceu, A., Naylor, F., Soulié, G., and Brightwell, T. (2023). "Large language models in the workplace: a case study on prompt engineering for job type classification," in *Natural Language Processing and Information Systems*, 3–17. doi: 10.1007/978-3-031-35320-8_1

Cuffin, B. N., and Cohen, D. (1979). Comparison of the magnetoencephalogram and electroencephalogram. *Electroencephalogr. Clin. Neurophysiol.* 47, 132–146. doi: 10.1016/0013-4694(79)90215-3

Devlin, J., Chang, M.-W., Lee, K., and Toutanova, K. (2018). BERT: Pre-training of deep bidirectional transformers for language understanding. *arXiv:1810.04805*.

Floridi, L., and Chiriatti, M. (2020). GPT-3: Its nature, scope, limits, and consequences. *Minds and machines* 30, 681–694. doi: 10.1007/s11023-020-09548-1

Gentile, E., and Barragan, A. C. (2023). "EEG/FNIRS," in *Psychophysiology Methods* (Cham: Springer), 181–202. doi: 10.1007/978-1-0716-3545-2_9

Gijsen, S., and Ritter, K. (2024). EEG-language modeling for pathology detection. *arXiv:2409.07480*.

Han, I., Lee, J., and Ye, J. C. (2024). Mindformer: Semantic alignment of multi-subject fmri for brain decoding. *arXiv preprint arXiv:2405.17720*.

Hao, Y., Dong, L., Wei, F., and Xu, K. (2019). "Visualizing and understanding the effectiveness of BERT," *Proceedings of the 2019 Conference on Empirical Methods in Natural Language Processing and the 9th International Joint Conference on Natural Language Processing (EMNLP-IJCNLP)*. doi: 10.18653/v1/D19-1424

Harati, A., Golmohammadi, M., Lopez, S., Obeid, I., and Picone, J. (2015). "Improved EEG event classification using differential energy," in *2015 IEEE Signal Processing in Medicine and Biology Symposium (SPMB)* (IEEE), 1–4. doi: 10.1109/SPMB.2015.7405421.

Hong, K.-S., Khan, M. J., and Hong, M. J. (2018). Feature extraction and classification methods for hybrid FNIRS-EEG brain-computer interfaces. *Front. Hum. Neurosci.* 12:246. doi: 10.3389/fnhum.2018.00246

Jiang, W.-B., Wang, Y., Lu, B.-L., and Li, D. (2024). NeuroLM: A universal multi-task foundation model for bridging the gap between language and EEG signals. *arXiv:2409.00101*.

Kalajdzievski, D. (2024). Scaling laws for forgetting when fine-tuning large language models. *arXiv preprint arXiv:2401.05605*.

Kim, J. W., Alaa, A., and Bernardo, D. (2024). EEG-GPT: Exploring capabilities of large language models for EEG classification and interpretation. *arXiv:2401.18006*.

Koroteev, M. V. (2021). BERT: A review of applications in natural language processing and understanding. *arXiv:2103.11943*.

Lee, D. H., and Chung, C. K. (2024). "Enhancing neural decoding with large language models: A GPT-based approach," in *2024 12th International Winter Conference on Brain-Computer Interface (BCI)* (IEEE), 1–4. doi: 10.1109/BCI60775.2024.10480499

Liu, X., Wang, Y., Ji, J., Cheng, H., Zhu, X., Awa, E., et al. (2020). "The microsoft toolkit of multi-task deep neural networks for natural language understanding," in Proceedings *of the 58th Annual Meeting of the Association for Computational Linguistics: System Demonstrations* (Stroudsburg, PA, USA: Association for Computational Linguistics). doi: 10.18653/v1/2020.acl-demos.16

Liu, X., Zheng, Y., Du, Z., Ding, M., Qian, Y., Yang, Z., et al. (2021). GPT understands, too. *arXiv:2103.10385*.

Ma, S., Wang, L., Hou, S., and Yan, B. (2024). Aligned with llm: a new multi-modal training paradigm for encoding fmri activity in visual cortex. *arXiv preprint arXiv:2401.03851*.

McCandlish, S., Kaplan, J., Amodei, D., and OpenAI Dota Team (2018). An empirical model of large-batch training. *arXiv:1812.06162*.

Mishra, A., Shukla, S., Torres, J., Gwizdka, J., and Roychowdhury, S. (2024). Thought2Text: text generation from EEG signal using large language models (LLMs). *arXiv:2410.07507*.

Nori, H., King, N., McKinney, S. M., Carignan, D., and Horvitz, E. (2023). Capabilities of GPT-4 on medical challenge problems. *arXiv:2303.13375*.

Parani, P., Mohammad, U., and Saeed, F. (2024). Utilizing pretrained vision transformers and large language models for epileptic seizure prediction. *bioRxiv*. doi: 10.1101/2024.11.03.621742

Radford, A., Wu, J., Child, R., Luan, D., Amodei, D., and Sutskever, I. (2019). Language models are unsupervised multitask learners. *OpenAI blog* 1:9.

Sano, A., Amores, J., and Czerwinski, M. (2024). Exploration of LLMs, EEG, and behavioral data to measure and support attention and sleep. *arXiv:2408.07822*.

Tung, C.-S., Liang, S.-F., Chang, S.-F., and Young, C.-P. (2024). A hybrid artificial intelligence system for automated EEG background analysis and report generation. *IEEE J. Biomed. Health Inform.* 29, 2629–2641. doi: 10.1109/JBHI.2024.3496996

Vaswani, A., Shazeer, N., Parmar, N., Uszkoreit, J., Jones, L., Gomez, A. N., et al. (2017). Attention is all you need. *arXiv:1706.03762*.

von Weltin, E., Ahsan, T., Shah, V., Jamshed, D., Golmohammadi, M., Obeid, I., et al. (2017). "Electroencephalographic slowing: a primary source of error in automatic seizure detection," in *2017 IEEE Signal Processing in Medicine and Biology Symposium (SPMB)* (IEEE), 1–5.

Wang, J., Song, Z., Ma, Z., Qiu, X., Zhang, M., and Zhang, Z. (2024a). "Enhancing EEG-to-text decoding through transferable representations from pre-trained contrastive EEG-text masked autoencoder," in *Proceedings of the 62nd Annual Meeting of the Association for Computational Linguistics (Volume 1: Long Papers)*, 7278–7292. doi: 10.18653/v1/2024.acl-long.393

Wang, Y., Gong, X., Meng, L., Wu, X., and Meng, H. (2024b). Large language model-based fmri encoding of language functions for subjects with neurocognitive disorder. *arXiv preprint arXiv:2407.10376*.

Wang, Y., Lipka, N., Rossi, R. A., Siu, A., Zhang, R., and Derr, T. (2023). Knowledge graph prompting for multi-document question answering. *arXiv:2308.11730*.

White, J., Fu, Q., Hays, S., Sandborn, M., Olea, C., Gilbert, H., et al. (2023). A prompt pattern catalog to enhance prompt engineering with ChatGPT. *arXiv:2302.11382*.

Wu, S., Koo, M., Blum, L., Black, A., Kao, L., Scalzo, F., et al. (2023). A comparative study of open-source large language models, GPT-4 and claude 2: multiple-choice test taking in nephrology. *arXiv:2308.04709*.

Yang, Y., Duan, Y., Jo, H., Zhang, Q., Xu, R., Jones, O. P., et al. (2024). Neugpt: unified multi-modal neural gpt. *arXiv preprint arXiv:2410.20916*.

Zhang, S., Alam, E., Baber, J., Bianco, F., Turner, E., Chamanzar, M., et al. (2024a). Mindspeech: Continuous imagined speech decoding using high-density fnirs and prompt tuning for advanced human-ai interaction. *arXiv preprint arXiv:2408.05362*.

Zhang, Y., Li, F., and Chang, D. (2024b). Vr rehabilitation system evaluator: a fnirs-based and llm-enabled evaluation paradigm for mild cognitive impairment. *Adv. Eng. Inf.* 62:102734. doi: 10.1016/j.aei.2024.102734

Zhang, Y., Li, Q., Nahata, S., Jamal, T., Cheng, S.-K., Cauwenberghs, G., et al. (2023). Integrating LLM, EEG, and eye-tracking biomarker analysis for word-level neural state classification in semantic inference reading comprehension. *arXiv:2309.15714*.

Zhang, Y., Yang, S., Cauwenberghs, G., and Jung, T.-P. (2024c). From word embedding to reading embedding using large language model, EEG and eye-tracking. *arXiv:2401.15681*.

Zheng, W.-L., and Lu, B.-L. (2015). Investigating critical frequency bands and channels for EEG based emotion recognition with deep neural networks. *IEEE Trans. Auton. Ment. Dev.* 7, 162–175. doi: 10.1109/TAMD.2015.2431497

Zhou, Y., Muresanu, A. I., Han, Z., Paster, K., Pitis, S., Chan, H., et al. (2022). Large language models are human-level prompt engineers. *arXiv:2211.01910*.

Zyma, I., Tukaev, S., Seleznov, I., Kiyono, K., Popov, A., Chernykh, M., et al. (2019). Electroencephalograms during mental arithmetic task performance. *Data* 4:14. doi: 10.3390/data4010014

Frontiers in Neuroinformatics

Leading journal supporting neuroscience in the information age

Part of the most cited neuroscience journal series, developing computational models and analytical tools used to share, integrate and analyze experimental data about the nervous system functions.

Discover the latest Research Topics

See more →

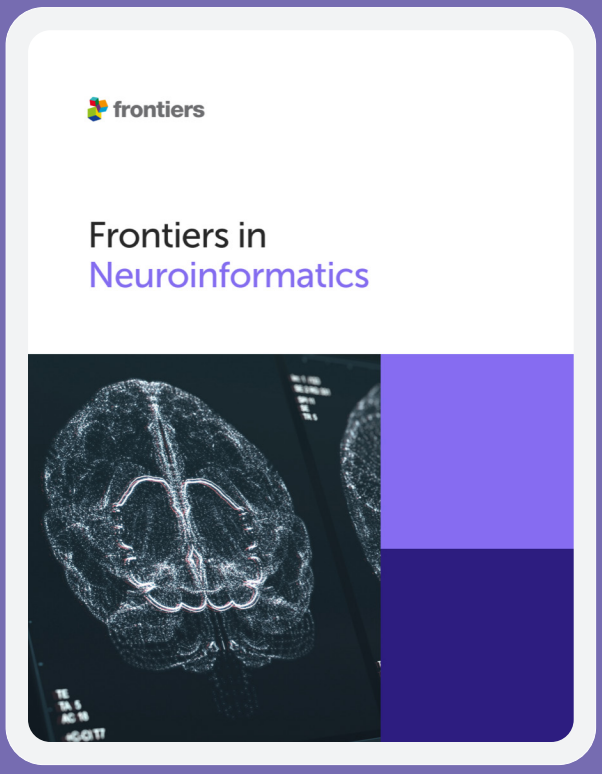

Frontiers

Avenue du Tribunal-Fédéral 34
1005 Lausanne, Switzerland
frontiersin.org

Contact us

+41 (0)21 510 17 00
frontiersin.org/about/contact